Université de Liège

Faculté des Sciences

First-Principles study of ferroelectric oxide nanostructures

Dissertation présentée en vue de l'obtention du grade de
Docteur en Sciences Physiques

par

Eric BOUSQUET

Promoteur:

Prof. Philippe GHOSEZ

Menbres du jury:

Prof. Jean-Pierre GASPARD

Prof. Maryse HOEBEKE (présidente)

Dr. Javier JUNQUERA

Dr. Jean-Yves RATY

Prof. Gian-Marco RIGNANESE

Prof. Jean-Marc TRISCONE

Juillet 2008

Acknowledgements

Well, almost five years now that I started my PhD thesis under a cloudy weather of Belgium but so well compensated by the hundred's Belgian beers and chocolates… Above all, in any case the works presented in this thesis could not have been possible without the morale support of many people. Mentor, family, friends but also people met at conferences and meetings were a source of ideas and understanding.

Foremost, I warmly thank my advisor Philippe, first for giving me the opportunity to make my thesis with him and second, for his scientific guidance, for his encouragement in anytime and especially for his sympathy.

Besides Philippe, I would like to thank my colleagues whom gave a pleasant and scientific ambiance in the lab: Marek, Gregory, Patrick, Daniel, Marco, Frederico, Satadeep and Engine.

I specially thank Gregory for his warmly *joie de vivre* during our mutual first year in Liège through the jokes, beer/good-food/wine meal and then some.

I also peculiarly thank Patrick for his friendship and our scientific discussions which improve strongly my mathematical understanding and strictness of physics (even if it was partly made in the 1,000 beers pub…).

Obviously, I also thank the colleagues from the "nearby" labs of the physics building: Céline, Marc, Huguette, Mickael, Jean-Yves, Jean-Pierre, Duy, Marcel, Pierre and most of the people from the GRASP, even if sometimes their experiments were a bit noisy…

I thank a lot the people from the DPMC group in Geneva for the good experiment/theory collaboration and their warm friendship, particularly Jean-Marc, Matt, Céline, Nicolas and Stefano.

I thank the people met in conference or in visit at Liège for the interesting scientific discussions as Xavier, Javier or Karin who gave me some help and clarification for my works. I also thank a lot the people with whom I commiserate in conferences and enliven strongly my travels. I will not enumerate them, but I think that they will recognize themselves, mostly the Quebeckers.

This is well known: to perform simulations, it is necessary to use computers and whoever says computers means computer specialists, mostly for large architectures as used in *ab-initio* calculations. I thank so the members of the SEGI group at the University of Liège as well as the members of the CISM group at the Université Catholique de Louvain.

They arrive at the end of the acknowledgements but are no more less important, family and friends. I thank a lot my parents whom overspend for my

sister and me by supporting and encouraging us during our studies. Therefore, even if what I'm doing in physics is far from their life, the open-mindedness and the humanity of my parents and my sister have really motivated me to continue in this way.

I would also like to thank my aunt Tata Bébelle for our long fascinating discussions of physics and sciences phenomena in general which help me to improve my pedagogy and my own understanding of these phenomena.

I thank the friends met in Belgium, especially Weily who, among other things, help me to improve my english pronunciation, Cheuk, Michel and Lin for their help in many occasions.

Last but not least, I also thank Delphine for her whole time support and love. Of course, many thanks to her family.

At last, I will finish with some funny statistical analysis. Trying to estimate the total CPU time used during the thesis with the output files of ABINIT and SIESTA present on my local hard-drive, I found the following data: I have about 5,000 and 600 output files for respectively ABINIT and SIESTA codes, which gives an average of 3 calculations per day during five years. From these output files, it results a cumulative CPU time of about 250,000 and 50,000 hours for respectively ABINIT and SIESTA. So, the total CPU time is about 300,000 hours, that is a little bit more than 34 years. It means that if the present thesis had been done on one processor only, it would have taken more than 34 years! And even more, this estimation do not include the crashed, restarted or cancelled calculations…

Contents

Introduction

To be ferroelectric, a material must be an insulator, exhibit a spontaneous electric polarization, and the direction of the latter must be switchable between two equivalent states by the application of a physically realizable electric field [1]. Such behavior was first experimentally observed in 1920 by Valasek in Rochelle salt [2]. Afterwards, the “ferro” term was used by analogy to the already known phenomenon of “ferromagnetism” in which a material exhibits a permanent magnetic moment, the direction of which can be reoriented by the application of a magnetic field [3].

Ferroelectricty was first associated to the presence of hydrogen since, for a long time, it was mainly observed in the family of phosphates and arsenates which contain hydrogen bounds. This link was questioned when, incidentally, ferroelectricity was observed in $BaTiO_3$, a cubic oxide perovskite, which was particularly significant in the search of ferroelectricity in other materials. From that time, the perovskite family became the subject of tremendous studies. Due to their simple crystalline structure, five atoms per cubic unit cell with generic formula ABX_3, the perovskites were used as a model for theoretical studies and were at the origin of various technological applications.

Nowadays, the family of ABO_3 perovskites is one of the most studied class of materials and beyond ferroelectricty has shown the capacity to exhibit a wide variety of properties: piezoelectricity, pyroelectricity, non-linear optics, superconductivity, magnetism, multiferroism … Due to their large dielectric constant, $BaTiO_3$ based compounds are widely used in capacitors. Since ferroelectric materials are also pyroelectric and piezoelectric, much interest was focused on the ferroelectric ABO_3 perovskites for their use in transducer applications. For example, $PbTiO_3$ based oxides like PZT are widely used in pyroelectric detector, thermal imaging, sonar, atomic force microscope (AFM), acoustic sensors, *etc.* The use of the ferroelectric property itself was only recently exploited in the electronic memory technologies: since it is possible to switch the polarization between two opposite orientations by applying an external electric field, they were considered to be good candidates for the non-volatile memory devices [4]. Nowadays, ferroelectric memories (FeRAM) integrate various devices such as smart-card or the Play Station 2.

Linked to the miniaturization of the electronic chips, the use of perovskite oxides in microelectronics has motivated the study of their properties at the nanoscale. It was argued that reducing the physical dimensions should alter the ferroelectric properties and large critical thicknesses for ferroelectricity were first suggested in thin films (∼10 nm). Nevertheless, as the quality of ultra-thin films was improving, recurrent smaller and smaller critical sizes were demonstrated. This was undermined by recent results whom suggested a much smaller critical size [5, 6]. It is now better understood that the evolution of the ferroelectric properties in nanostructure is not an intrinsic effect but is mainly driven by extrinsic mechanical and electrical boundary conditions [7].

In this context, since 20 years, ferroelectric oxides have been intensively studied from first-principles calculations. First-principles simulations allow to describe the properties of materials at the atomic-scale level through the fundamental laws of quantum mechanics and electromagnetism. Since they are only based on the fundamental physics laws, no empiric adjustable parameter is needed. For this reason, even if some approximations are made in practice, they are called *first-principles* or *ab-initio* techniques. Density functional theory (DFT) is nowadays the most widely used first-principles method in condensed matter physics [8]. It offers the opportunity to obtain valuable information about the microscopic origin of the material properties, among others ferroelectricity. This method revealed particularly interesting for the study of the ferroelectric nanostructures like thin films, superlattices, nanowires and nanoparticles. This was made possible thanks to the fast increase of the computational power as well as the development of more efficient algorithms. The increasing power of the first-principles calculations was recently joined up the increasing possibilities to control and characterize the compound synthesis at the atomic scale, opening up a fruitful dialogue between theory and experiment.

In this context, our purpose will be to investigate the finite-size effects in ferroelectric oxide nanostructures from first-principles. Starting from a description of the established ferroelectric properties at the bulk level, we will anticipate the possible finite-size effects in nanostructures. Then, from a discussion of the already known finite-size effects in ferroelectric nanostructures, we will investigate such size effects in thin films, superlattices and nanowires and, going beyond previous studies, we will explore the possibilities to have new and unexpected behaviors in such nanostructures. Moreover, the present work will be in the continuity of the opened theoretical/experimental dialogue, since we will work with experimentalists to highlight some finite-size effects in grown ferroelectric nanostructures as well as to propose new materials to be synthetized.

The manuscript is organized as follows. In Chapter 1, we describe the theoretical details associated to the first-principles method used all along the thesis. We briefly present the density functional theory, its numerical implementation as it is performed in the ABINIT package [9] as well as the modern theory of polarization. In Chapter 2, we review the general properties of the ABO_3 oxides through the case of four selected perovskites: $BaTiO_3$, $SrTiO_3$, $PbTiO_3$ and $CaTiO_3$. The concept of soft mode is introduced and will allow to describe the two main structural phase transitions occurring in such compounds: the ferroelectric (FE) phase transition and the antiferrodistortive (AFD) phase transition. From the expected main properties potentially sensible to be modified in the finite-size heterostructures, we present in the Chapter 3 the known finite-size effects on the physics of the ABO_3 nanostructures. The mechanical and electrical boundary conditions are the main effects discussed through the epitaxial strain, the surface/interface relaxations or the concept of depolarizing field. From that general considerations, we present in Chapter 4 results obtained for $BaTiO_3$ under high pressure and the effect of the epitaxial strain on the $SrTiO_3$, $PbTiO_3$ and $CaTiO_3$ at the bulk level. Going beyond previous works, we investigate in details the effect of strain on the competition between FE and AFD instabilities. In Chapter 5 we report an example of theoretical/experimental dialogue through the study of $PbTiO_3$/$SrTiO_3$ superlattices, which constitute a typical case of ferroelectric/incipient-ferroelectric interface. We show that $PbTiO_3$/$SrTiO_3$ superlattices exhibit in the limit of ultra-short periods an unexpected behavior, distinct from that of the parent compounds and demonstrate that is due to an unexpected coupling between the FE and the AFD structural instabilities at the layer interface. Afterwards, we consider different bicolor superlattices and discuss how the intrinsic properties of the different compounds tend to shift or even suppress the interface coupling. In Chapter 6, we consider a prototypical example of ferroelectric/insulator superlattices: $BaTiO_3$/BaO. We analyze the phonon dispersion curves and point out the existence of antiferroelectric instabilities at the zone boundary, which are more relevant than the ferroelectric instability itself. In Chapter 7 we investigate the unexpected possibility to induce ferroelectricty in thin films and superlattices of AO oxides. In Chapter 8, finite-size effects in one dimensional $BaTiO_3$ nanowires is presented. As a second part, the concept of the ferroelectric correlation volume is also reinvestigated, highlighting that it is ill-defined concept that cannot be uniquely defined. At last, we summarize all the results in the conclusion and propose some future perspectives.

Chapter 1

First-principles background

1.1 Introduction

The aim of this chapter is to provide a brief overview of first-principles techniques used all along the present thesis. No mathematical details are reported, only the general equations and approximations are described, allowing to show the general framework within which the physical properties discussed later have been determined.

First-principles calculations in solid state physics are based on the equations of quantum mechanics and electromagnetism. In the first part of this chapter we describe the general way to access the properties of materials at the atomic scale within the widely used Born-Oppenheimer approximation. In the next two sections, we present the basics of Density Functional Theory (DFT) and the related exchange-correlation approximations. The accessible physical quantities coming from Density Functional Perturbation Theory (DFPT) are introduced in the fourth section. The special case of the polarization is discussed separately in the next section as it is calculated in the framework of the modern theory of polarization. We then detail the practical numerical implementation as it is used in the present study: pseudopotentials, k-point sampling, supercell, ...

1.2 Many-body problem

In the time-independent quantum mechanics, the physics of a system of interacting particles is described by the following Schrödinger equation:

$$H\Psi = E\Psi, \tag{1.1}$$

where H is the Hamiltonian of the system, Ψ is the wave function for all the particles ("many-body" wave function) and E is the corresponding energy.

In solid state physics, the starting point is the Hamiltonian for a system of interacting electrons and nuclei:

$$H(\boldsymbol{R}, \boldsymbol{r}) = T_N(\boldsymbol{R}) + T_e(\boldsymbol{r}) + V_{NN}(\boldsymbol{R}) + V_{ee}(\boldsymbol{r}) + V_{eN}(\boldsymbol{R}, \boldsymbol{r}), \tag{1.2}$$

where $\boldsymbol{R} \equiv \{\boldsymbol{R}_I\}$ labels the set of all the nuclear coordinates $\boldsymbol{R}_I$ and $\boldsymbol{r} \equiv \{\boldsymbol{r}_i\}$ labels the set of all the electronic coordinates $\boldsymbol{r}_i$. T_N and T_e are respectively the kinetic energy operator of nuclei and electrons, V_{NN}, V_{ee}, V_{eN} are the electrostatic potential energy operators between respectively nuclei, electrons and electrons and nuclei:

$$T_N = -\frac{\hbar^2}{2} \sum_I \frac{1}{M_I} \frac{\partial^2}{\partial \boldsymbol{R}_I^2}, \tag{1.3}$$

$$T_e = -\frac{\hbar^2}{2m} \sum_i \frac{\partial^2}{\partial \boldsymbol{r}_i^2}, \tag{1.4}$$

$$V_{NN} = \frac{e^2}{2} \sum_{I \neq J} \frac{Z_I Z_J}{\|\boldsymbol{R}_I - \boldsymbol{R}_J\|}, \tag{1.5}$$

$$V_{ee} = \frac{e^2}{2} \sum_{i \neq j} \frac{1}{\|\boldsymbol{r}_i - \boldsymbol{r}_j\|}, \tag{1.6}$$

$$V_{eN} = -e^2 \sum_{iI} \frac{Z_I}{\|\boldsymbol{r}_i - \boldsymbol{R}_J\|}, \tag{1.7}$$

where Z_I is the charge of ion I with mass M_I, m is the mass of the electron and $-e$ its elementary charge.

In the Born-Oppenheimer approximation, by considering the large nuclei masses appearing in Eq. (1.3), the kinetic energy of the nuclei is treated as a perturbation on the Hamiltonian for the electrons:

$$H_e(\boldsymbol{R}, \boldsymbol{r}) = T_e(\boldsymbol{r}) + V_{NN}(\boldsymbol{R}) + V_{ee}(\boldsymbol{r}) + V_{eN}(\boldsymbol{R}, \boldsymbol{r}). \tag{1.8}$$

It results that no differential operator is acting on the set of atomic positions $\boldsymbol{R}$ that can consequently be treated as parameters in H_e. In this context, the electronic Hamiltonian includes the kinetic energy operator of the electrons T_e, plus their interaction energy operator V_{ee} and the potential energy operator due to the interaction of the nuclei on the electrons V_{eN} which can be seen as the energy of the electrons in the fixed external potential of the nuclei. The V_{NN} term is the classical interaction of nuclei that can be trivially obtained.

In summary, the quantum description of a solid is achieved through the Schrödinger equation and a relaxed many-body electronic wave function $\Psi(\boldsymbol{r})$. From the quantum Hamiltonian and the electronic wave function, the total energy, electronic density and eigenstates of any operator can be calculated at any ionic positions. Moreover, the forces (Hellmann-Feynman theorem [10]) and stresses (generalized Virial theorem [11]) can also be computed and minimized to find the equilibrium ionic geometry of the system.

1.3 Density Functional Theory

As introduced in the previous section, the description of solids consists into the determination of the total energy of a system of interacting electrons and ions. However, even by using the Born-Oppenheimer approximation, the description of interacting electrons of N ions in a macroscopic solid ($N \sim 10^{23}$) remains impossible. In practice other simplifications are required to estimate the electron-electron interactions in a fine down way.

Density Functional Theory (DFT) was built in the 60's by Hohenberg and Kohn [12] and Kohn and Sham [13] who provided a method for estimating the many-body electron-electron interactions. In the first paper, the authors showed that the electronic density of the ground state of a quantum many-body system can be considered as the fundamental quantity of the problem so that all ground-state properties of the system can be considered as unique functional of the ground state density. It means that the electronic ground-state of the system is given by the density which minimizes an appropriate energy functional. Although the theorem of Hohenberg and Kohn demonstrated the existence of such a functional but did not provide any indication on its explicit form.

The second paper provided an *ansatz* formulation of the density functional theory allowing to treat in practice the many-body system that corresponds to the actual first-principles implementation for treating electrons in condensed matter. In this approach, the idea is to replace the original many-body electron problem by an alternative fictitious independent-particles problem. In this framework, the density of the system is given througth the one-electron orbital $\psi_i(\boldsymbol{r})$ as following (assuming the spin-degeneracy):

$$n(\boldsymbol{r}) = \sum_i |\psi_i(\boldsymbol{r})|^2. \tag{1.9}$$

The total electronic energy is given by

$$\begin{aligned} E_{KS}[\psi_i] = & -\frac{1}{2}\sum_i < \psi_i|\,\nabla^2\,|\psi_i > + \frac{1}{2}\int \frac{n(\boldsymbol{r})n(\boldsymbol{r'})}{||\boldsymbol{r}-\boldsymbol{r'}||}d\boldsymbol{r}d\boldsymbol{r'} \\ & + E_{xc}[n(\boldsymbol{r})] + \int V_{ext}(\boldsymbol{r})n(\boldsymbol{r})d\boldsymbol{r} + E_{NN}, \end{aligned} \tag{1.10}$$

where the first term corresponds to the kinetic energy of the independent electrons, the second terms is the classical Coulomb energy (Hartree energy E_H) of the electron density $n(\boldsymbol{r})$, the third term is the exchange and correlation energy between electrons, the fourth term is the energy of electrons in the external potential V_{ext} created by the ions and the last term is the interaction between nuclei [see Eq. (1.5)]. All of these terms are well defined except the exchange-correlation energy functional $E_{xc}[n(\boldsymbol{r})]$ that contains all the electronic interactions going beyond the classical Coulomb interaction. If the exact functional $E_{xc}[n(\boldsymbol{r})]$ is provided, then the exact ground-state energy and density of the many-body electrons problem can be determined.

For a given set of atomic positions, the ground state is determined via the minimization of Eq. (1.10) under the following orthonormalization constraints:

$$< \psi_i|\psi_j >= \delta_{ij}, \tag{1.11}$$

giving rise to the total energy and the the electronic density of the system. The minimisation of Eq. (1.10) with the constraint 1.11 can be achieved using the

Lagrange multiplier method by minimizing the following equation:

$$F[\psi_i] = E[\psi_i] - \sum_{i,j}^{occ} \Lambda_{ij} \left(< \psi_i | \psi_j > - \delta_{ij} \right), \tag{1.12}$$

where Λ_{ij} are the Lagrange multipliers. The corresponding Euler-Lagrange equation is:

$$H|\psi_i >= \sum_j \Lambda_{ij} |\psi_j >, \tag{1.13}$$

where the Hamiltonian is:

$$H = -\frac{1}{2} \bigtriangledown^2 + v_{ext} + v_H + v_{xc}. \tag{1.14}$$

The Hartree and exchange-correlation potentials, respectively v_H and v_{xc} are defined as the functional derivative of the Hartree and exchange-correlation energy with respect to the density:

$$v_H = \frac{\delta E_H[n]}{\delta n(\boldsymbol{r})}, \tag{1.15}$$

and

$$v_{xc} = \frac{\delta E_{xc}[n]}{\delta n(\boldsymbol{r})}. \tag{1.16}$$

The solution of Eq. (1.13) is not unique since we can always apply a unitary transformation U to the wave functions of the occupied states,

$$|\psi_i > \longmapsto \sum_j^{occ} U_{ij} |\psi_j >, \tag{1.17}$$

and keep invariant the energy or the density. Such a freedom is called gauge transformation and in practice we must fix the gauge. Since the Hamiltonian is a hermitian operator, we can fix the gauge to the so-called diagonal gauge where the Lagrange multiplier matrix is diagonal:

$$\Lambda_{ij} =< \psi_j | H | \psi_i >= \varepsilon \delta_{ij}. \tag{1.18}$$

In practice, the resolution of Eq. (1.10) is obtained by a self-consistent procedure. The starting point of this procedure is to give an initial configuration of the ions (set of positions $\boldsymbol{R}$) and the electronic density $n(\boldsymbol{r})$ and to solve the following Kohn-Sham equations:

$$\begin{cases} \left[-\frac{1}{2} \bigtriangledown^2 + v_s \right] |\psi_i >= \varepsilon_i |\psi_i > \\ \\ v_s(\boldsymbol{r}) = v_{ext}(\boldsymbol{r}) + \int \frac{n(\boldsymbol{r}_1)}{|\boldsymbol{r}_1 - \boldsymbol{r}|} d\boldsymbol{r}_1 + \frac{\delta E_{xc}[n]}{\delta n(\boldsymbol{r})} \\ \\ n(\boldsymbol{r}) = \sum_i^{occ} \psi_i^*(\boldsymbol{r}) \psi_i(\boldsymbol{r}) \end{cases} \tag{1.19}$$

The resulting new electronic density $n'(\boldsymbol{r})$ is compared with the previous density $n(\boldsymbol{r})$ and if differences exist between them, the Kohn-Sham Eq. (1.19) are solved again by starting with a new density which is a mix of $n(\boldsymbol{r})$ and $n'(\boldsymbol{r})$ densities. This procedure is done until the self-consistency is achieved [*i.e.* $n(\boldsymbol{r})$=$n'(\boldsymbol{r})$] [1].

1.4 Approximate exchange-correlation functionals

The Kohn-Sham method allows to determine the exact ground state of a system of many-body electrons if the exchange and correlation between electrons are known. However, the exact exchange-correlation term is not known and approximations are needed to estimate this term.

The first approximation proposed was the Local Density Approximation (LDA) in which the exchange-correlation energy per electron is supposed to only depend on the density at this point, and that this exchange-correlation energy is assumed to be the same than homogeneous electron gas with that density:

$$E_{xc}^{LDA}[n] = \int \epsilon_{xc}^{hom}[n(\boldsymbol{r})]n(\boldsymbol{r})d\boldsymbol{r}. \tag{1.20}$$

The exchange part of the homogeneous gas can be obtained from Hartree-Fock technique, which gives a simple analytic form:

$$\epsilon_{x}^{hom}[n] = -\frac{3}{4\pi}\left(3\pi^2 n\right)^{1/3}. \tag{1.21}$$

The correlation part $\epsilon_c^{hom}[n]$ was calculated with Monte-Carlo simulation of the homogeneous electron gas [14].

Even if the LDA approximation is strong, it works remarkably well in many cases, which makes this approximation the most widely used in solid state simulations [15]. Typical errors of LDA approximation with respect to experimental data, are within about 1% on atomic positions and lattice constants and within 5% on phonon frequencies. The strongest error is obtained on the electronic bandgap estimation, which is systematically underestimated with respect to the experiments.

Let us simply mention that alternative available approximations such as the generalized gradient approximations (GGA) [16, 17], the weighted density approximation (WDA) [18] or hybrid functionals were also developed to go beyond the LDA and improve its deficiencies.

1.5 Density Functional Perturbation Theory

A wide range of physical properties (mechanical, dielectric, dynamical, ...) depends on the derivative of the total energy with respect to perturbations like

---

[1] In practice the maximum difference between $n(\boldsymbol{r})$ and $n'(\boldsymbol{r})$ at any point is below a given threshold.

strain, electric field, atomic displacement... The Hellmann-Feynman theorem allows to provide the first-order derivatives of the energy as the forces and stresses while the Berry phase approach gives access to the polarization (this last approach will be describe in the next section). The higher-order derivatives can be determined through a finite difference of the first-order derivatives, giving access to properties like phonons, elastic constants or dielectric tensors. This can be done by freezing into the structure finite values of the perturbation and extracting derivatives from a finite difference formula (frozen-phonon technique).

It is also possible to access to these derivatives by using the perturbation theory. The application of the perturbation theory on the DFT is called the Density Functional Perturbation Theory (DFPT) [19]. An accurate way to calculate the energy-derivatives was proposed by X. Gonze [20–24] which is based on a variational principle involving a minimization procedure rather than solving the Sternheimer equation and giving also access to non-linear responses thanks to the '$2n+1$" theorem.

Let us consider the three types of perturbations associated to atomic displacements $\boldsymbol{R}$, homogeneous strain η, and homogeneous electric field $\mathcal{E}$, and summarize them into a single parameter λ, then the energy functional $E(\lambda)$ can be expanded in a power series of λ around the ground state structure λ=0:

$$E(\lambda) = E(0) + \sum_i \left.\frac{\partial E}{\partial \lambda_i}\right|_0 \lambda_i + \frac{1}{2}\sum_{i,j} \left.\frac{\partial^2 E}{\partial \lambda_i \partial \lambda_j}\right|_0 \lambda_i \lambda_j + ... \tag{1.22}$$

If, for the purpose of the illustration, we limit the expansion to second order, the corresponding physical quantities accessible are reported in Table 1.1. The first-order derivatives with respect to atomic positions allow to determine the forces on the atoms (F), the first-order derivatives with respect to strains allows to access to the stress tensor (σ) and the first-order derivatives with respect to electric field allow to compute the spontaneous polarization (P). The second-order derivatives give access to the linear response of solid as the interatomic force constants (C), the optical dielectric tensor (ϵ^∞), the clamped-ion elastic constant (c^0), the Born effective charges tensor (Z^*), the clamped-ion piezoelectric tensor (e^0) and the internal strain coupling parameters (γ). From those quantities, additional physical properties can be computed such as the phonon frequencies and dispersion curves, the static dielectric tensor, the piezoelectric and elastic tensors, the LO-TO splitting, *etc.*

λ	1^{st} order	2^{nd} order		
		$\boldsymbol{R}$	η	$\mathcal{E}$
$\boldsymbol{R}$	F	C	γ	Z^*
η	σ	γ	c^0	e^0
$\mathcal{E}$	P	Z^*	e^0	ϵ^∞

Table 1.1: Physical quantities related to first and second-order derivatives of the energy with respect to atomic positions $\boldsymbol{R}$, homogeneous strains η and electric fields $\mathcal{E}$.

1.6 Polarization

The spontaneous polarization is an essential quantity for the description of dielectric materials and related properties (pyroelectricity, piezoelectricity, ferroelectricity, dynamical effective charges, *etc*). However, during long time, the exact microscopic polarization definition in periodic systems was an ambiguous concept. The main standard description of the polarization was based on the Clausius-Mossoti model, which was usually associated to the calculation of a dipolar moment by unit cell originating from the differentiation of the mass center of the positive and negative charges. However, in real materials it is not possible to localize unambiguously the "position" of the electronic charge, mainly in the ferroelectric oxides ABO_3 which have a mixed ionic/covalent character of bounds. It resulted that the tentative to define the polarization via the charge distribution is totally inadequate [25–27].

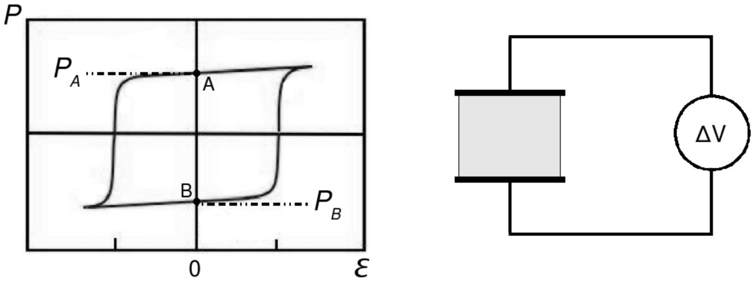

Figure 1.1: (Left) A typical hysteresis loop measurement of the polarization with respect to the electric field. The spontaneous polarization of the ferroelectric material is the twice of the difference between the zero field polarizations P_A and P_B. (Right) Schematic view of the experimental device for the measure of the spontaneous polarization with respect to an applied electric field: the crystal is squeezed into a capacitor and the current flowing through the circuit is measured [26].

Absolute polarization in periodic systems is an ill-defined quantity and only changes in polarization are affordable. Experimentally, the method to estimate the spontaneous polarization of ferroelectric materials is through the polarization differences rather than the extraction of the polarization itself. In a ferroelectric material, the spontaneous polarization ($\boldsymbol{P}$) can be reversed to its symmetric opposite direction (-$\boldsymbol{P}$) via an electric field. This switchability of the polarization is exploited in experimental measurements through the resulting hysteresis loop of $\boldsymbol{P}$ versus electric field $\mathcal{E}$ (Figure 1.1). From the two zero electric field positions A and B in Figure 1.1, the spontaneous polarization can be evaluated as $(P_A\text{-}P_B)/2$. This histeresis loop is obtained experimentally by the measurement of the integrated macroscopic current $\boldsymbol{j}(t)$ through the sample (as schematically represented in Figure 1.1, right) during a time Δt:

$$\Delta\boldsymbol{P} = \int_0^{\Delta t} \boldsymbol{j}(t)dt = \boldsymbol{P}(\Delta t) - \boldsymbol{P}(0) \tag{1.23}$$

In periodic solids, the electric field is fixed to vanish and the application of the Born-Oppenheimer approximation allows to decompose the Eq. (1.23) into an ionic contribution and an electronic contribution:

$$\Delta \boldsymbol{P} = \Delta \boldsymbol{P}_{ion} + \Delta \boldsymbol{P}_{el}. \tag{1.24}$$

If the starting point is considered as the unpolar high symmetric phase $\boldsymbol{P}(0)$=0, the difference of polarization becomes:

$$\Delta \boldsymbol{P} = \boldsymbol{P} = \boldsymbol{P}_{ion} + \boldsymbol{P}_{el}, \tag{1.25}$$

where $\boldsymbol{P}$ is the total polarization of the system in its final state, $\boldsymbol{P}_{ion}$ its ionic contribution and $\boldsymbol{P}_{el}$ its electronic contribution. The ionic part can be written in the same way than in the Clausius-Mossotti definition:

$$\boldsymbol{P}_{ion} = \frac{e}{\Omega} \sum_{\kappa} Z_{\kappa} \boldsymbol{R}_{\kappa}, \tag{1.26}$$

where Ω is the volume of the cell and Z_{κ} is the charge of the ion κ at the position $\boldsymbol{R}_{\kappa}$. The electronic polarization can be formulated as a Berry phase of the occupied bands [28]:

$$\boldsymbol{P}_{el} = -\frac{2ie}{(2\pi)^3} \sum_{n=1}^{m} \int_{BZ} < u_{n\boldsymbol{k}} | \nabla_{\boldsymbol{k}} | u_{n\boldsymbol{k}} > d\boldsymbol{k}, \tag{1.27}$$

where m is the number of occupied electronic bands, $u_{n\boldsymbol{k}}$ is the lattice-periodical part of the Bloch wave function $\psi_{n\boldsymbol{k}}(\boldsymbol{r})$=$\mathrm{e}^{i\boldsymbol{k}.\boldsymbol{r}}$ $u_{n\boldsymbol{k}}(\boldsymbol{r})$. This expression of the electronic contribution is the main result of the modern theory of polarization as developed by King-Smith and Vanderbilt [28]. Implicitly, this expression is allowed only if the system stays insulating everywhere along the path and this expression is independent of the path and depends only on the final state.

In practical calculations, the integration over the Brillouin zone is performed on a discrete grid of k-points. Moreover this expression of the polarization is only defined modulo a quantum of polarization e$\boldsymbol{R}/\Omega$, where $\boldsymbol{R}$ is a lattice vector. However, typical magnitudes of spontaneous polarization in ferroelectric systems are usually less than 0.8 C/m^2 while the order of the quantum phase of polarization is larger than 1 C/m^2 and so, a reference choice for the phase is usually easy to fix. When ambiguity appears about the identification of the quantum factor, the polarization should be computed between two points on the path involving small change of the polarization to identify the quantum factor [26].

1.7 Practical implementation

Even if the Born-Oppenheimer approximation, DFT approach, and approximations on the exchange-correlation energy are powerful to estimate the many-body interactions of electrons in solids, other simplifications should be performed to solve numerically the Kohn-Sham equations.

1.7.1 Basis set approximation: plane waves and cutoff energy

For an infinite solid with the Born-Von Karman periodic boundary conditions, the wave function can be written in the Bloch form as a product between a plane wave and a lattice periodic function $u_n(\boldsymbol{k}, \boldsymbol{r})$:

$$\psi_{n,\boldsymbol{k}}(\boldsymbol{r}) = \frac{1}{\sqrt{\Omega}} u_n(\boldsymbol{k}, \boldsymbol{r}) e^{i\boldsymbol{k}\boldsymbol{r}}, \tag{1.28}$$

where Ω is the volume of the cell, $\boldsymbol{k}$ a wave-vector of the reciprocal space and n the energy band indice. These Bloch functions are in practice decomposed in a Fourier expansion:

$$\psi_{n,\boldsymbol{k}}(\boldsymbol{r}) = \frac{1}{\sqrt{\Omega}} \sum_{\boldsymbol{G}} C_{n,\boldsymbol{k}}(\boldsymbol{G}) e^{i(\boldsymbol{k}+\boldsymbol{G})\boldsymbol{r}}, \tag{1.29}$$

where $\boldsymbol{G}$ is a vector of the reciprocal space.

However, this Fourier transform of the Bloch functions involves infinite number of plane waves to describe exactly the Bloch functions. In practice, the plane wave expansion is truncated to plane waves with energy lower than a cut-off energy E_{cut} such as:

$$\frac{\hbar^2}{2m} |\boldsymbol{k} + \boldsymbol{G}|^2 \leq E_{cut}. \tag{1.30}$$

Obviously, convergence studies must be performed in each case by increasing this cut-off energy.

1.7.2 Brillouin zone grid

The electronic density is calculated from the integration of the square modulus of the Bloch functions on all occupied energy bands n and over the Brillouin zone. The integration over the reciprocal space involve the knowledge of the Bloch functions over an infinite $\boldsymbol{k}$ points. Therefore, a finite selection of $\boldsymbol{k}$ points must be used in practice for the integration. One of the techniques developped to sample the reciprocal space is the one of H. J. Monkhorst and J. D. Pack [29] which allows to define judiciously a finite mesh of $\boldsymbol{k}$ points in each direction. This set of k-points depends on the symmetry of the system and must be converged in each case study by increasing its size.

1.7.3 Pseudopotentials

The truncation on the plane wave expansion is mandatory to perform numerical calculations, but rises problems for a good description of the core electrons as well as the valence electrons close to the nucleus. Since the wave functions of these particular electrons evolve strongly in the central region around the nuclei, a large number of plane wave must be used to describe correctly these electrons, which increases strongly the time consuming of the calculations [8].

To solve this problem, the pseudopotential approach [30] was created by considering the following approximations: (i) the electronic properties of the molecules and the solids are mainly governed by the valence electrons while the core electrons can be considered as frozen (frozen-core approximation); (*ii*) the central region of the valence electronic wave functions is tiny involved in the chemical properties of the atoms and so, the nucleus potential can be replaced by a smooth pseudo-potential.

The first approach is based on the observation that in many situations, the physical and chemical properties of solids are essentially dependent on the valence electrons. Additionally to that, it is expected that the core electrons that do not directly participate to the chemical bonding are only slightly affected by modifications of the atomic environment. It may therefore reasonably be expected that the configuration of the core electrons within the solid is equivalent to that of the isolated atoms.

The second problem is solved by the pseudopotential approximation in which the ionic potential screened by the core electrons is replaced by another fictitious potential such that the valence wavefunctions remain unchanged beyond a given cut-off radius and are replaced by smoothly varying function inside the core region. In practice, a reference calculation is performed for the isolated atom with all of its electrons and then, an analytical pseudopotential is fitted in order to reproduce the all-electron calculation. It is then expected that such pseudopotential is transferable to the solid.

These two approximations allow to decrease strongly the number of plane waves involved in the Bloch expansion as well as the number of electrons to be considered in the Kohn-Sham equation and so to decrease the time demanding calculation. Let us mention that many types of pseudopotential constructions were developed [31] and in our calculations we adopted extended norm-conserving, highly transferable pseudopotentials, as proposed by Teter [32].

1.7.4 Supercell approach

The periodic boundary conditions allow the study of atoms in the unit cell of a bulk material. However these periodic boundary conditions are less appropriate for the study of isolated systems surrounded by vacuum (thin films, nanowires, nanodots, . . .). In such systems, a supercell approach must be used, embedding the isolated system to be studied by a vacuum region sufficiently large to avoid artificial interactions with its periodic images as shown in Figure 1.2.

In the case of a plane-wave expansion, the plane waves are not localized around the atoms and also expand in the vacuum region. This is particularly tricky for the computational cost which will increase rapidly with the size of the vacuum region. In such cases, a better solution is to use a local basis set for the wave functions [33].

Moreover, in case of ferroelectric compounds the periodic boundary conditions can generate non-vanishing electric field in the vacuum region which generate an artificial interaction between periodic images. These interactions can be minimized by increasing the distances between periodic images but when a polarization is present perpendicularly to the surface, a depolarizing electric field will prevent the states with polarization perpendicular to the surface.

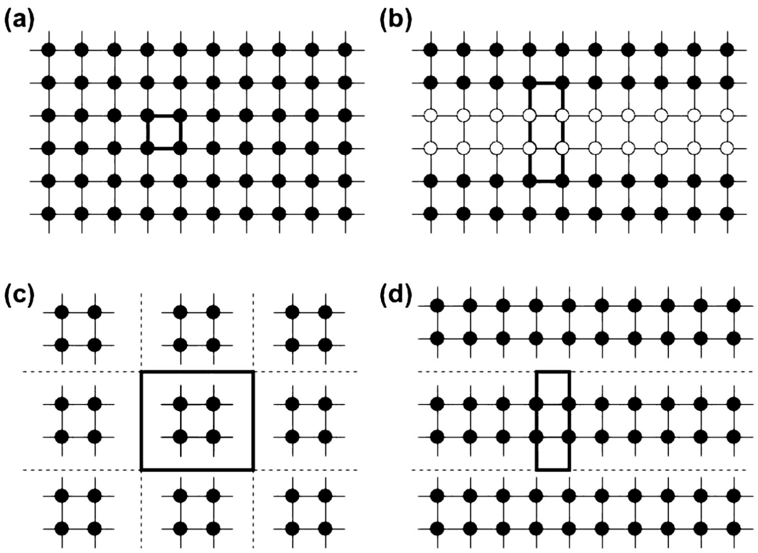

Figure 1.2: Schematic view of the possible unit cell with the periodic boundary conditions for a bulk crystal (a), for a superlattice (b), for a nanoparticle surounded by vacuum (c) and for a thin film embedded in vacuum (d) (from [7]).

1.8 Technical details

All the results reported in this thesis are based on the theoretical and practical considerations presented in the previous sections. Most of them were obtained using the ABINIT package [2] [9]. The ABINIT package is an open source software, made under a General Public License GNU, which allows to access freely to the sources of the program and eventually modify it as well as to distribute it. ABINIT is a DFT program allowing to access to the total energy, charge density and electronic structure of systems made of electrons and nuclei as the molecules and periodic solids. It is possible to perform optimization of the geometries from the DFT forces and stresses as well as to access to the response functions as the phonons, Born effective charges or dielectric tensors through the Density Functional Perturbation Theory (DFPT). The Berry phase method to compute the spontaneous polarization is also implemented. For the most implemented possibilities, it employs planewave basis set and pseudopotential method. Another capabilities are also present as the exited states (TDDFT [34], GW [35] methods) or the PAW [36] basis set, but are not used in the present thesis.

All of the results were calculated through the LDA approximation for the exchange-correlation energy and the most simulations were done with an energy

---

[2] `http://www.abinit.org`

cut-off of 45 Ha [3] for the planewave expansion. The Teter parametrization [32] for pseudopotentials was used where the following orbitals are treated as valence states: 5s, 5p and 6s for the Ba atom, 5s, 5p and 6s for the Pb atom, 4s, 4p and 5s for the Sr atom, 3s, 3p and 4s for the Ca atom, 3s, 3p, 3d and 4s for the Ti atom and 2s and 2p for the O atom. In the 5 atoms perovskite unit cell ABO_3, a Monkorsh-Pack mesh of 6×6×6 k-points was used in the Brillouin zone, giving accurate results. The vibrational properties, Born effective charges and dielectric tensors were calculated using the DFPT [23] while the piezoelectric constants were calculated using the metric tensor formulation of strain as described in Ref.[37].

These technical details are the main general characteristics of the most simulations performed here, but for some studies other criterions or even codes (SIESTA, [33]) were employed, which will be specified in the corresponding sections.

1.9 References

Good reviews of the DFT methods can be found in the following:

- R. M. Martin, "*Electronic Structure, Basic Theory and Practical Methods*", Cambridge University Press (2004).
- R. O. Jones and O. Gunnarsson, Rev. Mod. Phys. **61**, 689 (1989).

For the DFPT theory:

- X. Gonze and C. Lee, Phys. Rev. B **55**, 10355 (1997).
- S. Baroni, S. de Gironcoli, A. Dal Corso and P. Giannozzi, Rev. Mod. Phys. **73**, 515 (2001).

Reviews for the modern theory of polarization:

- R. Resta, Rev. Mod. Phys. **66**, 899 (1994).
- R. Resta, J. Phys: Condens. Matter **112**, R107 (2000).
- R. Resta and D. Vanderbilt, in "*Physcis of Ferroelectrics, A modern Perspective*", edited by K. Rabe, Ch. H. Ahn and J.-M. Triscone, Springer (2007).

Free useful tools for group theory and symmetry analysis can be found in the following web sites:

- `http://www.cryst.ehu.es/`
- `http://stokes.byu.edu/isotropy.html`

---

[3] 1 Hartree (Ha) = 27.2113961 eV $\simeq$ 2 Rydbergs

Chapter 2

Physics of ABO_3 perovskites

2.1 Introduction

A wide range of ABO_3 oxide compounds adopts a cubic *perovskite* structure. This generic name comes from the mineral *perovskite* $CaTiO_3$ which crystallizes into a cubic unit cell with five atoms at high symmetric positions as presented in the Figure 2.1: taking the A atom as reference, at the corner of the cube, the B atom is at the center and the O atoms are located at the center of the faces. The space group of this cubic perovskite is $Pm\bar{3}m$ (No 221) that corresponds in most cases to the high temperature paraelectric structure. When the temperature is lowered, these compounds can undergo different types of polar or non-polar structural phase transitions.

For example, $BaTiO_3$ exhibits a sequence of three ferroelectric (FE) phase transitions from cubic to successively: (i) a tetragonal phase ($T_C \simeq 130°C$) in which the polarization is oriented along the [001] axis ($P4mm$, No 99), (ii) an orthorhombic phase ($T_C \simeq 0°C$) with polarization oriented along [011] ($Pmm2$, No 25) and (iii) a rhombohedral phase ($T_C \simeq -80°C$), with polarization oriented along [111] ($P3m1$, No 156). If the center of mass is taken as reference, the transition from cubic to tetragonal phase is characterized by an opposite shift of cations and O atoms, giving rise to a spontaneous polarization. Furthermore, these polar distortions are associated to a small modification of the cell size and shape.

Differently, $SrTiO_3$ has only one phase transition from a paraelectric cubic phase to a non-polar antiferrodistortive (AFD) tetragonal phase ($I4/mcm$, No 140) at a temperature $T_C \simeq 100$ K. This AFD phase arises from rotations of oxygen octahedra around the tetragonal axis, such that the total atomic displacements keep the crystal non-polar (see Figure 2.4). Nevertheless, $SrTiO_3$ compound is nearly ferroelectric in the sense that the herald of a ferroelectric phase transition is expected at very low temperature, but is never observed. It was demonstrated that the suppression of the ferroelectric phase transition is due to quantum fluctuations [38]. Materials presenting such behavior ($SrTiO_3$

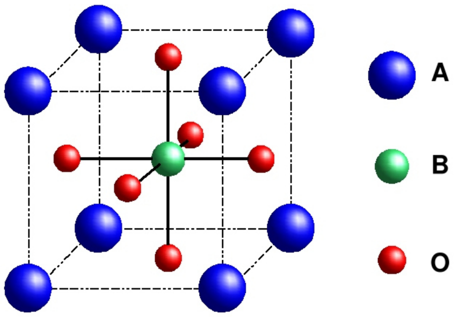

Figure 2.1: Schematic representation of the ideal ABO_3 perovskite.

[38], $CaTiO_3$ [39, 40], $KTaO_3$ [41, 42], ...) are called incipient-ferroelectrics (or quantum ferroelectrics).

The tendency of ABO_3 perovskites to be either ferroelectric or antiferrodistortive can be estimated from the Goldschmidt tolerance factor :

$$t = \frac{R_A + R_O}{\sqrt{2}\,(R_B + R_O)}, \tag{2.1}$$

where R_A, R_O and R_B are the ionic radii of respectively the A, O and B atoms in the ABO_3 structure. Perovskites with tolerance factor $t > 1$ have usually the tendency to be ferroelectric, while a tolerance factor $t < 1$ usually leads to a phase with tilts of the oxygen octahedra.

We note however that these two types of distortions are not necessarily exclusive and some perovskite related compounds can combine both of them, like $BiFeO_3$ [43, 44]. Moreover, other type of distortions can also develop like in $PbZrO_3$ that is anti-ferroelectric [45, 46].

In this Chapter we will discuss the physical properties of four perovskites which will be used in the present thesis: $BaTiO_3$, $PbTiO_3$, $SrTiO_3$ and $CaTiO_3$. We will start this description from first-principles considerations, through the notion of unstable modes and their characteristics. Then, we will analyse the relaxation of the two main kind of instabilities present in these compounds: FE and AFD distortions. Finally, first-principles model Hamiltonians are described that allow to address larger systems at finite temperature. This approach is then compared to the popular phenomenological Landau theory.

2.2 Soft modes and related properties

2.2.1 Phonon instabilities

The microscopic origin of ferroelectricity was the subject of many studies in the past. One of the first model highlighting the microscopic origin of the ferroelectricity was reported by Cochran [47] who proposed that the ferroelectricity can be described in the framework of soft modes. In this model, when the temperature is lowered the ferroelectric phase transition is due to a softening polar transverse optical (TO) mode in the structure that freezes-in below the transition temperature, giving rise to a dipolar moment in each unit cell.

Within the harmonic approximation, the phonons frequencies and eigenvectors can be obtained from the dynamical equation:

$$\sum_{\kappa'\beta} \widetilde{D}_{\kappa\alpha,\kappa'\beta}(\boldsymbol{q})\gamma_{m\boldsymbol{q}}(\kappa'\beta) = \omega^2_{m\boldsymbol{q}}\gamma_{m\boldsymbol{q}}(\kappa\alpha), \tag{2.2}$$

where α and β label the directions, $\omega_{m\boldsymbol{q}}$ is the phonon frequency of mode m at wave vector $\boldsymbol{q}$, $\gamma_{m\boldsymbol{q}}$ its associated phonon eigenvector related to the phonon eigendisplacement $\eta_{m\boldsymbol{q}}$=$\sqrt{M}\gamma_{m\boldsymbol{q}}$ and $\widetilde{D}_{\kappa\alpha,\kappa'\beta}$ the dynamical matrix. The dynamical matrix is defined as:

$$\widetilde{D}_{\kappa\alpha,\kappa'\beta}(\boldsymbol{q}) = \widetilde{C}_{\kappa\alpha,\kappa'\beta}(\boldsymbol{q})/\sqrt{M_\kappa M_{\kappa'}}, \tag{2.3}$$

where M_κ is the mass of the atom κ and $\widetilde{C}_{\kappa\alpha,\kappa'\beta}(\boldsymbol{q})$ is the Fourier transform of the interatomic force constants (IFC) in real space [48]:

$$C_{\kappa\alpha,\kappa'\beta}(l,l') = \frac{\partial^2 E}{\partial\tau_{\kappa\alpha}(l)\partial\tau_{\kappa'\beta}(l')} \tag{2.4}$$

where l and l' label the unit cells, κ and κ' label the atoms, τ their displacements while α and β label the directions in which the atoms are displaced.

When the reference structure corresponds to a stable phase, all the atomic positions are such as the energy is minimum and so the curvature of the energy with respect to any kind of atomic displacements is positive, giving rise to positive ω^2 and so *real* frequencies. However, when the reference structure is not the ground-state (in terms of atomic position), there are atomic distortions that allow to decrease the energy and for which the energy curvature at the origin is negative. For such pattern of atomic displacements, ω^2 is negative and so ω is imaginary frequency. Patterns of displacements yielding imaginary frequencies correspond therefore to crystal instabilities. The computation of phonons in the high symmetry phase and the search of imaginary frequency modes appear therefore to be an interesting way to identify structural instabilities.

2.2.2 Ferroelectric and antiferrodistortive instabilities

In this context, we have determined the phonon dispersion curves of $BaTiO_3$, $SrTiO_3$, $PbTiO_3$ and $CaTiO_3$ in their high temperature cubic perovskite structure ($Pm\bar{3}m$). Calculations have been performed at the experimental volume[1]. We report the results in Figure 2.2.

$BaTiO_3$

In Figure 2.2 (a) we report the calculated phonon dispersion curves of $BaTiO_3$. A strong, three times degenerated, instability is present at the Γ point which is

---

[1] The optimized LDA lattice parameters of $BaTiO_3$ (3.938 Å), $SrTiO_3$ (3.841 Å), $PbTiO_3$ (3.890 Å) and $CaTiO_3$ (3.799 Å) slightly underestimate the experimental values. As previously done for bulk $BaTiO_3$ [49], we have decided to work at the experimental volume in this Chapter.

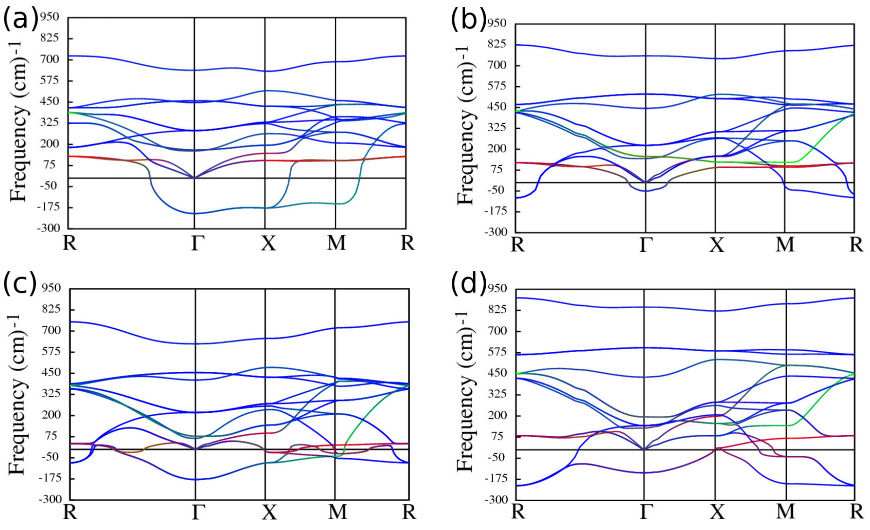

Figure 2.2: Phonon dispersion curves of (a) $BaTiO_3$, (b) $SrTiO_3$, (c) $PbTiO_3$ and (d) $CaTiO_3$ in their high symmetric cubic phase, computed at their experimental volume (respectively 4.000 Å, 3.902 Å, 3.969 Å and 3.836 Å) where the imaginary frequencies are ploted as negative numbers. The coordinates of reported zone boundary points are: X=$[\frac{1}{2}\ 0\ 0]$, M=$[\frac{1}{2}\ \frac{1}{2}\ 0]$ and R=$[\frac{1}{2}\ \frac{1}{2}\ \frac{1}{2}]$.

mainly characterized by vibrations of Ti against the O atoms and correspond to a polar pattern of displacements (Figure 2.3). This polar unstable mode at the Γ point is related to the ferroelectric (FE) instability. The freezing of the related eigendisplacements allows to decrease the energy and will bring the system in to its FE ground-state. It has been shown that there is an overlap of 99% between the eigendisplacements of this unstable mode and the distortion bringing the system to its tetragonal ferroelectric structure.

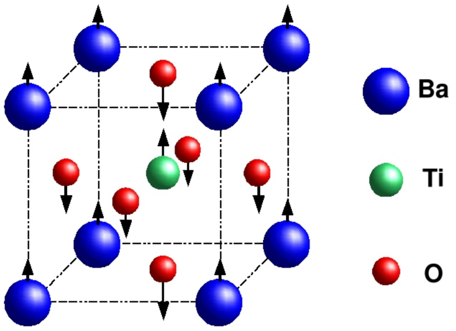

Figure 2.3: Schematic representation of the pattern of displacements related to the ferroelectric unstable mode in $BaTiO_3$.

The FE unstable mode remains unstable along the Γ-X line, with very little dispersion. A separation takes place between X and M points where one branch stabilizes along the X-M line and one becomes stable while all the branches become stable when going to the R point. These features are related to chain instabilities in real space and will be discussed in Section 2.2.5.

$SrTiO_3$

As presented in the introduction, the ground-state of $SrTiO_3$ corresponds to an antiferrodistorted (AFD) tetragonal structure with octahedral tilting of the oxygens.

Octahedral tilting in perovskite structures were the subject of particular studies and were classified according to their possible combinations [50–53]. From the known perovskites, the octahedral tilting are the most commonly observed distortions of the cubic $Pm\bar{3}m$ structure. A notation was created by Glazer [50] to classify the different octahedral tilting patterns. This classification consists to report only the octahedral tilting around each axis as follows: if each successive oxygen octahedra rotate in the same direction (in-phase) along one axis, a sign "+" is associated while if each successive oxygen octahedra rotates in opposite directions (out-of-phane), the sign "−" is reported. If no rotation takes place, then the sign "0" is reported. For the three possible directions, a letter is associated, "a", "b" or "c", depending on the relative amplitude of rotation about respectively the x, y or z directions.

So, if we suppose in-phase tilts of successive oxygen octahedra around the z axis, the following Glazer notation applies: $a^0a^0c^+$. If successive oxygen octahedra rotate in phase-opposition, we then have $a^0a^0c^-$. With these notations, the low temperature structure of bulk $SrTiO_3$ corresponds to $a^0a^0c^-$. A group-theoretical analysis was made to determine the possible tilting combinations of the octahedra and has shown that 15 structures are possible as describe in Figure 2.5.

In Figure 2.2 (b) we show the calculated phonon dispersion curves of $SrTiO_3$. Here, a weak FE instability is present at the Γ point, but contrary to $BaTiO_3$, other instabilities are present at the M and R points. The eigendisplacements of these new instabilities are related to AFD kind of distortions: the M point AFD instabilities correspond to $a^0a^0a^+$ kind of tilts while the R point AFD instabilities correspond to $a^0a^0c^-$ kind of tilts.

Therefore, AFD and FE instabilities are present together in the cubic phase. It means that freezing-in individually these distortions in the structure allows to decrease the energy of the crystal. However, in spite of the presence of many kind of instabilities in the paraelectric reference, the final ground-state involves the condensation of only one mode: the R point instability. This is related to the fact that FE and AFD instabilities are in competition and in the case of $SrTiO_3$ [54, 55], the $a^0a^0c^-$ is dominant. This will be further discussed in Section 2.3.

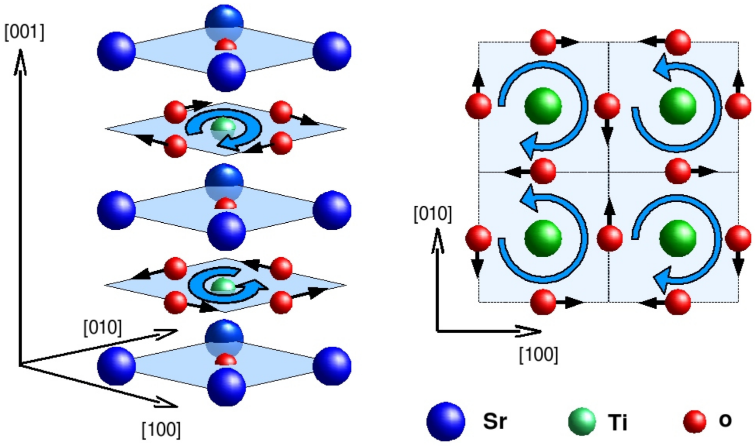

Figure 2.4: Schematic representation of the oxygen pattern of displacements in the low temperature tetragonal bulk $SrTiO_3$, corresponding to the $a^0a^0c^-$ AFD distortions. At left is reported a view allowing to see the out-of-phase rotation of each successive oxygen plane along the [001] direction. At right is reported a projection on the TiO_2 atomic plane.

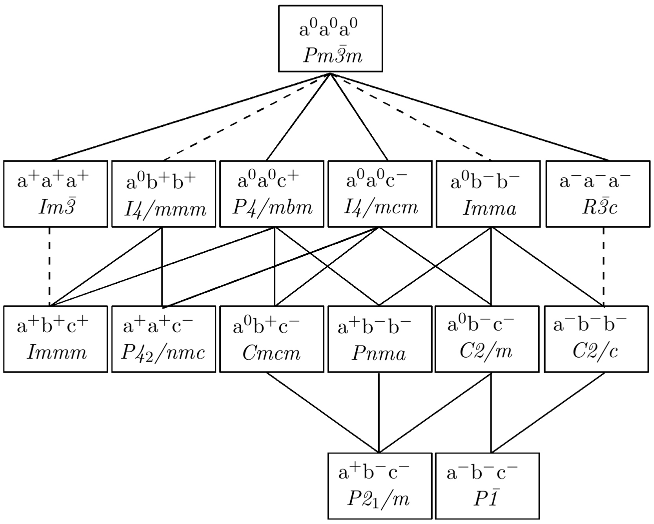

Figure 2.5: Schematic diagram indicating the group-subgroup relationship between the 15 possible configurations of AFD tilts. A dashed line indicates that the corresponding phase transition is required by Landau theory to be first order. From Ref. [51].

	$BaTiO_3$	$SrTiO_3$	$PbTiO_3$	$CaTiO_3$
a_0 (Å)	4.000	3.902	3.969	3.836
Γ	-209i (FE)	-51i (FE)	-179i (FE)	-196i (FE)
X	-176i		-80i	
			-20i	
M	-152i	-45i (AFD)	-54i (AFD)	-201i (AFD)
			-40i	-41i
			-26i	-41i
R		-89i(AFD)	- -80i (AFD)	-213i (AFD)

Table 2.1: Amplitude of the main instabilities (cm^{-1}) of Figure 2.2 at Γ, X, M and R points of bulks $BaTiO_3$, $SrTiO_3$, $PbTiO_3$ and $CaTiO_3$.

$PbTiO_3$

As for $SrTiO_3$, in the case of $PbTiO_3$ (Figure 2.2 (b)), FE and AFD instabilities are present together. However, the ground-state of $PbTiO_3$ is a tetragonal FE ground-state with polarization oriented along the c-axis and no AFD distortion is observed [56]. In first approximation, this can be related to the weak amplitude of the M and R instabilities while the FE instability at Γ is strong. Therefore, the resulting competition between these instabilities makes the FE distortions dominant in $PbTiO_3$.

Contrary to $BaTiO_3$, the FE eigenvector of $PbTiO_3$ is no longer strongly dominated by the displacement of the Ti against the oxygen along the Ti–O chains, but contains a significant component of the Pb moving against the O atoms in the Pb–O planes. As for $BaTiO_3$, unstable Ti-dominated modes are present a X and M points but Pb now plays a larger role in the character of the unstable modes. The branch emanating from the FE mode at Γ point has a much weaker dispersion when going to the R point. In consequence, the FE distortion in real space is nearly isotropic, in contrast to the strong anisotropy in $BaTiO_3$.

$CaTiO_3$

As shown in Figure 2.2 (d), the same instabilities are also simultaneously present in $CaTiO_3$. The phonon dispersion curves show FE instability at the Γ point as well as AFD instabilities at the M and R zone boundary points. In Table 2.2 we report the amplitude of the these instabilities and we can see that, for $CaTiO_3$, they are all larger than in $SrTiO_3$ or $PbTiO_3$ bulks: -213i cm^{-1} for $a^0a^0c^-$ AFD distortion, -201i cm^{-1} for $a^0a^0c^+$ AFD distortion and -196i cm^{-1} for the FE distortion.

In $CaTiO_3$ bulk, these instabilities give rise to a more complex sequence of phase transitions when the temperature decreases [55, 57]. The low temperature ground-state corresponds to an orthorhombic structure which involves the mix between three AFD distortions, $a^-a^-c^+$ and the displacement of Ca atoms from their ideal perovskite positions [58]. This ground-state corresponds to two identical out-of-phase oxygen rotations along two directions and an in-phase oxygen rotations around the third axis. So, here in spite of the presence of strong FE instabilities, the ground-state involves only the AFD distortions, but through a coupling between different AFD instabilities.

Summary

In summary, except for BaTiO$_3$, the calculation of the phonon dispersion curves show that FE and AFD instabilities often coexist. At the bulk level, these two types of instabilities usually compete and are exclusive yielding pure FE or AFD ground-states. However the competition can be modified under hydrostatic pressure [59] or epitaxial strain [60] which will be addressed in Chapter 4.

2.2.3 Origin of the structural instabilities

One might questioned why some specific modes are unstable while other are not. In the model of Cochran for ferroelectricity, the softening of the FE mode was explained trough the competition between the short-range (SR) forces and the long-range (LR) dipole-dipole interactions. The SR interactions tend to keep the atoms in their high symmetric positions while the LR dipolar forces tend to destabilize the paraelectric cubic structure.

First-principle calculations allowed to reinvestigate the balance between the SR and LR interactions in the ferroelectric ABO$_3$ materials [61]. The total frequency (ω) of the unstable mode can be decomposed into two terms: a contribution coming from the SR forces and a contribution coming from the LR dipolar forces:

$$\underbrace{\langle\gamma|\tilde{D}_{tot}|\gamma\rangle}_{\omega^2} = \underbrace{\langle\gamma|\tilde{D}_{LR}|\gamma\rangle}_{\omega^2_{LR}} + \underbrace{\langle\gamma|\tilde{D}_{SR}|\gamma\rangle}_{\omega^2_{SR}} \tag{2.5}$$

where $|\gamma>$ is the eigenvector of the mode. This procedure is done by dividing the dynamical matrix ($\tilde{D}_{tot}$) into two parts: first, a model dipole-dipole long-range Coulomb part ($\tilde{D}_{LR}$) is calculated from the Born effective charges and the dielectric tensor of the material and, second, the SR part is obtained by subtracting this Coulomb part to the total dynamical matrix ($\tilde{D}_{SR}$=$\tilde{D}_{tot}$-$\tilde{D}_{LR}$).

In Table 2.2 we report the results of such SR-LR decomposition for the FE and AFD instabilities in BaTiO$_3$, SrTiO$_3$, PbTiO$_3$ and CaTiO$_3$. For the four considered perovskites, the decomposition confirms that the origin of the FE instability is due to the compensation of the SR part, stabilizing the system and giving a positive contribution to ω^2 (ω^2_{SR} >0), by the LR Coulomb part which tends to destabilize the system and gives the negative contribution to ω^2 (ω^2_{LR} <0) [61].

Interestingly, performing the same decomposition on the R point AFD instability (Table 2.2) shows an opposite behavior: the SR component is destabilizing while the LR part is stabilizing. This has to be related to the fact that the AFD instabilities are macroscopically non-polar and that negatively charged oxygen atoms only are involved in this type of distortion.

	$BaTiO_3$	$SrTiO_3$	$PbTiO_3$	$CaTiO_3$
ω^2(FE)	-43773	-2603	-31976	-18541
ω^2_{SR}(FE)	672017	295484	271537	54285
ω^2_{LR}(FE)	-715790	-298088	-303513	-72825
ω^2(AFD)	-	-8396	-6431	-45235
ω^2_{SR}(AFD)	-	-109819	-74097	-151343
ω^2_{LR}(AFD)	-	101423	67666	106108

Table 2.2: SR and LR decomposition of the square frequency (cm^{-2}) of the FE soft mode and of the R point AFD instability for $BaTiO_3$, $SrTiO_3$, $PbTiO_3$ and $CaTiO_3$ at their experimental volume.

2.2.4 Anomalous Born effective charges

Basically, the LR part of the dynamical matrix is calculated through the Born effective charges and the electronic dielectric constant. In the context of the SR/LR description, the anomalous values of the Born effective charges of ferroelectric perovskites [62] were shown to be an essential feature to produce large destabilizing Coulomb interactions responsible for ferroelectricity.

The Born effective charge tensor of an atom κ can be related to the change of the spontaneous polarization produced by the displacement of this atom under the condition of zero macroscopic electric field $\mathcal{E}$:

$$Z^*_{\kappa,\alpha\beta} = \Omega \frac{\partial P_\beta}{\partial \tau_{\kappa,\alpha}}\bigg|_{\mathcal{E}=0} \tag{2.6}$$

where α and β label the cartesian coordinates. According to this definition, high values of these dynamical charges would lead to large spontaneous polarization, even for small distortions.

	$BaTiO_3$	$SrTiO_3$	$PbTiO_3$	$CaTiO_3$	nominal
Z^*(A)	2.74	2.55	3.87	2.58	+2
Z^*(Ti)	7.35	7.26	7.21	7.20	+4
$Z^*(O_\perp)$	-2.14	-2.04	-2.58	-2.04	-2
$Z^*(O_\parallel)$	-5.80	-5.73	-5.92	-5.71	-2
ε^∞	6.74	6.29	8.62	6.25	-

Table 2.3: Born effective charges (electrons) and electronic dielectric tensor of $BaTiO_3$, $SrTiO_3$, $PbTiO_3$ and $CaTiO_3$ at their experimental volume. The $O_\perp$ and $O_\parallel$ are the elements referring respectively to an atomic displacement perpendicular and parallel to the Ti–O bond. In the last column is reported the nominal charge of corresponding ions (e).

In Table 2.3 we report the Born effective charges of $BaTiO_3$, $SrTiO_3$, $PbTiO_3$

and $CaTiO_3$ in their cubic paraelectric structure at the experimental volume. All of these compounds are characterized by anomalously large Born effective charges of the Ti and O atoms since the nominal charge of these atoms are respectively +4 and -2 while their Born effective charges are about +7.2 for Ti and -5.8 for $O_{\|}$. These anomalous Born effective charges indicate that dynamical charge transfers occur along the Ti–O chains when the bond length is modified, which are related to hybridization changes between the O 2p and the Ti 3d orbitals. The Born effective charge of A and $O_{\perp}$ are less anomalous and closer to their nominal values of respectively +2 and -2. This result is related to the fact that the $ATiO_3$ compounds exhibit a mixed ionic-covalent nature of their bonding. The A atoms can be described as having a more ionic character while the Ti and O have a more covalent character. However, the case of $PbTiO_3$ is an exception, showing higher anomalous charge of Pb and $O_{\perp}$ which is attributed to a more covalent bonding between the lead and oxygen atoms.

These Born effective charges are directly involved in the mode effective charge and the LO-TO splitting of the phonons and their anomalous values make these quantities giant in ABO_3 compounds [63]. The mode effective charge of a mode in a direction α can be defined as follows:

$$\bar{Z}^*_{\alpha} = \frac{\sum_{\kappa,\beta} Z^*_{\kappa,\alpha\beta}\ \eta_{\kappa,\beta}}{\sqrt{\langle\eta|\eta\rangle}} \tag{2.7}$$

where Z^*_{κ} are the individual atomic Born effective charge tensors and η is the phonon eigendisplacement vectors. The values of such mode effective charges are reported in Table 2.4 (last line) for the unstable FE mode. There are large for all the four considered compounds. As shown in Table 2.4, by separating the partial contribution due to each atom we can see that the large mode effective charge originates essentially from the large Born effective charges of Ti and O atoms and the specific polar pattern of eigendisplacement associated to the FE mode, where the Ti move against the O atoms. Here, for $BaTiO_3$, $SrTiO_3$ and $PbTiO_3$ the largest contribution is mainly due to the Ti and $O_{\|}$ while for $CaTiO_3$ the contribution of Ti is reduced and involve larger Ca contribution.

2.2.5 Collective phenomenon

The ferroelectricity was also associated as being a collective phenomenon and the concept of a “correlation volume” [1] was proposed to explain the physics of such collective behavior.

This feature can be highlighted from the inspection of the on-site interatomic force constants (IFC) $C_{\alpha,\alpha}$(l,κ,l,κ) of the different A, B and O atoms in the cubic ABO_3 structure [64]. These on-site IFC are reported in Table 2.5 for the four considered compounds. The IFC matrix $C_{\alpha,\beta}$(κ,κ’) relates the force F_{α}(κ) on atom κ associated to the displacement τ_{β}(κ’) of atom κ’ such as:

$$F_{\alpha}(\kappa) = -C_{\alpha,\beta}(\kappa,\kappa')\ \tau_{\beta}(\kappa'), \tag{2.8}$$

where α and β label the directions x, y or z. Therefore, the fact that the calculated on-site IFC are always all positive, means that the forces are always

	$BaTiO_3$	$SrTiO_3$	$PbTiO_3$	$CaTiO_3$
η_A	3.845 10^{-05}	9.53 10^{-04}	3.84 10^{-04}	2.36 10^{-03}
η_{Ti}	2.253 10^{-03}	1.16 10^{-03}	1.34 10^{-03}	5.07 10^{-04}
$\eta_{O_\perp}$	-1.722 10^{-03}	-3.02 10^{-03}	-2.91 10^{-03}	-2.90 10^{-03}
$\eta_{O_\parallel}$	-3.628 10^{-03}	-2.65 10^{-03}	-3.17 10^{-03}	-1.63 10^{-03}
$\bar{Z}$(A)	0.02	0.46	0.28	1.21
$\bar{Z}$(Ti)	3.37	1.61	1.80	0.72
$\bar{Z}(O_\perp)$	0.75	1.17	1.40	1.17
$\bar{Z}(O_\parallel)$	4.28	2.90	3.49	1.85
$\bar{Z}^*$(total)	9.17	7.31	8.36	6.13

Table 2.4: Phonon eigendisplacements of the FE mode, its mode effective charge (electrons) and its associated atomic partial contribution of cubic $BaTiO_3$, $SrTiO_3$, $PbTiO_3$ and $CaTiO_3$ at their experimental volume. The eigendisplacements η are normalized with the mass as follows: $< \eta|M|\eta >$=1 with M in electronic mass unit.

opposed to the displacement of one atom alone and tend to bring it back in its initial position. It results that no instability can be produced by isolated atomic displacements. Therefore, the cubic structure is only unstable trough the displacement of many atoms together.

Atom	direction	$BaTiO_3$	$SrTiO_3$	$PbTiO_3$	$CaTiO_3$
A	$x = y = z$	0.0820	0.0507	0.0285	0.0261
Ti	$x = y = z$	0.1471	0.1931	0.1373	0.2256
O	$x = y$	0.0686	0.0550	0.0449	0.0418
O	z	0.1277	0.2054	0.1519	0.2684

Table 2.5: On-site IFC (Ha.Bohr^{-2}) on the different atoms of cubic $BaTiO_3$, $SrTiO_3$, $PbTiO_3$ and $CaTiO_3$ at their experimental volume. The O atom is the one placed at the reduced position (0.5, 0.5, 0.0)

This feature was also studied from first-principles through the phonon dispersion curves of the cubic ABO_3 compounds [64]. As shown in Figure 2.2 (a), for $BaTiO_3$ the unstable mode at the Γ point stays unstable at the X and M zone boundary points. The associated unstable branch is fairly flat between Γ and X and between X and M but rapidly harden and becomes stable when going to the R point. As shown in Figure 2.6 left, the instabilities in $BaTiO_3$ are confined in three perpendicular interpenetrating slab-like regions of the Brillouin zone around the Γ point. This planar character of the unstable region in reciprocal space is related to a linear correlation of the atomic displacements in real space and allows to estimate the length of the smallest unstable chain to 4-5 unit cells. This means that in $BaTiO_3$ it is possible to decrease the energy by freezing the FE mode in at least 4-5 unit cells together. Moreover, the calculation of the IFC in real space pointed out that the instability is associated to a strong anisotropic correlation of the atomic displacements along the Ti–O chains. This will be further discussed in Chapter 8.

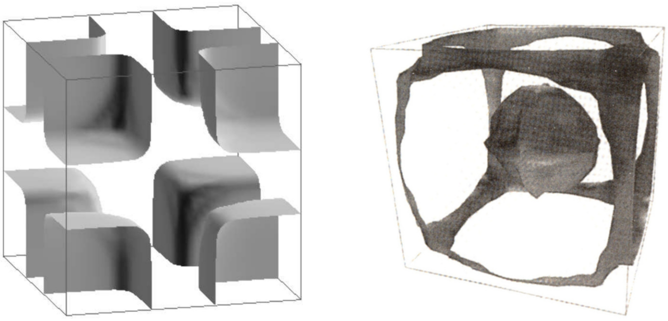

Figure 2.6: Zero-frequency isosurface of the lowest unstable phonon branchs over the Brillouin zone of $BaTiO_3$ (left, from [49]) and $SrTiO_3$ (right, from [65]). Γ point is located at the center of the cube, X point at the center of each face, M at the middle of each line and R point at the corners of the cube.

As for $BaTiO_3$, in Figure 2.6-right we report the zero frequency isosurfaces of the lowest unstable phonon branch over the entire Brillouin zone for $SrTiO_3$. The AFD instabilities are confined to quasi one-dimensional tubes of reciprocal space running along the edges of the Brillouin zone. In real space, these instabilities appear as a cooperative rotation of oxygen octahedra with strong correlations in the plane perpendicular to the axis of rotation, and small correlations between rotations in different planes. The $SrTiO_3$ FE instability is interior to a Γ centered isosurface which can be visualised as three interpenetrating "cookies", one perpendicular to each cartesian direction. Since the FE unstable branch rapidly stabilizes when going away from Γ, in real space the distortions will be strongly isotropic and with larger range than in $BaTiO_3$.

As discussed in Section 2.2.2, in $PbTiO_3$ the Pb has a stronger role in the FE instability than in $BaTiO_3$ and the unstable branch has a much weaker dispersion when going toward the R point. In consequence, the unstable FE distortion is much more isotropic in real space for $PbTiO_3$ than for $BaTiO_3$.

For $CaTiO_3$, the unstable branches are mainly dominated by the O and Ca displacements, with less significant Ti character. The AFD branch is flat between R and M points and are larger than the one in $SrTiO_3$ or $PbTiO_3$.

2.3 Freezing instabilities

The calculation of the unstable modes in the harmonic approximation allows to determine the curvature of the energy at the origin for a given pattern of displacement. However, to determine the exact ground-state, atomic relaxations should be performed by freezing-in the eigendisplacements of the unstable modes in order to properly include anharmonic effects.

2.3.1 Ferroelectric distortions

For simplicity, in this section we will discuss the effects of the FE distortions oriented in one direction only (here the z direction) and the relaxation is performed at constant volume. The corresponding space group is $P4mm$, which corresponds to the ground-state of $PbTiO_3$. After the relaxation of the forces and stresses, we obtain slight deviations of the cell shape and atomic positions with respect to the cubic paraelectric phase.

In Table 2.6 we report, for this $P4mm$ phase, the atomic displacements and cell parameters, the tetragonality, the spontaneous polarization and the gain of energy with respect to the paraelectric phase (PE), taken as reference, for $BaTiO_3$, $SrTiO_3$, $PbTiO_3$ and $CaTiO_3$. As we can see, for all the considered compounds, the shape of the cell is changed with respect to the cubic cell. A contraction of the in-plane cell parameter and an extension of the out-of-plane cell parameter take place, giving rise to a tetragonality $c/a \neq 1$. This is a similar behavior for the four materials, but the amplitude of the tetragonality is different: a strong tetragonality is observed for $PbTiO_3$ while a small modification of the cell is observed for $SrTiO_3$. Among them, $CaTiO_3$ has a tetragonality larger than the one of $BaTiO_3$.

	$BaTiO_3$	$SrTiO_3$	$PbTiO_3$	$CaTiO_3$
a_0(PE)	4.000	3.905	3.969	3.836
a(FE)	3.969	3.902	3.863	3.790
c(FE)	4.064	3.911	4.190	3.929
c/a	1.024	1.002	1.085	1.037
δ_z(A)	0.002	0.004	0.026	0.059
δ_z(Ti)	0.016	0.003	-0.017	0.004
$\delta_z(O_\perp)$	-0.017	-0.011	-0.100	-0.061
$\delta_z(O_\parallel)$	-0.029	-0.009	-0.093	-0.037
P	34	13	96	65
ΔE	18.7	0.2	151.9	64.9

Table 2.6: Experimental cubic cell parameter (Å), relaxed a and c cell parameters (Å), tetragonality c/a, atomic displacements along z (reduced coordinates with mass center fixed to zero), spontaneous polarization (μC.cm^{-2}) and gain of energy (meV/cell) with respect to the paraelectric reference for the tetragonal FE phase of $BaTiO_3$, $SrTiO_3$, $PbTiO_3$ and $CaTiO_3$ at volume fixed to the cubic experimental volume.

These differences of tetragonality are consistent with the observed amplitude of polarization in these compounds: the strongest polarization is the one of $PbTiO_3$, followed by $CaTiO_3$, $BaTiO_3$ and $SrTiO_3$.

The same differences are also observed for the gain of energy (ΔE) with respect to the cubic structure: a large ΔE in the case of PbTiO$_3$ while a tiny ΔE is observed for SrTiO$_3$.

We notice also that the atomic distortions associated to the FE phases are relatively different in the four compounds. The FE distortions of BaTiO$_3$ are mainly associated to a displacement of the Ti against the O atoms while in the case of PbTiO$_3$ both Ti and O atoms move in the same direction but with a different amplitude. In the case of SrTiO$_3$, the FE motion is dominated by a movement of the O atoms. For PbTiO$_3$ and CaTiO$_3$, the *A* cation is also involved in the FE displacements. The *A* cation contribution to the FE displacements can be related to their mass: large *A* mass gives rise to small contribution to the total distortion (Ba, Sr) while small *A* mass gives rise to large contribution (Ca). Exception is observed for PbTiO$_3$, since the mass of Pb is large but its contribution to the pattern of displacement is also large which is related to its hybridization with the $O_\perp$.

The overlap between the final atomic displacements in the FE tetragonal state and the eigenvector of the unstable mode which was freezing-in is larger than 90%, confirming the fact that the "unstable" mode is at the origin of the FE transition. However, since the tetragonal ferroelectric structure of BaTiO$_3$, SrTiO$_3$ and CaTiO$_3$ does not correspond to the ground-state at 0 K, other instabilities remain in the *P4mm* phase. These remaining instabilities are responsible to the real ground-state of these three compounds: the orthorhombic and the rhombohedric FE phases for BaTiO$_3$ and the AFD phases for SrTiO$_3$ and CaTiO$_3$.

2.3.2 AFD distortions

Here also, for simplicity we will discuss the effects of the AFD relaxations of the $a^0a^0a^-$ and $a^0a^0a^+$ tilts separately, where the oxygen octahedra are allowed to rotate around the z axis. The corresponding space group is *I4/mcm* for the $a^0a^0a^-$ distortions, which corresponds to the ground-state of SrTiO$_3$ while the space group associated to the $a^0a^0a^+$ distortions is *P4/mbm*. In Table 2.7 we report the relaxed cell parameters, tetragonality, angle of oxygen tilts and the gain of energy with respect to the cubic paraelectric reference for SrTiO$_3$, PbTiO$_3$ and CaTiO$_3$.

As for the FE phase, the $a^0a^0a^-$ and $a^0a^0a^+$ AFD distortions yield a modification of the cell shape by modifying the tetragonality. For SrTiO$_3$ and PbTiO$_3$ the amplitude of c/a is small comparatively to the FE phase. The amplitude of c/a is also directly related to the amplitude of oxygen rotations: the oxygen rotation is large for CaTiO$_3$ while it is small for SrTiO$_3$ and PbTiO$_3$ which is associated to a large (respectively small) tetragonality for CaTiO$_3$ (respectively PbTiO$_3$ and SrTiO$_3$).

The resulting gain of energy due to these AFD distortions is large in the case of CaTiO$_3$: it is equal to 255.7 meV for the $a^0a^0a^-$ tilt and 218.3 meV for the $a^0a^0a^+$ tilt, which is much more important than the gain of energy of the FE distortions reported in Table 2.6 (64.9 meV). However, for PbTiO$_3$ the gain of energy due to the AFD distortions (few meV) is significantly smaller than for the FE phase (151.9 meV). For SrTiO$_3$, the AFD gain of energy is small

		$SrTiO_3$	$PbTiO_3$	$CaTiO_3$
	a_0(PE)	3.905	3.969	3.836
$a^0a^0a^-$	a	3.896	3.963	3.807
	c	3.923	3.980	3.895
	c/a	1.007	1.004	1.023
	angle	4.3	3.4	9.5
	ΔE	10.7	5.1	255.7
$a^0a^0a^+$	a	3.902	3.966	3.805
	c	3.911	3.975	3.905
	c/a	1.002	1.002	1.026
	angle	2.3	2.3	9.3
	ΔE	0.8	1.1	218.3

Table 2.7: Experimental cubic cell parameter a_0(PE) (Å), relaxed a and c cell parameters (Å), angle of the oxygen rotations and gain of energy (meV/5-atoms-cell) with respect to the paraelectric reference of tetragonal $a^0a^0a^-$ and $a^0a^0a^+$ AFD phases of $SrTiO_3$, $PbTiO_3$ and $CaTiO_3$. The relaxations were done at a volume fixed to the cubic experimental volume (a_0^3).

comparatively to the other compounds, but this gain of energy is stronger for the AFD distortions than for its FE phase reported in Table 2.6, coherently with its AFD ground-state.

For all the considered compounds, the gain of energy due to the $a^0a^0a^+$ tilt is less important than the $a^0a^0a^-$ tilt meaning that the in-phase tilts are always less favorable than the out-of-phase tilts.

2.4 Dielectric and piezoelectric responses

Ferroelectric oxides exhibit not only a switchable polarization but also various interesting functional properties. Two of them make the ABO_3 interesting for technological applications: the large dielectric and piezoelectric constants which are directly related to their ferroelectric character [66, 67].

2.4.1 Dielectric response

The static dielectric constant can be expressed as follows:

$$\varepsilon_0^{\alpha\beta} = \varepsilon_{\alpha\beta}^{\infty} + \frac{4\pi}{\Omega}\sum_j \frac{S_j^{\alpha\beta}}{\omega_j^2}, \tag{2.9}$$

where α and β are related to the directions x, y or z, $\varepsilon_{\alpha\beta}^{\infty}$ is the electronic dielectric tensor, Ω is the volume of the cell, ω_j is the frequency of the mode j and $S_j^{\alpha\beta}$ its mode-oscillator strength tensor which can be define as follows:

$$S_{j,\alpha\beta} = \sum_{\kappa\alpha'} Z^*_{\kappa,\alpha\alpha'}\,(\eta_{j,\kappa\alpha'})^* \sum_{\kappa'\beta'} Z^*_{\kappa',\beta\beta'}\,\eta_{j,\kappa'\beta'}. \tag{2.10}$$

with η_j the eigenvector of the mode j and Z^*_κ the atomic Born effective charges, κ labelling the atoms.

In ferroelectric oxides, the electronic contribution (ε^∞) has a negligible importance on the total static dielectric constant and the strongest contributions come from the vibrational response. When a mode with non zero mode-oscillator strength (*i.e.* polar) becomes soft (*i.e.* its frequency decreases), its contribution to static dielectric constant becomes dominant in Eq. (2.9) and can be giant in the ferroelectric oxides since the FE soft mode has usually a large polarity. Near a phase transition, where the soft mode goes to zero frequency, its contribution to Eq. (2.9) gives a divergent static dielectric constant around the critical temperature and follows the Curie-Weiss law.

From DFT calculations, only the 0 K static dielectric constant can be computed. In Table 2.8 we report the static dielectric tensor of $BaTiO_3$, $SrTiO_3$, $PbTiO_3$ and $CaTiO_3$ in their tetragonal FE state as it is reported in Table 2.6. For $BaTiO_3$ and $SrTiO_3$ when freezing-in the FE distortions in the z direction only, the x/y FE instabilities still exist giving rise to imaginary frequency in the x and y directions. Since this imaginary frequency will provide a non-physical negative contribution in the sum of Eq. (2.9) the xx and yy components of the static dielectric tensor are not reported. For $PbTiO_3$ and $CaTiO_3$, however, freezing-in the FE distortion in the z direction shifts the frequency of the FE soft mode polarized along the in-plane directions to positive values. Finally, only the static dielectric constant of $PbTiO_3$ has a real physical meaning since the tetragonal FE phase corresponds to its ground-state while for $SrTiO_3$ and $CaTiO_3$ the ground-state involve the AFD distortions. The values are however reported for comparison.

The reported values of the dielectric constant in Table 2.8 show, for $PbTiO_3$ and $CaTiO_3$, differences between the in-plane components and the zz component. According to Eq. (2.9), this can be related to the higher frequency combined to lower mode effective charge of the FE_z mode with respect to the FE_x mode. As we can see in Table 2.8, the zz component of the dielectric constant of $SrTiO_3$ is strongly larger than the other compounds, which can also be related to the combination of a low frequency and large mode effective charge of the FE_z mode.

To determine properly the static dielectric constant of the high temperature phase, the temperature should be included in the simulations. Such results of simulations with temperature are shown in Figure 2.7 for $BaTiO_3$ but these methods will be described in the next section.

2.4.2 Piezoelectric response

Since the FE phases are polar, their piezoelectric responses can be non-zero. The piezoelectric coefficients are usually calculated as being the derivative of the polarization with respect to the strain at zero electric field:

$$e_{\alpha,\mu\nu} = \frac{\partial P_\alpha}{\partial \eta_{\mu\nu}} \tag{2.11}$$

and can be decomposed into two terms: (i) the clamped ion response ($e^0_{\alpha,\mu\nu}$) corresponding to the piezoelectric response where the fractional atomic coordi-

	$BaTiO_3$	$SrTiO_3$	$PbTiO_3$	$CaTiO_3$
$\varepsilon_{xx}= \varepsilon_{yy}$	-	-	96	65
ε_{zz}	28	290	24	25
$e_{31}=e_{32}$	(0.58)	(0.21)	-1.69	-0.67
e_{33}	(4.78)	(19.88)	-4.09	-5.17
$e_{24}=e_{15}$	-	-	-4.54	-3.87
$\omega(FE_z)$	163	76	154	189
$\bar{Z}^*(FE_z)$	2.93	6.18	2.98	3.65
$\omega(FE_x)$	92i	22i	86	127
$\bar{Z}^*(FE_x)$	8.74	7.17	3.75	3.85

Table 2.8: Diagonal terms of the static dielectric tensor as well as the non-zero piezoelectric constant ($C.m^{-2}$) computed in the tetragonal FE phase of $BaTiO_3$, $SrTiO_3$, $PbTiO_3$ and $CaTiO_3$ at volume fixed to the cubic experimental volume. The four last lines represent the frequency (cm^{-1}) and the mode effective charge (electrons) of the FE modes polarized along the z direction (FE_z) and along the in-plane direction (FE_x).

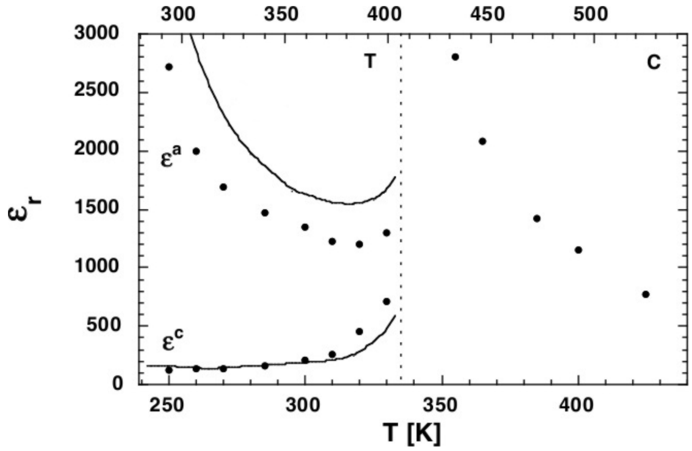

Figure 2.7: Temperature evolution of the static dielectric constant of $BaTiO_3$ between the cubic and tetragonal phases (from [7]). The bottom and top x-axes correspond to respectively the theoretical and experimental temperatures.

nates stay the same and (*ii*) a contribution coming from the ionic displacements such as:

$$e_{\alpha,\mu\nu} = e^0_{\alpha,\mu\nu} - \frac{1}{\Omega}\sum_m \frac{p_{m\alpha} g_{m\mu\nu}}{\omega_m^2}, \tag{2.12}$$

where $g_{m\mu\nu}$ depends on the internal strain parameters and $p_{m\alpha}$ is the mode polarity of the mode m with frequency ω_m. The piezoelectric constant will thus be strong if a mode with low frequency and high polarity has a strong coupling with the strain.

In a paraelectric phase, it is clear from Eq. (2.11) that the piezoelectric constants are strictly zero. Like for the dielectric constant, in ferroelectric oxides compounds, the soft mode has all the characteristics giving a divergent piezoelectric response near to the phase transition (in the FE phase). We report in Table 2.8 the calculated piezoelectric coefficients of the tetragonal phase of $BaTiO_3$, $SrTiO_3$, $PbTiO_3$ and $CaTiO_3$ with the structural parameters given in Table 2.6. These results are comparable with previous studies [66, 68–71] and show large piezoelectric coefficient e_{33} for all the compounds. Here also, the piezoelectric coefficients reported for $SrTiO_3$ and $CaTiO_3$ are artificial since their ground-state is not FE but they are mentioned to make a point of comparison with what will be discussed in other chapters. As for the static dielectric constant, the piezoelectric response diverges around the transition temperatures of the different FE phases and responsible to the giant $SrTiO_3$ e_{33} reported in Table 2.8.

2.5 Effective Hamiltonian

As shown previously, the functional properties as dielectric and piezoelectric coefficients are strongly dependent on the temperature, specially around the phase transition temperatures where they exhibit a divergent character. Theoretical predictions must therefore take into account the temperature behavior of these ABO_3 compounds and be able to reproduce the correct sequence of phase transitions.

The exact treatment of such temperature evolution should be to consider first-principles molecular dynamics simulations [8]. However, such approach is computationally strong and even nowadays, with the present computational power, it is still restricted to relatively small systems and time-scale. Moreover, because of the long-range character of the interactions in ferroelectric compounds, their accurate modelling requires large simulation boxes (∼thousands of atoms) and so more approximate approaches must be considered.

At the microscopic level, first-principles effective Hamiltonian approach has first been proposed by Rabe and Joannopoulos to study the phase transition of GeTe [72]. In this approach, the approximation is to identify the most important degrees of freedom governing the phase transitions and then to perform a low-order expansion of the energy with respect to these degrees of freedom only, the coefficients being determined from DFT calculations. Thereafter, suh approach was successfully applied to ferroelectric perovskite oxides [73–75].

The general framework to build an effective Hamiltonian for ferroelectric oxides, is to notice that FE phase transitions are driven by a restricted number of degrees of freedom. As shown previously, the relaxed FE distortions are related to the freezing of FE unstable modes and a subsequent strain relaxation. The effective Hamiltonian approximation is then to consider (*i*) the pattern of displacement ξ of the unstable modes of the paraelectric phase and (*ii*) the strains. As the amplitude of the FE distortion is relatively small, the Hamiltonian can be written as a Taylor expansion in terms of ξ and strains, limited to low order.

Depending on the authors and the compounds, slightly different expressions have been reported. We are going to briefly describe two of these different effective Hamiltonian approaches as it was developed for bulk perovskites: (*i*) the King-Smith and Vanderbilt model (KSV) [73, 76] and (*ii*) Zhong-Vanderbilt-Rabe (ZVR) [74, 77] or closely similar Waghmare-Rabe model (WR) [75].

2.5.1 KSV model

The purpose of the KSV model is to achieve a description of the energy landscape in terms of the instability that freezes-in at the transition and the homogeneous strains.

Internal energy and double well

The first step in the construction of the effective Hamiltonian is to identify the relevant ionic degrees of freedom ξ. In the KSV approach, the authors considered a local mode directly deduced from unstable modes at the Γ point for te FE instability and at the R or M points for AFD instabilities. The local mode is then a pattern of atomic displacements that reproduces homogeneous FE or AFD distortions when they are frozen with the same amplitude in each repeated cell.

Since the FE and AFD phase transitions involve only small atomic displacements from the paraelectric reference, it is possible to describe the internal energy as a low order Taylor expansion in the displacements from the cubic structure taken as reference. As mentioned in previous sections, the final atomic distortions are mainly related to the eigendisplacements of the unstable modes calculated in the paraelectric reference. The Taylor expansion can be expressed with respect to the pattern of atomic displacements ξ_k, where k={FE, AFD}.

Neglecting the elastic interactions, the internal energy associated to a distortion ξ has the form:

$$U(\xi) = \frac{1}{2}a\sum_i \xi_i^2 + \frac{1}{4}b\sum_i \xi_i^4 + \frac{1}{4}c\sum_{i<j} \xi_i^2\xi_j^2 + \textit{higher order} \tag{2.13}$$

where the indices i and j label the three space directions and a, b and c are the expansion parameters. Due to the cubic symmetries of the paraelectric reference, only even-order terms are allowed in the expansion. The parameters a, b and c can be determined from first-principles calculations. In case of FE (or AFD) distortions, the $U(\xi)$ of the system has a typical double-well shape in each direction as shown in Figure 2.8. This double well is characterized by a negative curvature at the origin, which is associated to a negative parameter a and also by two symmetric minima, corresponding to the two minima of the energy at the normalized ξ=±1 of the Figure 2.8. The a parameter is proportional to the harmonic curvature at the origin ξ=0 and so can be related to the square of the soft mode frequency ω^2 associated to the eigendisplacement η. The two stable states at ξ=±1 can be related to the two equivalent up and down states of the polarization in case of the FE instability.

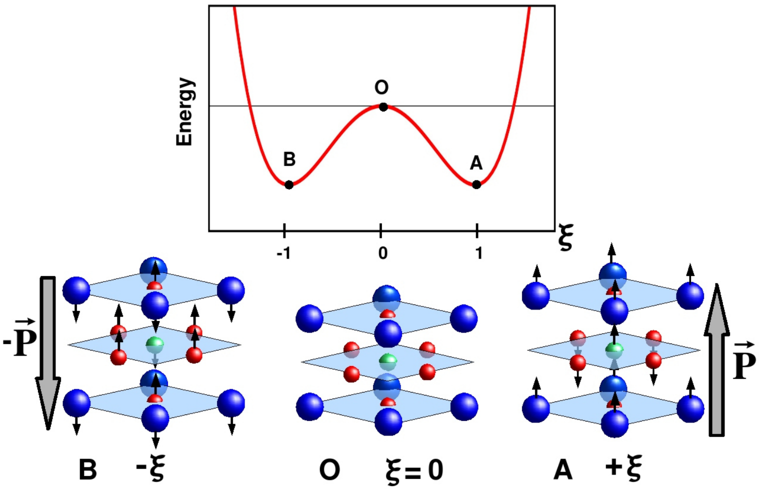

Figure 2.8: Schematic representation of the double well potential energy with respect to the pattern of displacements ξ of the FE mode in an ABO$_3$ perovskite structure. The bottom Figures show the atomic displacements at the minimum of energy A (right) and B (left) with respect to the paraelectric cubic structure O (center).

Elastic interactions

As presented in the previous section, the relaxation of the FE or AFD distortions induces a modification of the cell shape and size. So, to have a proper description of the FE and AFD phases, the elastic interactions must be properly included in the Taylor expansion of the energy. Calling η_α the components of the elastic strain tensor (α=1-6 in Voigt notation), we can include the elastic interactions in the energy through two terms:

$$E^E(\eta) = \frac{1}{2}C_{11}\sum_i \eta_i^2 + \frac{1}{2}C_{12}\sum_{i<j}\eta_i\eta_j + \frac{1}{2}C_{44}\sum_{i<j}\eta_{i+j+1}^2 \qquad (2.14)$$

and

$$E^{int}(\xi,\eta) = \frac{1}{2}g_{11}\sum_i \eta_i\xi_i^2 + \frac{1}{2}g_{12}\sum_{i,j\neq i}\eta_i\xi_j^2 + g_{44}\sum_{i<j}\eta_{i+j+1}\xi_i\xi_j \qquad (2.15)$$

where i and j labels the directions (i, j=1-3), E^E represents the elastic energy coming from the pure strain terms and E^{int} the interaction between the strain and the pattern of distortions ξ expanded up to second order. The C_{ij} and g_{ij} parameters are respectively the strain and distortion-strain coefficients. Here all the coefficients C_{ij} will be positive and are related to the elastic constants. The g_{ij} coefficients take into account the fact that a distortion ξ will induce a modification of the strain (and inversely).

The free energy of the system can be then summarized as follows:

$$F(\xi, \eta) = U(\xi) + E^E(\eta) + E^{int}(\xi, \eta). \tag{2.16}$$

When different kinds of instabilities are present together, as FE and AFD instabilities, the model can be generalized by including all the relevant degrees of freedom and takes into account the coupling between them.

These Taylor decompositions of the total energy in terms of the strain and the unstable mode eigendisplacements was originally proposed by King-Smith and Vanderbilt [73, 76] to describe the FE phase transitions. This model is particularly interesting to predict the structure and polarization of epitaxial thin films [76]. The simple form of the parametrization is useful since it allows to reduce the computational effort for generating the phase diagrams relative to first-principles calculations. Even if this model is based on the microscopic distortions, it can be considered as “macroscopic” in the sense it only includes homogeneous distortions.

2.5.2 ZVR model

A more general approach to build effective Hamiltonian is the model proposed by Zhong-Vanderbilt-Rabe model (ZVR) [74, 77] and Waghmare-Rabe (WR) [75]. Following this approach, the total energy is again described as a Taylor expansion around the paraelectric cubic phase in term of the selected degree of freedoms: distortion ξ and strain η. However, with respect to the KSV model, the decomposition includes the possibility for ξ to fluctuate in the different unit cells by fitting the parameters through the information given by the full unstable phonon branch. In this context ξ is no more a homogeneous distortion throughout the whole crystal but a local mode associated to each unit-cell that can be seen as the lattice Wannier function associated to the unstable phonon branch.

The development of the Taylor expansion is the same than the one previously reported for the KSV model but with a different and more detailed estimation of the harmonic term ξ^2 in Eq. (2.13). As it is considered for the KSV model, in the limit of uniform configuration, it simply reproduces the double-well energy of Figure 2.8. But, it must also properly describe the evolution of the energy when the ξ fluctuate independently in the different unit cells l. To that end it is decomposed into short-range (SR) and long-range dipole-dipole (LR) interactions:

$$U^{Harm}(\{\xi_l\}) = U^{SR}(\{\xi_l\}) + U^{LR}(\{\xi_l\}). \tag{2.17}$$

The quadratic SR interactions between ξ_l are written in terms of a tight-binding model including up to third nearest neighbours while the LR term corresponds to the dipole-dipole interactions and is evaluated using the Ewald summation technique. The parameters of these two terms are adjusted to reproduce the unstable phonon branch and so, instead of the KSV model, include informations from the whole Brillouin zone.

Even though the ZVR and WR approaches are more general, both KSV and ZVR/WR approaches are currently used and allow to achieve similar results. The effective Hamiltonian can then be used to investigate the temperature behavior of ferroelectrics thanks to classical Monte-Carlo simulations [75] and construct the temperature-pressure phase diagrams. When different kind of instabilities are present and compete, like FE and AFD instabilities, these models can be generalized to include all the relevant ionic degrees of freedom [55, 59].

2.6 Landau-Devonshire phenomenological model

Another and more popular approach to describe the temperature behavior of ferroelectrics at the macroscopic level is the phenomenological Landau-Devonshire theory [78].

2.6.1 First and second order phase transitions

The starting point to build a Landau theory is to characterize the phase transition in terms of an order parameter which is a physical quantity that is zero in the highest symmetry phase and changes to a finite value below the phase transition. The hypothesis of the Landau theory is that the free energy can be expressed in the vicinity of the transition as a polynomial expansion of the thermodynamic potential with respect to the order parameter, where only symmetry-compatible terms are retained, and this expansion is assumed to remain valid before and after the phase transition. The coefficients of the expansion are fitted from experiment and the temperature dependence of some parameters are assumed *a priori.*

When the pressure is neglected, at a given temperature, the stable phase is the one minimizing the free energy

$$F = U - TS, \tag{2.18}$$

where T is the temperature, S the entropy and U the internal energy.

In case of the FE phase transitions, the order parameter is the polarization P. Following a simplified Landau-Devonshire description where the strain is neglected, the free energy of a ferroelectric material can be then described as a Taylor expansion in terms of the polarization only as follows:

$$F = \frac{1}{2}A(T - T_0)P^2 + \frac{1}{4}BP^4 + \frac{1}{6}CP^6, \tag{2.19}$$

where the expansion is truncated at the sixth term, T is the temperature, A, B and C are temperature independent coefficients and T_0 is the Curie temperature. In this expression, the internal energy of Eq. (2.18) is:

$$U(P) = \frac{1}{2}AT_0P^2 + \frac{1}{4}BP^4 + \frac{1}{6}CP^6, \tag{2.20}$$

and the entropic term TS gives the temperature dependence with entropy:

$$S = \frac{1}{2}AP^2. \tag{2.21}$$

In this Landau description, the A and C coefficients are positive in all ferroelectrics while the sign of the B coefficient will determine the nature of the phase transition between the paraelectric and the FE phases. When $T >> T_0$, the system is paraelectric with a single-well shape of the free energy like shown in Figure 2.9 (a), while when $T << T_0$ the system is in its FE phase, with a double-well shape of the free energy with respect to the polarization.

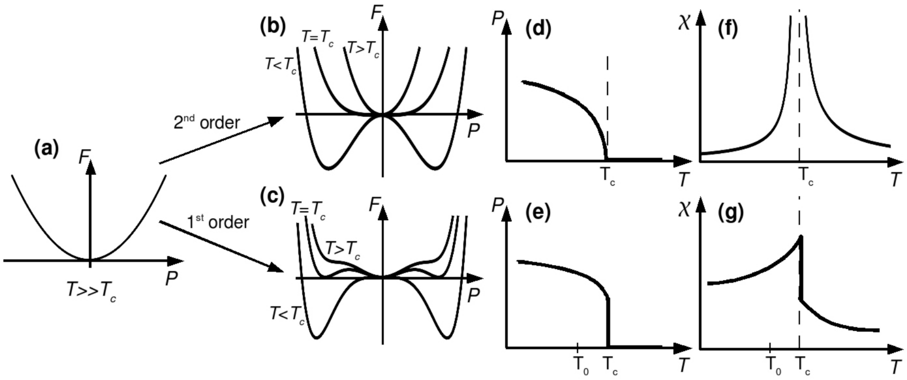

Figure 2.9: (a) Landau free energy as a function of polarization for the paraelectric phase. (b) Free energy as a function of the polarization for a ferroelectric material in a second-order phase transition at $T > T_0$, $T = T_0$ and $T < T_0$. (d) and (f) are respectively the spontaneous polarization P and the susceptibility as a function of the temperature for a second-order phase transition. (c) Free energy as a function of the polarization for a ferroelectric material in a first-order phase transition at $T > T_0$, $T = T_0$ and $T < T_0$. (e) and (g) are respectively the spontaneous polarization P and the susceptibility as a function of the temperature for a first-order phase transition.

If $B > 0$, then the paraelectric-ferroelectric transition takes place at T=T_0 and the free energy will evolve continuously from the single-well to the double well [Figure 2.9 (b)], which is related to a second-order phase transition. In the FE phase, the spontaneous polarization P_0 of the material is given at the two minima of the double well ($\pm P_0$) and can be estimated at E=0 by the conditions $\frac{\partial F}{\partial P}$=0 and $\frac{\partial^2 F}{\partial P^2}$ <0, giving rise to the following solutions (the sixth order term being neglected):

$$P_0 = \pm\sqrt{\frac{a}{b}(T_0 - T)}. \tag{2.22}$$

The spontaneous polarization will increase when decreasing the temperature and will vanish for $T \geq T_0$ as plotted in Figure 2.9 (d). The dielectric susceptibility χ=$\partial P/\partial E|_{P_0}$ will follow the Curie-Weiss evolution: χ=$[a(T - T_0)]^{-1}$ for $T > T_0$

and χ=$[2a(T_0-T)]^{-1}$ for $T<T_0$. Consequently, the dielectric susceptibility diverges at T=T_0 as represented in Figure 2.9 (f) which is consistent with the microscopic description of the dielectric constant of Eq. (2.9).

If $B<0$, the order parameter jumps discontinuously and the phase transition is called a first-order transition. It results that, even when $T>T_0$, the free energy may have two local minima at non-zero polarization P as shown in Figure 2.9 (c). When the temperature is reduced, the polar phase will become the most favorable at the Curie temperature T_c which will be different and larger than the T_0 define in Eq. (2.19). Between T_c and T_0 the paraelectric phase will correspond to a local minimum of the free energy. Here, the temperature evolution of the polarization will display a discontinuous jump to zero at T=T_c (Figure 2.9 (e)), while the dielectric susceptibility will display a finite jump at T_c (Figure 2.9 (g)).

In the case of AFD phase transitions, the same development can be made by attributing a new order parameter ϕ which will describe the rotation of the oxygen tilts. The free energy can be then expressed as:

$$F(\phi)=\frac{1}{2}A'(T-T_0')\phi^2+\frac{1}{4}B'\phi^4+\frac{1}{6}C'\phi^6 \tag{2.23}$$

where T_0' is the transition temperature between the undistorted reference and the AFD phase [60].

At last, the strain effects can also be included in the free energy and has a form similar to the one given in Eq. (2.14) [79]. When all P, ϕ and η are included, their coupling must be considered. This was for instance applied by Pertsev to $SrTiO_3$ [60].

2.6.2 Relationship between macroscopic and microscopic theories

In the Section 2.5.1, we have presented a parametrization of the energy by performing a Taylor expansion of the total energy with respect to the pattern of displacement ξ and the strain η. In the case of FE distortions, it is possible to have a good estimation of the spontaneous polarization P_α resulting from a pattern of FE displacements ξ_α in the direction α as follows:

$$P_\alpha=\frac{1}{\Omega}\sum_{\kappa,\beta}Z^*_{\kappa,\alpha\beta}\xi_{\kappa,\beta} \tag{2.24}$$

where α and β label the cartesian coordinates and Z^*_κ is the Born effective charge of the atom κ calculated in the paraelectric reference. Therefore, it is possible to re-express the internal energy of Eq. (2.13) in terms of the spontaneous polarization:

$$U(P)=\frac{1}{2}a'\sum_i P_i^2+\frac{1}{4}b'\sum_i P_i^4+\frac{1}{4}c\sum_{i<j}P_i^2P_j^2+\textit{higher order} \tag{2.25}$$

where a', b' and c' are the renormalized parameters for $U(P)$. As for a in Eq. (2.13), the coefficient a' is related to the square of the FE soft mode frequency. Since this FE mode is unstable it gives $a'<0$.

This result is valid at zero Kelvin and does not take into account the temperature dependence of the soft mode. In a displacive phase transition, the phase transition takes places when a mode becomes softer when the temperature decreases from high value, until freezing-in in the structure at the transition temperature T$_C$. At the atomistic level, it is possible to show that the temperature dependence of the soft mode arises from the anharmonic coupling of the soft mode with other modes, giving rise to a renormalization of the harmonic frequency [80]:

$$\widetilde{\omega}^2 = \omega_0^2 + \frac{k_B T}{2} \sum_i \frac{\alpha_i^4}{\omega_i^2} \tag{2.26}$$

where ω_0 is the harmonic frequency of the soft mode, k_B is the Boltzmann constant and α_i is the anharmonic coupling coefficient of the soft mode with the mode i of frequency ω_i. The transition temperature T$_C$ being the temperature where the frequency of the soft mode $\widetilde{\omega}$ reaches zero, we can deduce from Eq. (2.26) that:

$$T_C = -\frac{2\omega_0^2}{k_B \alpha} \tag{2.27}$$

where $\alpha=\sum_i \frac{\alpha_i^4}{\omega_i^2}$. The temperature dependence of $\widetilde{\omega}$ can be rewriten as follows:

$$\widetilde{\omega}^2 = \omega_0^2 - \frac{\omega_0^2}{T_C} T = -\frac{\omega_0^2}{T_C}(T - T_C) \tag{2.28}$$

This expression shows a linear dependence of the frequency with the temperature which corresponds to what is observed experimentally.

Taking this into account and assuming the polarization oriented in one direction only, it is now possible to rewrite the free energy as follows:

$$F(P) = -\frac{1}{2}\frac{\omega_0^2}{T_C}(T - T_C)P^2 + \frac{1}{4}b' P^4 + \textit{higher order.} \tag{2.29}$$

It is interesting to notice that this expression of the energy is similar to Eq. (2.19) coming from the Landau-Devonshire description and makes therefore the connection between the microscopic and phenomenological description. It also highlights that Landau theory is particularly suited to describe displacive phase transition since the temperature evolution of the soft mode is compatible with temperature independence of the parameters assumed by Landau.

2.7 Conclusion

In this Chapter we have reviewed the main characteristics of the ATiO$_3$ bulks materials through the cases of BaTiO$_3$, SrTiO$_3$, PbTiO$_3$ and CaTiO$_3$. From this overview we can point out the following main outlines:

(i) Two main kinds of instabilities can be present together in these compounds: the FE instability located at the Γ point and the AFD instability located at the zone boundary.

(ii) These instabilities originate in a delicate balance between the SR and LR interactions: the LR interactions are destabilizing and the SR interactions are stabilizing for the FE instability while the opposite is true for the AFD instabilities.

(iii) These two kinds of instabilities are in competition since freezing-in one tends to suppress the other, giving rise to two possible ground-states: FE for $BaTiO_3$ and $PbTiO_3$ or AFD for $SrTiO_3$ and $CaTiO_3$.

The fact that instabilities arise from a delicate balance between SR and LR interactions allows to anticipate the finite-size effects since both will be modified in nanostructures. The SR forces will be modified at the surface and interfaces because of the modification of the chemical environment and, obviously, the LR dipole-dipole interactions will be affected by the finite size of the nanostructures and will be strongly dependent on the electrical boundary conditions. Additionally to that, we have shown also that we must take into account the coupling of the FE and AFD distortions to the strain. Due to this coupling, we can expect that ABO_3 compounds will be strongly sensitive to external mechanical boundary conditions.

In nanostructures, all of these factors will compete with each other in such a way that is difficult to predict their properties without performing explicit calculations. Such finite-size effects will be descibed in details in the next Chapter.

2.8 References

An extensive review of the properties of ferroelectric compounds can be found in the following books:

- M. E. Lines and A. M. Glass, “Principles and applications of ferroelectrics and related materials”, Clarendon Press, Oxford (1977).
- “Physcis of Ferroelectrics, A modern Perspective”, edited by K. Rabe, Ch. H. Ahn and J.-M. Triscone, Springer (2007).

Chapter 3

Finite size effects

As presented in Chapter 2, the ferroelectricity of bulk perovskites is associated to a collective effect coming from a delicate balance between the short-range (SR) interactions and long-range (LR) Coulomb forces. Therefore, it can be expected that reducing the size of the compound in one or more directions will produce a change of the SR forces in the surface region, will cut the range of dipolar interactions in these directions and so will modify the balance between SR and LR forces. From these considerations, until the 90's, it was thought that a critical thickness in thin films for ferroelectricity will prevent the use of ferroelectric materials in devices smaller than this limit which was estimated to be 10-20 nm. However, recent improvements in the synthesis and characterization of ferroelectric oxide thin films have allowed the observation of the ferroelectricity well below the expected 10-20 nm critical thickness [5]. From these observations, many studies focussed on the understanding of the ferroelectric finite size effects in ferroelectrics nanostructures.

Due to the complexity of the physics of these ferroelectric nanostructures, the understanding of their properties has been investigated through empiric and phenomenological models as well as first-principles calculations. This complexity comes from the manifold effects that compete and might modify the delicate balance between the LR and SR forces, whose equilibrium is known to be at the origin of the ferroelectric instability. These different effects can be summarised as follows [7]:

- *Surface effects.* In nanostructures, one or more faces are free surfaces at which some of the interactions are missing due to the lack of neighboring atoms. The hybridizations between the Ti $3d$ and O $2p$ orbitals and the Born effective charges, directly related to the emergence of ferroelectricty in bulk (as discussed in Chapter 2), are affected and so the SR and LR forces can be significantly modified.

- *Mechanical effects.* Ferroelectric thin films are usually grown on top of a thick substrate, that imposes its in-plane lattice constant and symmetry. The epitaxial strain resulting from the lattice mismatch between the film and the substrate is known to strongly couple with the ferroelectric polarization.

- *Electrostatic effects.* When a polarization normal to the surface is present, a depolarizing electric field is created which conflicts with the ferroelectric instability. This can be related to a huge electrostatic energy cost and then, to preserve ferroelectricity the depolarizing field must be screened.

- *Finite conductivity.* Ferroelectric materials are a priori insulators but finite conductivity is often reported in ferroelectric thin films. This finite conductivity might interfere with the ferroelectric properties by modifying the amplitude of the depolarizing field. The leakage current mechanism changes depending on the kind of interface, which can also play a role.

- *Defects.* The presence of defects such as impurities, oxygen vacancies, *etc* modify the chemical composition of the surface and can influence the local strain that might play a critical role.

The two last effects, finite conductivity and defects, are potentially important but the proper treatment of their effect is not yet fully studied. In contrast, good progresses have been reported for surface effects, mechanical and electrical boundary conditions. All of these different factors can act independently to either enhance or suppress ferroelectricity and will compete with each other. However, in practice, two main factors were identified to play a major role: the mechanical and the electrical boundary conditions.

In this Chapter, we will restrict the discussion on the role of: *first*, the effects of surface atomic relaxations, *second*, the effects of mechanical epitaxial strains and, *third*, the electrostatic effects through the concept of the depolarizing electric field. The other effects like defects and vacancies, impurities at the surfaces, *etc*, are not reported here and are less issued since their study was less go into detail and they have not been taken into account in the present works.

3.1 Surface and interface atomic relaxations

3.1.1 Generalities

In ferroelectric nanostructures one or more faces of the ferroelectric material are free surfaces and the atoms at the surface miss interactions with respect to the bulk, giving rise to surface relaxations and even surface reconstructions. The smaller the nanostructure, the more important the surface effects due to the increasing surface/volume ratio.

The interface atomic relaxations can be expected to play a role in the physics of ferroelectric nanostructures since these relaxations affect the chemical bonding and the Born effective charges near to the interfaces. By comparison with the bulk environment, these modifications will alter the short-range and long-range interactions between atoms which play a crucial role in the ferroelectric compounds. It results from these effects that the distance between atomic planes and bulk ideal atomic positions are modified giving rise respectively to interplanar distance changes and rumpling effects.

In ionic systems, the rumpling relaxations give small displacements of cations (M) and anions (O) in opposite directions, which creates additional small dipolar moments on each atomic layer. If we define $\delta_z M_i$ and $\delta_z O_i$ as the displacements of respectively the cation and the anion along z in atomic layer i with respect to the reference configuration (unrelaxed truncated bulk), the rumpling of the atomic layer i is:

$$\eta_i = \frac{1}{2}\left[\delta_z(M_i) - \delta_z(O_i)\right]. \qquad (3.1)$$

This rumpling parameter describes the movement of the ions with respect to the mean position of each atomic plane and will be then positive when the cation M_i is above the oxygen, and negative otherwise. Usually the paraelectric reference of the nanostructures have nevertheless these dipolar moments, but the sum of each planar dipolar moments cancel together by symmetry considerations, keeping the total system unpolarised.

The change in the interplanar distance between consecutive planes i and j can be calculated as follows:

$$\Delta d_{ij} = \frac{1}{2}\left[\delta_z(M_i) + \delta_z(O_i)\right] - \frac{1}{2}\left[\delta_z(M_j) + \delta_z(O_j)\right]. \qquad (3.2)$$

3.1.2 Example: $PbTiO_3$ thin films

Here we illustrate the effect of atomic relaxations on $PbTiO_3$ thin films as reported in Ref. [81], where DFT calculations were performed in order to quantify the surface relaxation and help the experimentalists to interpret their data. These calculations were performed within the LDA approximation using the ABINIT package [9].

Two different supercells were considered : a thick $PbTiO_3$ slab in vacuum (Figure 3.1 c) and a $SrTiO_3$/(one unit cell)-$PbTiO_3$/vacuum stack (Figure 3.1 d). To reproduce the substrate clamping effect, we fixed the in-plane lattice constant to the relaxed a-axis value of $SrTiO_3$. Our calculations were restricted to (1×1) surface periodicity and did not allow for an eventual AFD $c(2 \times 2)$ reconstruction [82].

We report in Figure 3.1 c, d the distortions in the upper half of each supercell ("para-relaxed" state). For easy comparison with the experiment, in spite of the typical LDA underestimate of the lattice constant, the values are given as a percentage of the bulk out-of-plane cell parameter (3.84 Å for STO and 3.91 Å for PTO). We also defined a reference configuration ("para-unrelaxed") in Figure 3.1 a: it corresponds to the truncated bulk paraelectric structure of $PbTiO_3$ with the in-plane lattice constant constrained to that of $SrTiO_3$ (experimental cell parameter a_{STO} = 3.905 Å) and a consequent tetragonality $c_0/a_{STO} = 1.03$ [83]. Figure 3.1 b ("ferro-unrelaxed") shows the atomic distortion of the "up"-state as determined for bulk $PbTiO_3$ in Ref. [84] with $c = 4.17$ Å.

The magnitudes of the FE and surface relaxation effects can now be compared. First, the cation-oxygen displacements due to ferroelectricity (≈10% of c_0, Figure 3.1 b) are significantly larger than the displacements due to surface relaxation/rumpling (≈ 1-3 % of c_0, Figures 3.1, c and d). Second, the mean layer displacement for the "up"-state (Figure 3.1 b) and for the surface relaxation (Figures 3.1, c and d) are opposite. Third, the surface relaxation and

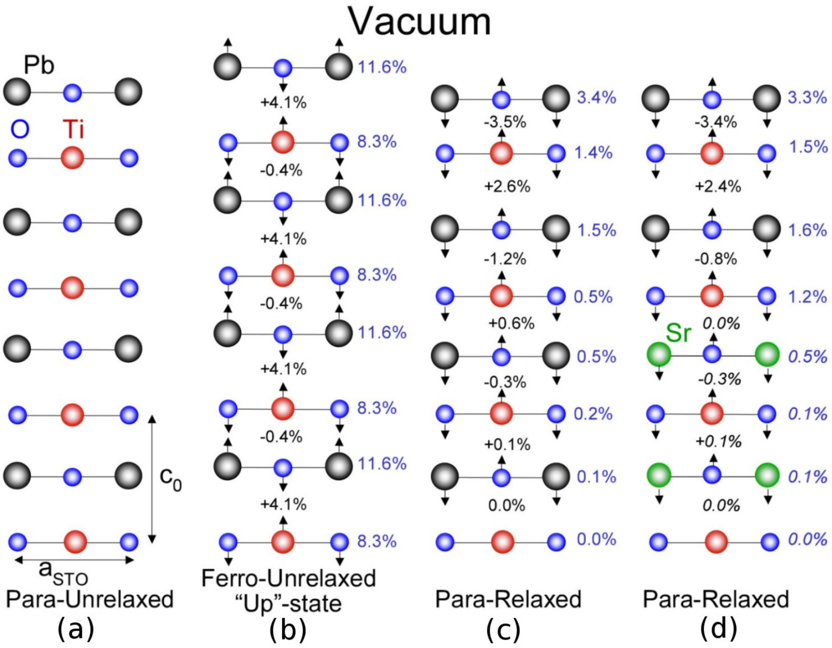

Figure 3.1: Schematic view of the atomic displacements resulting from FE distortion and from surface/interface relaxation in the uppermost layers of a $PbTiO_3$ film epitaxially grown on $SrTiO_3$. In bulk $PbTiO_3$, epitaxial strain produces a tetragonality at zero polarization that can be estimated from the macroscopic elasticity theory as $c_0/a_{STO} = 1.03$. The ionic configuration resulting from the truncation of such a strained bulk paraelectric state (a) is considered as the reference structure. Freezing the bulk FE distortion (as reported in Ref. [84]) into this reference structure results in the "up"-state shown in (b). Additionally, the natural ionic relaxation at the surface in the paraelectric state has been computed from first-principles both for a thick $PbTiO_3$ slab in vacuum (c) and a $SrTiO_3$/(one unit cell) $PbTiO_3$/vacuum stack (d). Numbers in black correspond to the change of interlayer distances. Numbers in blue corresponds to the atomic rumpling in each layer (cation-oxygen distance). All the values are in % of c_0, except those in italic that concern $SrTiO_3$ and are in % of a_{STO}.

rumpling effects are globally unaffected by the film thickness (Figures 3.1, c and d) and their amplitude decays very quickly when going to the interior of the film : they are already negligible two unit cells below the surface.

3.1.3 Summary

These results on $PbTiO_3$ thin film are general and were reported for other ABO_3 thin films like $BaTiO_3$ [85] or $SrTiO_3$ [86] and superlattices [87]: the rumpling and interplanar distances are small with respect to the bulk FE distortions and are mainly present in the vicinity of the surfaces and rapidly disappear in the interior of the nanostructure. In the case of interface with another compound, like in superlattices, these relaxations are smaller than at surface with vacuum and can even be negligible for interfaces between similar compounds [7].

These surface relaxations play therefore a minor role in most cases even if we notice that the surface or interface can possibly modify the competition between AFD and FE instabilities. As shown in Figure 3.2, this was demonstrated on $PbTiO_3$ surface when allowing a $c(2 \times 2)$ reconstruction which gives rise to unusual coupling of the AFD and FE distortions in the vicinity of the surface region [82, 88]. As shown in Figure 3.2-left, this surface reconstruction is confined to the first perovskite unit cell at the surface , while bulk-like behavior is recovered below. Another example of such modification of the AFD/FE instabilities competitions will be given in Chapter 5.

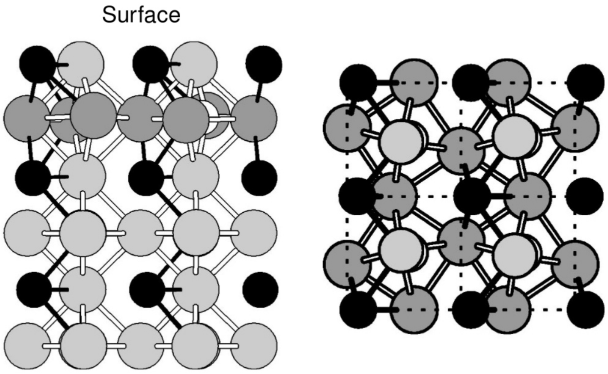

Figure 3.2: c(2×2) reconstruction of $PbTiO_3$ film with PbO termination. (Left) side view of the three first perovskite unit cells thickness below the surface. The oxygen atoms in the first cell are shown in a darker color, highlighting the AFD rotations in the TiO_2 subsurface layer. (Right) top view of the surface where only the first top two PbO and TiO_2 atomic layers are shown. From [82].

3.2 Mechanical boundary conditions

The study of the mechanical constraint imposed by the substrate on the ferroelectric thin films properties were extensively studied [89] and at the origin of what is currently referred to as strain engineering of the properties. Since the ferroelectric bulk compounds are strongly sensitive to the pressure and the mechanical constraints, the imposition of epitaxial strain has indeed been shown to play important role in the determination of the ferroelectric properties of thin films and superlattices.

The epitaxial strain allows to fix the in-plane atomic distances and the in-plane cell shape of the grown compound to the one of the substrate. In the case of thin films and superlattices, the out-of-plane direction is free to relax which yields "mixed" mechanical boundary conditions: fixed in-plane strain and fixed out-of-plane stress.

The thickness of the film plays an important role to have highly coherent strain between the substrate and the film. When the epitaxial strain is too large, the thin film will keep growing coherently with the substrate as long as the elastic energy required to strain the film and match the substrate is smaller than the energy required for the appearance of misfit dislocations. Beyond this limit, dislocation defects appear to reduce the strain by allowing the structure to recover the bulk geometry with zero-strain. It ensues that too strong epitaxial strains as well as films with too large thicknesses are not favorable since the desired strain effects will be loosed.

Previous studies have shown that in ferroelectric thin films, the epitaxial strain can allow to enhance or destroy the spontaneous polarization of the grown system with respect to its bulk value and can also modify the sequences of the temperature phase transitions. Recently, strain engineering of the ferroelectric properties has been demonstrated experimentally: a polarization 250% higher than in bulk single crystals has been reported in $BaTiO_3$ epitaxial films [90]. Epitaxial strain can also induce polarization in non-ferroelectric bulk compounds or create new combinations of instabilities as it was reported for $SrTiO_3$ thin films [60, 91].

These results can be understood from the energy expressions Eqs. (2.13)-(2.15) given in the previous chapter. Let us consider an epitaxial film with an homogeneous cubic in-plane strain: $\eta_1=\eta_2=\eta$ and $\eta_6=0$. In this epitaxial condition, the out-of-plane strain η_3 and the shear strains η_4 and η_5 are free to relax. Now, for simplification we will suppose the distortion ξ to exist only in the z direction ($\xi_x=\xi_y=0$). Replacing these conditions in Eqs. (2.13)-(2.15) allows to write the total energy as follows:

$$E(\xi_z,\eta,\eta_3,\eta_4,\eta_5) = \frac{1}{2}\left(a + g_{11}\eta_3 + 2g_{12}\eta\right)\xi_z^2 + \frac{1}{4}b\xi_z^4 + E^E(\eta,\eta_3,\eta_4,\eta_5). \quad (3.3)$$

From this expression, it is clear that the polarization-strain coupling induces a renormalization of the quadratic part of the internal energy U. Depending on the values of the coupling parameters g_{11} and g_{12}, and the strains η and η_3, we can see that it is possible to modulate the coefficient of ξ_z^2 by increasing or decreasing its negative value and so respectively enhancing or suppressing the instability.

In the case of the FE distortions, a general rule for epitaxial strain effects is that compressive in-plane strain will tend to favor the out-of-plane tetragonal phase, with polarization oriented in the z direction, while tensile in-plane strain

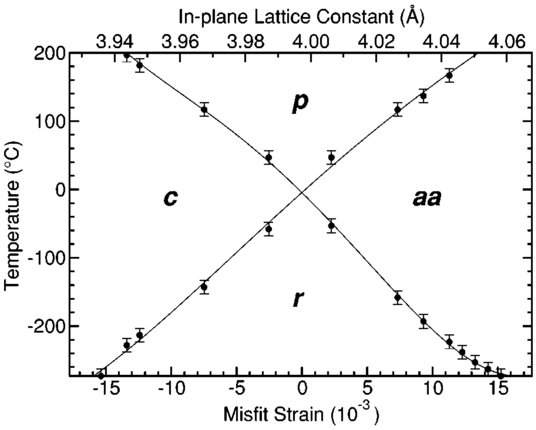

Figure 3.3: Phase diagram of $BaTiO_3$ in terms of epitaxial misfit strain and temperature (from [92]). The labels are: p= paraelectric phase, c= tetragonal phase with polarization oriented in the out-of-plane direction, aa= othorhombic phase with polarization oriented in the in-plane direction and r= monoclinic phase with polarization oriented in the three directions.

will tend to favor the FE phase with in-plane orientation of the polarization. This general rule is usually valid for large tension and compression while for intermediate amplitude of epitaxial strain, distinct behaviors can take place as a mix of in-plane and out-of-plane orientation of the polarization. A typical system for these rules is the case of $BaTiO_3$ [92–95] as illustrated in Figure 3.3. Furthermore, this artificial enhancement or suppression of the ferroelectricity will depend strongly on the amplitude of the polarization/strain coupling of the grown compounds [96].

Moreover, when AFD instabilities are present together with the FE instabilities, the epitaxial strain can also shift the phases with respect to the bulks by modifying the competition between the instabilities. Much more complicated phase diagrams are therefore possible. This has been previously investigated in $SrTiO_3$ [60]. We will present such epitaxial strain modification of the competition between AFD and FE instabilities in the Chapter 4 by exemplifying it on $SrTiO_3$, $PbTiO_3$ and $CaTiO_3$.

3.3 Electrical boundary conditions

As presented in the introduction of this chapter, another important key parameter that monitors the behavior of ferroelectric nanostructures is the electrostatic cost associated to the presence of non-vanishing electric fields in such systems.

3.3.1 Free slabs

If we try to polarise in the out-of-plane direction a ferroelectric slab in vacuum like represented in Figure 3.4.a, surface charges will be present on each surface. Due to the discontinuity of the polarization P_z at the surface, these surface charges will generate an electric field in the opposite direction than the polarization. This can be understood by the application of the continuity of the perpendicular component of electric displacement $D_\perp$ at the interface, being zero in the vacuum region:

$$D_\perp = \varepsilon_0 \mathcal{E} + P_z = 0 \tag{3.4}$$

which gives the following expression for the electric field:

$$\mathcal{E} = -\frac{P_z}{\varepsilon_0}. \tag{3.5}$$

This electric field will totally suppress the polarization in the out-of-plane direction and is called the depolarizing electric field. However, experimentally ferroelectric thin films can be polarised in the out-of-plane direction and can be switchable by applying an electric field. This is achieved by screening the depolarizing field (Figure 3.4 b).

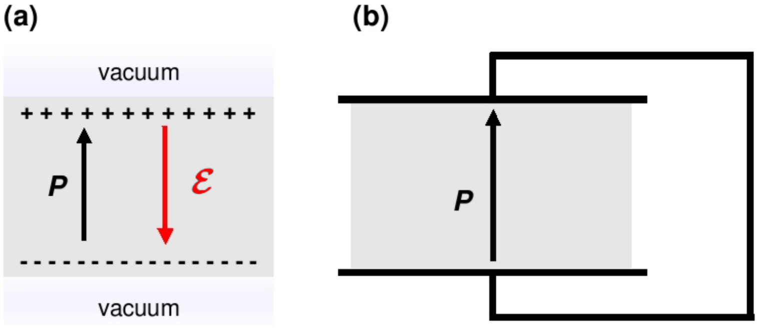

Figure 3.4: (a) Schematic representation of a free ferroelectric slab in vacuum with hypothetical out-of-plane polarization P generating depolarizing electric field $\mathcal{E}$. (b) Schematic representation of a short-circuited ferroelectric thin films between "perfect" metallic electrodes where the film is polarised homogeneously in the out-of-plane direction.

3.3.2 Thin films between metallic electrodes

Ideally, this depolarizing electric field could be totally suppressed if the surface charges are completely compensated. One possibility to screen these surface charges is to introduce the ferroelectric film between two metallic electrodes in short-circuit as presented in Figure 3.4.b. However, with realistic electrodes, it was demonstrated by Junquera and Ghosez [97] that the screening at the interface between the metal and the ferroelectric slab is not perfect and the depolarizing electric field is not totally compensated. Let us look at that in further details.

We have shown that when polarizing a thin ferroelectric film in the perpendicular direction to the interface, it gives rise to a net surface charge σ. At the surface of the electrode, screening charge is induced to compensate the surface charge of the ferroelectric film. This compensation charge can be considered in practice to be spread over a finite distance from the interface, giving rise to an interface dipole and a jump in the electrostatic potential at each film/electrode interface. This drop of potential ΔV is shown to be proportional to the polarization P as follows:

$$\Delta V = \frac{\lambda_{\text{eff}}}{\varepsilon_0} P \tag{3.6}$$

where λ_{eff} is a constant of proportionality called the effective screening length. So, for two equivalent interfaces, the total drop of potential will be ΔV and if we suppose the electrodes to be in short-circuit, a residual depolarizing electric field $\mathcal{E}_d$ should be present in the ferroelectric film (to compensate for the jump of potential at the interface):

$$\mathcal{E}_d = -\frac{2\Delta V}{l} \tag{3.7}$$

where l is the film thickness. Combining Eq. (3.6) and Eq. (3.7) gives rise to the following expression:

$$\mathcal{E}_d = -\frac{2\lambda_{\text{eff}}}{\varepsilon_0 l} P = -\beta \frac{P}{\varepsilon_0}. \tag{3.8}$$

This means that the residual depolarizing field in the ferroelectric film is proportional to the polarization and the ratio between the screening length and the film thickness. This can be described with a screening parameter $\beta = \frac{2\lambda_{\text{eff}}}{l}$ which is included between 0 and 1. β=0 is associated to a perfect screening of the surface charges (perfect short-circuit boundary conditions, achieved when $l >> \lambda_{\text{eff}}$) and β=1 will correspond to zero screening (open-circuit boundary conditions).

By determining the depolarizing field in $BaTiO_3$ ferroelectric thin films between two $SrRuO_3$ electrodes, Junquera and Ghosez reported a value of λ_{eff}=0.23Å which is relatively small compared to the interatomic distances (∼2 Å). However it was shown to have a sizeable effect on the polarization for films up to more than 100 Å. Therefore, the challenge for such interfaces is to optimize the ferroelectric/metal interface to reach the smallest imperfect screening length which will reduce the depolarizing electric field and so will allow to keep out-of-plane polarization in small ferroelectric films [98].

In terms of the model energy developed in Section 2.5, including the depolarizing electric field would give to a new term proportional to -$\mathcal{E}P$. Since the depolarizing electric field is proportional to $-P$, the additional term -$\mathcal{E}$P will be proportional to $+P^2$ and so to ξ^2. As for the strain (discussed in Section 4.2), by combining this term in the total energy will renormalize the ξ^2 term by a positive factor and so will always contribute to reduce the ferroelectricity.

Another way to avoid the depolarization field is the formation of ferroelectric domains when thin films are deposited on insulator substrate [99, 100]. The presence of alternating 180° domains also allows to prevent the appearance of a wide surface charges. Nevertheless, usually the systems with domains are not considered as ferroelectric since even if the system is locally polarised, its polarization is no more expected to be switchable [101], which makes the formation of domains less interesting for the ferroelectric applications.

3.3.3 Superlattices

In this section we will generalize the formulation of the depolarizing electric field effect through ferroelectric/dielectric superlattices using classical electrostatic considerations.

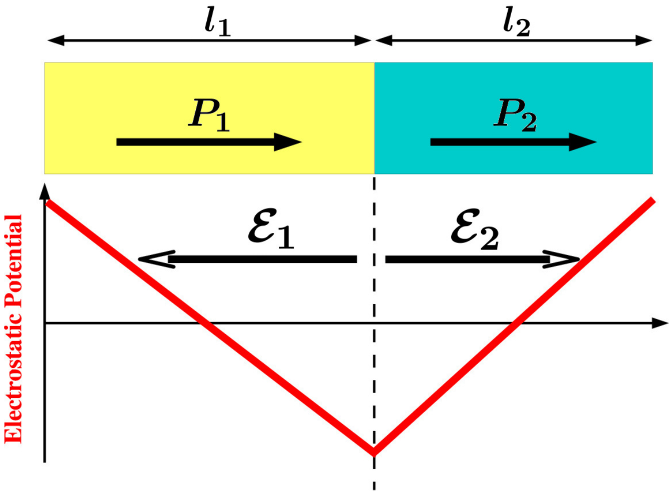

Figure 3.5: Shematic representation of a ferroelectric/dielectric interface.

Electrostatics

Following the Figure 3.5, the superlattice supercell can be decomposed in two parts: the ferroelectric part (index 1) of thickness l_1 and the dielectric part (index 2) of thickness l_2 (the dielectric can be ferroelectric or not).

If we suppose the ferroelectric uniformly polarized with polarization P_1, due to the finite size of the system a depolarizing electric field $\mathcal{E}_1$ appears in the opposite direction of P_1. Due to the short circuit boundary conditions, the electrostatic imposes an electric field $\mathcal{E}_2$ in the dielectric layer, which induces a polarization P_2 in this second layer. The amplitude of the polarizations and the electric fields in the both layers will adjust to minimize the energy. Let us now develop the details of these quantities.

In the superlattice, the electrostatic imposes the continuity of the perpendicular electric displacement at the interface ($D = \epsilon_0 \mathcal{E} + P$):

$$D_1 = D_2, \tag{3.9}$$

which imposes:

$$\sigma = P_1 - P_2, \tag{3.10}$$

where σ is the surface charge and $P = P_0 + \epsilon_0 \chi^\infty \mathcal{E}$ is the total polarization with $P_0 = \frac{Z^*}{\Omega}\xi$ the spontaneous polarization in zero field, where Z^* are the Born effective charges and ξ are the atomic displacements with respect to the paraelectric positions.

The short-circuit boundary conditions on the whole superlattice impose the continuity of the electrostatic potential:

$$\mathcal{E}_1 l_1 = -\mathcal{E}_2 l_2. \tag{3.11}$$

and the condition on the electric displacement [(Eq. (3.9)] imposes:

$$\epsilon_0 \epsilon_1^\infty \mathcal{E}_1 + P_1^0 = \epsilon_0 \epsilon_2^\infty \mathcal{E}_2 + P_2^0, \tag{3.12}$$

where ϵ^∞ is the electronic dielectric constant. Combining it with Eq. (3.11), we deduce:

$$\mathcal{E}_1 = \frac{1}{\epsilon_0} \frac{l_2}{l_1 \epsilon_2^\infty + l_2 \epsilon_1^\infty} \left(P_2^0 - P_1^0\right) = -\frac{l_2}{l_1} \mathcal{E}_2, \tag{3.13}$$

Opposite finite electric fields will therefore appear in both layers and it is clear that they will be present when the polarizations P_1^0 and P_2^0 will differ.

Model energy

These features allow us to consider a simple model, similar to that developed for $PbTiO_3/SrTiO_3$ superlattices in Ref. [102]. This model consists in an expression of the energy as a function of (i) the zero-field polarizations, P_1^0 and P_2^0, of the two compounds composing the superlattice and (ii) their respective thicknesses l_1 and l_2:

$$E(P_1^0, P_2^0, l_1, l_2) = l_1 U_1(P_1^0) + l_2 U_2(P_2^0) + E_{elec}(P_1^0, P_2^0, l_1, l_2) \tag{3.14}$$

The first two terms, U_1 and U_2, correspond to the internal energies of each layer, in terms of their polarization in zero field. By supposing the microscopic interface effects negligible, these internal energies can be approximated to first order at the bulk level. For ferroelectric compounds, the shape of this internal energy has the form of a double well while for the normal dielectric it has a single-well shape with respect to the spontaneous polarization.

The third term, E_{elec}, is the macroscopic electrostatic contribution originating from the presence of non-vanishing electric fields in the two layers when their polarization differs. It corresponds to an energy cost in the ferroelectric layer, where the field is depolarizing, and to an energy gain in insulator, where the field is polarizing. It induces a coupling between P_1^0 and P_2^0 that explains why normal insulator can be polarised in spite of its single-well internal energy. Its expression can be deduced from the expansion of the total energy of a dielectric with respect to the electric field $\mathcal{E}$ [103]:

$$E_{tot} = E_{(\mathcal{E}=0)} - \mathcal{E}P^0 - \frac{1}{2}\epsilon_0\chi^\infty\mathcal{E}^2. \tag{3.15}$$

where in the present case the zero-field energy is the internal energy of the system:

$$E_{(\mathcal{E}=0)} = l_1U_1(P_1^0) + l_2U_2(P_2^0) \tag{3.16}$$

and the electrostatic energy for the superlattices can be written as follows:

$$E_{elec}(P_1^0, P_2^0, \mathcal{E}_1, \mathcal{E}_2) = -l_1(\mathcal{E}_1P_1^0 + \frac{1}{2}\epsilon_0\chi_1^\infty\mathcal{E}_1^2) - l_2(\mathcal{E}_2P_2^0 + \frac{1}{2}\epsilon_0\chi_2^\infty\mathcal{E}_2^2). \tag{3.17}$$

Including the expressions of electric fields of Eq. 3.13 allows to write the electrostatic energy as follows:

$$E_{elec}(P_1^0, P_2^0, l_1, l_2) = C(l_1, l_2).(P_2^0 - P_1^0)^2 \tag{3.18}$$

where

$$C(l_1, l_2) = \frac{l_1l_2}{2\epsilon_0}\,\frac{l_1(\epsilon_2^\infty + 1) + l_2(\epsilon_1^\infty + 1)}{(l_1\epsilon_2^\infty + l_2\epsilon_1^\infty)^2}. \tag{3.19}$$

This simple model clearly highlights that different terms compete to have a stable polarization state in the superlattice. In U_1, a finite polarization P_1 will decrease the energy but polarizing the ferroelectric layer alone produces a huge electrostatic energy cost E_{elec}. This energy penalty can be avoided by polarizing the insulating layer but this also has an energy cost (U_2 with single shape).

Such kind of electrostatic model was used to reproduce the experimental results for the ferroelectric characteristics of $PbTiO_3/SrTiO_3$ superlattices and was able to reproduce quite accurately these experimental results as well as the first-principles calculations [102]. Similar model was also applied on $BaTiO_3/SrTiO_3$ superlattices [104] and successfully reproduces the global trends of the first-principles simulations. In these two examples where the insulator ($SrTiO_3$) is highly polarizable, the superlattice sustain a finite polarization in its ground-state with polarization nearly uniform in order to minimize the electrostatic energy. When the insulator becomes less polarizable, both polarizations will be totally suppressed when the energy cost to polarize the insulator becomes too large. Such example will be discussed in Chapter 6.

These successes to reproduce the global physics in such systems point to the fact that the electrostatic effects strongly monitor the ferroelectric properties in ferroelectric thin films and superlattices.

3.4 Conclusion

In this chapter, we have presented three finite-size effects: epitaxial strains, interface atomic relaxations and depolarizing electric fields. We have shown that the atomic relaxations effects are almost negligible and are strongly localised to the interfaces while the epitaxial strain and the depolarizing field effects play an important role in the physics of such finite size systems since they can suppress (depolarizing field) or enhance (epitaxial strain) the polarization of the system. It results that the challenge for ferroelectric nanostructure engineering is not only to improve the sample quality but also to optimize and find the relevant mechanical and electrical boundary conditions for desired applications. For these last two conditions, the theoretical studies are useful to probe and highlight the finite-size effects.

3.5 References

Good overviews for the discussion of the finite-size effects in ferroelectric nanostructures can be found in the following references:

- Ph. Ghosez and J. Junquera, *First-principles modeling of ferroelectric oxide nanostructures*, in the *Handbook of Theoretical and Computational Nanotechnology*, edited by M. Rieth and W. Schommers, vol. 9, p. 623 (ASP, Stevenson Ranch, 2006).
- J. Junquera and Ph. Ghosez, *First-principles study of ferroelectric oxide epitaxial thin films and superlattices: role of the mechanical and electrical boundary conditions*, to appear in Journal of Computational and Theoretical Nanoscience.
- C. Lichteinsteiger, M. Dawber and J.-M. Triscone: *Ferroelectric Size Effects*, in *Physcis of Ferroelectrics, A modern Perspective*, edited by K. Rabe, Ch. H. Ahn and J.-M. Triscone, Springer (2007).
- M. Dawber, K. M. Rabe and J. F. Scott, *Physics of thin-film ferroelectric oxides*, Rev. Mod. Phys. **77**, 1083 (2005).

Chapter 4

Strain and stress effects

As previously presented in Chapter 3, due to the polarization-strain coupling in ferroelectric materials, ferroelectricity is highly sensitive to mechanical constraints as strains and stresses, that can be used in practice to tune the phase transition temperatures and the multifunctional properties [1]. First, for a long time, the ferroelectric instability was predicted to be reduced and even suppressed in the presence of isotropic pressure. This was however recently questioned by studies showing the reappearance of the ferroelectricty at ultra-high pressure [105]. Second, as previously discussed in Chapter 3, it has been observed that many properties of ferroelectric oxide thin films are quite different from those of the same material in the bulk. In ferroelectric thin films it is predicted that the epitaxial strain can produce a polarization enhancement and can modify the phase diagram of the constituent compound.

From those considerations, in this chapter we first describe the effects of hydrostatic pressure on the ferroelectric properties of cubic perovskites and analyse these effects for $BaTiO_3$ under high pressure. In a second part, we present the effects of a cubic in-plane strain on the properties of $SrTiO_3$, $PbTiO_3$ and $CaTiO_3$ bulks and show that such constraint can modify the competition between FE and AFD structural instabilities. This last point will allow us to clarify the main mechanical effect on thin films and nanosized materials epitaxially grown on a substrate.

4.1 Bulks under isotropic pressure

4.1.1 Generalities

Samara et al. [106], demonstrated that hydrostatic pressure reduces and even totally suppresses the ferroelectricity at high enough values in perovskite compounds. Using a simple model, they attributed this behavior to the fact that SR repulsions increases more rapidly than LR destabilizing forces as pressure increases. The strong sensitivity of ferroelectricity to pressure was also widely discussed at the first-principles level [107] and the sensitivity of the delicate balance between SR and LR forces in $BaTiO_3$ at small pressure was investigated in Ref. [61].

Recently, Kornev *et al.* [105, 108] demonstrated, both at the theoretical and experimental levels, that although ferroelectricity is indeed progressively suppressed at low pressure, an unexpected reappearance of the ferroelectricity is observed at ultra-high pressure. Exemplified on $PbTiO_3$, this surprising behavior was demonstrated to be a general property of various ferroelectric perovskites [108]. Moreover, from the inspection of SR and LR interactions, it was highlighted that high-pressure ferroelectricity is different in nature from conventional ferroelectricity and is driven by an original electronic effect rather than by LR interactions.

Since this was particularly astonishing, in order to achieve improved understanding of high pressure ferroelectricity, we investigated from first-principles the FE instability of $BaTiO_3$ under increasing isotropic pressure.

4.1.2 $BaTiO_3$ under high pressure

Technical details

Our calculations were performed within the technical details given in Section 1.8 except that we used denser 8×8×8 mesh of k-points to sample the Brillouin zone which was required to ensure the convergence.

Following Ref. [105], we first investigated the pressure behavior of the three polar F_{1u} zone-center (Γ) transverse optical (TO) modes of $BaTiO_3$ in the $Pm\bar{3}m$ paraelectric cubic structure. These modes are hereafter referred to as TO_1, TO_2 and TO_3. To that end, we computed the Γ dynamical matrix at independent lattice parameters, corresponding to different external isotropic pressures.

In our LDA calculations, the relaxed lattice parameter of the cubic phase corresponds to 3.94 Å that slightly underestimates the experimental value of 4.00 Å so that, in our simulation, the experimental structure corresponds to a negative LDA pressure of -10 GPa.

Phonon frequencies and mode effective charges

In Figure 4.1 a, we report the pressure evolution of the TO frequencies of $BaTiO_3$, where imaginary phonon frequencies corresponding to unstable modes are represented as negative numbers. The figure shows similar trends than for $PbTiO_3$ in Ref. [105] : ferroelectricity is first suppressed at low pressures and then reinforced at larger pressures. Nevertheless, contrary to $PbTiO_3$, in $BaTiO_3$ the FE instability is totally suppressed at $\approx$ 20 GPa (ω_{TO_1} becomes real) and only reappears at the extremely high LDA pressure of $\approx$ 140 GPa (ω_{TO_1} becomes imaginary again).

In Figure 4.1 b, we report for the three TO modes the isotropic mode effective charges defined as in Eq. (2.7). At zero pressure, the unstable TO_1 mode exhibit a giant mode effective charge ($9.17e$), typical of this class of compounds and compatible with an unusually large LR interaction [63]. When pressure increases, however, an abrupt change in $\bar{Z}^*_{TO1}$ is observed at a pressure of $\approx$

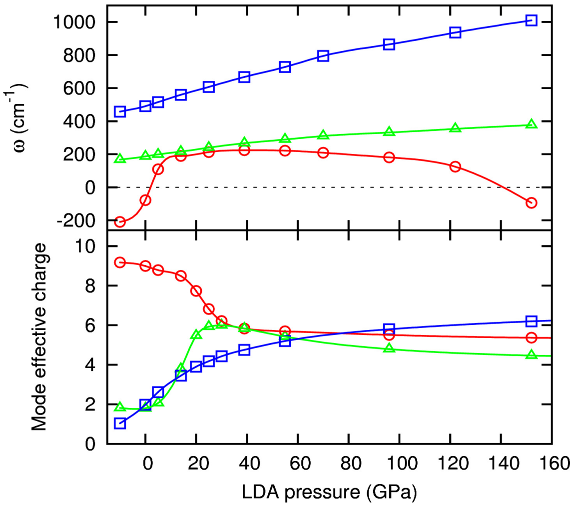

Figure 4.1: Pressure dependence of the frequency (a) and mode effective charge (b) of the three zone-center F_{1u} transverse optic modes in the $Pm\bar{3}m$ cubic phase of BaTiO$_3$: TO$_1$: red circles, TO$_2$: green triangles and TO$_3$: blue squares.

20 GPa. Beyond that pressure, none of the mode keeps a large mode effective charge.

In order to track the origin of this change of behavior, we computed the individual atomic Born effective charges Z^*_κ. At the experimental volume we found: $Z^*_{Ba} = +2.74e$, $Z^*_{Ti} = +7.35e$, $Z^*_{O_\parallel} = -5.80e$ and $Z^*_{O_\perp} = -2.15e$ where $Z^*_{O_\parallel}$ and $Z^*_{O_\perp}$ refer respectively to oxygen displacements parallel to Ti–O chains and perpendicular to them [62]. As previously reported [109], we observed that Z^*_κ are almost insensitive to isotropic pressure. The highly anomalous Ti and O$_\parallel$ charges changes by less than 3% between 0 and 150 GPa. The nearly nominal Ba and O$_\perp$ charges linearly increase by about 13 % over the same pressure range. This last feature attests for a gradual increase of the covalency between Ba and O but cannot explain the jump of $\bar{Z}^*_{TO_1}$ of Figure 4.1b.

Phonon eigendisplacements

The intriguing change of TO$_1$ mode effective charge results in fact from a sudden modification of the TO$_1$ soft mode pattern of atomic displacements. This clearly appears in Table 4.1 where we have reported the evolution of the components of η^{TO_1} for increasing pressure. Below ≈ 20 GPa, we observe the typical FE pattern of BaTiO$_3$ dominated by the displacement of Ti and O$_1$ atoms in opposite direction along Ti–O chains and the negligible role of Ba [110]. At 20 GPa, the direction of Ti displacement suddenly changes so that Ti and O$_1$ are now moving together. The Ba atom becomes much more involved in the soft mode, coherently with its increasing covalent character. Also, the oxygen atoms are no more all moving in the same direction but O$_1$ and O$_{2-3}$ are moving out of phase. These major changes arise from the mixing between the three different TO modes allowed by symmetry and is clearly attested in Table 4.1 from the overlap between η^{TO_1} at increasing pressure and the three η^{TO_i} at the experimental volume.

Pressure	TO$_1$ eigenvector				Overlap		
(GPa)	Ba	Ti	O$_1$	O$_{2-3}$	TO$_1$	TO$_2$	TO$_3$
-10	-0.002	-0.096	0.155	0.073	100	0.0	0.0
0	-0.002	-0.098	0.131	0.090	99.1	1.3	13.5
5	-0.001	-0.101	0.111	0.099	97.3	0.2	23.0
25	-0.033	0.127	0.005	-0.048	67.5	62.3	39.4
96	-0.024	0.116	0.038	-0.088	64.0	44.4	62.7
152	-0.019	0.110	0.043	-0.103	63.7	34.8	68.7

Table 4.1: Pressure dependence of the components of the eigendisplacements vector of the zone-center soft TO$_1$ mode (η^{TO_1}) and of his overlap (%) with the three η^{TO_i} at the experimental volume.

The FE instability that reappears at 140 GPa has therefore a totally different character than the one existing at usual pressure and the change of eigenvector is not limited to the Γ point. At the experimental volume, the FE instability of BaTiO$_3$ has a chain-like character in real space, corresponding in reciprocal space to three slab-like planar zones of instability in the Brillouin zone, intersecting at Γ and containing X and M points [64]. In line with the larger involvement of Ba, the pressure induced FE instability beyond 140 GPa has a much more isotropic character. The inspection of the full dispersion curves (Figure 4.2) reveals that the instability is now confined in a small and nearly spherical region around the Γ point (i.e. no instability at X and M anymore) corresponding to a larger and more isotropic volume of correlation in real space.

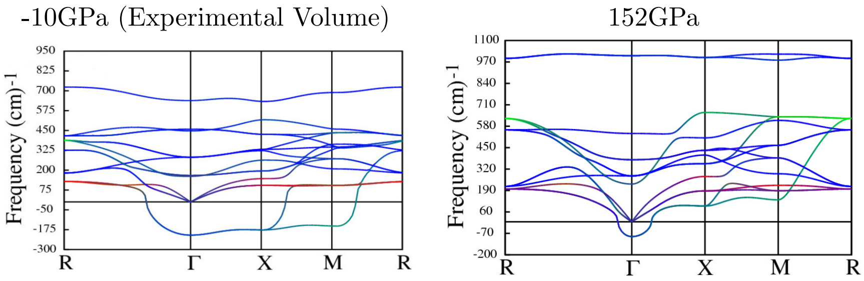
-10GPa (Experimental Volume)

152GPa

Figure 4.2: Phonon dispersion curves of cubic BaTiO$_3$ at the experimental volume (left) and under hydrostatic pressure of 152 GPa (right).

SR/LR decomposition and IFC

In the spirit of what we proposed in Chapter 2, we separated SR and LR contributions to the soft TO_1 mode. Our results on $BaTiO_3$ in Figure 4.3 are similar to those previously reported on $PbTiO_3$ [105] and highlights an interchange of the stabilizing and destabilizing roles of SR and LR parts. At low pressure, the instability originates in the LR forces ($\omega^2_{LR} < 0$) while, at high pressure, it is induced by destabilizing SR forces ($\omega^2_{SR} < 0$).

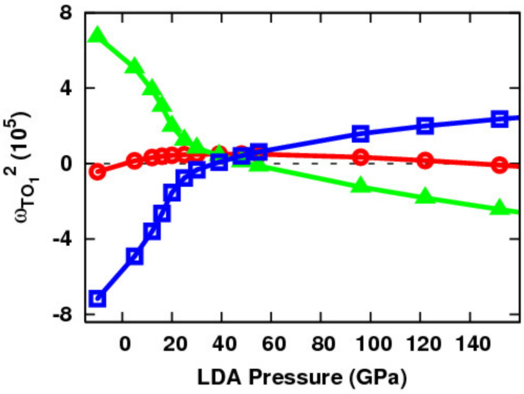

Figure 4.3: Pressure behavior of the soft TO_1 mode in the cubic paraelectric phase of $BaTiO_3$. The square of the frequency (red circles) is reported together with its SR (green triangles) and LR (blue square) contributions. The decomposition has been performed following Eq. (2.5).

In order to get a microscopic insight on the change of behavior of SR and LR forces, we computed the interatomic force constants (IFC) in real space, $C_{\kappa\alpha,\kappa'\beta}$, at different pressures following the technique described in Ref. [23]. As shown in Chapter 2, these IFC are defined through the relation $F_{\kappa\alpha} = -C_{\kappa\alpha,\kappa'\beta}\Delta\tau_{\kappa'\beta}$ where $\Delta\tau_{\kappa'\beta}$ is a displacement of atom κ' in direction β and $F_{\kappa\alpha}$ is the α component of the force so induced on atom κ. We summarized the results in Table 4.2 for selected pairs of atoms [the positions of the selected atoms are defined as follows in reduced coordinates : Ti_0 (0.5, 0.5, 0.5); O_1 (0.5, 0.5, 0); Ba_0 (0, 0, 0); Ba_1 (0, 0, 1)].

The values at the experimental volume are similar to those previously discussed in Ref. [64]. The self-force constants are all positive, meaning that $BaTiO_3$ is only unstable under collective atomic displacements. As pressure increases most of the IFC evolve very smoothly while very drastic changes are restricted to the Ti-O and Ba-O interactions only. The modification of the dynamics under pressure can therefore be directly related to the modification of the respective interactions of Ti and Ba with oxygen.

Going further, we also isolated SR and LR contributions to these individual IFC [64, 111]. The results are presented in Figure 4.4. The changes both of the total IFC and of their SR and LR contributions are almost linear and

Pressure	-10 GPa	5 GPa	25 GPa	150 GPa
Ba$_0$-Ba$_0$	**0.082**	+33	+76	+279
Ti$_0$-Ti$_0$	**0.156**	+33	+73	+240
O$_1$-O$_1$ (x=y)	**0.069**	+11	+23	+55
O$_1$-O$_1$ (z)	**0.132**	+50	+113	+405
Ti$_0$-O$_1$($\|$)	**0.008**	-330	-754	-2806
Ti$_0$-O$_1$($\perp$)	**-0.021**	+11	+30	+173
Ti$_0$-Ti$_1$($\|$)	**-0.067**	-9	-19	-60
Ti$_0$-Ti$_1$($\perp$)	**0.007**	+13	+26	+64
Ti$_0$-Ba$_0$($\|$)	**-0.029**	-16	-35	-118
Ti$_0$-Ba$_0$($\perp$)	**0.013**	+11	+24	+73
Ba$_0$-O$_1$($\|$)	**-0.001**	-697	-1629	-6543
Ba$_0$-O$_1$($\perp$)	**-0.004**	+1	+5	+56
Ba$_0$-O$_1$($\perp$)	**-0.011**	-7	-13	-29
Ba$_0$-Ba$_1$($\|$)	**-0.011**	-15	-33	-109
Ba$_0$-Ba$_1$($\perp$)	**0.004**	+13	+28	+89

Table 4.2: Selected interatomic force constants at different pressures. The values (Ha/Bohr^2) at the experimental volume (P=-10GPa) are taken as references. For the other volumes, the relative deviation with respect to this reference is reported in %.

surprisingly no change in the sign of the SR and LR contributions under pressure is observed. At the opposite, in all cases the SR and LR parts to the IFC reinforce their initial positive or negative character. This contrasts with the interchange of stabilizing and destabilizing role of ω^2_{SR} and ω^2_{LR} in Figure 4.3.

The inconsistency between these results is however only apparent. From Eq. 2.5, the SR and LR contributions to ω^2 does not only depend on the dynamical matrix and of the IFC but also on the eigenvector η. At the experimental volume, the giant destabilizing LR interaction ($\omega^2_{LR} < 0$) arises mainly from the unusually large attractive LR part of the longitudinal Ti$_0$–O$_1$ IFC (related to the giant Born effective charges of Ti and O) *combined* with a soft mode eigenvector in which these atoms are moving in opposite direction. At increasing pressure, the Born effective charges remain nearly similar so that the attractive LR part of the IFC between Ti and O remains roughly constant and only affected by the modification of the interatomic distance, as illustrated in Fig. 4.4. The change of sign of ω^2_{LR} that becomes positive is in fact related to the change of eigenvector of the unstable mode, with Ti and O moving in the same direction beyond 20 GPa. From this point of view, the change of behavior is not the result of a new unusual electronic interaction but the result of a change of the soft-mode eigenvector induced by the gradual evolution of Ti–O and Ba–O interactions.

Summary

To summarize, we have shown that the FE instability of BaTiO$_3$ is totally suppressed at a pressure of 20 GPa but reappears beyond 140 GPa. We highlighted

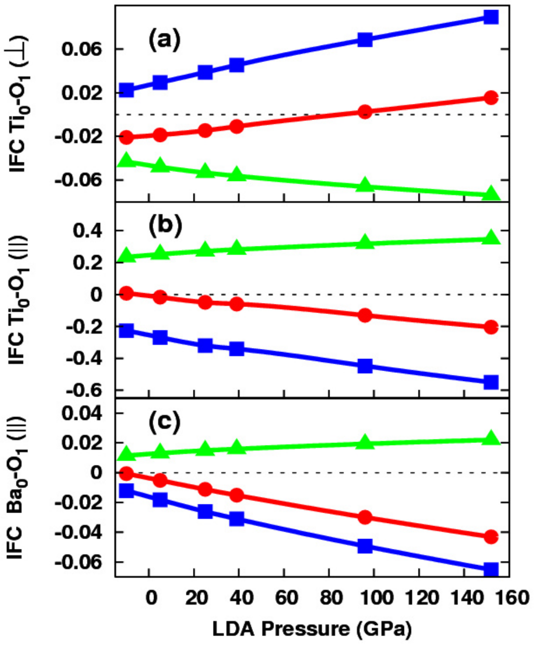

Figure 4.4: Pressure dependence of selected real-space interatomic force constants (Ha/Bohr^2). For each of them, the total value (red circle) as well as the SR (blue square) and LR (green triangle) contributions are shown. The successive panels correspond respectively to longitudinal and transverse Ti–O IFC and to longitudinal Ba–O IFC.

that the effect of pressure is mainly to gradually change the nearest neighbor Ti–O and Ba–O interactions producing a sudden change of the soft mode eigendisplacement vector at $\approx$ 20 GPa. The FE instability at high pressure has therefore a totally different character than at atmospheric pressure : the Ba atom participate to the soft mode and the instability has a much more isotropic character. The fact that ω^2_{SR} becomes destabilizing at high pressure is directly related to the change of η_{TO_1} while the sign of LR and SR parts of the IFC is always preserved. In this context, the change of the nature of the FE instability highlighted by Kornev et al. must be understood as a drastic change of the unstable mode eigenvector rather than as a new original electronic effect suddenly modifying the SR forces. We hope that our work will stimulate experimental measurements that might confirm the abrupt change of eigenvectors and mode effective charges that we have reported at $\approx$ 20 GPa.

4.2 Epitaxial strain

As discussed in Chapter 3 it is possible to modify the phase diagrams of the perovskites by applying to them an epitaxial strain. The effects of such epitaxial strains can be isolated by studying them at the bulk level by artificially imposing an in-plane lattice constant to an infinite bulk. This allows to cancel the surface and depolarizing field effects and gives access to polarization perpendicular to the surface. It was demonstrated that such studies give rise to results comparable to the experiments [93].

The most previous studies focus on the effect of strains on the FE instability alone [76] and, at that time, only Pertsev [60] and Lin [112] investigated the effects of epitaxial strain on FE and AFD instabilities in $SrTiO_3$ thin films. Here, in the spirit of Lin [112], we present such epitaxial strain effects on bulk $SrTiO_3$, $PbTiO_3$ and $CaTiO_3$ perovskites by considering the FE and AFD instabilities.

4.2.1 Technical details

From our DFT calculations, the epitaxial constraint is imposed by fixing a cubic in-plane lattice constant. The misfit strain is calculated as follows: $\frac{a-a_0}{a_0}$, where a_0 is the cubic cell parameter of the paraelectric bulk reference and a is the in-plane cell parameter imposed.

For structural relaxations, we used a cell doubled both in-plane and out-of-plane to allow the AFD distortions, giving a 20 atoms supercell (see Figure 4.5) [112]. This supercell has the in-plane cell parameters equal to $\sqrt{2}a_0$ and $2c$ in the out-of-plane direction, where a_0 and c are respectively the in-plane and out-of-plane cell parameters of the five atoms unit cell. However, in all cases the out-of-plane cell parameter is relaxed as well as the atomic positions until the maximum residual forces (stresses) were less than 10^{-5} Ha.Bohr^{-1} ($\sim$0.5 meV.Å^{-1}). In this section, we will use the following notations for directions: [100], [010] and [001] will refer to the ABO_3 perovskite unit cell directions, where the origin is on A atom and the [100] direction is along A-A direction. In the supercell we will use the x, y, z notations for directions, where x and y are 45^o

rotated with respect to the [100] and [010] directions, such as x=[110], y=[1-10] and z=[001] (see Figure 4.5).

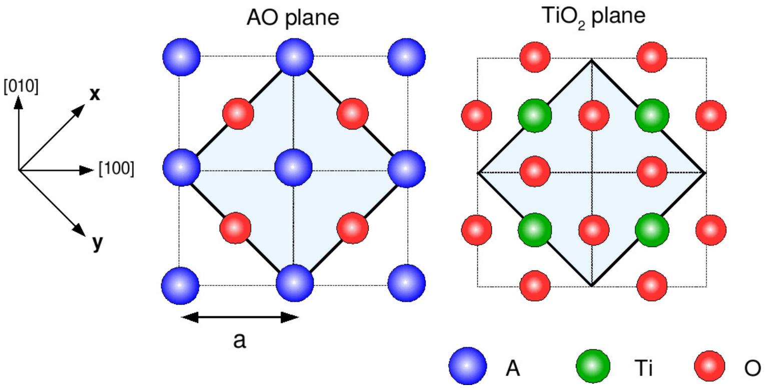

Figure 4.5: Schematic representation of the 20 atoms cell chosen for the simulations. The in-plane limit of the cell corresponds to the bold lines, forming a square rotated by 45 degrees with respect to [100] and [010] directions.

4.2.2 Instabilities and related symmetries

According to the calculated phonon band structures of the PbTiO$_3$, SrTiO$_3$ and CaTiO$_3$ paraelectric cubic structures (Figure 2.2 in Chapter 2), the instabilities responsible for the observed phase transitions are located at the zone center for FE distortions, and M ($\frac{1}{2}$,$\frac{1}{2}$,0) and R ($\frac{1}{2}$,$\frac{1}{2}$,$\frac{1}{2}$) zone boundary points for AFD distortions.

Under epitaxial conditions the cubic bulk symmetry is broken. By fixing the in-plane cell parameter a to the values of hypothetical cubic substrates, the out-of-plane cell parameter c relax, making it larger or smaller than its cubic value, depending on the applied strain (respectively tensile or compressive). In this constrained structure, the shape of the perovskite bulk cell becomes tetragonal instead of cubic, which modifies the symmetries of the crystal. In this resulting tetragonal structure, the highest symmetry phase corresponds to the space group No.123 ($P4/mmm$). According to this space group, the cubic three times degenerated FE mode is split into two modes: one corresponding to out-of-plane direction of polarization (FE$_z$) and one (degenerated two times) corresponding to in-plane direction of polarization (FE$_{xy}$). The same lifting of degeneracy appears for the AFD instabilities at the zone boundary: the cubic R zone boundary point becomes the A point ($\frac{1}{2}$,$\frac{1}{2}$,$\frac{1}{2}$) in the tetragonal structure and the AFD instabilities split into $a^0a^0c^-$ kind of displacements, degenerated one time and $a^-a^0c^0$ kind of distortions, degenerated two times ($a^-a^0c^0$ being equivalent to $a^0a^-c^0$). The three equivalent cubic M points responsible for ($a^0a^0c^+$) instabilities are split into two different points in the tetragonal structure: one M point ($\frac{1}{2}$,$\frac{1}{2}$,0) associated to $a^0a^0c^+$ distortions and two equivalent R points (0,$\frac{1}{2}$,$\frac{1}{2}$) and ($\frac{1}{2}$,0,$\frac{1}{2}$) associated to $a^+a^0c^0$ and $a^0a^+c^0$ distortions.

It must be noticed that the eigendisplacements of the in-plane AFD instabilities in the constrained tetragonal phase are slightly different from the related $a^-a^-c^0$ motions of the cubic cell. The calculated eigendisplacements of these modes hold the $a^-a^-c^0$ movements of the oxygens but additionally to those motions the A atom (Pb, Ca or Sr) has a contribution in the in-plane direction (δ_{xy}A). According to group theory, this contribution is allowed, but from the calculated eigendisplacements, this contribution is smaller than the $a^-a^-c^0$ motions.

We notice also that the oxygen motions of the $a^-a^-c^0$ instability can be described in term of the out-of-phase rotations around the [100] and [010] directions ($a^-a^0c^0$ and $a^0a^-c^0$) or as in-phase rotations around the x and y directions when combining the two distortions as the following two equivalent structure ($a^-a^-c^0$):

- $a'^+a'^0c^0=[a^-a^0c^0+a^0a^-c^0]$
- $a'^0a'^+c^0=[a^-a^0c^0 - a^0a^-c^0]$

where $a'=\sqrt{2}a$. The out-of-plane AFD instabilities, $a^0a^0c^-$ and $a^0a^0c^+$, are not modified in the strained tetragonal structure.

Here we will use the following notation : AFD$_{zi}$ for $a^0a^0c^+$ distortions, AFD$_{zo}$ for $a^0a^0c^-$ distortions and AFD$_{xy}$ for $a^-a^-c^0+\delta_{xy}$A motions.

Label	Space group	No.	distortions
FE$_z$	*P4mm*	99	FE$_z$
FE$_{xy}$	*Amm2*	38	FE$_{xy}$
AFD$_{zo}$	*I4/mcm*	140	$a^0a^0c^-$
AFD$_{zp}$	*P4/mbm*	127	$a^0a^0c^+$
AFD$_{xy}$	*Imma*	74	$a^-a^-c^0+\delta_{xy}$(A)
AFD/FE$_{zo}$	*I4cm*	108	$a^0a^0c^-$+FE$_z$
AFD/FE$_{xy}$	*Ima2*$_1$	46	AFD$_{xy}$+FE$_{xy}$

Table 4.3: Space groups of related phases in $PbTiO_3$ or $SrTiO_3$ bulks under epitaxial strains.

According to the identified AFD and FE instabilities, structural relaxations under symmetry constraints corresponding to each instabilities were performed for a wide range of epitaxial strains. Starting from the highest symmetry structure (*P4/mmm*), the following space groups associated with instabilities are used (Table 4.3): *I4/mcm* for the AFD$_{zo}$ phase, *P4/mbm* for the AFD$_{zp}$ phase, *Imma* for the AFD$_{xy}$ phase, *P4mm* for the FE$_z$ phase and *Amm2* for the FE$_{xy}$ phase. For each new relaxed structures, we checked if instabilities still exist. If yes, we lowered the symmetry according to the remaining instabilities and perform new structural relaxations. This was done until no instability was present which allowed to determine the ground-state of the system.

This procedure allowed us to identify two additional phases in $SrTiO_3$ and $PbTiO_3$ that involve the mix between FE and AFD distortions: *I4cm* where the $a^0a^0c^-$ mix with the FE$_z$ distortions (called AFD/FE$_{zo}$) and *Ima2* phase which involves the mix between AFD_{xy} and FE_{xy} distortions (called $\mathrm{AFD/FE}_{xy}$) (see Table 4.3). The $\mathrm{AFD/FE}_{xy}$ phase can be describe according two energetically equivalent distortions: in-phase oxygen rotations around the x axis ($\mathrm{a'^{+}a'^{0}c^{0}}$) with polarization along the y axis or in-phase oxygen rotations around the y axis ($\mathrm{a'^{0}a'^{+}c^{0}}$) with polarization along the x axis.

Here we report only the phase which involve the initial FE and AFD instabilities and the coupled phases which correspond to an observed ground-state. Another mixed AFD and FE phases can exist [60], but since they are not observed as being ground-state in the present study, they are not reported for clarity. Moreover, the space group of the AFD_{xy} phase reported here, is different than the one reported in Ref. [112] (*Fmmm*) for the same distortions, but is in agreement with the usual space group reported for the $\mathrm{a^{-}a^{-}c^{0}}$ distortions [50–53]. At last, different structures where found for $\mathrm{CaTiO_3}$, which will be discussed in its corresponding section.

4.2.3 SrTiO$_3$

As presented in Chapter 2, bulk $\mathrm{SrTiO_3}$ has a phase transition from paraelectric (PE) cubic phase to an AFD $\mathrm{a^{0}a^{0}a^{-}}$ tetragonal phase at a critical temperature $T_c \simeq$100 K. However, under epitaxial constraints the $\mathrm{SrTiO_3}$ thin films show more complex phase diagrams [60, 76, 93]. Phenomenological Landau model [60] and first-principles study [112] of $\mathrm{SrTiO_3}$ thin films under epitaxial strain predict a rich temperature-strain phase diagram which bring into play the mix between AFD and FE distortions.

Using the highest symmetry phase *P4/mmm* as energy reference for each epitaxial strain considered, we obtain the energy diagram of Figure 4.6 for $\mathrm{SrTiO_3}$. These energy diagrams show the evolution of the energy difference (ΔE) between the *P4/mmm* structure and the considered lower symmetry phases of Table 4.3. We can see here that each phase is strongly sensitive to the epitaxial strain. We observe the sequence $\mathrm{AFD/FE}_{zo}$, AFD_{zo}, AFD_{xy} and $\mathrm{AFD/FE}_{xy}$ phases as ground-state for a misfit strain going from -4% to +4%.

These successive phases are similar to the ones reported in previous studies [60, 112]. However, the misfit strain where the phase transitions take place are not the same. We observe a phase transition between AFD_{zo} and $\mathrm{AFD/FE}_{zo}$ at a negative misfit strain larger than in the previous studies (-3.0% instead of -0.558% for Ref. [112]). Afterwards, we observe a transition between AFD_{zo} and AFD_{xy} phases around a misfit strain of 0.2% and a transition between AFD_{xy} and $\mathrm{AFD/FE}_{xy}$ phases at a misfit strain of 1.7% which differ also from Ref. [112]. These differences with previous studies can be mainly related to the difference between the pseudopotentials and method used. In the present study, the LDA volume relaxation of cubic $\mathrm{SrTiO_3}$ is found to be 3.84 Å, while the previous first-principles study obtained 3.87 Å [112]. Since the FE instabilities are strongly sensitive to the volume, larger volume favors the FE instability while smaller volume penalizes the FE distortions. According to this behavior, the FE instability is slightly more penalized in the present study than in Ref. [112] or than in Ref. [60] where the experimental volume is used (a_0=3.905 Å). For example, at the experimental volume, the paraelectric cubic $\mathrm{SrTiO_3}$

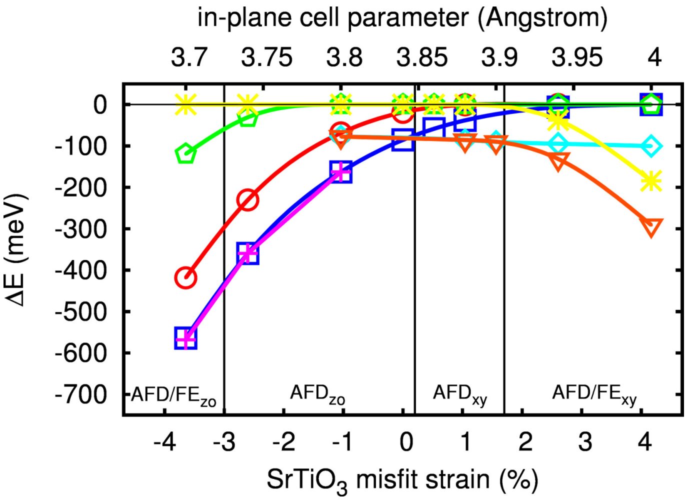

Figure 4.6: Gain of energy ΔE (meV/supercell) with respect to the paraelectric reference of different phases for SrTiO$_3$ in term of misfit strain. The considered phases are the following: FE$_z$ (green pentagons), FE$_{xy}$ (yellow stars), AFD$_{zo}$ (blue squares), AFD$_{zi}$ (red circles), AFD$_{xy}$ (light-blue diamonds), AFD/FE$_{zo}$ (purple crux) and AFD/FE$_{xy}$ (orange triangles). The vertical lines mark the misfit strain where a switch of phase takes place and the corresponding ground-states are written at the bottom of the graph.

shows small FE instability at the Γ point (mode frequency calculated at -51i cm^{-1} in the present study), however, this FE instability disappears at the LDA volume (mode calculated at 99 cm^{-1}) and so performing simulations at the LDA volume will penalize the FE phases.

The difference of energy between the AFD$_{zo}$ and the AFD/FE$_{zo}$ phases is relatively small (few meV) even at misfit strain where the AFD/FE$_{zo}$ phase becomes the ground-state, while the difference of energy between AFD$_{xy}$ (or FE$_{xy}$) and AFD/FE$_{xy}$ phases increases rapidly when the AFD/FE$_{xy}$ becomes the ground-state.

In the spirit of what was reported in the previous section, to determine the contribution of each unstable mode to the reported ground-states, we perform overlap calculations between the atomic displacements in the relaxed ground-states and the modes of the paraelectric reference. Such overlaps are reported in Table 4.4 for five different misfit strains. It is clear that the AFD$_{zo}$ ground-state is related to the condensation of the AFD$_{zo}$ unstable mode only. At a misfit strain of -3.65% (compressive misfit strain), the contribution to the total relaxation mainly comes from the AFD$_{zo}$ instability (0.993) while small contribution is associated to the FE$_z$ mode giving rise to the FE state. At a misfit strain of 1.04% (tensile misfit strain), the relaxation is mainly due to the AFD$_{xy}$ instability (0.997), but small contributions also comes from high frequency modes which are not unstable. This high frequency mode contributions can be related to a stronger anharmonicity of the distortions in the AFD$_{xy}$ phases. At last, for the high tensile misfit strain of 2.60%, the contribution to the final distortions is mainly related to the AFD$_{xy}$ instabilities but a non negligible FE$_{xy}$ contribution is also present, giving rise to the AFD/FE$_{xy}$ FE state. As for the AFD$_{xy}$ phase, the presence of non-zero high frequency modes contributions allows to point out that the final distortions of the AFD/FE$_{xy}$ phase are slightly anharmonic.

misfit	Ground state	Overlaps					
		AFD$_{zo}$	AFD$_{zi}$	AFD$_{xy}$	FE$_z$	FE$_{xy}$	others
-3.65%	AFD/FE$_z$	**0.993**	0.000	0.000	**0.113**	0.000	**0.036**
-1.04%	AFD$_{zo}$	**1.000**	0.000	0.000	0.000	0.000	**0.001**
-0.00%	AFD$_{zo}$	**1.000**	0.000	0.000	0.000	0.000	0.000
1.04%	AFD$_{xy}$	0.000	0.000	**0.987**	0.000	0.000	**0.164**
2.60%	AFD/FE$_{xy}$	0.000	0.000	**0.845**	0.000	**0.508**	**0.166**

Table 4.4: Overlaps between the relaxed distortions of the epitaxial SrTiO$_3$ ground-states and the AFD$_{zo}$, AFD$_{zi}$, AFD$_{xy}$, FE$_z$ and FE$_{xy}$ modes of the paraelectric reference. The “other” column is the remaining overlap associated to the contribution of higher frequency modes.

In Table 4.5, we report the SrTiO$_3$ c/a ratio for four misfit strains. In the PE reference, c/a evolves with the misfit strain: it is larger for compressive in-plane strain and smaller for tensile epitaxial strain, which is the expected response to the epitaxial strain. In the AFD$_{zo}$ and AFD$_{zp}$ phases, c/a is larger than for the PE structure and has about the same value. When it is present, the FE$_z$ also tends to increase c/a, but more strongly than the AFD$_{zo}$ phase. The combined

$SrTiO_3$ misfit strain	-3.65%	-1.04%	1.04%	4.17%
PE	1.063	1.019	0.986	0.943
FE_z	1.083	-	-	-
FE_{xy}	-	-	-	0.937
AFD_{zo}	1.072	1.023	0.987	-
AFD_{zp}	1.074	1.022	0.987	-
AFD_{xy}	-	1.015	0.982	0.937
AFD/FE_{zo}	1.075	-	-	-
AFD/FE_{xy}	-	1.015	0.982	0.932

Table 4.5: $SrTiO_3$ c/a for selected misfit strain on every related phases of Table 4.3.

phase AFD/FE_{zo} also increases c/a with an amplitude larger than AFD_{zo}, but smaller than in the FE_z phase. In the AFD_{xy} and FE_{xy} phases, c/a is lowered with respect to the PE phase. However, the c/a of the combined AFD/FE_{xy} phase stays about the same than in the separated phases.

misfit	FE_z	AFD/FE_z	FE_{xy}	AFD/FE_{xy}
-3.65%	53	18	-	-
-2.60%	34	-	-	-
1.56%	-	-	17	13
2.60%	-	-	34	32

Table 4.6: Spontaneous polarization ($\mu C.cm^{-2}$) of FE_z, AFD/FE_z, FE_{xy} and AFD/FE_{xy} phases of $SrTiO_3$ for selected misfit strains.

In Table 4.6 we report the spontaneous polarizations of the polar phases involving the FE distortions. In both in-plane and out-of-plane directions, the spontaneous polarization of the AFD/FE coupled phases is lower than for the FE phases. This effect is particularly strong for the out-of-plane direction where the polarization of the AFD/FE_{zo} phase is about 40% of the pure FE_z phase, whereas the polarization of the AFD/FE_{xy} phase is few percent lower than the polarization calculated in the FE_{xy} phase. This effect can be related to the reported competition between AFD and FE instabilities, where the tendency is to suppress each other, even when the two kinds of distortions are present together.

4.2.4 $PbTiO_3$

In the case of $PbTiO_3$, a phase transition from PE cubic state to a FE tetragonal phase is observed when decreasing the temperature [56]. As shown in Chapter 2, AFD instabilities are also present in the cubic $PbTiO_3$ but are never observed as being involved in the bulk ground-states, which has been related to the supremacy of the FE distortions in the competition with AFD distortions [56, 74]. Nevertheless, a coexistence between AFD and FE distortions was observed at the surface of $PbTiO_3$ thin films [82, 88].

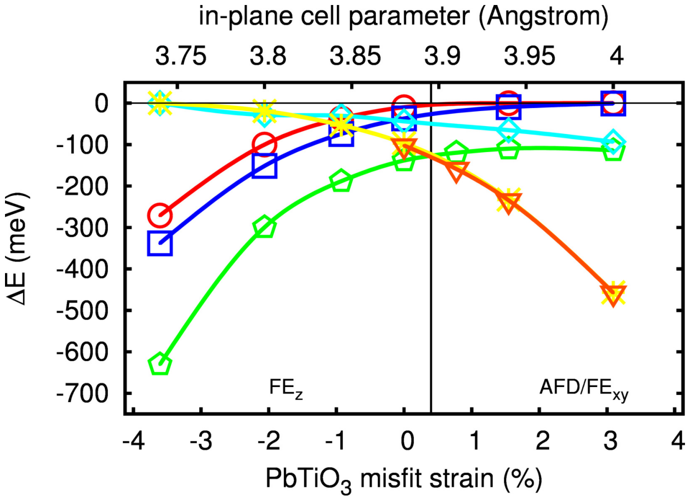

Figure 4.7: Gain of energy ΔE (meV/supercell) with respect to the paraelectric reference of different phases for $PbTiO_3$ in terms of misfit strain. The labels for phases are the same as those reported in Figure 4.6.

In the case of $PbTiO_3$, no previous study was done taking into account the possibility of mixed AFD/FE phases through epitaxial strain. The ΔE versus misfit strain diagram (Figure 4.7) shows a less rich number of ground-states than for $SrTiO_3$. Here, for compressive epitaxial strains, the FE$_z$ distortions dominate the system. No mixed phase between FE$_z$ and AFD distortions is observed for a misfit strain going from -4% to 0.3%. The gain of energy ΔE of the FE$_z$ phase is always larger than AFD$_{zo}$ and AFD$_{zp}$ phases, which is the opposite than for $SrTiO_3$. However, for tensile epitaxial strains larger than 0.3%, the calculated ground-state always involves a mix between the FE$_{xy}$ and the AFD$_{xy}$ distortions which is unexpected for $PbTiO_3$. The difference of energy between the FE$_{xy}$ and the AFD/FE$_{xy}$ phases is small (few meV) and stays small for larger tensile strain, which is also a different behavior than for $SrTiO_3$ (differences of about hundred meV).

As done for $SrTiO_3$, we report in Table 4.7 the overlaps between the relaxed distortions of the ground-states of $PbTiO_3$ and the eigendisplacements of the modes calculated in the paraelectric reference. Contrary to $SrTiO_3$, here the main contributions to the relaxed atomic displacements comes from the FE unstable modes: FE$_z$ for compressive epitaxial strains and FE$_{xy}$ for tensile epitaxial strains. For tensile AFD/FE$_{xy}$ ground-state, the AFD$_{xy}$ mode contributes slightly to the relaxed displacements and its contribution tends to decrease when the tensile misfit strain increases. Moreover, for both FE$_z$ and AFD/FE$_{xy}$ ground-states, the contributions of higher frequency modes are more important than the one reported for $SrTiO_3$. This means that the corresponding distortions have much more anharmonic character than the ones reported for $SrTiO_3$. This anharmonic tendency increases when the amplitude of epitaxial strain increases (tensile or compressive) and becomes as large as the unstable FE mode contributions.

misfit	Ground state	Overlaps					
		AFD_{zo}	AFD_{zi}	AFD_{xy}	FE_z	FE_{xy}	others
-2.06%	FE_z	0.000	0.000	0.000	**0.869**	0.000	**0.496**
-0.93%	FE_z	0.000	0.000	0.000	**0.929**	0.000	**0.371**
0.00%	FE_z	0.000	0.000	0.000	**0.953**	0.000	**0.302**
1.55%	AFD/FE_{xy}	0.000	0.000	**0.239**	0.000	**0.852**	**0.467**
3.09%	AFD/FE_{xy}	0.000	0.000	**0.177**	0.000	**0.757**	**0.629**

Table 4.7: Overlaps between the relaxed distortions of the epitaxial $PbTiO_3$ ground-states and the eigendisplacements of the AFD_{zo}, AFD_{zi}, AFD_{xy}, FE_z and FE_{xy} modes of the paraelectric reference. The "other" column is the remaining overlap associated to the contribution of higher frequency modes.

misfit	P			c/a			
	FE_z	FE_{xy}	AFD/FE_{xy}	Para	FE_z	FE_{xy}	AFD/FE_{xy}
-2.06%	91	40	30	1.038	1.077	1.039	1.016
-0.93%	79	51	46	1.014	1.042	1.018	1.017
0.00%	71	76	73	1.000	1.019	1.002	1.001
1.55%	61	75	74	0.974	0.987	0.975	0.975
3.09%	57	89	88	0.950	0.961	0.950	0.950

Table 4.8: Spontaneous polarization (μC.cm^{-2}) and tetragonality c/a of FE_z, FE_{xy} and AFD/FE_{xy} phases of $PbTiO_3$ and the c/a of the paraelectric reference for selected misfit strains.

In Table 4.8, we report the spontaneous polarization of the FE_z, FE_{xy} and AFD/FE_{xy} phases for selected misfit strains. As reported for the unconstrained bulks, the amplitude of the spontaneous polarizations in epitaxial $PbTiO_3$ are larger than for $SrTiO_3$. The polarization of FE_z and FE_{xy} phases are enhanced for respectively compressive and tensile epitaxial strains like it is reported for $BaTiO_3$. In the AFD/FE_{xy} phase, the spontaneous polarization has almost the same amplitude than for the FE_{xy} phase with a slight reduction.

In the Table 4.8 we also report the tetragonality of the paraelectric reference, the FE_z phase and the AFD/FE_{xy} phase. Here, we confirm the strong increase of c/a in the FE_z phase as reported for the unconstrained bulk or in $SrTiO_3$. The c/a of the FE_{xy} and AFD/FE_{xy} phases, however, is almost unchanged with respect to the paraelectric c/a, even for large tensile strain where these phases are favored, which is a behavior distinct from the one reported for $SrTiO_3$ in Table 4.5.

4.2.5 $CaTiO_3$

As shown in Chapter 2, the ground-state of $CaTiO_3$ is orthorhombic with the space-group *Pnma* (No 62) and involves only tilts of the oxygens. Moreover, we have shown that the amplitude of AFD distortions are large with respect to the ones observed in $SrTiO_3$ or $PbTiO_3$.

misfit	Space group	No	ΔE	P	c/a	$(c/a)_0$
-3.68%	*Pnma*	62	2289	-	1.048	1.059
-2.63%	*Pnma*	62	2051	-	1.026	1.041
-1.58%	*Pnma*	62	1877	-	1.007	1.024
-0.00%	*Pnma*	62	1687	-	0.981	1.000
1.05%	*Pnma*	62	1588	-	0.965	0.984
2.63%	$Pmc2_1$	26	1501	30	0.941	0.962

Table 4.9: Space groups, gain of energy with respect to the paraelectric reference (mev/super-cell) and spontaneous polarization (μC.cm^{-2}) and tetragonality c/a of the ground-states of $CaTiO_3$ and the tetragonality of the paraelectric phase $(c/a)_0$ for selected misfit strains.

In Table 4.9, we report the calculated ground-states of $CaTiO_3$ at six different epitaxial strains. The ground-states and space groups observed for $CaTiO_3$ are not the same as those reported for $SrTiO_3$ and $PbTiO_3$ under epitaxy. Here, for each considered compressive epitaxial strain the ground-state stays the same than for the unconstrained bulk: the *Pnma* phase. For small tensile strain, $CaTiO_3$ stays in its *Pnma* phase while at large enough tensile epitaxial strain, it condenses in a new phase with the space group $Pmc2_1$. Interestingly, even if no polar phase is observed for compressive epitaxial strains, for enough tensile strains the $Pmc2_1$ phase is FE with polarization oriented in the in-plane directions and amplitude of 30 μC.cm^{-2}. As for the unconstrained bulks reported in Chapter 2, the gain of energy with respect to the paraelectric reference is larger for $CaTiO_3$ than for $SrTiO_3$ or $PbTiO_3$. In Table 4.9, we also report the tetragonality of these ground-states, showing that for all phases, c/a is reduced with respect to the paraelectric reference.

As for $SrTiO_3$ and $PbTiO_3$, we computed the overlap between the eigendisplacements of the unstable modes calculated in the paraelectric reference and the displacements obtained in the relaxed ground-state structure. The results are reported in Table 4.10 where we can see that the *Pnma* structure is only related to AFD$_{xy}$ and AFD$_{zi}$ kind of distortions which correspond to the $a^-a^-c^+$ tilts. As reported for the bulk, the contributions of other modes are relatively important and tends to increase with the amplitude of epitaxial strain. In the $Pmc2_1$ phase, the FE$_{xy}$ contribution is non-zero confirming the presence of in-plane FE distortions. However, by comparison with the other non-zero contributions, this FE$_{xy}$ overlap is relatively small, the system keeping an AFD dominant distortion.

misfit	Space	Overlaps					
	group	AFD$_{zo}$	AFD$_{zi}$	AFD$_{xy}$	FE$_z$	FE$_{xy}$	others
-3.68%	*Pnma*	0.000	**0.707**	**0.548**	0.000	0.000	**0.447**
-2.63%	*Pnma*	0.000	**0.637**	**0.611**	0.000	0.000	**0.470**
-1.58%	*Pnma*	0.000	**0.582**	**0.654**	0.000	0.000	**0.483**
-0.00%	*Pnma*	0.000	**0.708**	**0.675**	0.000	0.000	**0.223**
1.05%	*Pnma*	0.000	**0.490**	**0.717**	0.000	0.000	**0.496**
2.63%	$Pmc2_1$	0.000	**0.470**	**0.716**	0.000	**0.177**	**0.485**

Table 4.10: Overlaps between the relaxed distortions of the epitaxial $CaTiO_3$ ground-states reported in Table 4.9 and the eigendisplacements of the AFD$_{zo}$, AFD$_{zi}$, AFD$_{xy}$, FE$_z$ and FE$_{xy}$ modes of the paraelectric reference. The "other" column is the remaining overlap associated to the contribution of higher frequency modes.

4.3 Conclusion

In this chapter, we have presented the effects of pressure and epitaxial strain on the properties of $BaTiO_3$, $SrTiO_3$, $PbTiO_3$ and $CaTiO_3$ and shown that those stress and strain shift the bulk phases.

First, looking at $BaTiO_3$ we have seen that small pressure tends to suppress the ferroelectricity while at high enough isotropic pressure ferroelectricity is recovered.

In the second part, we have discussed the effects of an epitaxial strain as it is applied when thin films are grown on a substrate. We reported the results obtained on $SrTiO_3$, $PbTiO_3$ and $CaTiO_3$ and shown that, due to the presence of AFD instabilities, the phase diagrams of such compounds under epitaxial strain is much more complex than anticipated by Diéguez *et al.* [76] and involves the mixing of many instabilities.

The study of the strain effects are done at the bulk level in order to isolate these effects, but to have a simulation matching the reality, the effects of truncated bulks should be performed in addition to the epitaxial strain by the study of the surfaces or interfaces effects. These additional effects will be considered in the next chapters.

4.4 References

The results reported for bulks under high isotropic pressure have been mainly discussed in the following papers:

- I. A. Kornev, L. Bellaiche, P. Bouvier, P.-E. Janolin, B. Dkhil and J. Kreisel, *Ferroelectricity of perovskites under pressure*, Phys. Rev. Lett. **95**, 196804 (2005).
- E. Bousquet and Ph. Ghosez, *First-principles study of barium titanate under hydrostatic pressure*, Phys. Rev. B **74**, 180101(R) (2006)

- I. A. Kornev and L. Bellaiche, *The nature of ferroelectricty under pressure*, Phase Transitions **80**, 385 (2007).

An overview of the effects of epitaxial strain on ferroelectric oxides can be found in the following references:

- K. M. Rabe, *Theoretical investigations of epitaxial strain effects in ferroelectric oxide thin films and superlattices*, Current Opinion in Solid State and Materials Science **9**, 122 (2006).
- Ph. Ghosez and J. Junquera, *First-principles modeling of ferroelectric oxide nanostructures*, in the *Handbook of Theoretical and Computational Nanotechnology*, edited by M. Rieth and W. Schommers, vol. 9, p. 623 (ASP, Stevenson Ranch, 2006).
- D. G. Schlom, L-Q. Chen, C-B. Eom, K. M. Rabe, S. K. Streiffer and J-M. Triscone, *Strain Tuning of Ferroelectric Thin Films*, Annu. Rev. Mater. Res. **37**, p589 (2007).

Chapter 5

Ferroelectric/Incipient-Ferroelectric superlattices

5.1 Introduction

Ferroelectric/Incipient-Ferroelectric (FE/iFE) superlattices are a particular case of Ferroelectric/Insulator structures in which the insulating layer is highly polarizable. Incipient ferroelectrics, like $SrTiO_3$ or $KTaO_3$, are "almost" ferroelectric. They exhibit a high dielectric constant ($\varepsilon_0 \approx 300$ for $SrTiO_3$ at room temperature), which is associated to a low frequency polar mode related to their nearly ferroelectric behavior. As discussed in Chapter 3 and 4, they can easily be made ferroelectric under constraint such as epitaxial strain. All this illustrates the fact that the internal energy cost to polarize these compounds is much lower than in the case of regular insulators like AO oxides as will be further discussed in Chapter 6. Bicolor superlattices in which a ferroelectric compound alternates with an incipient-ferroelectric material might therefore exhibit ferroelectric phases, even in a limit of ultrathin ferroelectric layers.

The most studied FE/iFE superlattices are $BaTiO_3/SrTiO_3$ [104, 113–124], $PbTiO_3/SrTiO_3$ [102, 125–127] and $KNbO_3/KTaO_3$ [128–132]. It was shown that in such systems macroscopic electrostatic still apply and that the ferroelectric properties can be efficiently tuned by playing with epitaxial strain and the ferroelectric volume fraction.

Here we go one step further: focussing mainly on $PbTiO_3/SrTiO_3$ superlattice, we highlight that novel and unexpected properties can be induced in artificial superlattices. We first show from first-principles that, contrary to what was implicitly assumed in previous studies, the ground-state of the system is not purely ferroelectric in the limit of ultrathin layers but also primarily involves antiferrodistortive rotations of the oxygen atoms in a way compatible with improper ferroelectricity. We then present the experimental evidence that, in contrast to pure $PbTiO_3$ and $SrTiO_3$ compounds, the artificial system indeed behaves like a prototypical improper ferroelectric and exhibits a very large dielectric constant which, at the same time, is fairly temperature independent. At last, we investigate to which extent $PbTiO_3/CaTiO_3$ and $CaTiO_3/SrTiO_3$ superlattices might exhibit a similar behavior.

5.2 Technical details

The structural relaxations were done by imposing the in-plane cell parameter on a 20 atoms supercell as describe in Section 4.2.1. The technical details are those given in Section 1.8, with a Monkorsh-Pack mesh of 4×4×4 k-points.

For large periodicities presented in Section 5.5, we used the SIESTA[1] code [33]. A Perdew-Zunger parametrisation of Ceperley-Alder [14] data is used for the exchange correlation functional and norm conserving Troullier-Martin [133] pseudopotentials approximation were used for valence electrons. The 3s, 3p, 3d and 4s orbitals for Ti, 4s, 4p and 5s orbitals for Sr, 4f, 5s, 5p and 6s orbitals for Pb and 2s and 2p orbitals for O were treated as valence electrons. An equivalent plane-wave cut-off of 200 Ry was used for the charge density for the real-space treatment. The technical details used are the same than the ones given in Ref. [87]. In reciprocal space a 4×4×1 k-points mesh was used and the maximum residual forces on each atom was fixed to 20 meV.Å^{-1} for the structural relaxations.

5.3 $(PbTiO_3)_n/(SrTiO_3)_m$ superlattices

5.3.1 Electrostatic model and unexpected recovery of ferroelectricity

$(PbTiO_3)_n/(SrTiO_3)_m$ (n/m) superlattices were grown experimentally by Dawber *et al.* [102], considering $n/3$ periodicities. They studied the ferroelectric properties of the superlattices with respect to the $PbTiO_3$ layer thicknesses n. Thanks to the strain-polarization coupling, measurement of the tetragonality (c/a ratios between the cell parameters c and a of the constituent compounds) allowed to deduce the thickness evolution of the out-of-plane polarization.

The c/a was found to decrease with the $PbTiO_3$ thickness n, meaning that the out-of-plane polarization decreases with n. The polarization was observed to vanish at n=3 while unexpected recovery of ferroelectricity was reported for n=2 and n=1.

An electrostatic model, as presented in Chapter 3, was built to explain the evolution of the polarization and the c/a ratio with n. The experimental decrease of the out-of-plane polarization was recovered and the model predicted a total suppression of the polarization below n=4. However, the model was not reproducing any recovery of the ferroelectricity for n <4. In Ref. [134], a Landau theory involving only bulk parameters has been used on this $PbTiO_3/SrTiO_3$ superlattices and demonstrated that this approach is also predictive for large

---

[1] `http://www.uam.es/departamentos/ciencias/fismateriac/siesta/`

$PbTiO_3$ volume fractions (>40%) but failed to explain the unexpected recovery of the ferroelectricty.

DFT study was also reported for this superlattice with n going from 1 to 7. Only the out-of-plane FE distortions were considered and the calculations predicted similar behavior than the electrostatic model: the polarization is homogeneous along the whole structure and decreases with n until disappearance. Here again, no unexpected recovery of ferroelectricity was observed at the smallest thicknesses. Intermixing [126] or space charge effects [125] at the interfaces were evoked to explain this recovery of ferroelectricity but without being fully conclusive.

In the present study [127], we show that $(PbTiO_3)_n/(SrTiO_3)_m$ superlattices with very short periods do not behave as usual ferroelectrics but exhibit a new form of interface coupling between AFD and FE instabilities, in a way compatible with improper ferroelectricty [135–137]. This result, further confirmed experimentally, also allows to explain the unexpected recovery of ferroelectricity highlighted by Dawber *et al.*

5.3.2 Paraelectric structure reference

In its *P4/mmm* paraelectric reference, the $(PbTiO_3)_n/(SrTiO_3)_m$ have all the atoms in their high symmetric positions in the in-plane directions while in the out-of-plane direction the structure posses two mirror symmetry planes located on the central PbO and SrO layers when n or m are odd numbers while their are located on the central TiO_2 layers when n or m are even numbers (conditions valid when $n + m$ is an even number, which will be the only case used in the present work). These mirror symmetry planes fix the atomic positions of the central layers but atomic relaxation must be performed for all the other out-of-plane atomic positions giving rise to the rumpling distortions and a modification of the interplanar distances (see Chapter 3).

For the 1/1 periodicity, this paraelectric reference corresponds to a 10 atoms unit cell. We report in Table 5.1 the relaxed structure at an in-plane lattice constant corresponding to a $SrTiO_3$ substrate. As discussed in Chapter 3, the rumpling relaxations are small (0.008 Å). The interplanar distances are modified with respect to the bulk: the distance between the SrO and TiO_2 atomic planes are smaller than the distance between the PbO and TiO_2 atomic planes. The SrO-TiO_2 distances are smaller in the superlattice than in bulk $SrTiO_3$ (1.908 Å in the superlattice and 1.920 Å in bulk $SrTiO_3$) while the PbO-TiO_2 distances are larger in the superlattice than in bulk $PbTiO_3$ at the same epitaxial strain (1.970 Å in the superlattice and 1.950 Å in bulk $PbTiO_3$ epitaxially strained on $SrTiO_3$ substrate).

5.3.3 Phonon Instabilities

As discussed in Chapter 2, although they present a different ground-state, both $PbTiO_3$ and $SrTiO_3$ exhibit tendency to the FE and AFD instabilities. Although both are exclusive at the bulk level it is not excluded that they can couple in epitaxial thin films as shown in Chapter 4 and so we cannot rule out the existence of such coupling in superlattices.

	atomic positions			plane	rumpling	interplanar distances
	x	y	z			
Pb	0.000	0.000	0.000	PbO	0.000	
O	0.500	0.500	0.000			
						1.970
Ti	0.500	0.500	0.252	TiO_2	0.008	
O	0.000	0.500	0.256			
O	0.500	0.000	0.256			
						1.908
Sr	0.000	0.000	0.500	SrO	0.000	
O	0.500	0.500	0.500			
						1.908
Ti	0.500	0.500	0.748	TiO_2	0.008	
O	0.000	0.500	0.744			
O	0.500	0.000	0.744			
						1.970

Table 5.1: Relaxed atomic positions (reduced coordinates) of the *P4/mmm* phase of $PbTiO_3/SrTiO_3$ 1/1 superlattice with in-plane cell parameter of 3.840 Å and out-of-plane cell parameter of 7.755 Å. The rumpling relaxation and interplanar distances are given in Å.

In Figure 5.1 we show the calculated phonon dispersion curves of the highest symmetry phase (*P4/mmm*) of the $PbTiO_3/SrTiO_3$ (1/1) superlattice at an epitaxial strain corresponding to the theoretical $SrTiO_3$ cubic parameter (3.84 Å). The calculated unstable modes have imaginary frequencies and are plotted with negative frequencies. In these dispersion curves, the FE instabilities FE_z (out-of-plane direction of polarization) and FE_{xy} (in-plane direction of polarization) and the AFD instabilities AFD_{zo} ($a^0a^0c^-$), AFD_{zi} ($a^0a^0c^+$) and AFD_{xy} ($a^-a^-c^0$) are recovered like in the $PbTiO_3$ and $SrTiO_3$ bulks (Chapter 2). The FE instabilities are located at the zone center (Γ_3^- mode for FE_z and Γ_5^- mode for FE_{xy}), while the AFD distortions, equivalent to the bulk ones considering only the oxygen sublattice, are now all located at the M zone boundary point (M_4^- mode for AFD_{zo}, M_2^+ mode for AFD_{zi} and M_5^- mode for AFD_{xy}) instead of M and A points for the bulks [2]. We note that other instabilities are also present at the Z, X and A points, but they are never observed to play a role in the ground-state of the superlattice so that they will not be further discussed here.

As represented by the colors assigned to the different atoms, in Figure 5.1 the AFD modes are mainly dominated by O motions while the FE modes involve O atoms as well as the Ti, Sr and Pb atoms (see Figure 5.2 for the representation of the atomic displacements of the FE_z, AFD_{zo} and AFD_{zi} distortions). The AFD_{zo} and AFD_{zi} instabilities involve only the contribution of O atoms, while

---

[2] With respect to the bulks, the unit cell is doubled along the [001] axis in the 1/1 superlattice and therefore the tetragonal bulk A point is folded up to the M point and the bulk Z point is folded up to Γ.

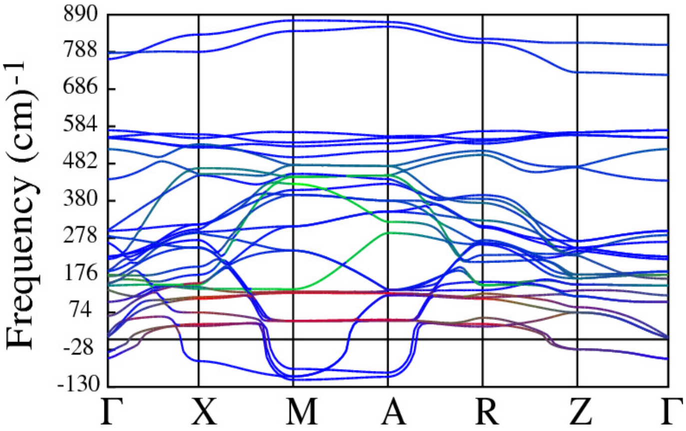

Figure 5.1: Phonon dispersion curves of the highest achievable symmetry (*P4/mmm*) of $(PbTiO_3)_1/(SrTiO_3)_1$ superlattice constrained at an epitaxial strain corresponding to the cubic relaxed $SrTiO_3$ bulk (3.84 Å). Colors have been assigned according to the contribution of each kind of atom to the associated eigenvector of each mode: red for Sr and Pb atoms, green for Ti and blue for O.

the AFD_{xy} involve also the Pb and Sr motion. As discussed in Section 4.2 for the bulks, these contributions of Pb and Sr atoms to the AFD_{xy} eigenvectors are compatible with the group theory but their calculated contributions are strongly smaller than the O atoms and will be neglected in the notation.

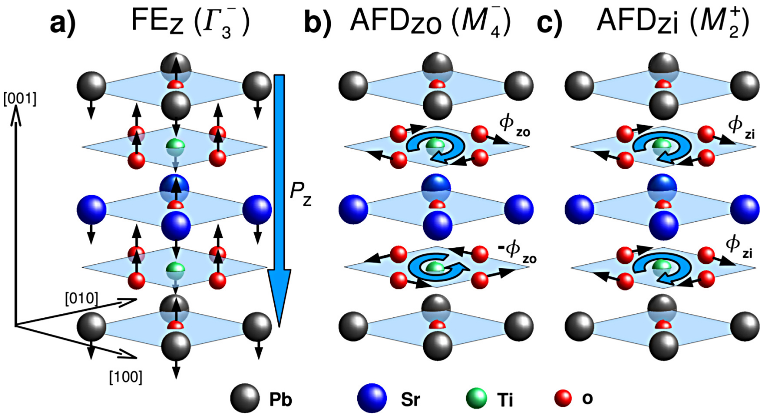

Figure 5.2: Schematic view of the prototype *P4/mmm* unit cell of the $PbTiO_3/SrTiO_3$ 1/1 superlattice and atomic motions associated to three instabilties: (a) FE_z (Γ_3^- mode) giving rize to a polarization P_z, (b) AFD_{zo} (M_4^- mode) with oxygen rotation angle ϕ_{zo} and (c) AFD_{zi} (M_2^+ mode) with oxygen rotation angle ϕ_{zi}.

The AFD instabilities are stronger than the FE unstable modes, however, these differences of amplitude are strongly sensitive to the epitaxial strain. In Figure 5.3 we have represented the evolution of the frequency of Γ and M point instabilities of the 1/1 superlattice over a wide range of epitaxial strain. Compressive epitaxial strain amplifies strongly the AFD$_{zo}$, AFD$_{zp}$ and FE$_z$ instabilities while tensile strain favors strongly the FE$_{xy}$ mode. The AFD$_{xy}$ mode is less sensitive to the epitaxial strain than the other instabilities, but its frequency tends to soften slightly with tensile epitaxial strain. For SrTiO$_3$ misfit strains from 0.2% to -2.5%, the AFD$_{zo}$ mode is the most unstable while the FE$_z$ mode is the deepest instability for a SrTiO$_3$ misfit strain lower than -2.5%. From 0.2% to 1.6%, the AFD$_{xy}$ becomes the most unstable mode, while after 1.6% the FE$_{xy}$ mode has the lowest frequency. After 0.5%, the FE$_z$ mode is no more unstable, but its frequency remains smooth. The same is observed for the FE$_{xy}$ mode but for a misfit strain lower than -1.2%, and the AFD$_{zp}$ becomes also stable for a SrTiO$_3$ misfit strain larger than 1.9%.

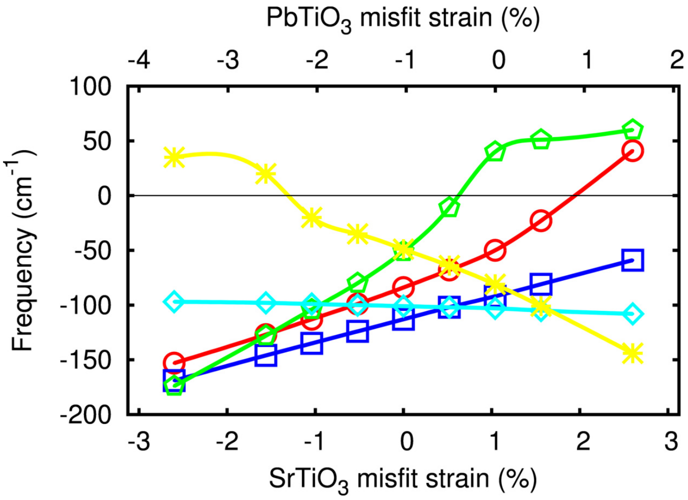

Figure 5.3: PbTiO$_3$/SrTiO$_3$ 1/1 phonon frequencies of Γ and M unstable mode as a function of SrTiO$_3$ misfit strain (bottom) and PbTiO$_3$ misfit strain (top). The following instabilities are reported: FE$_z$ (green pentagons), FE$_{xy}$ (yellow stars), AFD$_{zo}$ (blue squares), AFD$_{zi}$ (red circles), AFD$_{xy}$ (light-blue diamonds).

5.3.4 Ground state structure

Since there are many FE and AFD instabilities potentially involved and since due to anharmonic effects it is not necessarily the strongest instability that will produce the largest gain of energy, in order to identify the ground-state structure, we performed full atomic relaxations under symmetry constraints corresponding to the condensation of separated or combined unstable modes. Phonons calculations were then performed in each phase where the energy is minimum to determine if instabilities still exist. The results are summarized in the ΔE diagram shown in Figure 5.4.

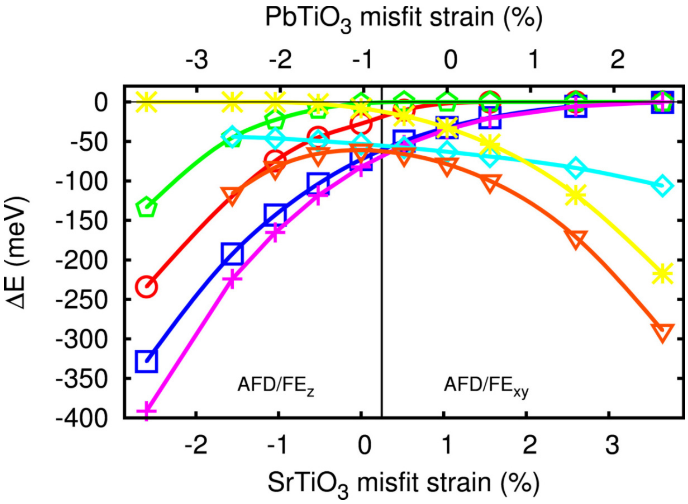

Figure 5.4: Gain of energy ΔE (meV/supercell) with respect to the paraelectric reference of different phases for the $PbTiO_3/SrTiO_3$ 1/1 superlattice in term of misfit strain. The same label as in Figure 4.6 are used, by replacing the bulk AFD-FE_{zo} phase by the AFD/FE_z phase.

The space groups and distortions of each reported phases are reported in Table 5.2. Surprisingly, the ground-state of the $PbTiO_3/SrTiO_3$ 1/1 superlattice always involves the mixing between AFD and FE instabilities. For tensile epitaxial strain ($SrTiO_3$ misfit strain ≥0.2%), the ground-state corresponds mainly to a combination between AFD_{xy}, FE_{xy} and AFD_{zi} distortions (called AFD/FE_{xy}) while for a $SrTiO_3$ misfit strain smaller than 0.2% the ground-state involves the coupling between AFD_{zo}, AFD_{zi} and FE_z distortions (called here AFD/FE_z). These couplings were totally unexpected, since they had never been observed at the bulk level.

In Table 5.4 we report the contribution of the eigenvectors of the unstable modes of the paraelectric reference (η_{FE_z}, $\eta_{AFD_{zo}}$, $\eta_{AFD_{zi}}$, $\eta_{AFD_{xy}}$ and $\eta_{FE_{xy}}$) to the total displacements producing the ground-states. These contributions are obtained by making the overlap between the eigenvectors of each modes and the pattern of displacement from the $P4/mmm$ to the AFD/FE phases. For a positive $SrTiO_3$ misfit strain larger than 0.2%, the ground-state involves mainly the contribution of AFD_{xy} and FE_{xy} displacements, but also the AFD_{zi} type of distortions. Moreover, as the $SrTiO_3$ misfit strain increases, the total contribution to the AFD/FE_{xy} ground-state of these three modes decreases. This decrease is related to the growing contribution of other $P4/mmm$ modes at higher frequencies (0.467 at 2.60% $SrTiO_3$ misfit strain).

For zero and negative $SrTiO_3$ misfit strains, the FE_z, AFD_{zo} and AFD_{zi} modes contribute predominantly to the ground-state. This specific coupling

Label	Space group	No.	distortions
PE	$P4/mmm$	123	
FE_z	$P4mm$	99	FE_z
FE_{xy}	$Amm2$	38	FE_{xy}
AFD_{zo}	$P4/nbm$	125	$a^0a^0c^-$
AFD_{zp}	$P4/mbm$	127	$a^0a^0c^+$
AFD_{xy}	$Pmma$	51	$a^-a^-c^0+\delta_{xy}(\mathrm{A})$
$\mathrm{AFD/FE}_z$	$P4bm$	100	$a^0a^0c^++a^0a^0c^-+\mathrm{FE}_z$
$\mathrm{AFD/FE}_{xy}$	$Pmc2_1$	26	$\mathrm{AFD}_{xy}+\mathrm{FE}_{xy}+\mathrm{AFD}_{zi}$

Table 5.2: Space groups and distortions of related phases in the $PbTiO_3/SrTiO_3$ 1/1 superlattice under epitaxial strains. The PE phase correspond to the bulk high symmetric position with rumpling distortions of the z components of the TiO_2 atomic planes.

corresponds to tilts of oxygens of different amplitudes in consecutive oxygen octahedra along the z direction. At zero $SrTiO_3$ misfit strain ($SrTiO_3$ substrate), the oxygen rotation angles are respectively ϕ_1=+6.2° and ϕ_2=-1.8° and the polarization is equal to 26 μC.cm^{-2} (Table 5.3).

Phase Space group	FE_z $P4mm$	AFD_{zi} $P4/mbm$	AFD_{zo} $P4/nbm$	$\mathrm{AFD/FE}_z$ $P4bm$
P_z	18	0	0	26
ϕ_{zo}	0.0	0.0	4.7	4.0
ϕ_{zi}	0.0	3.4	0.0	2.2
ΔE	-3	-28	-73	-81

Table 5.3: Amplitude of the polarization P_z (μC.cm^{-2}), rotation angles ϕ_{zi} and ϕ_{zo} (degrees) and energy gain ΔE with respect to the prototype $P/4mmm$ phase (meV per supercell) in different low-symmetry phases of $PbTiO_3/SrTiO_3$ 1/1 superlattice epitaxially grown on $SrTiO_3$. The ϕ_{zo} corresponds to (ϕ_1+ϕ_2)/2 and ϕ_{zi} to (ϕ_1-ϕ_2)/2 where ϕ_1 and ϕ_2 are the amplitude of rotation of respectively the first and the second octahedra.

Since the square root of the sum of the square of the overlaps with these three modes is almost equal to 1, this means that only η_{FE_z}, $\eta_{AFD_{zo}}$ and $\eta_{AFD_{zi}}$ contribute to the $\mathrm{AFD/FE}_z$ ground-state. This sum only slightly deviates from 1 when the misfit strain decreases, and ever at a $SrTiO_3$ misfit strain of -2.60%, this deviation remains small (0.148). The relaxed distortions are strongly dominated by the AFD displacements, and in particular by the AFD_{zo} motions. However, the AFD_{zo} overlap contribution decreases with decreasing the $SrTiO_3$ misfit strain, while the AFD_{zi} contribution increases. The FE_z contribution is the smallest and increases with the decrease of the $SrTiO_3$ misfit strain.

In Figure 5.5 we show the evolution of the amplitude of the spontaneous polarization with respect to the misfit strain. Over a wide range of epitaxial strains

misfit strain	η_{FE_z}	$\eta_{AFD_{zo}}$	$\eta_{AFD_{zi}}$	$\eta_{AFD_{xy}}$	$\eta_{FE_{xy}}$	total
-2.60%	0.391	0.758	0.500	0.000	0.000	0.989
-1.04%	0.353	0.796	0.481	0.000	0.000	0.995
0.00%	0.326	0.824	0.456	0.000	0.000	0.997
1.04%	0.000	0.000	0.270	0.659	0.669	0.978
2.60%	0.000	0.000	0.174	0.541	0.676	0.884

Table 5.4: Overlaps between the eigenvectors η_{FE_z}, $\eta_{AFD_{zo}}$, $\eta_{AFD_{zi}}$, $\eta_{AFD_{xy}}$ and $\eta_{FE_{xy}}$ of the paraelectric reference and the atomic distortions of the ground-state of the $PbTiO_3/SrTiO_3$ 1/1 superlattice for five $SrTiO_3$ misfit strains. The total corresponds to the square root of the sum of the square of the overlaps.

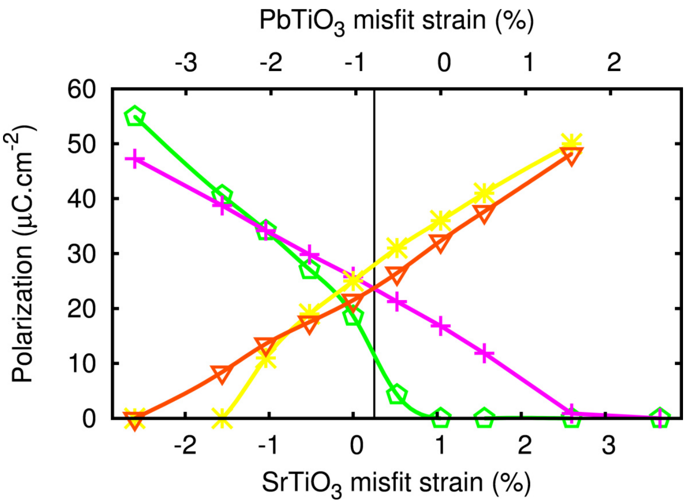

Figure 5.5: Evolution of the spontaneous polarization with the misfit strain in FE_z phase (green pentagons), AFD/FE_z phase (purple crux), FE_{xy} phase (yellow stars) and AFD/FE_{xy} phase (orange triangles).

(from -1.3% to 2.6%), the AFD/FE$_z$ phase gives a significant enhancement of the spontaneous polarization compared to that of a purely FE$_z$ state. Moreover it can produce a sizeable polarization in cases where it would not be observed otherwise. This enhancement of the spontaneous polarization strongly suggests that the unexpected recovery of ferroelectricity in $PbTiO_3$/$SrTiO_3$ multilayers experimentally reported in the limit of ultra thin $PbTiO_3$ layers originates from the coupling of the FE$_z$ and AFD distortions. However, for a $SrTiO_3$ misfit strain lower than -1.3% the spontaneous polarization of the FE$_z$ phase becomes larger than in the AFD/FE$_z$ phase.

At the opposite, in the case of the AFD/FE$_{xy}$ ground-state, the spontaneous polarization is lowered with respect to that of the FE$_{xy}$ phase. However, difference of amplitude of the spontaneous polarization remains small and tends to disappear with tensile epitaxial strain.

In Table 5.5 we report the c/a value of the different phases at five selected epitaxial strains. The evolution of c/a with the misfit strain of AFD/FE$_z$ and FE$_z$ follows the same behavior as the spontaneous polarization. The c/a of the AFD/FE$_z$ phase is larger than the one of FE$_z$ phase for $SrTiO_3$ misfit strain between -2.1% and 2.6% and is smaller for a $SrTiO_3$ misfit strain lower than -2.1%. Like for $SrTiO_3$ and $PbTiO_3$ bulks, the AFD$_{xy}$ and FE$_{xy}$ distortions make the c/a lower than the one of the paraelectric phase while AFD$_{zi}$ and AFD$_{zo}$ increase c/a. In the AFD/FE$_{xy}$ phase c/a is lowered with respect to the paraelectric phase but with smaller amplitude than the AFD$_{xy}$ or FE$_{xy}$ distortions alone. Moreover, the c/a becomes larger than in the paraelectric phase for $SrTiO_3$ misfit strain smaller than -0.5%. This inversion on the evolution of c/a in the AFD/FE$_{xy}$ phase can be attributed to the AFD$_{zi}$ contribution to the AFD/FE$_{xy}$ ground-state. As shown in the Table 5.4, the AFD$_{zi}$ contribution to the AFD/FE$_{xy}$ phase increases when the misfit strain is lowered. Since the AFD$_{zi}$ tends to increase c/a, its contribution to c/a evolution is in competition with the tendency of the AFD$_{xy}$ and FE$_{xy}$ distortions to reduce c/a.

misfit strain	Para	AFD$_{zi}$	AFD$_{zo}$	FE$_z$	AFD$_{xy}$	FE$_{xy}$	AFD/FE$_z$	AFD/FE$_{xy}$
-2.60	2.114	2.129	2.128	2.159	2.110	2.114	2.154	0.000
-1.04	2.056	2.065	2.065	2.071	2.051	2.056	2.077	2.061
0.00	2.020	2.022	2.026	2.024	2.014	2.021	2.033	2.018
1.04	1.986	1.987	1.990	1.986	1.979	1.987	1.993	1.981
2.60	1.938	1.938	1.939	1.938	1.929	1.937	1.939	1.931

Table 5.5: c/a of the paraelectric reference (Para), AFD$_{zi}$, AFD$_{zo}$, FE$_z$, AFD$_{xy}$, FE$_{xy}$, AFD/FE$_z$ and AFD/FE$_{xy}$ phases of $PbTiO_3$/$SrTiO_3$ 1/1 superlattice for five $SrTiO_3$ misfit strains.

For FE$_z$ and AFD/FE$_z$ phases we report in Figure 5.6 the evolution of c/a-$(c/a)_0$ versus the polarization. Interestingly both FE$_z$ and AFD/FE$_z$ phases keep a usual polarization-strain coupling of the form c/a=$(c/a)_0$+αP^2 where the coupling parameter α is larger for AFD/FE$_z$ than for FE$_z$.

After having characterized the ground-state of $PbTiO_3$/$SrTiO_3$ 1/1 superlattice, we will now try to determine the microscopic origin of the unexpected

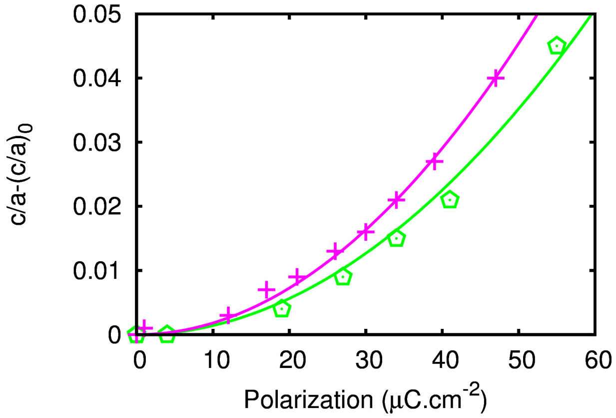

Figure 5.6: Evolution of c/a-$(c/a)_0$ with the spontaneous polarization of the FE$_z$ phase (green pentagons) and the AFD/FE$_z$ phase (purple crux) where $(c/a)_0$.is the paraelectric c/a. The curves are a fit of the data with αP^2 where α is equal to 1.41 10^{-05} for FE$_z$ and 1.82 10^{-05} for AFD/FE$_z$.

coupling between AFD and FE distortions.

5.3.5 Origin of the AFD/FE$_z$ coupling

Contrary to the bulk, the ground-state of the superlattice always combines FE and AFD distortions and it is therefore important to clarify the origin of the coupling between these two type of instabilities.

The condensation of individual instabilities shows that for SrTiO$_3$ substrate, the maximum gain of energy is obtained for the condensation of the AFD$_{zo}$ distortions. Since the ground-state additionally involves the coupling with FE$_z$ and AFD$_{zi}$ distortions, a remaining instability is present in the AFD$_{zo}$ phase. This remaining instability has an imaginary frequency that is associated to an eigenvector which involves together FE$_z$ and AFD$_{zi}$ kind of displacements and corresponds in good approximation to $|\eta_{FE_z} + \eta_{AFD_{zi}}>$. The square of the unstable frequency can be decomposed as follows:

$$\begin{array}{ccc}
<\eta_{FE_z}+\eta_{AFD_{zi}}|D_{AFD_{zo}}|\eta_{FE_z}+\eta_{AFD_{zi}}> & \Leftrightarrow & \omega^2 \\
= & & = \\
<\eta_{FE_z}|D_{AFD_{zo}}|\eta_{FE_z}> & \Leftrightarrow & \omega^2_{FE_z} \\
+ & & + \\
<\eta_{AFD_{zi}}|D_{AFD_{zo}}|\eta_{AFD_{zi}}> & \Leftrightarrow & \omega^2_{AFD_{zi}} \\
+ & & + \\
2<\eta_{FE_z}|D_{AFD_{zo}}|\eta_{AFD_{zi}}> & \Leftrightarrow & 2\omega^2_{coupling}
\end{array} \tag{5.1}$$

where D$_{AFD_{zo}}$ is the dynamical matrix of the AFD$_{zo}$ phase. According to this decomposition, the eigenvalue of the remaining instability can be decomposed into FE_z and AFD_{zi} individual contributions plus a coupling term between AFD_{zi} and FE_z.

At an epitaxial strain corresponding to a $\mathrm{SrTiO_3}$ substrate, ω^2 is equal to -3709 cm^{-2} for the $\mathrm{PbTiO_3/SrTiO_3}$ 1/1 superlattice. In Table 5.6 we report the matrix elements of the decomposition proposed in Eq. 5.1 for bulk $\mathrm{PbTiO_3}$ and $\mathrm{SrTiO_3}$ as well as for the $\mathrm{PbTiO_3/SrTiO_3}$ 1/1 superlattice, all at an epitaxial strain corresponding to $\mathrm{SrTiO_3}$ substrate. In all cases, the chosen η_{FE_z} and $\eta_{AFD_{zi}}$ are the eigenvectors originally from the unstable FE_z and AFD_{zi} modes of the PE reference. For bulk $\mathrm{PbTiO_3}$, only $\omega^2_{FE_z}$ is negative, which is expected since the ground-state of bulk $\mathrm{PbTiO_3}$ on $\mathrm{SrTiO_3}$ substrate is the tetragonal FE_z phase. Since in bulk $\mathrm{SrTiO_3}$ the ground-state is the AFD_{zo} phase, there is no more any instability in this phase and all the contributions are positive. For the superlattice, $\omega^2_{FE_z}$ and $\omega^2_{AFD_{zi}}$ are positive and only the coupling term $\omega^2_{coupling}$ gives negative contribution to the total ω^2. The remaining instability in the AFD_{zo} phase comes therefore only from the *coupling* between the FE_z and the AFD_{zi} displacements and not from one of these instabilities individually. Moreover, such coupling terms are negligible in bulk $\mathrm{PbTiO_3}$ and $\mathrm{SrTiO_3}$, pointing out that the remaining instability $|\eta_{FE_z} + \eta_{AFD_{zi}} >$ is a specific property of the superlattice.

	bulk $\mathrm{PbTiO_3}$	bulk $\mathrm{SrTiO_3}$	$\mathrm{PbTiO_3/SrTiO_3}$ 1/1
$\omega^2_{FE_z}$	-11309	25725	6494
$\omega^2_{AFD_{zi}}$	13126	23029	17372
$\omega^2_{coupling}$	3	5	-12808
total	1823	48764	-1750
$\omega^2(\mathrm{AFD}_{zo})$	-	-	-3709

Table 5.6: Matrix elements (cm^{-2}) of the contribution of the PE eigenvectors η_{FE_z} and $\eta_{AFD_{zi}}$ on the dynamical matrix of the AFD_{zo} condensed phase ($\mathrm{D}_{AFD_{zo}}$) for bulk $\mathrm{PbTiO_3}$, bulk $\mathrm{SrTiO_3}$ and $\mathrm{PbTiO_3/SrTiO_3}$ 1/1 superlattice at zero $\mathrm{SrTiO_3}$ misfit strain as presented in Eq.(5.1). The sum of the contributions is reported (total=$\omega^2_{FE_z} + \omega^2_{AFD_{zi}} + 2\omega^2_{coupling}$) as well as the ω^2 of the remaining unstable mode in the AFD_{zo} condensed phase for the $\mathrm{PbTiO_3/SrTiO_3}$ 1/1 supercell.

To understand the microscopic origin of the coupling between FE_z and AFD_{zi} modes in the AFD_{zo} phase, we are going to determine the link between the z displacement of the cations associated to the FE_z mode and the the oxygen rotations associated to AFD_{zi} by inspecting the interatomic force constants (IFC). In the 20 atoms unit cell, as mentioned in Chapter 2, the IFC matrix $\mathrm{C}_{\alpha,\beta}(\kappa,\kappa')$ relates the force $\mathrm{F}_\alpha(\kappa)$ on atom κ associated to the displacement $\tau_\beta(\kappa')$ of atom κ' where α and β label the directions x, y or z [Eq. (2.8)]. The selected atoms are labelled according to Table 5.7.

The IFC matrix elements $\mathrm{C}_{z,x}(\kappa,\kappa')$ between the atoms of Table 5.7 are reported in Table 5.8. By symmetry the $\mathrm{C}_{z,x}(\kappa,\kappa')$ elements are equal to the $\mathrm{C}_{z,y}(\kappa,\kappa')$ elements, and the IFC on the oxygen O_7 are equivalent to some IFC

label	x	y	z
Pb_1	0.0	0.0	0.0
Sr_{11}	0.000	0.00	0.75
Pb_2	0.500	0.500	0.500
Sr_{12}	0.500	0.500	0.750
O_7	0.279	0.279	0.256
$O_{17'}$	0.221	0.221	-0.256
O_{17}	0.221	0.221	0.744

Table 5.7: Label of selected atoms with their position in reduced coordinate in the AFD_{zo} condensed phase of the $PbTiO_3/SrTiO_3$ 1/1 supercell.

on the O_{17} and $O_{17'}$ as it is reported in the last column of Table 5.8. To make a comparison between the bulk and the superlattice, we also report the equivalent IFC of bulk $SrTiO_3$ in Table 5.8 such as the Pb atom labels of Table 5.7 are all replaced by Sr. Since the main difference between the superlattice and the bulk are the inequivalent cation atomic planes shown by the oxygen of the TiO_2 atomic planes, we report here only the IFC elements which correspond to a displacement of the cations in the z directions and of the oxygens in the in-plane direction (along which the AFD_{zo} oxygen rotation displacements take place).

	$C_{z,x}(\kappa,O_7)$		
κ	1/1	$SrTiO_3$ bulk	
Pb_1	0.00545	0.00496	$= C_{z,x}(Pb_2,O_{17'})$
Pb_2	-0.00294	0.00085	$= C_{z,x}(Pb_1,O_{17'})$
Sr_{11}	-0.00512	-0.00496	$= C_{z,x}(Sr_{12},O_{17})$
Sr_{12}	-0.00238	-0.00085	$= C_{z,x}(Sr_{11},O_{17})$
total	-0.00499	0.00000	

Table 5.8: Interatomic force constants $C_{z,x}(\kappa,\kappa')$ ($Ha/Bohr^2$) between atoms κ and κ' with label from Table 5.7. The cartesian coordinates are used by following the x, y and z directions as define in the Section 5.2. For both, superlattice and bulk $SrTiO_3$, the IFC are reported for in-plane lattice constant fixed to an equivalent cubic $SrTiO_3$ substrate.

First, we examine the IFC in the $PbTiO_3/SrTiO_3$ 1/1 superlattice and to highlight the discussion we report in Figure 5.7 a schematic representation of the cell and forces. As reported in the Table 5.8, the sum of the IFC coming from the effect of cation z displacement on the O_7 is non-zero. The value of the resulting IFC is negative, which corresponds to a resulting force in the opposite direction. According to the atomic position of O_7 in Table 5.7, this force tends to amplify the oxygen rotation of the AFD_{zo} phase. However, by symmetry the resulting force on the O_{17} due to the same cation displacements, has the same amplitude and the same direction than the force on O_7. Since, in the AFD_{zo}

condensed phase, the O_{17} is moved in the opposite direction than the O_7, the resulting force on O_{17} tends to decrease the displacement of this atom in the AFD_{zo} condensed phase. Therefore, the cooperative motion of cations along z direction and $O_{7,17}$ along x and y directions allows to decrease the energy of the $PbTiO_3/SrTiO_3$ 1/1 superlattice and so, contribute to the remaining unstable mode. Since the displacement of atoms along z direction are associated to the FE_z motions and the rotation of oxygens in the in-plane directions with the same amplitude and the same direction are associated to the AFD_{zi} motions, the IFC allow to elucidate the origin of the remaining FE_z-AFD_{zi} mode in the AFD_{zo} phase.

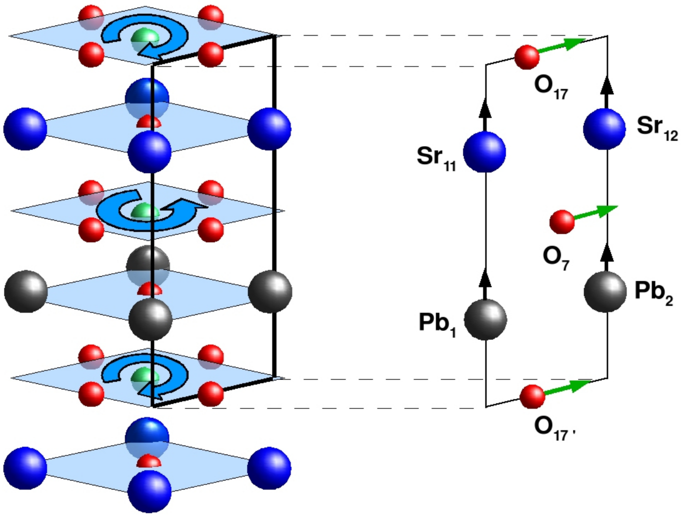

Figure 5.7: Schematic representation of the IFC. Left, representation of the cell in the AFD_{zo} phase where the blue arrows represent the direction of rotation for each TiO_2 plane. Right, selected atoms with labels of Table 5.7. The Black arrows represent out-of-plane displacements of cations ($\tau_\beta(\kappa')$ of Eq. 2.8) while green arrows represent the resulting force (Eq. 2.8) on the oxygens. It is interesting to remark that these forces are in the same direction than the AFD_{zo} rotation for O_7 and in opposite direction for O_{17} and $O_{17'}$.

For bulk $SrTiO_3$ the resulting force associated to the same kind of atomic displacements is zero, since the oxygen atoms show the same top and bottom cations. It results that no net coupling between FE_z and AFD_{zi} motions is permitted in $SrTiO_3$ at the bulk level. The same is true for bulk $PbTiO_3$. This comparison between the bulks and the $PbTiO_3/SrTiO_3$ 1/1 superlattice demonstrates that the coupling between FE_z and AFD_{zi} motions results from the asymmetry of the oxygen environment at the interface between the two types of layers of the superlattice. Even if a coupling between AFD_{zo} and FE_z distortions is possible in $SrTiO_3$ bulk under appropriate compressive epitaxial strain, this coupling does not involve the AFD_{zi} motions.

5.4 Improper Ferroelectricity

5.4.1 Theoretical analysis

Since the ground-state of short-period superlattice is no more purely ferroelectric, we can expect a phase transition mechanism distinct from that of ordinary ferroelectrics. For the $PbTiO_3/SrTiO_3$ 1/1 superlattice, on $SrTiO_3$ substrate, the ground-state results from the condensation of three distortions, FE_z, AFD_{zo} and AFD_{zi} which can be related to independent order parameters: P_z, ϕ_{zo} and ϕ_{zi} respectively. Because FE_z is virtually suppressed at this epitaxial strain, P_z will certainly not appear as the primary order parameter.

The coupling of the polarization with other order parameters was previously discussed by Levanyuk [135, 136] and Holakovský [138]. Two different phase-transition mechanisms were reported, depending on how the order parameters couple with the polarization P: improper ferroelectric for couplings at the linear order and triggered ferroelectricity for couplings at the quadratic order. From Levanyuk [135, 136], typical improper ferroelectrics with primary order parameter ϕ_1 and ϕ_2 exhibit a generic Landau expansion of the form:

$$F = (T - T_C)(a_1\phi_1^2 + a_2\phi_2^2) + \alpha P^2 - \gamma\phi_1\phi_2 P + b_1\phi_1^4 + b_2\phi_2^4 + \beta\phi_1^2\phi_2^2 \quad (5.2)$$

where T_C is the transition temperature related to the order parameters ϕ_1 and ϕ_2 and a_1, a_2, b_1, b_2, α, β and γ are temperature-independent parameters. This free energy expansion contrasts with that of ordinary ferroelectrics that allows only for even-power terms in P: the lowest-order P invariant term in the Landau expansion of improper ferroelectric is linear and has the form $-\gamma\phi_1\phi_2 P$. It results that improper ferroelectrics show critical behavior and temperature dependencies of the polarization and dielectric constant different from that of ordinary ferroelectrics.

In ordinary ferroelectrics, the polarization P is expected from Landau theory to evolve like $(T_C\text{-}T)^{1/2}$ with the temperature T (Figure 5.8 left-top graph). In improper ferroelectrics, the primary order parameter is no longer the polarization P and it is instead ϕ_1 and ϕ_2 that are expected to evolve each like $(T_C\text{-}T)^{1/2}$. From the linear P term in the Landau expansion, the conditions $\frac{\partial F}{\partial P}$=0 and $\frac{\partial^2 F}{\partial P^2}$ <0 yield $P=\frac{\gamma\phi_1\phi_2}{2\alpha} \propto (T_C\text{-}T)$. It results that, below the transition temperature T_C, the polarization evolves linearly with the temperature in improper ferroelectrics (Figure 5.8 right-top graph). As a consequence, the tetragonality c/a that is evolving like P^2, will evolve quadratically in improper ferroelectrics (Figure 5.8 right-midle graph) instead of linearly for normal ferroelectrics (Figure 5.8 left-midle graph).

Furthermore, in improper ferroelectrics it is expected that the dielectric susceptibility will not obey to a conventional Curie-Weiss law at the phase transition because the order parameter is no longer polar and will not directly couple with an external electric field. It can be shown that dielectric susceptibility will remain largely independent of temperature, with a step discontinuity at the transition temperature (Figure 5.8 right-bottom graph).

The possibility of a linear term in P in the Landau expansion is not straightforward but submitted to strict symmetry considerations: in practice the prod-

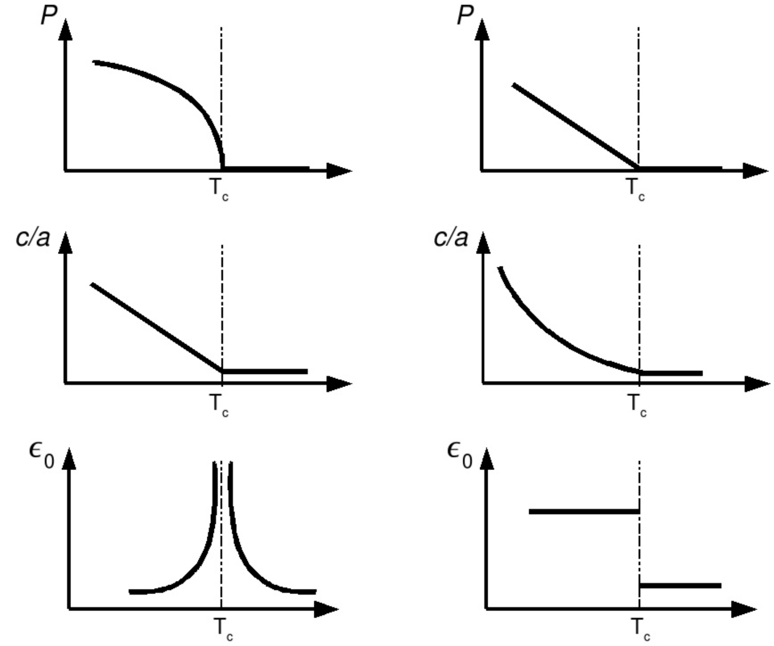

Figure 5.8: Theoretical temperature evolution of polarization (P, top graphs), tetragonality (c/a, midle graphs) and static dielectric constant (ε_0, bottom graphs) of a regular ferroelectric (left, second-order phase transition) and an improper ferroelectric (right) around the transition temperature T_C.

uct $\phi_1\phi_2$ must transform like the order parameter P to keep the symmetry invariance of the free energy. In the *P4/mmm* phase (D_{4h}) of the $PbTiO_3$/$SrTiO_3$ 1/1 superlattice, the irreducible representations at Γ can be written, following Miller and Love notations [139], as :

$$2\Gamma_1^+ \oplus \Gamma_2^+ \oplus 3\Gamma_5^+ \oplus 6\Gamma_3^- \oplus \Gamma_4^- \oplus 7\Gamma_5^-$$

and the irreducible representations at the M (1/2,1/2,0) point are:

$$M_1^+ \oplus M_2^+ \oplus M_3^+ \oplus 2M_4^+ \oplus 2M_5^+ \oplus M_1^- \oplus 4M_2^- \oplus 3M_3^- \oplus M_4^- \oplus 6M_5^-$$

The table of character of the unstable modes at Γ and M as well as their main characteristics are summarized in Table 5.9. According to the symmetry character of AFD_{zo} and AFD_{zi}, we can see that the product of the corresponding order parameter $\phi_{zo}\phi_{zi}$ (see Table 5.3 for the definition of ϕ_{zo} and ϕ_{zi}) transform like the order parameter P_z of FE_z. It results that a linear term in P_z such as $\gamma\phi_{zo}\phi_{zi}P_z$ is allowed in the Landau expansion which is compatible with improper ferroelectricity as discussed above.

In Figure 5.9 (left) we report the calculation of the energy for the 1/1 superlattice as a function of P_z around P_z=0 with fixed ϕ_{zi} and ϕ_{zo} that not only demonstrates the existence of such a linear term in P_z but also highlights the sizeable value of the coupling parameter γ. We also provide in Figure 5.9 (right) a three-dimensional plot of the energy versus polarization and oxygen tilt angle in the vicinity of the high symmetry phase for the $PbTiO_3$/$SrTiO_3$ 1/1 superlattice grown on an $SrTiO_3$ substrate. This was obtained from a fit of our first-principles data provided in Table 5.3. The energy of the highly symmetric *P4/mmm* structure was taken as reference. Since we have in fact three parameters (P_z, ϕ_{zo} and ϕ_{zi}), we had to project within a given subspace. In order to include the global minimum associated to the ground-state AFD/FE_z structure (ΔE=-81.5 eV), we chose the subspace defined by $\phi_{zi} = 2.2/4.0\ \phi_{zo}$. The existence of a sizeable term linear in P_z in the energy expansion can be inferred from the evolution of the energy with P_z along the line $\phi_{zo} = 4.0°$ (inset of Figure 5.9-right).

We finally note that from Eq. (5.2), the existence of a linear term in P is mandatory but not a totally sufficient requirement for improper ferroelectricity, which additionally requires that ϕ_{zi} and ϕ_{zo} have identical transition temperature. Although this is automatically fulfilled in previous prototypical examples of improper ferroelectrics in which ϕ_{zi} and ϕ_{zo} are components of a two-dimensional order parameter, this condition cannot be unambiguously inferred here from theoretical arguments because ϕ_{zi} and ϕ_{zo} belong to different one-dimensional irreducible representations. It is, however, achieved in practice, which was demonstrated experimentally from the observation of a unique T_C and a typical improper ferroelectric behavior of the temperature properties of the smallest $(PbTiO_3)_n$/$(SrTiO_3)_m$ periodicities as we will discuss in the next section.

5.4.2 Experimental evidence

As stated above, improper ferroelectrics show critical behaviors different from that of ordinary ferroelectrics and the fingerprints of improper ferroelectricity

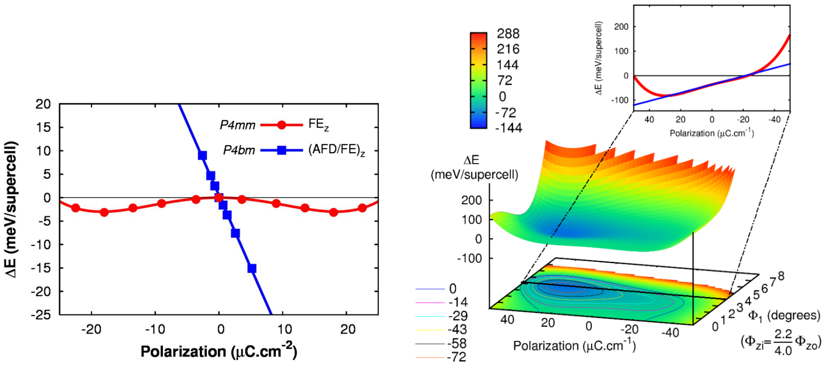

Figure 5.9: (Left) Evolution of the energy with P in the FE$_z$ phase (ϕ_{zi}=ϕ_{zo}=0.0°) and in the AFD/FE$_z$ phase (ϕ_{zi}=2.2° and ϕ_{zo}=4.0°) for a PbTiO$_3$/SrTiO$_3$ 1/1 superlattice epitaxially grown on SrTiO3. (Right) Three-dimensional plot of the energy (ΔE) versus P_z and ϕ_{zo} within the subspace defined by ϕ_{zi}=2.2/4.0ϕ_{zo}. The highly symmetric *P4/mmm* structure is taken as reference. Inset: cut in the 3D graph showing the plane defined by ϕ_{zo} = 4.0°. The red curve represent ΔE and the blue line is its tangent at P_z=0.

Name	ω	Label	E	2C$_4$	C$_2$	2C$'_2$	2C$''_2$	I	2S$_4$	σ_h	2σ_v	2σ_d
AFD$_{zo}$	113i	M_4^-	1	-1	1	-1	1	-1	1	-1	1	-1
AFD$_{xy}$	101i	M_5^-	2	0	-2	0	0	-2	0	2	0	0
AFD$_{zi}$	84i	M_2^+	1	-1	1	1	-1	1	-1	1	1	-1
FE$_z$	51i	Γ_3^-	1	1	1	-1	-1	-1	-1	-1	1	1
FE$_{xy}$	49i	Γ_5^-	2	0	-2	0	0	-2	0	2	0	0

Table 5.9: Frequency (cm^{-1}), label and symmetry characters of the unstable modes at Γ and M points in the paraelectric reference *P4/mmm* (D$_{4h}$) of PbTiO$_3$/SrTiO$_3$ 1/1 superlattice on SrTiO$_3$ substrate. The labels and character table follow the notation of Miller and Love [139].

can be tracked in the distinct temperature dependencies of the polarization and dielectric constant. Therefore the behavior of $PbTiO_3/SrTiO_3$ superlattices corresponding to the two regimes identified in Ref. [102] were compared. The first regime corresponds to a range of compositions and thicknesses producing ordinary ferroelectric behavior (such as 9/3 samples) and the second regime corresponds to superlattices exhibiting an anomalous recovery of ferroelectricity (such as the 2/3 or 1/3 samples) (see Ref. [127] and Ref. [102] for experimental details of process and growth techniques).

For the samples of the first regime, the polarization, tetragonality and dielectric constant evolves as in regular ferroelectrics (see Figure 5.10 panels a, c and e for a 9/3 sample). At the opposite, the samples of the second regime do not show regular temperature evolution of the polarization and dielectric constant (see Figure 5.10 panel b, d and f for a 2/3 sample). As we can see on Figure 5.10 panel b, for the 2/3 and 1/1 samples the polarization evolves linearly with the temperature which corresponds exactly to the theoretical prediction of the temperature evolution of the polarization of an improper ferroelectric (Figure 5.8 top-right graph). Moreover, the experimentally measured polarization for the 1/1 sample extrapolates to 23 μC.cm^{-2} at zero temperature in close agreement with the theoretical prediction of 26 μC.cm^{-2}. This distinct evolution of the polarization in the two kinds of samples is further confirmed in the measurement of the tetragonality c/a, which shows linear dependence with temperature for the 9/3 sample (Figure 5.10.c) and quadratic dependence for the 2/3 sample (Figure 5.10 panel d), in agreement with the behavior expected from the strain-polarization coupling (Figure 5.8 midle graphs). Finally, the evolution of the dielectric constant with temperature is also coherent with the previous observations in Figure 5.10 e and f for the two kinds of samples. Whereas a typical Curie-Weiss law is observed for the 9/3 sample, the dielectric constant of the 2/3 sample remains fairly constant over a wide range of temperature, except for a small step at the transition temperature, as expected for an improper ferroelectric transition (see Figure 5.8 bottom graphs).

All this is fully compatible with the theoretical prediction of an unexpected coupling between the FE instability and AFD oxygen rotations. To further confirm the role of the oxygen rotations, X-ray diffraction measurements were performed on samples exhibiting typical improper ferroelectric behavior. Since the predicted rotations along (001) are responsible for unit cell doubling in-plane, they should result in additional X-ray diffraction peaks. We provide in Figure 5.11 X-ray measurements revealing a (1.5, 0.5, 0.5) reflection for 2/2 and 2/3 superlattices, directly grown on $SrTiO_3$ and Nb-doped $SrTiO_3$. This peak is a direct indication that the unit cell is doubled in plane, definitely confirming the theoretical prediction.

It is worth noticing that the large values of the spontaneous polarization and dielectric constant of the 2/3 sample (P_s=11 μC.cm^{-2} and $\varepsilon_r \approx$600 at 300K) strongly contrast with what was previously reported for typical improper ferroelectrics [136] (in gadolynium molybdate, P_s=0.2 μC.cm^{-2} and $\varepsilon_r \approx$10). In the anomalous experimental samples, although ferroelectricity is unambiguously improper, the polarization and dielectric constant are comparable to those in usual proper ferroelectrics owing to the intrinsically high polarizability of $PbTiO_3$ and

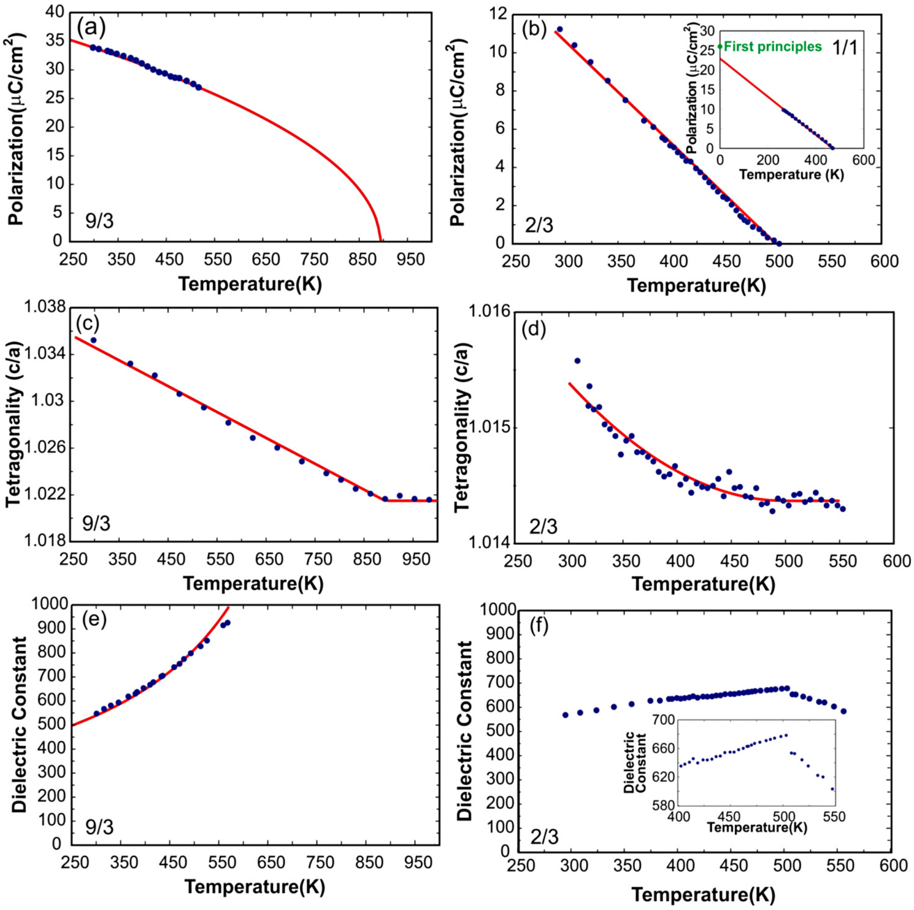

Figure 5.10: Experimental measurements of phase transition behavior in normal and anomalous $(\mathrm{PbTiO_3})_m/(\mathrm{SrTiO_3})_n$ samples. The panels **a**, **c** and **e** are respectively the ferroelectric polarization, tetragonality c/a and dielectric constant of a 100-nm-thick $\mathrm{PbTiO_3/SrTiO_3}$ 9/3 superlattice as a function of temperature. The panels **b**, **d** and **f** are respectively the ferroelectric polarization, tetragonality c/a and dielectric constant of a 100-nm-thick $\mathrm{PbTiO_3/SrTiO_3}$ 2/3 superlattice as a function of temperature. The inset of the panel **b** shows the ferroelectric polarization as a function of the temperature for a 100-nm-thick $\mathrm{PbTiO_3/SrTiO_3}$ 1/1 superlattice. The inset of the panel **f** is a zoom of the panel **f** highlighting the step in the dielectric constant at the transition temperature. The red lines are fits of the experimental datas.

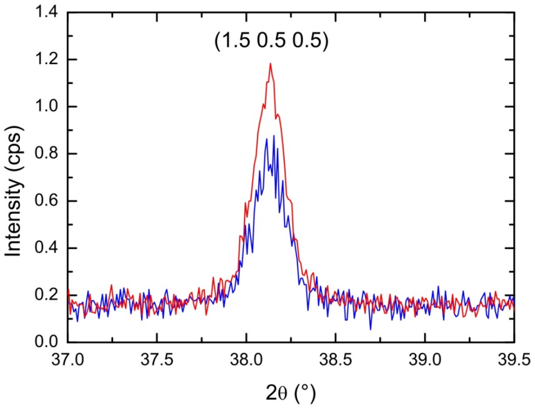

Figure 5.11: Experimental evidence for unit-cell doubling in plane. X-ray diffraction pattern of a peak corresponding to (1.5, 0.5, 0.5) reflexion, for 2/2 and 2/3 superlattices directly grown on $SrTiO_3$ and Nb-doped $SrTiO_3$.

$SrTiO_3$. The fact that as well as being large the dielectric constant is very stable over a wide range of temperature makes these artificial superlattices particularly attractive for dielectric applications.

5.5 Larger Periodicities

The gound state of $(PbTiO_3)_m/(SrTiO_3)_n$ with m/n= 3/3, 5/3, 7/3 and 9/3 were also examined for an epitaxial strain corresponding to $SrTiO_3$ substrate. Due to the number of TiO_2 atomic planes in the unit cell of these large periodicities, many combinations of oxygen rotation are possible. The following notation will be used in this section: the first oxygen octahedra and its direction of rotation is taken as the reference and is noted with the sign + and corresponds to the first layer of $PbTiO_3$ next to the interface with $SrTiO_3$. A + or − sign is then assigned to successive oxygen octahedra, from $PbTiO_3$ to $SrTiO_3$ layer, depending if the rotation is in the same direction than in the first $PbTiO_3$ layer (+) or in opposite direction (−) (the amplitudes are not reported and are not necessary the same for all oxygen octahedra).

For the 3/3 superlattice, we report in Table 5.10 the AFD instabilities with rotations about the z axis, calculated in the paraelectric reference. The $PbTiO_3/SrTiO_3$ 1/1 equivalent AFD_{xy}, FE_z and FE_{xy} instabilities are also present in the 3/3 periodicity with the amplitudes -103i, -57i and -72i cm^{-1}.

The large number of AFD instabilities compared to the 1/1 periodicity makes the analysis of the ground-state of the larger periodicities much more complicated. The calculated ground-state of the 3/3 superlattice on $SrTiO_3$ substrate, is a combination between FE_z distortions and most of the AFD instabilities around the z axis. The overlap between the atomic displacements of the ground-state and the instabilities of the PE reference are given in the Table 5.10. The

instabilities	ω	overlap
$(+-+-+-)$	-115i	0.797
$(+--+-+)$	-107i	0.451
$(++-++-)$	-107i	0.109
$(+++--+)$	-98i	0.274
$(+---++)$	-87i	0.000
$(++++++)$	-74i	0.181
FE_z	-57i	0.172
total		0.994

Table 5.10: Amplitude of the AFD instabilities with oxygen rotations around the z axis and FE_z instabilities in the paraelectric reference of the 3/3 periodicity. In the third column is reported the overlap between the eigenvector of the unstable modes and the atomic displacements in the AFD/FE_z phase.

strongest overlap corresponds to the AFD instability where consecutive oxygen octahedra rotate out-of-phase. It can be associated to the AFD_{zo} distortion of the 1/1 periodicity, with the difference that the amplitudes of rotation of each successive octahedra are not the same.

In Figure 5.12 we report the amplitudes of rotation of the oxygen octahedra in the AFD/FE_z ground-state for the 3/3, 5/3, 7/3 and 9/3 periodicities. Here only the amplitudes are reported, but consecutive rotations are in opposite direction. All thicknesses shown a strong oxygen rotation ($\simeq 6°$) in the $\mathrm{PbTiO_3}$ octahedra at the interface, when the polarization is oriented from $\mathrm{SrTiO_3}$ to $\mathrm{PbTiO_3}$ layers, while at the second interface, the amplitude of rotation of the $\mathrm{SrTiO_3}$ octahedra is small ($\leq 1°$) for all periodicities. In the $\mathrm{PbTiO_3}$ layer, the amplitude of rotations decreases from the interface to the center of the layer and this effect increases when the thickness of the $\mathrm{PbTiO_3}$ layer increases, revealing that the AFD/FE coupling is essentially an interfacial effect.

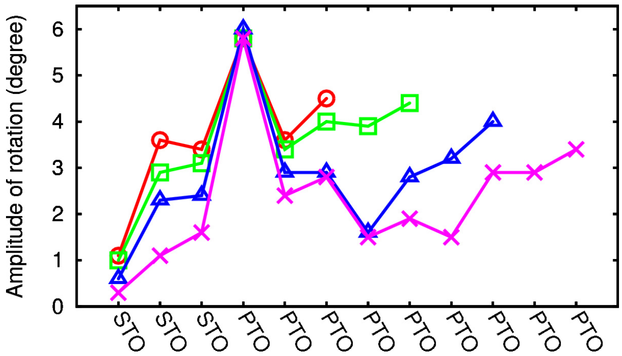

Figure 5.12: Amplitude of rotations of each oxygen octahedra in the AFD/FE_z ground-state of the 3/3 (red circles), 5/3 (green squares), 7/3 (blue triangles) and 9/3 (purple crux).

In Table 5.11 we report an estimation of the layer polarization of the ground-state by using the bulk Born effective charges and the atomic displacements with respect the paraelectric reference [Eq. 2.24)]. The out-of-plane polarization is nearly homogeneous through the whole structure for all the periodicities, which is electrostatically required to avoid large depolarizing fields. This polarization tends to increase with the size of the $PbTiO_3$ layer but start from high value, even for the 1/3 periodicity (~30 μC.cm^{-2}).

	1/3	3/3	5/3	7/3	9/3
($PbTiO_3$)	26.7	35.8	39.7	45.3	52.3
($SrTiO_3$)	33.2	37.5	39.7	45.0	51.6
Total	30.5	35.9	39.7	45.2	52.1
Berry Phase	31.8	35.5	38.8	–	–

Table 5.11: (Left) Estimated spontaneous polarization (μC.cm^{-2}) in the out-of-plane direction of the ground-state of the 1/3, 3/3, 5/3, 7/3 and 9/3 $PbTiO_3/SrTiO_3$ superlattices by using the Eq. (2.24) and the bulk Born effective charges. The lines ($PbTiO_3$) and ($SrTiO_3$) are the integrated value of the spontaneous polarization in respectively $PbTiO_3$ and $SrTiO_3$ layers. In the last line is reported the polarization calculated with the Berry phase method for some superlattices, allowing to check the validity of the approximation of Eq. (2.24).

5.6 Alternative systems

In the previous sections, we have shown that $PbTiO_3/SrTiO_3$ superlattices exhibit in the limit of ultra-short periods an unexpected behavior, distinct from that of the parent compounds. This was explained from a specific coupling between FE and AFD structural instabilities at the layer interfaces, yielding improper ferroelectric behavior. Here, we are going to investigate to which extent a similar type of FE/AFD coupling can be induced in other artificially layered systems.

5.6.1 $PbTiO_3/CaTiO_3$

In its paraelectric cubic structure, $CaTiO_3$ is similar to $SrTiO_3$. We calculated a relaxed cubic cell parameter of 3.80 Å, in good agreement with previous LDA calculations [140]. As reported in Chapter 2, the phonon dispersion curves show FE instability at the Γ point as well as AFD instabilities at the M and R zone boundary points. At the LDA volume, the amplitude of these instabilities are all larger than in bulk $SrTiO_3$ or $PbTiO_3$: -226i cm^{-1} for $a^0a^0a^-$ AFD mode, -98i cm^{-1} for $a^0a^0a^+$ AFD mode and -123i cm^{-1} for the FE mode (respectively -113i, -73i, 99 cm^{-1} for $SrTiO_3$ and -98i, -73i and -109i for $PbTiO_3$ at their LDA volume). As shown in Chapter 2, the corresponding low temperature ground-state is an orthorhombic structure which involves the mix between three AFD distortions ($a^-a^-c^+$) and the displacement of Ca atoms from their ideal perovskite positions [58]. In Chapter 4 we have shown that under epitaxial strain, $CaTiO_3$ keeps this orthorhombic structure for a wide range of epitaxial strain. We reported however a FE phase combining the in-plane FE_{xy} distortions and the AFD tilts of the orthorhombic structure for large tensile strain. It results that the AFD instabilities dominate the structure in $CaTiO_3$ compounds although in a different way than in bulk $SrTiO_3$. We notice however that both materials exhibit incipient ferroelectric behavior.

Replacing $SrTiO_3$ by $CaTiO_3$ in the $PbTiO_3/SrTiO_3$ 1/1 superlattice, gives a new supercell where the Sr atoms are replaced by Ca atoms: $PbTiO_3/CaTiO_3$ 1/1. Here, the mismatch between $PbTiO_3$ and $CaTiO_3$ is more important than the one between $PbTiO_3$ and $SrTiO_3$. Following the same procedure than in Section 5.3, the ΔE versus misfit strains was computed and is shown in Figure 5.13. The two ground-states obtained are the same than for $PbTiO_3/SrTiO_3$ superlattice: AFD/FE_z and AFD/FE_{xy}. However, for $PbTiO_3/CaTiO_3$ supercell, the critical in-plane strain limiting these two ground-states is shifted towards a larger compressive strain. For $PbTiO_3/SrTiO_3$ superlattice, the critical misfit strain was 0.2% for $SrTiO_3$ and -0.8% for $PbTiO_3$ while for the $PbTiO_3/CaTiO_3$ superlattice, the critical misfit strain is -2.1% for $CaTiO_3$ and -4.0% for $PbTiO_3$. It results that the AFD/FE_{xy} phase is more favored in the $PbTiO_3/CaTiO_3$ 1/1 superlattice. Moreover, the amplitude of ΔEs are much more important in the $PbTiO_3/CaTiO_3$ superlattice than for $PbTiO_3/SrTiO_3$ superlattice. These strong gains of energy are related to the stronger amplitude of atomic displacements in $CaTiO_3$ than in $SrTiO_3$, which are induced by the strong instabilities of the $CaTiO_3$ compound. In $PbTiO_3/CaTiO_3$ superlattice, the amplitude of rotations are between 6.4° and 10.0° in the AFD_{zo} phase and between 5.8° and 9.8° in the AFD_{zi} phase respectively for $CaTiO_3$ misfit strain going from +3.16% to -3.68%. These amplitudes of rotations are much more important than the one observed in the $PbTiO_3/SrTiO_3$ 1/1 supercell or in bulk $PbTiO_3$ and $SrTiO_3$, but are of the same amplitude than the ones observed in the bulk $CaTiO_3$ (about 9.5° in the AFD_{zo} phase at the relaxed volume).

Contrary to what was reported for the $PbTiO_3/SrTiO_3$ 1/1 superlattice, the AFD/FE_z phase in $PbTiO_3/CaTiO_3$ 1/1 does not show an enhancement of the polarization with respect to the FE_z phase. Here, the AFD/FE_z phase appears below a $CaTiO_3$ misfit strain of -2.1%, while the FE_z is already present for tensile $CaTiO_3$ misfit strain (always present at +3.2%). At a $CaTiO_3$ misfit strain of -2.63%, the polarization of the AFD/FE_z phase is about 20 μC.cm^{-2} while it is about 100 μC.cm^{-2} in the FE_z phase.

The corresponding c/a follows the same evolution than the polarization: strong increase of the c/a for the FE_z phase with respect to the PE reference, while this increase is strongly smaller in the AFD/FE_z phase but larger than in the AFD_{zo} phase. The oxygen rotations are in phase opposition with small difference of amplitude between the two oxygen octahedra (ϕ_1=9.6 and ϕ_2=8.9 degrees at a $CaTiO_3$ misfit strain of -2.63%). The AFD/FE_{xy} phase gives the same behavior than for $PbTiO_3/SrTiO_3$ 1/1 superlattice: smaller polarization than the FE_{xy} phase (about 20% smaller) and c/a smaller than the one in the PE phase and of the same amplitude than in the AFD_{xy} phase for tensile

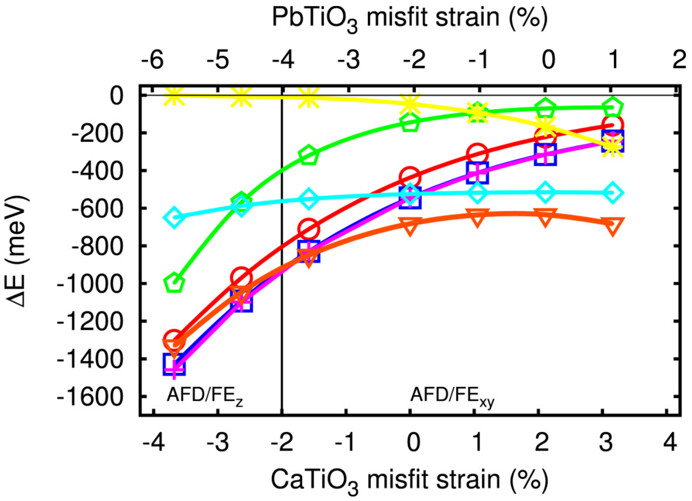

Figure 5.13: Gain of energy ΔE (meV/supercell) with respect to the paraelectric reference of different phases for the $(PbTiO_3)_1/(CaTiO_3)_1$ superlattice in term of misfit strain. The same label than Figure 5.4 are used.

epitaxial strain.

5.6.2 CaTiO$_3$/SrTiO$_3$

The CaTiO$_3$/SrTiO$_3$ superlattice is not strictly speaking a FE/iFE superlattice since none of the parent compounds is ferroelectric at the bulk level. In this type of incipient-ferroelectric/incipient-ferroelectric (iFE/iFE) it is however interesting to see if the asymmetry at the interface can eventually induce a FE instability in an otherwise paraelectric material.

In Figure 5.14 we show the gain of energy ΔE with respect to the paraelectric reference of CaTiO$_3$/SrTiO$_3$ 1/1 supercell as a function of the misfit strain. Here, like for PbTiO$_3$/CaTiO$_3$ 1/1 superlattice, the AFD/FE$_{xy}$ phase corresponds to the ground-state of the CaTiO$_3$/SrTiO$_3$ 1/1 superlattice for a wide range of CaTiO$_3$ misfit strain (from -1.5% to 3.5%). However, below a CaTiO$_3$ misfit strain of -1.5%, the AFD$_{zo}$ phase alone gives the maximum gain of energy and no AFD/FE$_z$ phase is observed as being the ground-state of the system like in PbTiO$_3$/SrTiO$_3$ or PbTiO$_3$/CaTiO$_3$ superlattice. Like for PbTiO$_3$/CaTiO$_3$ superlattice, the association of CaTiO$_3$ with SrTiO$_3$ in the supercell shifts the transition between AFD/FE$_{xy}$ and AFD$_{zo}$ to compressive misfit strain for CaTiO$_3$ (-1.5%) which correspond to a stronger compressive epitaxial strain for SrTiO$_3$ (-2.5%) while at the bulk level the transition with AFD$_{zo}$ in SrTiO$_3$ is around a misfit strain of +0.2%.

Here, the gains of energy are strong with respect to the PbTiO$_3$/SrTiO$_3$ 1/1 superlattice and are comparable to the ones reported for PbTiO$_3$/CaTiO$_3$ 1/1 superlattice. The amplitude of distortions in the CaTiO$_3$/SrTiO$_3$ superlattice

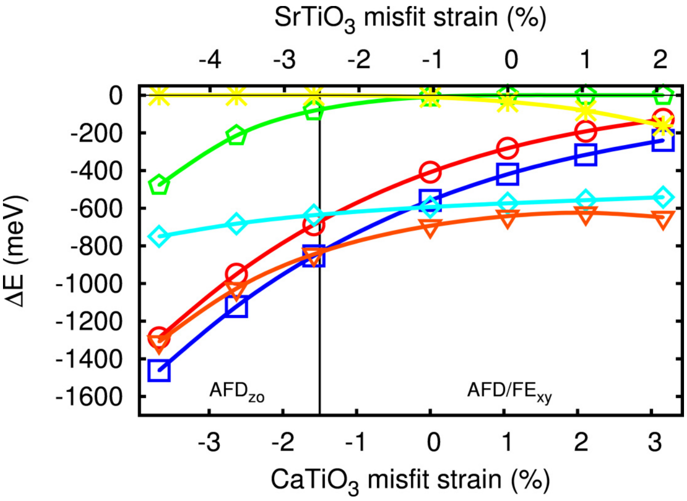

Figure 5.14: Gain of energy ΔE (meV/supercell) with respect to the paraelectric reference of different phases for the $(CaTiO_3)_1/(SrTiO_3)_1$ superlattice in term of misfit strain. The same label than Figure 5.4 are used. The AFD/FE$_z$ is not reported here since it is not observed as being the ground-state for the selected misfit strains.

are of the same order as for $PbTiO_3/CaTiO_3$ superlattice and the AFD/FE$_{xy}$ ground-state has the same characteristics than in $PbTiO_3/CaTiO_3$ and $PbTiO_3/SrTiO_3$ superlattices.

5.6.3 Coupling term

Let us analyse the coupling properties in the different superlattices. In Table 5.12 we report the contribution coming from the decomposition proposed in Eq. (5.1) for $PbTiO_3/CaTiO_3$ and $CaTiO_3/SrTiO_3$ superlattices. For the three superlattices, the coupling term is non zero and only this term gives a negative contribution. However, in $CaTiO_3/SrTiO_3$ superlattice, the coupling term ($2\omega^2_{coupling}$) is much smaller than $\omega^2_{FE_z}$ and $\omega^2_{AFD_{zi}}$, while in $PbTiO_3/CaTiO_3$ the coupling term is larger than $\omega^2_{FE_z}$ but stays smaller than $\omega^2_{AFD_{zi}}$. Therefore, the contributions of the paraelectric unstable modes to the ground-state distortions are different than in the $PbTiO_3/SrTiO_3$ superlattice. In $PbTiO_3/SrTiO_3$, the coupling term had the strongest contribution and therefore was more favorable than in the $PbTiO_3/CaTiO_3$ and $CaTiO_3/SrTiO_3$ superlattices. In $CaTiO_3/SrTiO_3$, the ground-state for strong compressive epitaxial strains is the AFD$_{zo}$ phase and no more the AFD/FE$_z$ phase, but the coupling term stays non zero and has a negative contribution, which makes the superlattice different from the bulks.

In spite of the strong negative coupling term in the $PbTiO_3/CaTiO_3$ 1/1 superlattice, the sum of the contributions coming from the decomposition Eq. (5.1) gives a positive total ω^2 while from the DFT calculation an instability is ob-

	$PbTiO_3/CaTiO_3$	$CaTiO_3/SrTiO_3$	$PbTiO_3/SrTiO_3$
$\omega^2_{FE_z}$	4786	30020	6494
$\omega^2_{AFD_{zi}}$	69311	79341	17372
$\omega^2_{coupling}$	-20175	-1815	-12808
total	33747	105731	-1750
$\omega^2(\mathrm{AFD}_{zo})$	-8341	13249	-3709

Table 5.12: Matrix elements (cm^{-2}) of the contribution of η_{FE_z} and $\eta_{AFD_{zi}}$ on the dynamical matrix of the AFD_{zo} condensed phase ($D_{AFD_{zo}}$) for $PbTiO_3/CaTiO_3$ and $CaTiO_3/SrTiO_3$ superlattices at a $CaTiO_3$ misfit strain of -2.63%. The sum of the contributions is reported (total, see caption of Table 5.6) as well as the ω^2 of the remaining unstable mode in the AFD_{zo} condensed phase (from direct DFT calculations). For easier comparison, we remind the contributions of the $PbTiO_3/SrTiO_3$ superlattice reported in Table 5.6.

served in the AFD_{zo} phase. Moreover, for $CaTiO_3/SrTiO_3$ superlattice the same sum is positive, as for the DFT calculation, but gives rise to a strong difference on the amplitude while these differences are less important for the $PbTiO_3/SrTiO_3$ superlattice.

These deviations with the DFT calculations come from the set of eigendisplacements chosen for the decomposition proposed in Eq. (5.1), in which the η_{FE_z} and $\eta_{AFD_{zi}}$ applied on the AFD_{zo} dynamical matrix are the ones of the paraelectric reference. Now, if we choose the displacements FE_z and AFD_{zi} coming from the $|\eta_{FE_z} + \eta_{AFD_{zi}} >$ eigenvector (obtained with the AFD_{zo} dynamical matrix) as the new set of eigendisplacements, we obtain the results reported in Table 5.13. For all the superlattices, this new set of eigendisplacements gives rise to a total frequency consistent with the exact DFT calculations but the decomposition in terms of $\omega^2_{FE_z}$, $\omega^2_{AFD_{zi}}$ and $\omega^2_{coupling}$ is different than the one performed with the paraelectric set of eigendisplacements given in Table 5.12. Here, the $\omega^2_{coupling}$ remains negative for all the superlattices, but is strongly reduced in the case of $PbTiO_3/CaTiO_3$ and $CaTiO_3/SrTiO_3$. In the $PbTiO_3/CaTiO_3$ superlattice the FE_z gives a negative contribution to the total ω^2 and therefore the final unstable mode is native from the coupling term but also from the FE_z contribution which was not observed with the paraelectric set. Moreover, in the $CaTiO_3/SrTiO_3$ superlattice, the FE_z gives the maximum contribution to the mode while the AFD_{zi} contribution is small. In the $PbTiO_3/SrTiO_3$ superlattice, however, these differences are present but do not modify the relative contributions of each component by comparison with the paraelectric set.

These differences of contributions originate from the differences between the paraelectric set of eigendisplacements and the η_{FE_z} and $\eta_{AFD_{zi}}$ displacements coming from the $|\eta_{FE_z} + \eta_{AFD_{zi}} >$ eigenvector of the AFD_{zo} phase. To highlight these differences, we report in Table 5.14 the overlaps between the η_{FE_z} and $\eta_{AFD_{zi}}$ eigendisplacements of the paraelectric reference and the $|\eta_{FE_z} + \eta_{AFD_{zi}} >$ eigendisplacement of the AFD_{zo} phase. In the $PbTiO_3/SrTiO_3$ su-

	$PbTiO_3/CaTiO_3$	$CaTiO_3/SrTiO_3$	$PbTiO_3/SrTiO_3$
$\omega^2_{FE_z}$	-5380	13266	5978
$\omega^2_{AFD_{zi}}$	2387	26	6788
$\omega^2_{coupling}$	-2674	-22	-8237
total	-8341	13248	-3708

Table 5.13: Matrix elements (cm^{-2}) of the contribution of η_{FE_z} and $\eta_{AFD_{zi}}$ part of the exact eigenvector $|\eta_{FE_z}+\eta_{AFD_{zi}}>$ on the dynamical matrix of the AFD_{zo} condensed phase ($D_{AFD_{zo}}$) for $PbTiO_3/CaTiO_3$, $CaTiO_3/SrTiO_3$ superlattices at a $CaTiO_3$ misfit strain of -2.63% and for $PbTiO_3/SrTiO_3$ superlattice at zero $SrTiO_3$ misfit strain. The sum of the contributions is reported (total, as defined in the caption of Table 5.6).

perlattice both η_{FE_z} and $\eta_{AFD_{zi}}$ eigendisplacements, contribute equally to the $|\eta_{FE_z}+\eta_{AFD_{zi}}>$ eigendisplacement and since the sum of their contributions is almost equal to 1, it means that the $|\eta_{FE_z}+\eta_{AFD_{zi}}>$ eigenvector is mainly formed by the paraelectric unstable FE_z and AFD_{zi} modes.

	$\eta_{AFD_{zi}}$	η_{FE_z}	sum	others
$PbTiO_3/SrTiO_3$	0.625	0.761	0.985	0.173
$PbTiO_3/CaTiO_3$	0.186	0.947	0.965	0.262
$CaTiO_3/SrTiO_3$	0.018	0.873	0.873	0.488

Table 5.14: Overlaps between the $|\eta_{FE_z}+\eta_{AFD_{zi}}>$ eigenvector coming from the AFD_{zo} phase and the paraelectric reference η_{FE_z} and $\eta_{AFD_{zi}}$ eigenvectors for $PbTiO_3/SrTiO_3$, $PbTiO_3/CaTiO_3$ and $CaTiO_3/SrTiO_3$ superlattices. The third column (sum) reports the square root of the sum of the square of η_{FE_z} and $\eta_{AFD_{zi}}$ overlaps while the last column (others) gives the remaining contribution coming from another paraelectric modes. The reported overlaps were done at zero $SrTiO_3$ misfit strain for the $PbTiO_3/SrTiO_3$ superlattice and at -2.63% $CaTiO_3$ misfit strain for $PbTiO_3/CaTiO_3$ and $CaTiO_3/SrTiO_3$ superlattices.

For $PbTiO_3/CaTiO_3$ superlattice, however, the distribution is less homogeneous since the paraelectric η_{FE_z} contribute strongly to $|\eta_{FE_z}+\eta_{AFD_{zi}}>$ while the $\eta_{AFD_{zi}}$ contribution is small. Moreover, the contribution coming from other paraelectric modes is larger than this $\eta_{AFD_{zi}}$ contribution. The same global distribution is observed for the $CaTiO_3/SrTiO_3$ superlattice, but here the contributions coming from the other modes are large.

All of this illustrate that, for $PbTiO_3/CaTiO_3$ and even more for $CaTiO_3/SrTiO_3$ superlattices, the $|\eta_{FE_z}+\eta_{AFD_{zi}}>$ eigenvector can not be describe in terms of the paraelectric FE_z and AFD_{zi} mode alone. This can be related to the amplitude of distortions induced by the $CaTiO_3$ which, as we have shown in Chapter 4, is associated to a stronger deviation between the final distortions and the initial paraelectric unstable modes.

At last, we can see that the possibility of the AFD/FE_z coupling is strongly dependant on the characteristic of the AFD and FE distortions of the parent compounds.

5.7 Conclusion

In this chapter we have presented the study of $PbTiO_3$/$SrTiO_3$, $PbTiO_3$/$CaTiO_3$ and $CaTiO_3$/$SrTiO_3$ superlattices. We have shown that, in all cases, the ground-state involves the mixing between FE and AFD distortions, giving rise to new phases, never reported in bulk. We have demonstrated that the coupling between AFD_{zo}, AFD_{zi} and FE_z distortions is specific to the interface of the superlattices and can not be produced in bulk compounds. Moreover, this AFD/FE_z coupling was associated to be coherent with the definition of the improper ferroelectrics, that was confirmed experimentally on $PbTiO_3$/$SrTiO_3$ superlattice.

The emergence of improper ferroelectricity as a direct product of the interfaces in the artificially layered structure, suggests a promising new approach where "interface engineering" is used to tune material properties. In the present example, FE and AFD instabilities were inherent to $PbTiO_3$, $SrTiO_3$ and $CaTiO_3$ at the bulk level but competing differently in each system and generating a different ground-state. What was demonstrated here is the possibility of using artificial layering and interfaces to change the nature of the coupling between these instabilities and produce a new ground-state and properties. The large variety of perovskite oxides exhibiting different tendencies to FE and AFD instabilities suggests that there is tremendous potential to generate artificial materials with totally new behavior by following this idea. However, the present study of $PbTiO_3$/$CaTiO_3$ and $CaTiO_3$/$SrTiO_3$ superlattices has shown that choosing compounds exhibiting FE and AFD instabilities together is not sufficient to give the AFD/FE_z improper ferroelectric ground-state. Although a full set of "design rules" cannot be provided at this stage, combining compounds in which cations interact differently with oxygen atoms is certainly an interesting pathway to create interfacial asymmetry and thus modify the FE/AFD coupling.

We note that the interface engineering approach complements rather than replaces other strategies to material tuning, such as strain engineering. Indeed, the role of epitaxial strain is crucial in the present case. The strain can be used to switch from the AFD/FE_z to the AFD/FE_{xy} state. Especially intriguing is the equivalence in energy for these states which might allow considerable freedom for polarization rotation and a high piezoelectric response.

A clear benefit of the present approach, which uses the FE/AFD coupling instead of relying solely on the FE instability, is that it allows manipulation of the temperature dependence of the polar order parameter, which in the $PbTiO_3$/$SrTiO_3$ superlattice leads to a high, nearly temperature independent dielectric constant, a property highly desirable from a technological standpoint. In the different context of magneto-electrics and multiferroics, where the magnetic order is frequently associated with rotational structural distortions, changing similarly the nature of the FE/AFD coupling would likely allow tuning of the magnetoelectric response [138, 141, 142] in some materials.

5.8 References

The results presented in this chapter have been partly discussed in the following papers:

- M. Dawber *et al.*, *Unusual Behavior of the Ferroelectric Polarization in $PbTiO_3/SrTiO_3$ Superlattices*, Phys. Rev. Lett. **95**, 177601 (2005).
- M. Dawber *et al.*, *Tailoring the Properties of Artificially Layered Ferroelectric Superlattices*, Adv. Mater **19**, 4153 (2007).
- E. Bousquet *et al.*, *Improper Ferroelectricity in Perovskite Oxide Artificial Superlattices*, Nature **452**, 732 (2008).

A review for the theory of improper ferroelectricty:

- A. P. Levanyuk and D. G. Sannikov, *Improper Ferroelectrics*, Usp. Fiz. Nauk **112**, 561 (1974).

Chapter 6

Ferroelectric/Insulator superlattices

6.1 Introduction

The case of Ferroelectric/Insulator superlattices in which a ferroelectric alternates with a regular insulator was only marginally addressed in the literature. This might be due to the fact that no enhancement of the ferroelectric properties is expected in such systems because of the non-ferroelectric character of the regular insulator. Only the study of the interface between AO and ABO_3 oxides has generated some interest when searching for alternative high κ dielectric to replace SiO_2 as gate oxide in MOSFET devices. In this context the AO oxide is indeed used as a buffer layer between the silicon substrate and the perovskite [143].

In this chapter, we will consider the case of $(BaTiO_3)_m/(BaO)_n$ superlattices that constitutes a prototypical example of ferroelectric/insulator superlattice. A first principles study was previously reported for $(BaTiO_3)_m/(BaO)_n$ and $(SrTiO_3)_m/(SrO)_n$ superlattices [87], but only the paraelectric periodicity n=6 and m=5 was considered and the ferroelectric properties were not explicitly discussed. Here, we will first consider the predictions of an electrostatic model as reported in Chapter 3, and second, we will present first-principles calculations of the phonon band structures of the paraelectric $(BaTiO_3)_m/(BaO)_n$ superlattices for various thicknesses m and n. We will discuss the effects of the layer thicknesses on the vibrational properties and will show that the predicted ground state differs from that expected from of the simple electrostatic model.

6.2 Technical details

The technical details are similar to those given in Section 1.8, with the only difference that from the smallest to the biggest superlattices, tetragonal Monkorsh-Pack meshs from respectively 6×6×3 to 6×6×1 have been considered for the Brillouin zone sampling in order to produce accurate results.

Here again, the epitaxial strain was treated by fixing the cubic in-plane lattice constant of the superlattices. Only the case of an epitaxial strain corresponding to an hypothetical $SrTiO_3$ substrate was considered (theoretical relaxed cubic cell parameter of $SrTiO_3$: a=3.84 Å). For each considered thickness, we performed structural optimization of the atomic positions and out-of-plane cell parameter of the superlattice in its highly symmetric phase corresponding to the tetragonal space group $P4/mmm$ (No 123).

6.3 $(BaTiO_3)_m/(BaO)_n$ Multilayers

6.3.1 Structure

$BaTiO_3$ can be epitaxially growth on BaO oxide [144]. At the interface, the two compounds are aligned as follows: $ABO_3(001)\|AO(001)$ and ABO_3 <110>‖AO-<100> which means that the $BaTiO_3$ unit cell is rotated by 45 degrees around the (001) BaO direction as shown on Figure 6.1. For each interface, the generic $(BaO\text{-}TiO_2)_m/(BaO)_n$ formula is used and labeled by n/m where n is the number of BaO oxide atomic layer and m the number of $BaTiO_3$ formula units [87, 145].

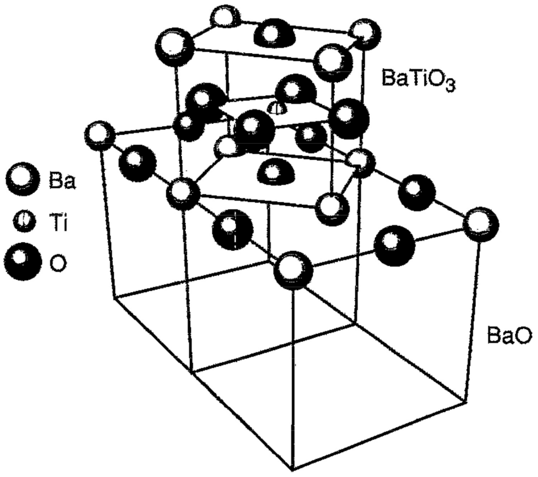

Figure 6.1: Picture of $BaTiO_3$/BaO interface showing the epitaxial arrangement of $BaTiO_3$ on BaO (from [144]).

6.3.2 Electrostatic model

As explain in Chapter 3, the energy of a superlattice can be formulated within a simple model as the sum of the internal energy for the two compounds forming the superlattice and an electrostatic energy:

$$E = U_1 + U_2 + E_{elec}. \tag{6.1}$$

In first approximation, the internal energies U_1 and U_2 can be determined at the bulk level while the electrostatic term E_{elec} takes into account the energy cost related to the difference of polarization in the two types of layers.

Bulk internal energies

In their relaxed cubic structures, we obtained the lattice constants a_{BO}=5.46 Å and a_{BT}=3.94 Å for BaO and $BaTiO_3$ respectively, which are in good agreement with previous LDA results. In the NaCl structure, a cell parameter of 5.46 Å in the BaO bulk corresponds to a Ba-Ba distance of 3.86 Å. Therefore, when grown on $SrTiO_3$ substrate with a cubic in-plane lattice constant of 3.84 Å both BaO (the epitaxial strain being applied on the Ba-Ba distance) and $BaTiO_3$ are under compressive strain and become tetragonal. After relaxation with this epitaxial constraint, the out-of-plane cell parameters of the paraelectric references are c_{BO}=5.48 Å and c_{BT}=4.01 Å for BaO and $BaTiO_3$ respectively. The associated Born effective charge and electronic dielectric tensors are reported in Table 6.1. The values are comparable to those in the cubic structure, with a small anisotropy due to the tetragonal symmetry: most components of the Born effective charges and electronic dielectric tensors are smaller in the z than in the x/y directions. The frequency of the lowest TO mode are also reported in Table 6.1 together with their mode effective charges. In this constrained paraelectric configuration, BaO is stable but the mode polarized along the z direction has a lower frequency than those along the x/y directions. $BaTiO_3$ shows a ferroelectric instability along the z direction with a imaginary frequency of 180i cm^{-1} and an associated mode effective charge of 8.47 e while in the x/y directions, the frequency of the soft mode is shifted to real frequency (195 cm^{-1}) and its mode effective charge is slightly reduced (8.00 e).

	BaO		$BaTiO_3$	
	x/y	z	x/y	z
a	3.84	5.48	3.84	4.01
Z^*(Ba)	2.83	2.78	2.81	2.77
$Z^*(O_1)$	-2.83	-2.78	-2.27	-5.29
Z^*(Ti)	-	-	7.48	6.80
$Z^*(O_{2/3})$	-	-	-2.13/-5.90	-2.14
ϵ^∞	4.39	4.38	6.65	6.45
ω_{TO}	118	74	195	180i
$\bar{Z}^*$	3.14	3.08	8.00	8.47

Table 6.1: Cell parameters (Å), Born effective charges tensors (e), optical dielectric constant tensors, frequency of the lowest TO modes (cm^{-1}) and associated mode effective charges (e) for the bulk paraelectric BaO and $BaTiO_3$ bulk constrained in-plane to the lattice constant of $SrTiO_3$ (3.84 Å).

Allowing the out-of-plane ferroelectric instability of $BaTiO_3$ to relax gives rise to a ferroelectric ground state with a spontaneous polarization of 38 μC.cm^{-2} and a relaxed out-of-plane cell parameter of 4.07 Å. The difference of energy between the ferroelectric ground state and the paraelectric reference is ΔE=16 meV which corresponds to the depth of the double well associated to the evolution of the potential energy with the polarization (Figure 6.2). This double well can be described with the following expression:

$$U_1(P_1) = a_1 P_1^2 + b_1 P_1^4 + c_1 P_1^6, \tag{6.2}$$

where a$_1$, b_1 and c_1 are the parameters and P_1 is the out-of-plane polarization. The sixth order term was needed to ensure better agreement of the fit with the first-principles data. In principle, determining $U(P)$ would require calculation at constrained P as proposed in Ref. [103]. Here we used a more approximate but still reasonable approach. The Eq. (6.2) was fitted by freezing different fractions of the pattern of atomic displacements ξ_1 coming from the relaxed ground state structure with a polarization of 38 μC.cm^{-2}. The relaxation of the out-of-plane cell parameter is included in the internal energy by relaxing this cell parameter at each frozen fraction of ξ_1. The corresponding polarization is approximated by $P_1 = \frac{\sum_i \xi_{1i} Z_i^*}{\Omega}$, where ξ_{1i} is the displacement of atom i with respect to its high symmetric position, Z$_i^*$ its Born effective charge and Ω the volume of the unit cell.

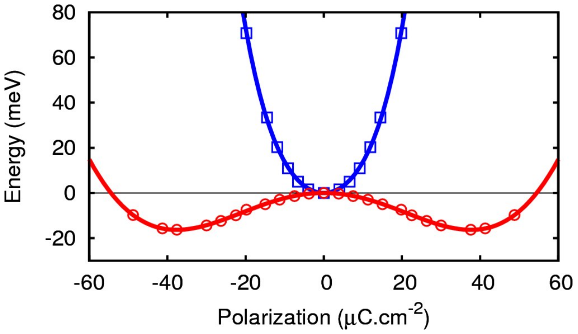

Figure 6.2: Energy as a function of spontaneous polarization for epitaxial bulks. The blue curve with squares corresponds to the tetragonal bulk BaO and the red curve with circles is the double well of tetragonal BaTiO$_3$ bulk. For each single point energy, the out-of-plane cell parameter is relaxed.

The only way to polarize BaO is within the subspace spanned by its TO modes. In the superlattice, the BaO layer is expected to be polarized by BaTiO$_3$ along the z direction and so the evolution of its associated internal energy U_2 was determined by freezing the pattern of displacements of the TO mode along the z direction given in Table 6.1. As for BaTiO$_3$ the out-of-plane cell parameter is relaxed for each amplitude of the frozen pattern of displacements. Since BaO is not ferroelectric, to polarize it has an energy cost and the shape of the internal energy corresponds to a single well (Figure 6.2) that can be approximated as follows:

$$U_2(P_2) = a_2 P_2^2 + b_2 P_2^4 \tag{6.3}$$

where a_2 and b_2 are the parameters and P_2 corresponds to the out-of-plane spontaneous polarization. Here again, a fourth order term has been included to achieve a better agreement in the fit of the energy which slightly deviates from the harmonic approximation at larger amplitude of polarizations. In Table 6.2 we report the values of the fitted parameters a_1, b_1, c_1, a_2 and b_2 in Equations 6.2 and 6.3.

a_1	b_1	c_1	a_2	b_2
-0.0239392	9.3690 10^{-6}	-4.37308 10^{-10}	0.122051	1.51357 10^{-4}

Table 6.2: Values of the fitted parameters a_1, b_1, c_1, a_2, b_2 of Eq. (6.2) and Eq. (6.3), where the polarization is in μC.cm^{-2} and the energy is in meV, giving rise to the curves of Figure 6.2.

Electrostatic energy cost

In ferroelectric/incipient-ferroelectric superlattices, we have shown in Chapter 5 that the incipient ferroelectric layer is polarized with the same spontaneous polarization as the ferroelectric layer, resulting in homogeneous polarization through the whole structure. Here, in the $BaTiO_3$/BaO superlattices, the BaO layer is less polarizable and is no more expected to have necessarily the same polarization than the $BaTiO_3$ layer. The polarization misfit will give rise to electric fields and produce an additional electrostatic energy cost. Assuming that both layers are homogeneously polarized, this electrostatic energy can be formulated as [Eq. (3.18)]:

$$E_{elec}(P_1, P_2) = C(P_1 - P_2)^2 \tag{6.4}$$

where C corresponds to the factor given in Eq. (3.19), which depends on the thicknesses of the BaO and $BaTiO_3$ layers. The thicknesses l_1 and l_2 of each layer can be approximated as follows: $l_1{=}m \times c_1$ and $l_2{=}n \times c_2$ with c_1 and c_2 being the out-of-plane cell parameters of respectively $BaTiO_3$ and BaO bulks at a given P_1 and P_2.

Total energy

Combining the previous results, the electrostatic model for $(BaTiO_3)_m/(BaO)_n$ superlattices, writes:

$$E(n, m, P_1, P_2) = m \times U_1(P_1) + n \times U_2(P_2) + C(n, m) \times (P_1 - P_2)^2. \tag{6.5}$$

For each periodicity m/n, the ground state of the superlattice can be estimated by minimizing the total energy Eq. (6.5) with respect to P_1 and P_2. In Table 6.3 we report the results of such minimization for a set of periodicities n/m. It is interesting to see that at a fixed number of BaO layers n, the model predicts a critical ratio $m/n \simeq 4.5$ beyond which the system becomes ferroelectric: 9/2, 17/4 and 25/6. For all of these ferroelectric states, the minimum of energy is reached when the polarization of the BaO layer is about 20% smaller than the polarization of the $BaTiO_3$ layer, giving rise to an electrostatic energy of the same order of magnitude than the internal energy. We notice that, considering the internal energy alone (*i.e.* assuming P_1=P_2 and E_{elec}=0), we can also predict a critical ratio $m/n \simeq 5$ to get a ferroelectric state (11/2, 21/4 and 31/6). This critical ratio coming from the pure internal energies is however larger than the critical ratio ($m/n \simeq$4.5) calculated with the electrostatic energy, meaning that the quantity of $BaTiO_3$ to get ferroelectricity in the superlattice is lowered by polarizing the BaO layer with a different amplitude than the $BaTiO_3$ layer, a situation distinct from that observed in ferroelectric/incipient-ferroelectric superlattices.

n	m	P_1	P_2	U	E_{elec}	E_{tot}
2	8	0.0	0.0	0.00	0.00	0.00
2	9	6.5	5.2	-2.13	1.76	-0.37
2	10	9.7	7.6	-6.16	4.26	-1.90
2	11	12.1	9.4	-11.87	7.33	-4.53
2	12	13.9	10.8	-18.75	10.58	-8.17
4	16	0.0	0.0	0.00	0.00	0.00
4	17	3.8	3.1	-1.25	1.16	-0.09
4	18	6.5	5.2	-4.26	3.52	-0.74
4	19	8.3	6.6	-8.08	6.09	-1.98
4	20	9.7	7.6	-12.32	8.52	-3.80
6	24	0.0	0.0	0.00	0.00	0.00
6	25	2.3	1.9	-0.64	0.62	-0.02
6	26	4.8	3.9	-3.16	2.80	-0.36
6	27	6.5	5.2	-6.39	5.28	-1.11
6	28	7.7	6.1	-9.83	7.57	-2.25

Table 6.3: Polarizations P_1 and P_2 (μC.cm^{-2}) minimizing the total energy of Eq. (6.5) for a range of n and m. The corresponding internal, electrostatic and total energies (respectively U, E_{elec} and E_{tot}, in meV) are also reported.

6.3.3 First-principles results

As a second step, we have performed DFT calculations in order to verify to which extent the prediction of the simple electrostatic model are verified.

Paraelectric reference

In its paraelectric reference state with space group *P4/mmm* (No 123), the in-plane (x,y) atomic positions in each layer corresponds to the bulk high symmetric positions. In the out-of-plane direction (z) a mirror symmetry plane is present in the center of each layer. Since in the z direction the atoms are not in their high symmetry positions, atomic relaxations take place, giving rise to rumpling distortions. We recover the previous first-principles results of Ref. [87], showing that the rumpling distortions are mainly localized at the interface between the layers and rapidly vanish in the center of thick enough layers. This interface effect in the superlattices involves also a modification of the interplanar distances between atomic planes with respect to those in the bulks but this effect is also strongly located at the interface between the two layers [87]. As shown in Table 6.4, this feature tends to compress the total out-of-plane cell parameter of the multilayer. In spite of the different periodicities considered, a constant deviation is calculated between the bulk references and the relaxed superlattices confirming the fact that the differences with respect to the bulks are mainly located at the interface between the two layers.

n	m	$c_{relaxed}$	c_{bulk}	deviation
2	2	13.43	13.50	-0.07
2	4	21.45	21.52	-0.07
2	6	29.46	29.54	-0.08
2	8	37.48	37.56	-0.08
4	2	18.91	18.98	-0.07
4	4	26.93	27.00	-0.07
4	6	34.95	35.02	-0.07
4	8	42.95	43.04	-0.09
4	10	50.99	51.06	-0.07

Table 6.4: Out-of-plane cell parameter c (Å) for a range of n, m thicknesses. c_{relax} represent the perpendicular cell parameter of the paraelectric relaxed case, c_{bulk} correspond to the sum of the corresponding bulk unit cell: $c_{bulk}{=}m\times c_{BT}+\frac{1}{2}\times n\times c_{BO}$. The last column represents the deviation between c_{bulk} and c_{relax} (Å).

Since the ferroelectric instabilities are strongly sensitive to the volume and pressure, the reduction of the out-of-plane thicknesses in the superlattices could strongly influence the out-of-plane ferroelectric soft mode for the smallest periodicities. For example, in the 2/2 periodicity, this reduction is equal to 0.07 Å with respect to the bulk reference, which corresponds to an equivalent pressure of about 1 GPa.

6.3.4 Zone center instabilities

For two fixed BaO thicknesses, n=2 and n=4, the evolution of the square of the frequency of the out-of-plane zone center ferroelectric soft mode (FE_z), calculated in the relaxed paraelectric references, is shown in Figure 6.3. This ferroelectric soft mode FE_z is strongly sensitive to the thickness of $BaTiO_3$ layer, which is expected since the ferroelectric instability is coming from $BaTiO_3$. As shown in Figure 6.3, the square frequency of the FE_z mode goes from high values at the smallest m and decreases linearly with increasing the quantity of $BaTiO_3$ for both n=2 and n=4 BaO thicknesses. Beyond a critical m/n periodicity, the

FE_z mode becomes unstable (negative ω^2): 7/2 and 9/4. This means that in spite of the non-ferroelectric character of BaO layer, the entire supercell can develop a ferroelectric instability when a critical ratio between m/n is reached.

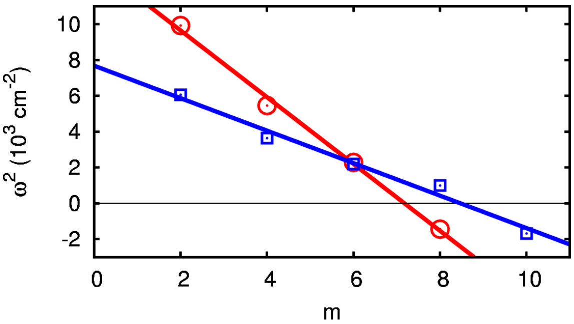

Figure 6.3: Square of the zone center phonon frequency for n=2 (red, circles) and n=4 (blue, squares) as a function of the $BaTiO_3$ thickness m.

This confirms the results predicted with the electrostatic model Eq. (6.5) but the critical periodicities at which the ferroelectricity appears are different and do not correspond to a constant ratio: 7/2 and 9/4 from the first-principles phonon calculations instead of 9/2 and 17/4 from the electrostatic model. Since the electrostatic model is built through the bulk mode eigendisplacements and the bulk Born effective charges (to estimate the polarization), the differences with the first-principles results could be first related to the modification of the dynamical charges and the eigendisplacements of the FE_z mode at the interface between BaO and $BaTiO_3$ layers.

To highlight the differences between the bulk and the superlattice we report the Born effective charges of individual atoms at the interface and in the middle of each layer in Table 6.5. In the middle of the BaO layer, the amplitude of the zz component of the Born effective charges are larger than their bulk values which is amplified when m increases and reduced when n increases. In the middle of $BaTiO_3$ the opposite take place: the amplitude of the Born effective charges are all smaller than in the $BaTiO_3$ bulk and tends to reach the bulk values when m increases while they are reduced when n increases. These global evolutions of the Born effective charges with n and m in the superlattices can be related to tendency to recover the BaO or $BaTiO_3$ bulk values when respectively n or m increase. For the O_1, Ti and and $O_{2/3}$ atoms at the interface, the same tendencies are observed for the Born effective charges than for the atoms in the middle of the $BaTiO_3$ layer but with larger deviations from the bulk amplitudes. The Born effective charges of the Ba atom at the interface increases with m and decreases with n, but reach values for large m higher than the BaO or the $BaTiO_3$ bulks. It results that the Born effective charges of the atoms in the superlattice are relatively different than those at the bulk level, mainly for the smallest periodicities m/n.

Since the Born effective charges of the atoms are modified, we can expect a modification in the mode polarity of the superlattice FE_z instability with respect

	2/2	4/2	6/2	8/2	2/4	4/4	6/4	8/4	Bulk
Ba	3.72	4.01	4.16	4.25	3.14	3.38	3.51	3.61	2.78
O	-3.10	-3.34	-3.46	-3.53	-3.15	-3.38	-3.53	-3.63	-2.78
Ba	2.65	2.84	2.95	3.02	2.50	2.69	2.79	2.87	
O_1	-3.75	-4.00	-4.17	-4.26	-3.53	-3.78	-3.95	-4.06	
Ti	5.11	5.51	5.73	5.85	4.83	5.20	5.43	5.58	
$O_{2/3}$	-1.68	-1.82	-1.88	-1.92	-1.59	-1.71	-1.78	-1.83	
Ba	2.32	2.41	2.50	2.55	2.20	2.28	2.38	2.44	2.77
O	-4.27	-4.59	-4.78	-4.88	-4.04	-4.37	-4.55	-4.67	-5.29
Ti	-	5.88	6.13	6.27	-	5.56	5.83	6.00	6.80
$O_{2/3}$	-	-1.86	-1.93	-1.97	-	-1.76	-1.83	-1.88	-2.14

Table 6.5: zz components of the Born effective charges (e) of atoms in the $BaTiO_3$/BaO superlattices with periodicity 2/2, 4/2, 6/2, 2/4, 4/4, 6/4, and 8/4. The two first lines refer the Ba and O atoms in the middle of the BaO layer, the lines 3-6 refer to the Ba, Ti and O atoms at the interface while the lines 7-10 refer to the Ba, Ti and O atoms in the middle of the $BaTiO_3$ layer.

to the bulk. To compare the evolution of the ferroelectric mode for different periodicities m/n, we report in the Figure 6.4 the evolution of the ratio between the oscillator strength and the volume of the unit cell (S/Ω_0, see Appendix B) for n=2 and n=4 with respect to m. This ratio S/Ω_0 increases strongly with m: it starts from values smaller than in bulk BaO at m=2 and then becomes rapidly larger than the BaO bulk value. At the considered thicknesses, S/Ω_0 is strongly smaller than for bulk $BaTiO_3$ but we can expect that it will reach the $BaTiO_3$ bulk value at large enough m.

The oscillator strength of one mode can be computed as follows:

$$S_{\alpha\beta} = \sum_{\kappa\alpha'} Z^*_{\kappa,\alpha\alpha'} \left(\eta_{\kappa\alpha'}\right)^* \sum_{\kappa'\beta'} Z^*_{\kappa',\beta\beta'} \, \eta_{\kappa'\beta'}. \tag{6.6}$$

where Z^*_κ are the individual atomic Born effective charge tensors and η is the phonon eigendisplacement vector. It is clear here that the modification of the ratio S/Ω_0 comes either from a modification of the Born effective charge and/or from a modification of the eigenvector η. As shown in Table 6.5, the Born effective charges tends to increase smoothly with m and cannot be responsible to the strong modification of S/Ω_0 shown in Figure 6.4.

In Figure 6.4 (bottom) we report the evolution of the square of the norm of the eigenvector η^2 with respect to m. Here, η^2 increases strongly with m, which can be related to a strong modification of the ferroelectric eigenvector η when m increases. Therefore, according to Eq. (6.6), the evolution of the ratio S/Ω_0 can mainly be attributed to the modification of the ferroelectric eigenvector when m is modified.

This analysis points out that the simple electrostatic model based on the bulks that we have developed can fail to reproduce the first-principles results

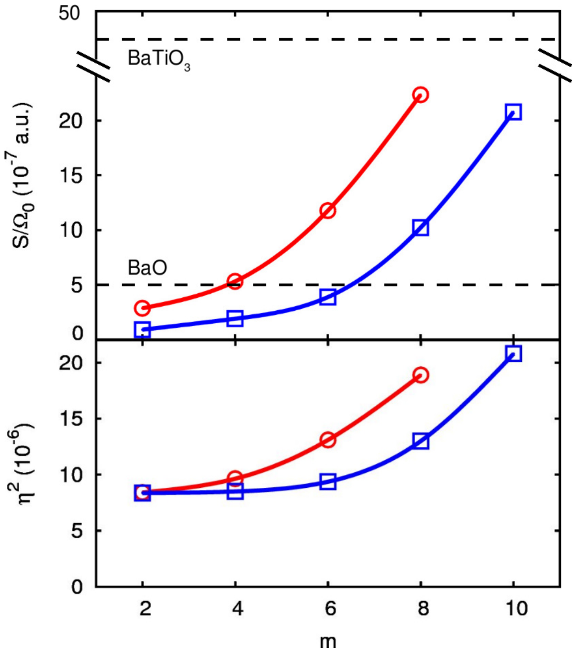

Figure 6.4: Evolution of the ratio S/Ω_0 (top) and $\eta^2 = \sum_\kappa \eta^*_\kappa \eta_\kappa$ (bottom) of the ferroelectric soft mode for n=2 (red, circles) and n=4 (blue, squares) as a function of the BaTiO$_3$ thickness m. The horizontal dashed lines correspond to the BaTiO$_3$ and BaO bulk limit S/Ω_0 values which are respectively equal to 43 10^{-7} and 5 10^{-7} a.u.

because of a strong modification of the ferroelectric eigenvector in the superlattice for the smallest periodicities. This ferroelectric mode is strongly sensitive to the thickness of the $BaTiO_3$ layer in the superlattice and do not reach the $BaTiO_3$ bulk ferroelectric soft mode, even for the largest m/n considered.

6.3.5 Phonon dispersion curves

The phonon dispersion curves between Γ (0,0,0), X ($\frac{1}{2}$,0,0) and M ($\frac{1}{2}$,$\frac{1}{2}$,0) points were also calculated and the results are shown in Figure 6.5 for periodicities 2/2, 4/2 and 6/2. At the smallest thickness 2/2, no instability is present, neither at Γ, X nor M point. This confirms that the ground state of the 2/2 multilayer is the non-polar symmetric *P4/mmm* phase. However, for the 4/2 periodicity an instability appears at the X zone-boundary point with a frequency of 42i cm^{-1} and its presence is amplified for larger m, with a calculated frequency of 92i cm^{-1} for the 6/2. Moreover, at the M zone boundary point, a low frequency mode is also present for the 4/2 thickness of Figure 6.5. This mode becomes unstable for the 6/2 periodicity, but with an amplitude smaller than the instability at the X point. The branch responsible for the M point instability is the same than the one responsible for X point instability and its dispersion is flat between the X and M points while it shifts rapidly to the positive frequency when going from X or M point to the Γ point. Similar behaviors are also observed for the periodicities $m/4$. An X point instability is also observed for $m \geq 4$ and its amplitude is also amplified with m: 42i cm^{-1} for 4/4 and 91i cm^{-1} for 6/4. So, here also the zone boundary instabilities appear before the zone center ferroelectric instability.

To clarify the atomic motions related to the X point instability, we report a schematic picture of the eigendisplacements in Figure 6.6 for the 6/4 periodicity. Since the instability is located at the X point, atoms in consecutive cells along the [100] direction move out-of-phase. As we can see on Figure 6.6, these eigendisplacements can be decomposed into two components: polar distortions along the z direction alone for atoms along the Ti–O chains and in-plane motions alone for Ba and O atoms which are along the Ba–O chains parallel to the Ti–O chains. The amplitudes of these in-plane displacements are however strongly smaller than the out-of-plane displacements, meaning that the Ti–O distortions along the z direction dominate the total motions (blue-green color of the unstable branch at the X point in Figure 6.5). Moreover, on the two BaO atomic planes corresponding to the two mirror planes of symmetry in the z direction, the in-plane motions disappear entirely. Additionally, we can notice that the polar distortions along the z direction remain in the BaO layer but only for the atoms aligned with the Ti–O chain, in order to preserve the flow of large polarization currents along those chains.

Since in consecutive unit cells along the [100] direction the polar displacements are in the opposite directions, these X point instabilities are related to an *antiferroelectric* distortion. To highlight this phenomena, we report also in Figure 6.6 (right) schematic vectors showing the direction of main local dipolar moments. From this picture, it is clear that along the z directions we have antiferroelectric distortions, with alternating planes of up and down polarizations.

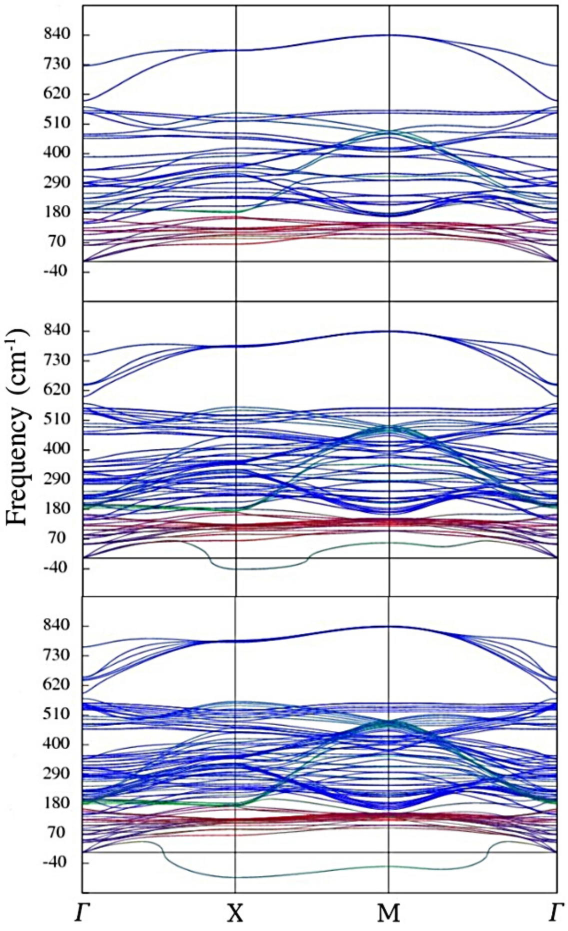

Figure 6.5: (Color on line) Phonon dispersion curves for m/n=2/2 (top), 4/2 (middle) and 6/2 (bottom). Color of curves are assigned according the the contribution of each chemical type of atom to the dynamical matrix eigenvector (red for Ba atom, green for Ti atom, blue for O atom).

For the in-plane Ba and O motions, the atoms move in the [100] direction alone giving rise to dipolar moments oriented along the x direction. Between the two plane of symmetries along the z direction, these in-plane dipolar moments are repeated in the z direction with the same orientation, but when going beyond these symmetry planes, the orientations are inverted. Interestingly, this inversion does not take place at the interface of the supercell but in the middle of each layer.

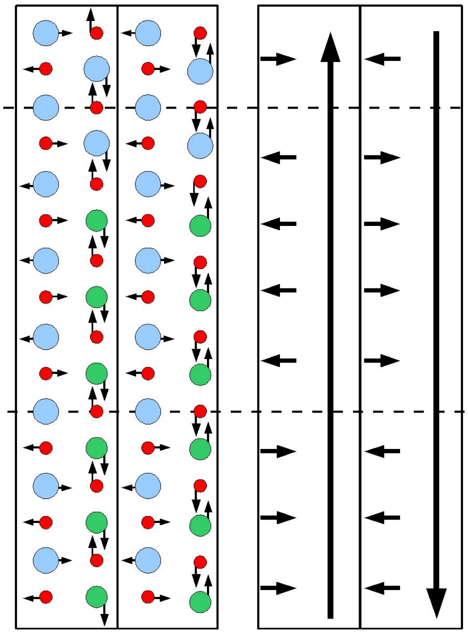

Figure 6.6: Left: atomic displacements of the X point unstable mode for the 4/6 thickness. The projection in the [201] plane is shown. Right: schematic representation of the direction of polarization resulting from local polar distortions.

If we analyse the dispersion of the unstable branch at the X point, we observe a rapid hardening from X to Γ for the 4/2 thickness. Nevertheless, this tendency decreases when m increases and goes closer to the Γ point. As shown in the previous section, a ferroelectric instability appears at 8/2 and so the X and M instabilities will coexist with this ferroelectric instability at the Γ point.

The evolution of the phonon dispersion curves of the $BaTiO_3/BaO$ superlattice can be explained in relationship with those of bulk $BaTiO_3$. As discussed in Chapter 2, $BaTiO_3$ exhibits a chain-like ferroelectric instability associated to modes similarly unstable at Γ, X and M. The ferroelectric mode at Γ is highly polar. Due to the difficulty to polarize BaO, in superlattice it will induce a huge depolarizing field that will strongly harden it. At the opposite, the zone-boundary ferroelectric modes, at X and M, are globally non-polar. They will therefore not induce any macroscopic depolarizing field and will keep a much stronger tendency to be unstable than the Γ mode. Consequently, the zone-boundary modes will always be more unstable than the Γ mode in the superlattice.

The evolution of the phonons instabilities in the superlattice can be summarized as follows. (i) For the smallest ratio m/n, the quantity of $BaTiO_3$ is not sufficient to polarize the BaO and the supercell remains a normal dielectric. (ii) For intermediate ratio m/n, the $BaTiO_3$ layer could polarize the BaO layer, but due to the strong cost of electrostatic energy coming from the depolarizing electric fields, the system becomes antiferroelectric, which is confirmed by the presence of the X point instability. (iii) When the critical ratio m/n to see the ferroelectric instability at Γ point is reached, we can expect the formation of ferroelectric domains of increasing size when m increases. (iv) When m>>n the superlattice should tend to be ferroelectric. Although the first two points have been demonstrated here, the last two should be further confirmed from full atomistic relaxations.

6.4 Conclusion

In this chapter we have studied the case of superlattices made when alternating a ferroelectric compounds, $BaTiO_3$ and an insulator, BaO. We first used an electrostatic model previously applied to ferroelectric/incipient-ferroelectric superlattices and which predicted that a ferroelectric state is possible in the whole superlattice if the quantity of $BaTiO_3$ is sufficiently important with respect to the quantity of BaO. However, comparing with the first-principles calculations, we have shown that the predicted critical ratios m/n to get ferroelectricty in the superlattice are overestimated in the electrostatic model. Moreover, the first-principles calculations of the phonon dispersion curves revealed that antiferroelectric instabilities are present at the zone boundary at critical ratios m/n lower than the ones for the ferroelectric instability. It results that the superlattice will go from a pure paraelectric state to an antiferroelectric state when m increases which was impossible to be predicted by the electrostatic model since it is built by taking into account only the ferroelectric instability at Γ.

We also extrapolated the possibility for the superlattices to generate ferroelectric multidomain structure when m becomes large with respect to n, but this should be further confirmed by performing full atomic relaxations

Finally, this study suggests that it might be interesting to explore the full phase diagram of ferroelectric/insulator superlattices to improve their use and optimize their eventual capabilities in high-κ engineering. Our results highlight again that taking into account the *whole* set of instabilities is mandatory to describe properly the physics of ferroelectric superlattices.

Chapter 7

Epitaxial AO oxide films and superlattices

7.1 Introduction

The alkaline earth AO oxides crystallize at ambient temperature and pressure in a highly symmetric cubic rock-salt structure. There are major constituents of the earth mantle and are widely used in the industry. Due to the simplicity of their structure and their technological importance, these oxides were intensively studied experimentally as well as theoretically to determine their electronic structure, elasticity, thermal properties as well as their equation of state [146–149]. MgO was the most widely studied [150–152] but CaO, SrO and BaO were also well characterized [146, 153–158].

Due to their potential interest for applications in microelectronics, many studies concerned AO oxide thin films and a lot of attention was devoted to the analysis of their affinity with silicon substrate: mismatch, coherence, band offset, *etc* [143, 159]. However, even if the pressure phase diagrams of AO oxides were intensively investigated, none of such phase diagrams were reported for epitaxial thin films.

In this chapter, we present a first-principles study of epitaxial BaO and SrO oxides as well as of an hypothetical superlattice made of the repetition of BaO and SrO oxide layers. The phonon analysis will allow us to identify the instabilities of these systems for a wide range of epitaxial strain and, in a second step, relaxing them to determine the related ground-states. These analysis will point out that epitaxial AO oxides can be made ferroelectric under an appropriate epitaxial strain. The dielectric properties and piezoelectric properties of these grounds states will be discussed and compared with those of the usual perovskite ferroelectric oxides.

7.2 Technical details

The main technical details are those given in Section 1.8. The epitaxial strain was imposed by fixing the in-plane lattice constant of the NaCl structure or equivalently the in-plane A-A distances d. The misfit strain is calculated using the A-A distance, $\eta = \frac{d-d_0}{d_0}$ where d_0 is the cubic A-A distance. To perform the structural relaxations, we considered a body centered tetragonal cell which consists in two A atoms respectively at (0, 0, 0) and ($\frac{1}{2}$,$\frac{1}{2}$,$\frac{1}{2}$) positions and two oxygens at ($\frac{1}{2}$,$\frac{1}{2}$,0) and (0,0,$\frac{1}{2}$) positions. The in-plane axis [100] and [010] are oriented along the A-A directions which corresponds to an in-plane cell parameter equal to d_0.

7.3 Epitaxial Bulk AO Oxides

7.3.1 Paraelectric references

The main properties of bulk BaO and SrO are summarized in Table 7.1. In their non-distorded cubic NaCl structure, we obtained a cell parameter of 5.463 Å (d_0=3.863 Å) for BaO and 5.044 Å (d_0=3.567 Å) for SrO which are similar to previous LDA results. The TO and LO modes at the Γ point are calculated respectively at 101 cm^{-1} and 402 cm^{-1} for BaO and 223 cm^{-1} and 479 cm^{-1} for SrO. These frequencies significantly underestimate the experimental results but are in agreement with previous LDA calculations on SrO oxides The same agreement is obtained for the Born effective charges ($|Z^*_{Ba,O}|$=2.81 e for BaO and $|Z^*_{Sr,O}|$=2.49 e for SrO) and for the electronic dielectric constant (ϵ^{∞}_{BaO}=4.69, ϵ^{∞}_{SrO}=3.90).

Under epitaxial strain, the constraint affects the out-of-plane cell parameter and the cell becomes tetragonal (space group *I4/mmm*, No 139). This tetragonality induces a split of the three-times degenerated cubic TO modes into a mode polarized along the [001] tetragonal axis, A$_{2u}$ (Figure 7.3 a), and a two-times degenerated mode with a polarization either along the [100] axis (Figure 7.3 b) or along the [010] axis (E$_u$ mode).

Let us consider BaO. Figure 7.1 shows the evolution of the A$_{2u}$ and E$_u$ frequencies with respect to a wide range of misfit strain. The results show that the TO modes are strongly sensitive to the misfit strain. For compressive in-plane strains (negative values) the E$_u$ frequency tends to increase smoothly whereas the frequency of A$_{2u}$ mode decreases strongly until it becomes imaginary for a critical misfit strain $\eta_c^z \simeq$-1.3% (left vertical line of Figure 7.1). The same behavior takes place for tensile epitaxial strains but here it is the E$_u$ mode that becomes unstable at $\eta_c^{xy} \simeq$1.8% (right vertical line of Figure 7.1). Since the mode effective charge associated to these TO modes is non zero, it means that its condensation will induce a spontaneous polarization into the crystal.

In Figure 7.2 we report the phonon dispersion curves for three different compressive misfit strains. For the smallest compression (-0.6%) no instability is present and the dispersion curves are similar to those of the cubic structure.

	present	previous LDA	exp.
BaO			
a_0	5.463	5.433^g	5.535^b
ω_{TO}	101		144^a
ω_{LO}	402		434^a
Z^*	2.81	2.72^b	$2.69/2.97^b$
ε^∞	4.38		3.83^f
ε_0	70		34^f
SrO			
a_0	5.044	5.101^c	5.159^c
ω_{TO}	223	210^c	224^d
ω_{LO}	479	476^c	485^d
Z^*	2.49	2.49^c	2.22^c
ε^∞	3.90	3.94^c	3.47^c
ε_0	18		13^e

[a] Reference [160]
[b] Reference [147]
[c] Reference [146]
[d] Reference [161]
[e] Reference [162]
[f] Reference [163]
[g] Reference [97]

Table 7.1: Cell parameter a_0 (Å), frequency ω of the TO and LO modes (cm^{-1}), amplitude of the Born effective charges Z^* (e) electronic dielectric constant (ε^∞) and static dielectric constant (ε_0) of the bulk BaO and SrO.

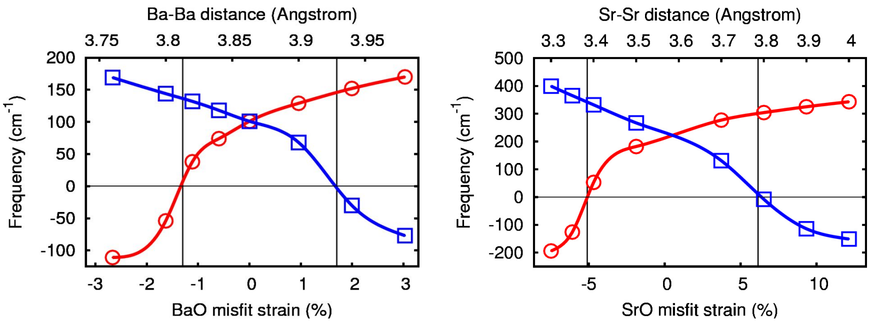

Figure 7.1: Frequencies of the A_{2u} (red circles) and E_u (blue squares) modes of BaO (left) and SrO (right) with respect to the misfit strain. Negative numbers correspond to imaginary frequencies. Top axis relates the corresponding in-plane A-A distances. The vertical lines give the position of η_c^z and η_c^{xy}.

For the intermediate misfit strain (-1.63%) we discover a zone center A_{2u} instability which is strongly localized around the Γ point. The unstable branch is strongly dispersive around Γ and becomes rapidly stable in any direction. Since in reciprocal space the instability is strongly localized in a small volume around Γ, in real space, the corresponding volume of correlation will be wide and isotropic. This Γ instability is preserved for larger in-plane compression (misfit strain of -2.63% in Figure 7.2) but with a larger amplitude. Here, however, a new instability, degenerated two times, also appears at the zone boundary (point $[\frac{1}{2}\frac{1}{2}0]$) which is strongly localized around this point. The amplitude of this zone-boundary instability is weaker than the A_{2u} instability and is related to polar distortion along the [001] direction with opposite orientation of the polarization in each successive plane along the [110] direction. This mode corresponds to an antiferroelectric distortion. A similar behavior is observed in the phonons dispersion curves for tensile epitaxial strain, with the progressive softening of the E_u mode at Γ and the softening of a zone boundary mode at the $[\frac{1}{2}00]$ point.

A similar global behavior is observed in SrO. Compressive (resp. tensile) epitaxial strain makes the A_{2u} (resp. E_u) mode softer and a critical misfit strain at which they become unstable also exists for the two modes (Figure 7.1 right). Since, at the bulk level, the cubic TO frequency of SrO has a higher frequency than the one of BaO, the calculated critical misfit strains are larger for SrO than for BaO: $\eta_c^z \simeq$-5.1% and $\eta_c^{x,y} \simeq 6.1\%$. In the next sections, the SrO results are not reported since the global behaviors are the same as for BaO, except that the transitions take place at critical misfit strains that are higher and too high to be experimentally imposed to coherent thin films.

7.3.2 Relaxed Structure

To predict the ground-state under high misfit strains, a full atomic relaxation is performed for each selected misfit strain exceeding the critical value. For compressive in-plane strain, the strongest instability correspond to polar distortions along the [001] direction (A_{2u}). Allowing for the condensation of this instability brings the system to a new ground-state, hereafter called c-phase, with a nonzero polarization along the [001] direction (P_z). The gain of energy with respect to the paraelectric reference (ΔE), the polarization (P) and the tetragonality c/a are reported in the Table 7.2. For the c-phase they are respectively 1.2 meV, 14 μC.cm^{-2} and 1.045 for a misfit strain of -1.63% and 21.7 meV, 29 μC.cm^{-2} and 1.080 for a misfit of -2.63%. These numbers are huge for an otherwise classical dielectric compounds and of the same amplitude than in usual ferroelectric like $BaTiO_3$ (P$\simeq$30 μC.cm^{-2}). Figure 7.4 shows the variation of energy with respect to the paraelectric reference when freezing a fraction of the polar atomic displacements (ξ) resulting from the atomic relaxation at a misfit strain of -2.63% (red circles curve). As imposed by symmetry, when the polarization is oriented up or down, the variation of energy is the same so that the energy displays a double-well shape which is typical of a ferroelectric compound. For comparison, the similar plot is shown for a case where no polar instability is

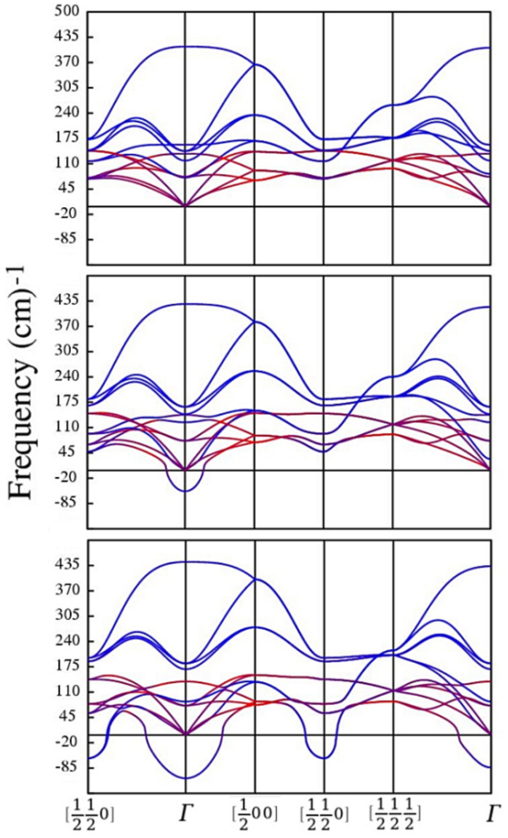

Figure 7.2: Phonon dispersion curves of BaO at a misfit strain of -0.6% (top), -1.63% (midle) and -2.63% (down). Color of curves are assigned according the the contribution of each chemical type of atom to the dynamical matrix eigenvector (red for Ba atom and blue for O atom).

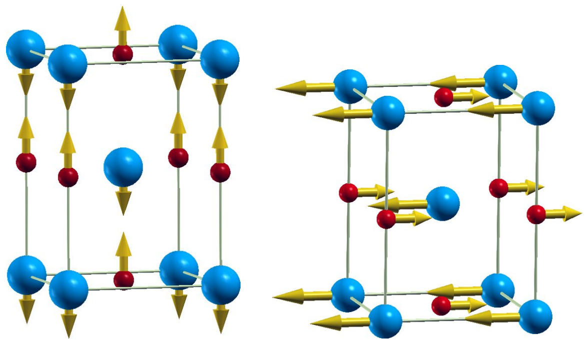

Figure 7.3: Unstable A_{2u} (a) and E_u (b) eigendisplacements.

present by freezing the A_{2u} eigendisplacements (misfit strain of -0.6% in Figure 7.4). Here a single-well shape is shown with no gain of energy when the compound is polarized along this mode. The absence of any another phonon instability in the polar phase confirms that the ground-state indeed corresponds to a ferroelectric state. As for the ferroelectric perovskites, the tetragonality is strongly modified by the polarization. Here also, the polarization tends to increase the tetragonality ($c/a=(c/a)_0+\alpha P^2$) of the structure with respect to the paraelectric reference and the change of c/a is continuous at η_c^z.

Misfit strain	phase	|P| (μC.cm^{-2})	ΔE (meV)	$(c/a)_0$	c/a
-2.66%	c	29	21.7	1.045	1.080
-1.63%	c	14	1.2	1.027	1.034
+1.99%	a	8	0.2	0.969	0.969
+2.51%	a	15	2.1	0.962	0.959
+3.03%	a	21	6.4	0.954	0.950

Table 7.2: Amplitude of the spontaneous polarization |P|, gain of energy ΔE with respect to the paraelectric reference (for 4 atoms in the cell), ratio between the out-of-plane and the in-plane cell parameter (Ba-O distances) of the paraelectric reference c/a_0 and of the ground-state c/a for five misfit strains where the c-phase or the aa-phase are stable.

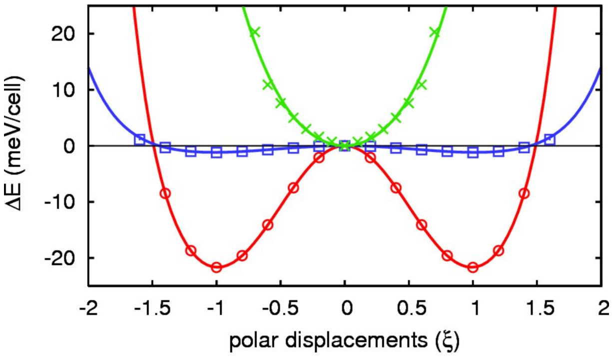

Figure 7.4: Energy as a function of out-of-plane polar displacements for epitaxial BaO. Green cross, blue squares and red circles correspond to a misfit strain of respectively -0.6%, -1.63% and -2.67%.

For tensile misfit strains two orientations are possible for the polarization since the polar instability is degenerated two times corresponding respectively to a polarization along the [100] direction or along the [010] direction. Performing full atomic relaxation and constraining the polarization either along the [100] direction, yielding a so-called a-phase (the [010] direction is equivalent by symmetry) or along to the [110] direction, yielding a so-called aa-phase, allows to decrease the energy of the system. However, the gain of energy with respect to the paraelectric reference is bigger in the a-phase where the polarization is oriented along [100] direction (P_x) than in the aa-phase where the polarization is in the [110] direction (P_{xy}). This results in a fundamental difference between the polar distortions in case of tensile and compressive misfit strains. As shown in Figure 7.1 a, the perpendicular polar P_z distortions are related to a motion of oxygen against barium along the Ba-O chains, while, in case of the a-phase (Figure 7.1 b), the oxygens also move against the bariums but along the Ba-Ba and O-O chains. The distortions of the aa-phase would have the same kind of displacements than the c-phase but the corresponding configuration is energetically less favorable than the a-phase. Except for this difference, the tensile polar aa-phase shows the same ferroelectric double well shape than in compressive in-plane strains. The value of the spontaneous polarization, depth of the double well and tetragonality are reported for the aa-phase in Table 7.2. For equivalent amplitude of strain, the spontaneous polarization and the depth of the double well are less important than for the c-phase but keep values comparable to typical perovskites. The modification of c/a with respect to the paraelectric $(c/a)_0$ is almost negligible with a tendency to decrease when the in-plane strain and P increase (α <0).

7.3.3 Dielectric constants and piezoelectric coefficients

The electronic dielectric constant ε^{∞}, the Born effective charges (Z*) and mode effective charges ($\bar{\text{Z}}^*$) are calculated and appear only slightly sensitive to the misfit strain. A maximum variation of ±2% on ε^{∞} and $\bar{\text{Z}}^*$ and ±5% on Z* with respect to their cubic values are observed for BaO in the range of epitaxial strain considered here.

Misfit strain	$\lvert\text{Z}^*_{xy}\rvert$	$\lvert\text{Z}^*_{z}\rvert$	$\varepsilon^{\infty}_{xy}$	ε^{∞}_{z}
-2.66%	2.93	2.69	4.45	4.34
-1.63%	2.88	2.74	4.42	4.36
-0.60%	2.83	2.78	4.39	4.38
+1.99%	2.71	2.90	4.32	4.41
+2.51%	2.69	2.92	4.30	4.41
+3.03%	2.67	2.94	4.29	4.42

Table 7.3: Amplitude of the Born effective charges (e) and electronic dielectric constant of the paraelectric reference of BaO under some epitaxial strains.

Figure 7.5.a shows the evolution of the three components ε_0^{xx}, ε_0^{yy} and ε_0^{zz} of the static dielectric tensor with respect to the misfit strain. At zero misfit strain, the dielectric tensor is isotropic since the three directions are equivalent in the cubic structure. Beyond this unconstrained point (positive and negative misfit strain), the zz component becomes different from the xx and yy components. Their values diverge around the η_c^z and η_c^{xy} critical misfit strains for respectively the zz component and the xx/yy components. However, for tensile in-plane

strains beyond η_c^{xy} the ε_0^{xx} and ε_0^{yy} differ which is related to the fact that the polar distortions relax along the x axis alone making the x and y direction different in the polar phase. These divergent static dielectric constants are usual at the approach of a ferroelectric phase transition as it can be understood from the softening of the polar mode as defined in Eq. 2.9 and highlighted from the linear evolution of $1/\varepsilon_0$ shown in Figure 7.5 b.

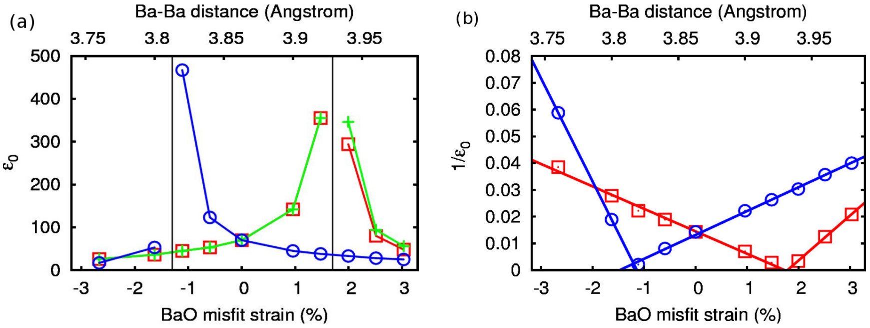

Figure 7.5: (a) BaO static dielectric constant ε_0 versus the misfit strain (ε_0^{xx} red squares, ε_0^{yy} green cross, ε_0^{zz} blue circles) and (b) $1/\varepsilon_0$ versus the misfit strain ($1/\varepsilon_0^{xx}$ red squares, $1/\varepsilon_0^{zz}$ blue circles). The vertical lines give the position of η_c^z and η_c^{xy}.

Since the system is non centro-symmetric beyond the critical misfit strains η_c, its piezoelectric response will be non-zero. In Table 7.4 we report the piezoelectric stress constant e_{ij} of BaO for selected misfit strain where the compound is ferroelectric. For negative misfit strains, in the P_z phase, the most important coefficient is e_{33}. This coefficient has a high value in epitaxial BaO, comparable to the one of ferroelectric perovskites like $PbTiO_3$ [68, 69, 164] and $BaTiO_3$ [70] or even PZT alloys [165, 166]. This value increases when approaching the critical misfit strain η_c^z and decreases when going away from η_c^z but keeping relatively high value. In case of tensile epitaxial strains, where the polarization is along the [100] axis (P_x), the piezoelectric constant e_{11}, e_{12}, e_{13} and e_{26} have high values. Here also, near to the critical misfit strain η_c^{xy}, these constants diverge [coherently with Eq. 2.12] and decrease when going away from η_c^{xy}.

7.4 BaO/SrO superlattice

A study similar to that of the previous section has been performed for a BaO/SrO superlattice built when alternating one layer of BaO and one layer of SrO along the [001] direction. The lattice mismatch between BaO and SrO is relatively large (∼7.7%). Such amplitude of misfit strain will strongly favor the formation of dislocations and will hamper the experimental growth of large period BaO/SrO superlattices with coherent strain. These dislocations have been experimentally studied for individual AO oxides thin films [167–170] and shown to have important effects for large mismatch even near to the interface with the

	-2.67%	-1.63%	1.99%	3.03%	$PbTiO_3$ [68]	$BaTiO_3$ [70]
e_{11}	0.00	0.00	**8.10**	**3.32**		
$e_{31}=e_{32}$	-0.82	-2.03	0.00	0.00	2.1	
e_{12}	0.00	0.00	**7.93**	**3.19**		
e_{13}	0.00	0.00	**-6.74**	**-2.56**		
e_{33}	**2.70**	**5.99**	0.00	0.00	5.0	3.64
$e_{24}=e_{15}$	-0.12	-0.10	0.00	0.00	4.4	
e_{35}	0.00	0.00	-0.01	-0.02		
e_{26}	0.00	0.00	**13.98**	**5.09**		

Table 7.4: Non-zero piezoelectric stress constants ($C.m^{-2}$) of epitaxial BaO.

substrate. However, it was possible to grow mixtures of BaO and SrO oxides experimentally on Si with good lattice matching [171] and so we can expect that short-period superlattice could be grown with good lattice matching even if the mismatch of the two individual bulks is strong.

The cell is built as reported in Section 7.2 with the difference that the two cations positions are now occupied by two different cations: Ba and Sr. In its paraelectric structure, the space group of the superlattice is *P4/mmm* No 123 with four atoms in the unit cell. The relaxed paraelectric structure has an in-plane cell parameter of 5.281 Å (A-A distance of 3.734 Å) and out-of-plane cell parameter of 5.275 Å (A-A distance of 3.730 Å) in agreement with Vegart's law. It is interesting to see that both in-plane and out-of-plane distances, are similar and are quite similar to the average between the BaO and SrO bulk cell parameters of 5.254 Å (A-A distance of 3.715 Å). In the following, all the misfit strains reported are calculated with respect to the relaxed in-plane cell parameter of the superlattice in its paraelectric phase.

The irreducible representation for phonons at the Γ point is $4A_{2u}\oplus 8E_u$ where the A_{2u} modes are polarized along the [001] direction of the superlattice and the E_u modes along an in-plane axis. The phonon dispersion curves of the BaO/SrO superlattice for an epitaxial strain of 0.70% is shown in figure 7.6.a. These dispersions are similar to those reported for epitaxial BaO in Figure 7.2. Instabilities are present at Γ point as well as at the zone boundary point [$\frac{1}{2}$ $\frac{1}{2}$ 0] and the Γ instabilities are the strongest. A main difference between BaO and the superlattice appears however for the ferroelectric instabilities at the Γ point: for compressive epitaxial strain, only the A_{2u} is unstable in BaO while both A_{2u} and E_u modes are unstable in the case of the superlattice. Moreover, looking at the evolution of these Γ instabilities with respect to the epitaxial strain as shown in Figure 7.6.b, for a range of epitaxial strains going from -0.24% to 1.58%, it appears that both A_{2u} and E_u modes are unstable and outside this range either A_{2u} or E_u are unstable. This strongly contrasts with the case of pure AO bulks where the A_{2u} and E_u modes are never unstable together, the regions in which they are respectively unstable being separated by a range of misfit strain without any instability. This difference with pure BaO and SrO makes the superlattice a priori even more interesting: whatever the in-plane strain, the superlattice is ferroelectric (at 0 K).

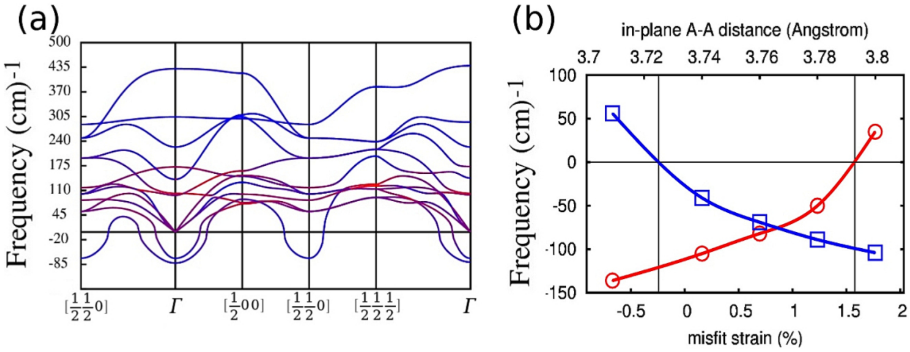

Figure 7.6: (a) Phonon dispersion curves of BaO/SrO superlattice at a misfit strain of 0.70%. The colors of curves are assigned as in Figure 7.2. (b) Frequencies of the A$_{2u}$ (red circles) and E$_u$ (blue squares) modes of BaO/SrO superlattice with respect to the misfit strain. Negative numbers correspond to imaginary frequencies. The top axis relates the corresponding in-plane A-A distances.

Since many instabilities are present together, to determine the ground-state of the BaO/SrO superlattice, we performed full atomic relaxations in different space groups corresponding to the symmetries allowing the condensation of the atomic displacements associated to each unstable mode. The in-plane strain was fixed while the out-of-plane cell parameter was relaxed with the atomic positions. For each new structure obtained, the presence of remaining unstable mode allowed us to determine if the ground-state is reached or not. If not, these remaining instabilities were relaxed until no instabilities were present in the structure. We found the following results: (*i*) for a compressive epitaxial strain, the frozen A$_{2u}$ mode gives the maximum gain of energy and the ground-state is ferroelectric with polarization along the out-of-plane direction (c-phase, space group *P4mm*, No 99); (*ii*) in a sharp region of tensile epitaxial strain, the ground-state corresponds to a phase where the polarization has a component in the in-plane direction and one in the out-of-plane direction giving rise to a small relaxation of the angle between the x and z axis (ac-phase, space group *Pm* No 6); (*iii*) for large tensile epitaxial strain, the superlattice is polarized in one in-plane direction only (a-phase, space group *Pmm2* No 25). As expected from the phonons analysis, the BaO/SrO superlattice displays always a ferroelectric ground-state for the considered range of epitaxial strain. Only the c, ac and a phases are found to correspond to a ground-state, while the cases where the polarization is oriented along xy or along xyz are never observed as being ground-state.

In Table 7.5 we report the amplitude of the spontaneous polarization, the gain of energy ΔE with respect to the paraelectric reference, the tetragonality and the static dielectric tensor of the ground-states of the BaO/SrO superlattice at five epitaxial strains. The amplitude of the spontaneous polarizations and the ΔE are comparable to the ones reported for BaO, with a reduction of their amplitudes in the intermediate ac phase, between the a and c states, instead of a complete disapearence of the ferroelectricity. Here also the tetragonality is amplified in the c phase with respect to the paraelectric tetragonality and decreases in the a phase while in the ac phase this tetragonality is slightly modified. At the misfit strain of 0.70% reported in Table 7.5, the ac phase gives a small deviation from 90 degree of the angle between the x and z axis of 0.15°. As for bulk BaO, the static dielectric constant diverges around the transitions between the a, ac and c phases with the difference that in the ac phase the dielectric tensor is slightly anisotropic due to the orientation of the polarization in both the x and z directions and to the slight deviation from 90° of the angle between these two axes. However, comparing the amplitudes of the static dielectric constant of BaO bulk and the BaO/SrO superlattice at the same distance from the critical misfit strains shows that these amplitudes are much smaller in the case of the superlattice than in the BaO bulk.

Misfit strain	Phase	|P| (μC.cm^{-2})	ΔE (meV)	(c/a)$_0$	c/a	ε_0^{xx}	ε_0^{yy}	ε_0^{zz}
-0.67%	c	17	16	1.009	1.024	43	43	17
-0.07%	c	12	8	1.000	1.010	86	86	20
0.70%	ac	12	3	0.988	0.990	59	82	34
1.23%	a	14	6	0.980	0.975	30	41	118
1.77%	a	16	12	0.972	0.966	26	34	47

Table 7.5: Amplitude of the spontaneous polarization |P|, gain of energy ΔE with respect to the paraelectric reference, ratio between the out-of-plane and the in-plane cell parameter (A-O distances) of the paraelectric reference c/a_0 and of the ground-state c/a and the xx, yy and zz components of the dielectric tensor (in the ac-phase, the eigenvalues of the dielectric tensor are reported) for five misfit strains where the c-phase or the aa-phase are stable.

To determine the critical epitaxial strain at which the transitions c-ac and ac-a phase occur, we built a model based on the parametrization of the energy as presented by King-Smith and Vanderbilt [73, 76] (KSV model). In this model, the contribution to the energy (per unit cell) is divided into three terms as follows:

$$E = E^{soft}\left(\{\xi_\alpha\}\right) + E^{elast}\left(\{\eta_i\alpha\}\right) + E^{int}\left(\{\xi_\alpha\},\{\eta_i\}\right) \qquad (7.1)$$

where E^{soft} is the contribution coming from the pure soft mode amplitudes $\{\xi_\alpha\}$, E^{elast} is the contribution coming from the pure strain $\{\eta_i\}$ and E^{int} is the contributions coming from the interaction between the strain and the soft modes. We have chosen the zero of the energy as being the energy of the unstrained paraelectric structure. The details of the energy decompositions are given in the Appendix A. This model allows to predict the ground-state of the system by minimizing the total energy Eq. 7.1 with respect to the variables and allows us to determine the critical epitaxial strains at which the transitions between the c, ac and a phases take place. We find that for a compressive misfit strain lower than 0.07%, the c phase corresponds to the ground-state of the superlattice, while for a tensile misfit strain larger than 1.15% the a phase is the ground-state. In the region of misfit strain between 0.07% and 1.15% the ac phase minimize the energy of the superlattice.

Since the polarization "rotates" between the c-phase to the a-phase when the misfit strain increases from compressive to large tensile epitaxial strain, we can expect a large piezoelectric response around the intermediate ac-phase. In Table 7.7, we report the piezoelectric stress tensor e_{ij} of the BaO/SrO superlattice at three misfit strains: one where the ground-state is the c-phase (-0.07%), one where the ground-state is the ac-phase (0.70%) and one where the ground-state is polarized in-plane, a-phase (1.23%). At -0.07%, only the piezoelelectric coefficients e_{33}, e_{24} and e_{15} have significant amplitudes, but comparatively to the epitaxial BaO bulk piezoelectric coefficients reported in Table 7.4, these amplitudes are small. For example, in BaO bulk, the e_{33} of the c-phase reach a value of 6.24 C.m^{-2} near to the phase transition while in the superlattice we obtain 2.74 C.m^{-2}. These differences could be related to a different divergence of the values with respect to the distance from the critical misfit strain. At 1.23% (a-phase), we observe similar results: the e_{11}, e_{12}, e_{13} and e_{26} piezoelectric coefficients are strongly smaller in the superlattice than in the epitaxial BaO bulk. For example, e_{26} is calculated to be 14.05 C.m^{-2} in the a-phase of BaO bulk near the phase transition while it is calculated to be 3.77 C.m^{-2} in the BaO/SrO superlattice. The e_{11} coefficient is equal to 8.02 C.m^{-2} in BaO bulk while it is equal to 1.91 C.m^{-2} in the superlattice. However, the e_{35} coefficient is negligible in the BaO bulk (-0.05 C.m^{-2}) while it is important in the BaO/SrO superlattice (-2.27 C.m^{-2}). At 0.70% (ac-phase), most of the piezoelectric coefficients are increased with respect to the ones of the a and c-phases of the superlattice. The e_{11}, e_{12}, e_{13}, e_{33} and e_{26} piezoelectric coefficients of the ac-phase are more than 50% larger than the corresponding non-zero coefficients of the a and c-phases. The e_{33} reaches a value similar to the ones reported for the tetragonal phase of PbTiO$_3$ [68, 69, 164] and BaTiO$_3$ [70]. The e_{31} and e_{32} coefficients of the ac-phase are doubled with respect to the ones reported for the c-phase but keep

-0.07% (c-phase)			0.70% (ac-phase)			1.23% (a-phase)		
0.00	0.00	**-0.84**	**3.29**	0.00	**-1.61**	**1.90**	0.00	0.00
0.00	0.00	**-0.84**	**3.22**	0.00	**-1.59**	**1.87**	0.00	0.00
0.00	0.00	**2.74**	**-3.92**	0.00	**4.49**	**-1.86**	0.00	0.00
0.00	**-1.43**	0.00	0.00	**-0.87**	0.00	0.00	0.00	0.00
-1.43	0.00	0.00	**-0.48**	0.00	**-0.31**	0.00	0.00	**-2.17**
0.00	0.00	0.00	0.00	**5.40**	0.00	0.00	**3.67**	0.00

Figure 7.7: Piezoelectric stress tensor e_{ij} (C.m^{-2}) of BaO/SrO superlattice at three misfit strains: -0.07%, 0.70% and 1.23%. The subscript i is going from 1 to 3 and corresponds to the subscript of columns in the tabular, while subscript j is going from 1 to 6 and correspond to the subscript of the lines.

relatively small values (~ 1.7 C.m^{-2}) with respect to the higher values of other coefficients. However, the e_{24}, e_{15} and e_{35} piezoelectric coefficients are strongly reduced with respect to their values in the a and c-phases. Nevertheless, as for the static dielectric constant, the large piezoelectric coefficients in the ac-phase of the superlattice never reach the giant values reported for the BaO bulk for the same misfit strain distances from the phase transitions.

7.5 Conclusion

In conclusion, we have proposed from first-principle calculations that BaO and SrO oxides, which are well known regular insulators, can be made ferroelectric under appropriate and moderate epitaxial strains. Out-of-plane and in-plane polar ferroelectric phases can be obtained for respectively compressive and tensile in-plane strain when the amplitude of misfit strain exceeds a critical value η_c. In the relaxed ferroelectric phase, the polarizations, dielectric and piezoelectric constants are strongly dependent of the strain and can reach values comparable to those of usual ferroelectric perovskites for experimentally achievable misfit strains.

Experimental evidence could be made to confirm these behaviors. Substrates could be selected in order to apply a sufficient in-plane constraint on BaO (or SrO) to observe a modification of its properties. If the experimental misfit strain is bigger than the critical value η_c, a ferroelectric phase with non-zero polarization and piezoelectric response should be observed. If the experimental strain is not large enough, the material will remain paraelectric but its dielectric constant should be strongly sensitive to strain as reported in Figure 7.5.

It is worth to notice however that since the calculated TO frequencies are underestimated in our calculations, the prediction of η_c will probably be also underestimated with respect to its experimental value. So, experimental values of η_c higher than the ones reported here should be expected but we believe that our global prediction (*i.e.* the possibility to induce ferroelectricity) should remain valid. Although it was not readily available when we performed the present study, improvements could be obtained by using the new GGA exchange correlation from Wu and Cohen [17] to give a better estimate of the volume as well as the PAW method [36, 172] which from our tests allows to give a better agreement on the TO frequencies in BaO.

In a second part, we have proposed to build an artificial superlattice by mixing BaO and SrO though the alternation of one atomic layer thickness of each compound. We have shown that, contrary to the BaO and SrO bulks, whatever the epitaxial strain the superlattice always displays ferroelectric instabilities. Depending on the amplitude of misfit strain, the calculated ground-states involve polarization either in-plane or out-of-plane like for BaO, but mixing in-plane and out-of-plane polarizations in an intermediate ac-phase. The analysis of the piezoelectric coefficients showed that they can reach values comparable to those in usual ferroelectric materials, but stay always smaller than the ones reported for epitaxial BaO.

Chapter 8

Ferroelectric nanowires

8.1 Introduction

In the previous chapters we focused on two-dimensional ferroelectric structures as thin films or superlattices. In the present chapter we study ferroelectric finite size effects in one-dimensional nanowires.

In the first part of this chapter, we investigate from first-principles DFT calculations the influence of lateral confinement on the ferroelectric properties of $BaTiO_3$ nanowires. A priori, the polarization could be perpendicular or parallel to the wire axis. In absence of external screening however, like for thin films in vacuum, polarization perpendicular to the wire axis and the lateral surfaces would produce large depolarizing field as discussed in Chapter 3 and is forbidden in practice[1]. In this part, we will restrict ourselves to discuss the existence of a ferroelectric distortions along the wire axis and will identify a critical diameter below which such distortion is totally suppressed. We will assign this behavior to surface atomic relaxation effects and will show that below the critical diameter, a ferroelectric state can be recovered under appropriate tensile strain conditions.

In the second part, the concept of ferroelectric correlation volume is reinvestigated through the use of the effective Hamiltonian techniques by considering barium titanate ($BaTiO_3$) as a prototypical example. The crucial role of the longitudinal interatomic coupling along Ti–O chains and the weak interchain interactions will also be discussed.

8.2 First-principles study of stoichiometric nanowires

8.2.1 The model systems

In this section, we focus on stoichiometric infinite $BaTiO_3$ nanowires. As illustrated in Figure 8.1, we consider model systems built from individual $BaTiO_3$

---

[1] However, it was shown in Ref.[173] that a perpendicular polarization to the surfaces can be sustained when polar molecules are present on the surface to screen the depolarizing field.

clusters that are assembled into infinite chains, themselves combined into wires of increasing diameters. These stoichiometric wires have two BaO and two TiO_2 lateral surfaces, as displayed in Figure 8.1(d). This asymmetry is responsible for a dipole perpendicular to the wire axis. However, it will not be further discussed since it is not relevant to the present study[2]. In what follows, we will focus on

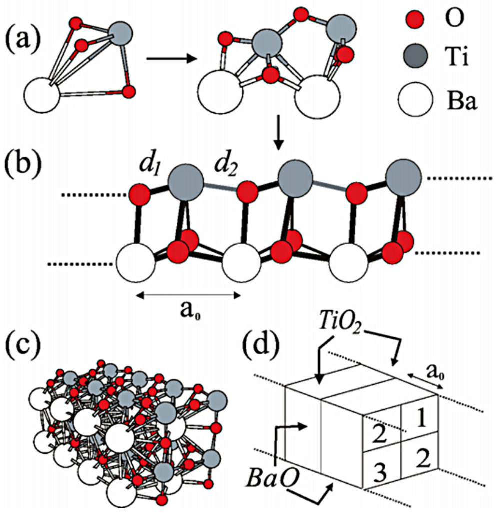

Figure 8.1: $BaTiO_3$ stoichiometric wires: $BaTiO_3$ clusters (a) assemble into infinite chains (b), themselves gathered into nanowires (c). The diameter of the nanowires is defined from the number of Ti–O chains (n) assembled together within the wire. Panels (c) and (d) correspond to $n = 4$.

the possible disappearance of the ferroelectric instability *along* the wire direction z. The equilibrium lattice parameter along z will be referred to as a_0, and the wire diameter will be specified by an integer n that corresponds to the number of Ti-O chains that are gathered together within the wire. The alternating Ti-O distances along z will be called d_1 and d_2, as shown in Figure 8.1(b).

8.2.2 Technical details

Our calculations have been performed within the local density approximation (LDA) to density functional theory (DFT) using a numerical atomic orbital method as implemented in the SIESTA code [33]. Technical details are similar to those of Ref. [87]. Some of the calculations have been double checked using the ABINIT package [9]. Periodic replicas of the wires are separated by more than 10 Å of vacuum. We explicitly checked that the replica of the wire generated by

---

[2] Similar calculations were performed for selected non-stoichiometric wires with full Ba-O and full TiO_2 coverage, yielding results similar to Figure 8.2 except that the crossing between a_c and a_0 curves was slightly shifted to larger (resp. smaller) cell parameters for BaO (resp. TiO_2) coverage.

	Ti-O_I	Ba-O_{II}	Ba-Ti	a_0
Wire	1.88	2.52	3.07	3.60
Bulk	1.97	2.78	3.41	3.94

Table 8.1: Interatomic distances and equilibrium lattice parameter a_0 along the wire axis, for the $n = 1$ wire. O_I (resp. O_{II}) refers to oxygen atoms along the Ti–O (resp. Ba–O) chains. Results for the bulk cubic paraelectric unit cell of $BaTiO_3$ are shown for comparison. Units in Å.

periodic boundary conditions is not affecting our results[3]. The atomic positions have been relaxed until the maximum component of the force on any atom is smaller than 0.01 eV/Å.

8.2.3 Critical diameter for ferroelectricity

For the thinnest wire ($n = 1$, Figure 8.1(b)) the bond lengths and the equilibrium lattice constant a_0 of the relaxed structure reported in Table 8.1 are significantly shorter than in bulk. This can be explained from the low coordination of the different atoms in the structure, the lack of some interactions being compensated by the strengthening of the the remaining bonds. The system remains insulating with a bandgap of 3.3 eV. The relaxed structure presents a plane of symmetry perpendicular to z ($d_1 = d_2$) and is therefore not spontaneously polarized along the wire direction, demonstrating that ferroelectricity has disappeared. However, imposing a tensile strain, we can recover a polar structural distortion along the Ti-O chains ($d_1 \neq d_2$) above a critical lattice constant $a_c = 4.05$ Å. This strain induced phase transition is second order. Above a_c, both $d_1 - d_2$ and the polarization, calculated from the Berry phase approach, [28, 174] increase smoothly with a_0.

The fully relaxed $n = 4$ wire, shown in Figure 8.1(c), is also non-polar along z. However, a_c has been reduced to 3.86 Å and a_0 is now larger (3.80 Å) as expected from the increase of the mean atomic coordination numbers with respect to the $n = 1$ wire. Figure 8.2 represents the evolution of a_0 and a_c for wires of increasing n. We observe that the difference, $a_c - a_0$, progressively decreases. A crossover between both curves is observed at $n_c = 9$, that corresponds to a diameter of 1.2 nm. Above n_c, unconstrained wires are ferroelectric whereas below this value, a spontaneous polarization only appears under tensile strain.

In Figure 8.2, a_c keeps a nearly constant value around 3.85 Å (except for $n = 1$) while the disappearance of the ferroelectric distortion at small sizes originates from the progressive decrease of a_0. The ferroelectric behavior of nanowires appears therefore to be monitored by the strong sensitivity of ferroelectricity to the unit cell volume, the latter affected by low coordination effects at free surfaces. As n increases, we recover a polar distortion, however, its amplitude only progressively increases as a_0 slowly evolves to its bulk value.

---

[3] To test the possible influence (especially in reason of the lateral dipole) of the artificial replica induced by the periodic boundary conditions, we repeated some calculations enlarging the vacuum regions up to 20 Å, without significant change in the results.

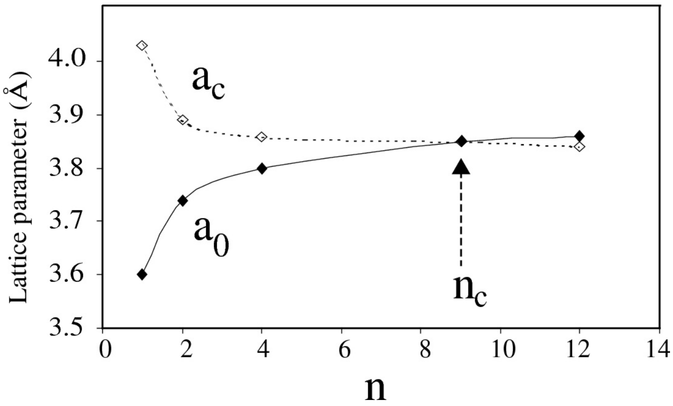

Figure 8.2: Evolution of a$_c$ (white diamonds) and a$_0$ (black diamonds) as a function of the number n of Ti–O chains in a transverse section of the wire.

Similarly, below n_c, a second-order phase transition to a polar state is observed under tensile strain, but the resulting polarization strongly depends on the lattice parameter. This is illustrated in Figure 8.3 for $n = 4$, where we quantify the polar distortion through the anisotropy of the interatomic distances $(d_2 - d_1)$ along the distinct Ti-O chains. This provides a qualitative measure of the contributions to the polarization of the individual chains since the Born effective charges (along z) are reasonably similar from one chain to the other (variations smaller than 20 %[4]). The strong inhomogeneity of the distortions for the different Ti-O chains highlights a deep influence of the surface: the ferroelectric distortion parallel to the wire surface is enhanced at TiO_2 surfaces and reduced around the BaO surfaces, a feature similar to what was previously reported for free-standing slabs [85]. Note that the transition to the polar state does not occur at the same lattice constant in the different chains, giving rise, within a given range of lattice constants, to mixed ferroelectric-paraelectric states in these nanosized systems.

The distinct behavior of the different Ti-O chains within the same wire suggests weak inter-chain interactions. This is further confirmed by the fact that the polarization of each chain can be reversed almost independently, with very small changes in the total energy of the system and in the amplitude of the polar displacements. It is the longitudinal coupling of the atomic displacements inside individual Ti–O chains that appears as the main origin of the ferroelectric distortion. This behavior is similar to what was previously discussed for the bulk [62] (see Chapter 2. In the phonon dispersion curves of $BaTiO_3$ [64], the unstable ferroelectric mode at Γ remains similarly unstable at X and M but *not* at R, pointing out a strong anisotropy of the interatomic force constants [62], a significant coupling of the atomic displacement along Ti–O chains, and the absence of strong interchain interactions. The resulting "chain-like" character of the ferroelectric instability is intrinsic to $BaTiO_3$. It is preserved in nanowires

---

[4] The Born effective charges along z for the four Ti in a section of the wire of Figure 8.1(c) are: $Z^*_{Ti1} = 5.10$ e, $Z^*_{Ti2} = 5.78$ e, $Z^*_{Ti3} = 5.93$ e (labels as in Figure 8.1(d))

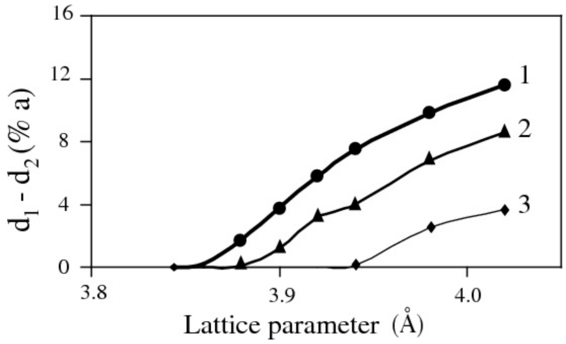

Figure 8.3: Local distortions as a function of the lattice parameter for the $n = 4$ wire. Labels of the chains as in Figure 8.1(d).

and provides a general argument to understand the survival of ferroelectricity along the wire axis down to very small radii. The situation might be different in other compounds such as $PbTiO_3$ in which the ferroelectric instability is more isotropic [64].

8.3 Ferroelectric correlation volume

8.3.1 General context

The previous discussion highlights that some correlation of the atomic displacements are required to produce the ferroelectric instability and motivate us to investigate in further details which minimum correlations are needed for a ferroelectric ground state to appear. In classical textbooks, the concept of *ferroelectric correlation volume*, V_c, was introduced and defined as the typical volume within which " near-neighbour-cell polar displacements ξ_i are strongly correlated in some sense" [1]. Since the parallel alignment of dipoles in a ferroelectric is primarily due, along the polar z-axis, to strong long-range DD interactions and, along a direction normal to this axis, to weaker SR forces (see Figure 8.4 a-b), the correlation volume is expected to be *highly anisotropic*. It is so usually viewed as a needle-shaped ellipsoid of size $l \times l \times L$ as illustrated in Figure 1c. Typical accepted values for ferroelectrics are $l \approx 1-2$ nm and $L \approx 10-50$ nm, leading to correlation volumes[5] $V_c \approx 10-100$ nm^3.

Although such estimate is plausible, reaching quantitative determination of V_c is not easy. Direct measurement of the correlation volume would be in principle possible by preparing ferroelectric nanostructures and studying the size evolution of the ferroelectric properties. This procedure is however complicated by the fact that, as discussed in Chapter 3, surface effects, epitaxial strains and electrical boundary conditions (such as screening of the depolarizing field) greatly influence the ferroelectric behavior. For instance, in ultrathin films between ideal metal electrodes [61], image dipoles into the metal restore artificially

---

[5] V_c concerns near neighbour motion and is a concept distinct from the correlation length. In particular it does not diverge at the phase transition.

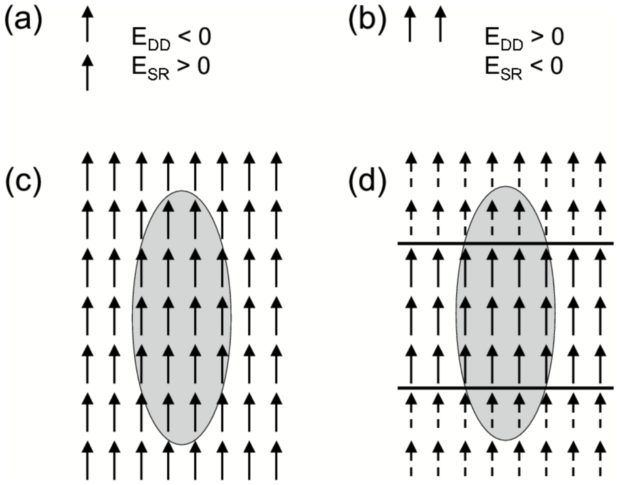

Figure 8.4: (a-b) Dipole-dipole (DD) and short-range (SR) contribution to the energy of a system made of two parallel dipoles aligned (a) along the polar z-axis or (b) along the normal to this axis: electrostatic DD interaction favors a ferroelectric order (parallel dipoles) along z but alone would produce an anti-ferroelectric order (anti-parallel dipoles) in the lateral configuration while the alignment of lateral dipoles in the ferroelectric state results from additional SR forces. (c) The schematic form of a needle-shape $l \times l \times L$ ferroelectric correlation volume. (d) An ultrathin ferroelectric film between metallic electrode : although the thickness $t < L$, image dipoles (dotted lines) into the metal restore an environment of dipoles identical to the bulk one for the DD interaction.

an electrostatic environment identical to that of the bulk (Figure 8.4 d) so that, even when the thickness $t < L$, the system can remain ferroelectric. This highlights that a crystal can remain ferroelectric even when its *physical* size is smaller than V_c. The correlation volume does therefore not define the physical size limit for ferroelectricity but should rather be viewed as a typical lengthscale at which ferroelectricity will become strongly sensitive to the boundary conditions.

Since the concept of correlation volume was previously introduced into different contexts with slightly different meanings, it is particularly important to start our discussion by stating clearly how it will be defined all along this section. In paraelectric $BaTiO_3$, like in other ferroelectric oxides, isolated atomic displacements cannot lower the energy of the crystal [64]: instead, cooperative atomic motions are needed to stabilize the ferroelectric distortion. In this context, we define here the correlation volume V_c as the smallest volume of an otherwise paraelectric crystal within which ferroelectric atomic displacements must be correlated in order to decrease the energy and produce a stable polar entity. Although there is some arbitrariness in this definition, it is a natural choice that corresponds to the most usual interpretation.

8.3.2 Technical details

Our calculations have been performed using a first-principles derived effective Hamiltonian for $BaTiO_3$ [77], with the formulation and parameters reported in Ref. [24]. This allows to calculate the evolution of the total energy when freezing a uniform polar distortion ξ (related to polarization $P = Z^*\xi/\Omega_0$, with Z^* the mode effective charge and Ω_0 the unit cell volume) along z into parallelepiped domains of increasing size ($l \times l \times L$) that are *embedded* into an otherwise paraelectric bulk environment. For a given $l \times l \times L$ domain, the total energy is calculated for different amplitude of the local mode ξ. From the curvature of the energy at $\xi = 0$, this allows to determine whether this polar entity is more stable than the paraelectric configuration. We use periodic boundary conditions and convergence was checked using cubic supercells of increasing size (from $18 \times 18 \times 18$ to $35 \times 35 \times 35$).

8.3.3 Discussion: the case of $BaTiO_3$

In agreement with first-principles DFT results [62], the smallest entity V_m found to be spontaneously ferroelectric is a $1 \times 1 \times 5$ chain-like volume that would thus correspond to the searched correlation volume V_c. However, if the lateral size l increases, the critical length L_c above which the ferroelectric state becomes stable surprisingly increases as well, showing that some volumes containing V_m are not ferroelectric themselves (for example $2 \times 2 \times 5$). Figure 8.5 a draws the limit between paraelectric and ferroelectric stable volumes as a function of l and L : it shows that L_c evolves almost linearly with l. From this graph, it appears clearly impossible to define a unique V_c; instead, the anisotropy of the correlations ($l/L \approx 0.25$) appears as the key parameter.

The dependence of V_c on the lateral size l seems paradoxical if the different chains behave independently as highlighted in the previous section from *ab initio* calculations performed on infinite nanowires [175]. To solve this apparent

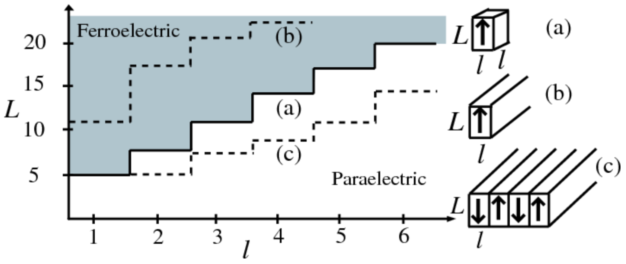

Figure 8.5: Solid line: phase boundary between paraelectric and z-polarized states for isolated $l \times l \times L$ parallelepiped domains (a) into an otherwise paraelectric matrix. Dashed line: the same phase boundary for isolated (b) and alternating (c) infinite $l \times \infty \times L$ stripe domains.

inconsistency, it is worth realizing that the weak inter-chain coupling is true only in the limit of infinite chains and does no more apply at small lengths: in the framework of the effective Hamiltonian, we can indeed decompose the energy into an *intra-chain* and an *inter-chain* contribution, each one being the sum of short-range and dipole-dipole terms. Figure 8.6 shows the evolution of the intra-chain and inter-chain parts of the total energy as a function of L, for the $2 \times 2 \times L$ domains. It appears that the inter-chain contribution, negligible at $L = \infty$, competes with the intra-chain one at small sizes and destabilizes the system, which explains why the ferroelectricity can be suppressed when enlarging the domain without increasing its length.

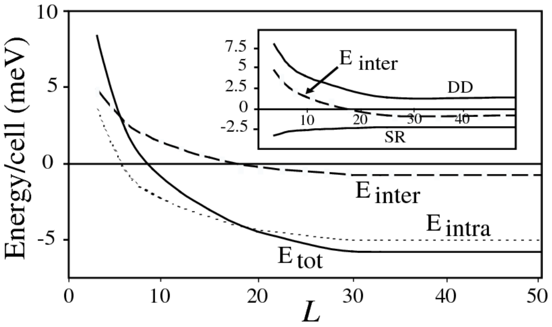

Figure 8.6: Change of energy (per cell) with respect to the paraelectric state when freezing the atomic soft mode displacement to 0.05 a_0 into $2 \times 2 \times L$ domains. The total energy (E_{tot}) is separated into its intra-chain (E_{intra}) and inter-chain (E_{inter}) parts. Inset: decomposition of E_{inter} into its electrostatic (DD) and short-range (SR) contributions.

We now turn to a more precise analysis of the inter-chain contribution to the energy. The evolution of this term cannot be deduced from pure electrostatic arguments but results from a delicate balance between short-range (SR) and dipole-dipole (DD) contributions (see Figure 8.6, inset). As a function of the length L, this term evolves from highly destabilizing to slightly stabilizing.

Indeed, the SR forces favor the alignment of lateral dipoles and are nearly independent of the length. At the opposite, the DD forces favor alternating chains and their contribution, destabilizing for any value of L, nevertheless decreases strongly when enlarging L. As a result, the energy cost for aligning lateral dipoles decreases with increasing lengths, explaining the absence of inter-chain coupling in infinite chains. More precisely this inter-chain term is positive, thus destabilizing, at short lengths, and negative (but much weaker than the intra-chain contribution) at large values of L.

The previous results might be useful to understand the shape and stability of polar nano-regions in relaxor materials. Moreover, they might provide a qualitative explanation to recent observations of a very fine stripe domain structure in thin/ultrathin ferroelectric films ($\infty \times \infty \times L$ on an *insulating* substrate [176, 177]. The extension of our results to the case of isolated and alternating $l \times \infty \times L$ stripe domains is reported in Figure 8.5 b, c. In absence of external screening, when L is constrained to the film thickness, only narrow polar regions can survive, and they become narrower as the thickness decreases. The appearance of alternating stripes allows to gain some energy (respect to an isolated domain) but l still scales linearly with L.

This linear scaling apparently differs from the well-known empirical Kittel's law according to which the film thickness should scale with the square of the domain size in any ferroic film ($L = \alpha l^2$) [178]. However, the comparison is not so straightforward : the FE limit of Figure 8.5 c represents, for a given thickness L, the stripe period for which the FE state becomes more stable than the uniform non-polar state. It does therefore not define the *optimal* stripe width l that will spontaneously appear and minimize the energy but provides the maximum threshold the period l cannot exceed at a given thickness L.

Alternating stripe domains have been recently reported in $BaTiO_3$ thin films [177]. It was highlighted that Kittel's law is respected in such systems over a wide range of thicknesses providing $L \approx 0.04 l^2$ for films thicker than 70 nm with polarizations parallel to the film surface and oriented along [110]. It was suggested that such a law could break down at small thikcnesses and indeed it is incompatible with our calculations :it suggest that domains of width $l = 5$ unit cells would still be stable in films one unit-cell thick (L=1) in contradiction with Figure 8.5.

Fong *et al.* [176], who studied ultrathin $PbTiO_3$ films, also observed the existence of alternating stripe domains, but with polarization perpendicular to the surface. In their case, Kittel's law was reproduced excepting at very small thickness, for which (i) the ferroelectric state disappears under a critical thickness of two monolayers, and (ii) the results deviate from Kittel's law when reaching very thin sizes [99]. This is more consistent with our calculation which shows a disappearance of the FE state below five lattice parameters (Figure 8.5 c), and illustrates the limit of Kittel's law when reaching very thin systems: for small enough thickness, the interchain contribution tends to become destabilizing and of the same order as the intrachain one, which can explain the deviation from Kittel's approach.

8.4 Conclusion

In the first part of this chapter, the ferroelectric behavior of infinite stoichiometric $BaTiO_3$ nanowires has been studied from first-principles. In $BaTiO_3$, the ferroelectric instability exhibits a marked "chain-like" character so that, in nanowires, it could a priori be preserved down to very small sizes. Nevertheless, at small radii, low atomic coordinations at the surface produce a contraction of the unit cell that is responsible for the suppression of the ferroelectric distortion at a critical radius estimated around 1.2 nm. Below this radius the ferroelectric distortion has disappeared at the equilibrium volume but can be recovered under appropriate tensile strain conditions.

In the second part, we have discussed the popular concept of ferroelectric correlation volume using an effective Hamiltonian. We have shown that V_c cannot be uniquely defined: the shape of polar regions in ferroelectrics is a more relevant criterion to discuss the stability of a polar phase. We have proposed to analyse the stability of a polar region in terms of intra-chain and inter-chain contributions. Our results also allowed to rediscuss the stripe domain structure of ultra-thin ferroelectric films on an insulating substrate. The situation would be different for films between metallic electrodes that partly screen the depolarizing field [97] as discussed in Chapter 3.

8.5 References

The results presented in this chapter have been discussed in the two following papers:

- G. Geneste, E. Bousquet, J. Junquera, Ph. Ghosez, Appl. Phys. Letters **88**, 112906 (2006).
- G. Geneste, E. Bousquet and Ph. Ghosez, Journal of Computational and Theoretical Nanoscience **5**, 517 (2008).

Conclusion

In the present thesis we presented a first-principles study of size effects in oxide thin films, superlattices and nanowires.

In Chapter 1 we briefly described the density functional theory formalism as well as the associated tools to extract physical properties in condensed mater simulations. Then, in Chapter 2 we showed their application to bulk $BaTiO_3$, $SrTiO_3$, $PbTiO_3$ and $CaTiO_3$ which allowed us to describe their two main structural instabilities: ferroelectric and antiferrodistortive. These two kinds of instabilities were described in terms of a delicate balance between short-range and long-range dipole-dipole interactions and we pointed out that these instabilities are in competition. In Chapter 3, these bulk characteristics were used as starting point for the discussion of the different parameters that influence the finite-size effects in ferroelectric nanostructures as thin films and superlattices. It resulted that, even if many issues still remain unclear, epitaxial strain and depolarizing electric field effects allow to understand the main ferroelectric finite size effects. We then analysed in Chapter 4 the effects of an isotropic pressure on the ferroelectricity of $BaTiO_3$ and pointed out that is totally suppressed at a given pressure but reappears beyond large enough pressure. In this chapter, we also analysed at the bulk level the effects of an epitaxial strain on the ferroelectric/antiferrodistortive phase diagram of $SrTiO_3$, $PbTiO_3$ and $CaTiO_3$ and showed that new combined phases can exist in these three compounds.

From Chapter 5 to the end, we presented the results obtained in finite-size elements: thin films, superlattices and nanowires. The case of ferroelectric/-incipient-ferroelectric superlattices allowed us to demonstrate in Chapter 5 that in the limit of ultra-thin thicknesses, new and unexpected properties with characteristics different from the parent compounds can occur through the interface between the composing layers. We demonstrated that a specific coupling between ferroelectric and antiferrodistortive structural instabilities at the layer interfaces yields improper ferroelectric behavior which was exemplified and experimentally confirmed in $PbTiO_3/SrTiO_3$ superlattices. We then discussed the possibility to reproduce the AFD/FE coupling in $PbTiO_3/CaTiO_3$ and $CaTiO_3/SrTiO_3$ superlattices and showed that even if $CaTiO_3$ exhibits FE and AFD instabilities, it is not a sufficient condition to have the improper ferroelectric ground-state.

In Chapter 6 we discussed the case of ferroelectric/insulator superlattices and showed that in the prototypical $BaTiO_3$/BaO case, the difficulty to polarize the insulator gave rise to the formation of antiferroelectric phase. We also extrapolated the possibility for the superlattices to generate ferroelectric multidomain structures when the thickness of the $BaTiO_3$ layer becomes large with respect to the thickness of the BaO layer.

Interestingly, we showed in Chapter 7 that playing with epitaxial strain, thin films of BaO and SrO oxides can be made ferroelectric without a mixing with a ferroelectric compound. Then, we showed that, whatever the epitaxial strain, superlattice build by alternating BaO and SrO oxides always display a ferroelectric ground state.

At last, in Chapter 8 we first presented the study of $BaTiO_3$ nanowires and showed that a ferroelectric polarization along the wire can be present for every thicknesses if appropriate tensile strain is applied. In a second part, we reinvestigated the concept of ferroelectric correlation volume and showed that a shape of polar regions in ferroelectrics is a more relevant criterion to discuss the stability of a polar phase.

Assembling the main conclusions of the present work would lead to the following outlines and perspectives. First, for the finite-size effects studies it appears mandatory to study the structural instabilities in the whole Brillouin-zone. Second, the emergence of unusual behaviors as a direct product of the interfaces in the artificially layered $PbTiO_3/SrTiO_3$ superlattices, suggests a promising new approach where the interface is used to tune and manage the material properties. Third, as shown with BaO and SrO oxides, producing ferroelectric phases in finite-size systems where no ferroelectric compound is used, open the door to the search of other unexpected candidates for ferroelectricty in non-ferroelectric oxides. Fourth, as shown with $PbTiO_3/SrTiO_3$ superlattices, first-principles calculations allow to clarify the “unexpected” experimental measurements and, as shown with BaO and SrO thin films and superlattices, to propose new possibilities for multifunctional materials. From these fruitful theory/experiment dialogues, a clear exciting benefit should be expected in the future.

Appendix A

KSV model for BaO/SrO superlattice

As discussed in Chapter 2, the King-Smith and Vanderbilt model (KSV) [73, 76] consist in a Taylor expansion of the total energy around the paraelectric reference with respect to the strain tensor components and the cartesian components of the eigendisplacements associated to the ferroelectric soft mode. Here we describe the application of such model to the strained BaO/SrO superlattice presented in Chapter 7. This approach allows to decrease the computational time to determine the phase diagram with respect to the epitaxial strain, mainly in the region where the polarization rotate in the x-z plane.

Under epitaxial conditions, the epitaxial cubic strain imposes η_1=η_2=η and η_6=0. We also restricted us to the case where the z components of the stress tensor vanish. Since the BaO/SrO superlattice has a tetragonal structure in its paraelectric reference structure, the x and y directions are equivalent but different to the z direction giving rise to a different treatment for the in-plane directions and the out-of-plane direction. Moreover, since in the BaO/SrO superlattice the cases where the polarization is oriented along the [110] direction or the [111] direction are never observed as being ground states and since the x and y directions are equivalent, we can restrict our model in two dimensional directions for the pattern of ferroelectric displacements: the x and z directions.

Taking the zero of the energy as being the energy of the unconstrained relaxed paraelectric structure, we can write the energy as follows:

$$E(\xi_x, \xi_z, \eta, \eta_3, \eta_5) = E^{FE}(\xi_x, \xi_z) + E^{E}(\eta, \eta_3, \eta_5) + E^{int}(\xi_x, \xi_z, \eta, \eta_3, \eta_5). \quad \text{(A.1)}$$

The E^{FE} is the energy coming from the ferroelectric displacements only and can be written as follows at the fourth-order:

$$E^{FE}(\xi_x, \xi_z) = a_1\xi_x^2 + b_1\xi_x^4 + a_3\xi_z^2 + b_3\xi_z^4 + b_{13}\xi_x^2\xi_z^2 \quad \text{(A.2)}$$

where ξ_x and ξ_z are the variables representing the ferroelectric pattern of displacements respectively in the x and z directions and a_1, a_3, b_1, b_3 and d_{13} are the coefficients of the allowed terms. The E^E is the elastic energy and can be written as follows:

$$E^E(\eta,\eta_3,\eta_5) = C_{11}\eta^2 + C_{33}\eta_3^2 + C_{55}\eta_5^2 + C_{13}\eta\eta_3 \tag{A.3}$$

where the C_{ij} are the parameters for the second-order strain expansion. The E^{int} corresponds to the energy coming from the interactions between the stain and the ferroelectric distortions and can be written as follows:

$$E^{int}(\xi_x,\xi_z,\eta,\eta_3,\eta_5) = g_{11}\eta\xi_x^2 + g_{33}\eta_3\xi_z^2 + g_{13}\eta\xi_z^2 + g_{31}\eta_3\xi_x^2 + g_{55}\eta_5\xi_x\xi_z \tag{A.4}$$

where the g_{ij} are the parameters of the interaction terms between the strain tensor components and the ferroelectric patern of displacements.

Minimizing the energy with respect to the η_3 and η_5 variables imposes:

$$\frac{\partial E}{\partial \eta_3} = 0 \tag{A.5}$$

$$\frac{\partial E}{\partial \eta_5} = 0. \tag{A.6}$$

It easily gives to the following solutions:

$$\eta_3 = -\frac{1}{2C_{33}}\left(C_{13}\eta + g_{33}\xi_z^2 + g_{31}\xi_x^2\right) \tag{A.7}$$

$$\eta_5 = -\frac{g_{55}}{2C_{55}}\xi_x\xi_z. \tag{A.8}$$

Substituting these expressions into Eqs. (A.2), (A.3) and (A.4) gives:

$$E^{FE} = a_1\xi_x^2 + B_1\xi_x^4 + a_3\xi_z^2 + B_3\xi_z^4 + B_{13}\xi_x^2\xi_z^2 \tag{A.9}$$

$$E^E = F_{11}\eta^2 \tag{A.10}$$

$$E^{int} = G_{11}\eta\xi_x^2 + G_{13}\eta\xi_z^2, \tag{A.11}$$

where the new coefficients are given by a combination of the initial coefficients from Eqs. (A.2), (A.3), A.4 and are as follows:

$$B_1 = b_1 - \frac{g_{31}^2}{4C_{33}} \tag{A.12}$$

$$B_3 = b_3 - \frac{g_{33}^2}{4C_{33}} \tag{A.13}$$

$$B_{13} = b_{13} - \frac{g_{33}g_{31}}{2C_{33}} - \frac{g_{55}^2}{4C_{55}} \tag{A.14}$$

$$F_{11} = C_{11} - \frac{C_{13}^2}{4C_{33}} \tag{A.15}$$

$$G_{11} = g_{11} - \frac{g_{13}C_{13}}{2C_{33}} \tag{A.16}$$

$$G_{13} = g_{13} - \frac{g_{33}C_{13}}{2C_{33}}. \tag{A.17}$$

Then, at a given epitaxial strain η the total energy can be expressed as follows:

$$E(\xi_x,\xi_z) = A_1\xi_x^2 + A_3\xi_z^2 + B_1\xi_1^4 + B_3\xi_z^2 + B_{13}\xi_x^2\xi_z^2 + F', \tag{A.18}$$

where the new coefficients are:

$$\begin{aligned} A_1 &= a_1 + G_{11}\eta \qquad &(A.19)\\ A_3 &= a_3 + G_{13}\eta \qquad &(A.20)\\ F' &= F_{11}\eta^2. \qquad &(A.21) \end{aligned}$$

With this simple model, we obtain accurate results for the paraelectric and the FE$_z$ phases but a less good agreement for the FE$_x$ phase. We find that this FE$_x$ phase is better described if we add 6th and 8th order terms in the expansion of the energy with respect to the ξ_x displacements:

$$E^{FE}(\xi_x, \xi_z) = a_1\xi_x^2 + b_1\xi_x^4 + c_1\xi_x^6 + d_1\xi_x^8 + a_3\xi_z^2 + b_3\xi_z^4 + b_{13}\xi_x^2\xi_z^2. \qquad (A.22)$$

Finally, 16 parameters must be fitted from the first-principles calculations. The paraelectric reference structure, the Born effective charges and the eigendisplacements ξ_x and ξ_z of respectively E$_u$ and A$_{2u}$ modes are given in Table A.1.

a$_0$	=	3.734	c$_0$	=	5.275
ξ_x(Ba)	=	5.149 10^{-4}	ξ_z(Ba)	=	1.621 10^{-4}
ξ_x(O$_1$)	=	-1.461 10^{-4}	ξ_z(O$_1$)	=	-5.4421 10^{-3}
ξ_x(Sr)	=	2.470 10^{-4}	ξ_z(Sr)	=	8.576 10^{-4}
ξ_x(O$_2$)	=	-5.6264 10^{-3}	ξ_z(O$_2$)	=	-6.463 10^{-4}
Z_x^*(Ba)	=	2.819	Z_z^*(Ba)	=	2.731
Z_x^*(O$_1$)	=	-2.889	Z_z^*(Ba)	=	-2.366
Z_x^*(Sr)	=	2.472	Z_z^*(Ba)	=	2.543
Z_x^*(O$_2$)	=	-2.402	Z_z^*(Ba)	=	-2.909

Figure A.1: Lattice parameters (Å), E$_u$ (ξ_x) and A$_{2u}$ (ξ_z) soft mode eigenvectors (in reduced coordinate, normalized to unity) and Born effective charges (e) of the paraelectric reference of BaO/SrO superlattice, calculated from first-principles.

Normalized values of the variables ξ_x, ξ_z, η, η_3 and η_5 were used to fit the model and the normalized references are reported in Table A.2.

According to these normalized variables, we found the fitted parameters reported in Table A.3.

Minimizing the total energy for a given epitaxial strain allows us to recover the sequence of transitions c-ac-a. In Figure A.4 we report the plot of the KSV model energies (plain lines) for the paraelectric state alone, the pure FE$_z$ and FE$_x$ phases (the out-of-plane strain being relaxed) and the minimum of energy calculated when all the variables are allowed to “relax”. To make a comparison of these energies with the first-principles calculations, the corresponding DFT single-point energies are also reported on the same plot (crux). The agreement between the energy coming from the KSV model and the DFT calculations is good for the considered range of epitaxial strain. However, some differences arise due to fact that the KSV model is based on a truncated Taylor expansion

variable	normalized	real
η	1	a = a_0+0.005 (Å)
η_3	1	c = c_0+0.01 (Å)
η_5	1	θ = 90+0.1 (degrees)
ξ_x	1	x(Ba) = ξ_x(Ba)
		x(O_1) = 0.5+ξ_x(O_1)
		x(Sr) = 0.5+ξ_x(Sr)
		x(O_2) = ξ_x(O_2)
ξ_z	1	z(Ba) = ξ_z(Ba)
		z(O_1) = ξ_z(O_1)
		z(Sr) = 0.5+ξ_z(Sr)
		z(O_2) = 0.5+ξ_z(O_2)

Figure A.2: Translation between the normalized parameters used in the model and the real parameters for the η, η_3, η_5, ξ_x and ξ_z variables of Eq. A.1. The ξ_x and ξ_z are given in terms of the reduced atomic positions of the atoms where the reduced atomic displacements ξ are those given in Table A.1. The normalization is such as the zero of η and η_3 corresponds respectively to a_0 and c_0, the zero of η_5 corresponds to 90 degrees, the zero of ξ_x and ξ_z corresponds to the high symmetric positions of the paraelectric reference.

a_1	=	-0.02027	C33	=	0.15291
a_3	=	-0.29623	C13	=	0.11323
b_1	=	0.00083	C55	=	0.02855
b_3	=	0.00507	g11	=	-0.01012
b_{13}	=	0.00043	g33	=	-0.03545
c_1	=	$1.67114\ 10^{-6}$	g13	=	0.01553
d_1	=	$2.39637\ 10^{-9}$	g31	=	0.00238
C_{11}	=	0.18350	g55	=	-0.00396

Figure A.3: Fitted coefficients of energy expansion Eqs. A.2-A.4 where the units correspond to the normalized variables reported in Table A.2.

around the relaxed paraelectric reference and so the errors are expected to grow as the strain and ferroelectric distorsions take away from the reference structure.

With this model, we find that the transition between c and ac phases occurs at a misfit strain of 0.07% and the transition between the ac and a phases occurs at a misfit strain of 1.15%.

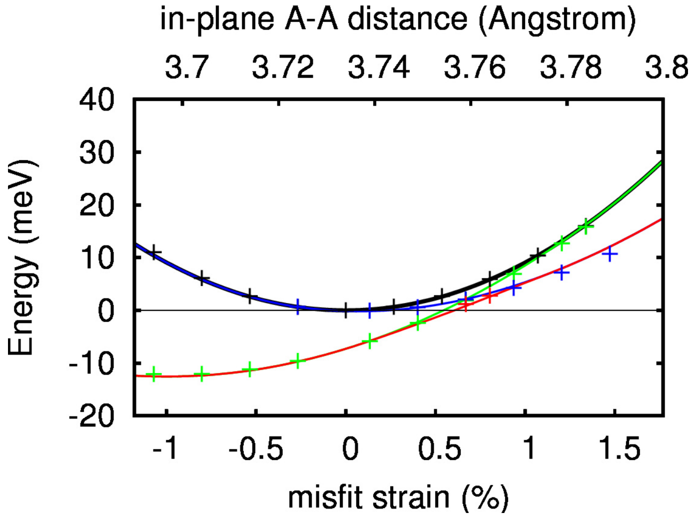

Figure A.4: Comparison of BaO/SrO energy curves from the KSV model (plain lines) and the energy coming from the direct DFT calculations (crux). Energies are relative to the relaxed paraelectric reference at zero misfit strain. The black color relates to the paraelectric energies, the green color relates the c phase, the blue color relates the a phase while the red line relates the minimum of energy coming from the model and the red crux relates the DFT energies in the ac phase.

Appendix B

Oscillator strength and mode effective charges

Following the definition of Ref.[23] the mode effective charge is define at Γ point as following:

$$\bar{Z}^*_\alpha(TO_i) = \frac{\sum_{\kappa,\beta} Z^*_{\kappa,\alpha\beta}\, \eta^{TO_i}_{\kappa,\beta}}{\langle \eta^{TO_i} | \eta^{TO_i} \rangle^{1/2}} \tag{B.1}$$

where Z^*_κ are the individual atomic Born effective charge and η^{TO_i} are the TO$_i$ phonon eigendisplacement vectors. However, this definition can not be used for supercells for the following reason. At the bulk level, if the unit cell is repeated j times, the mode effective charge for a given zone center mode must keep the same value for every j, since the mode is identical. However, from Eq.B.1 the mode effective charge will evolve as $\sqrt{j}$ since after renormalization of η^{TO_i} with the mass in the supercell, the numerator of Eq.B.1 evolves as $\frac{j}{\sqrt{j}}$ and the denominator stays the same. The use of this quantity is then tricky in case of superlattices where the unit cell is composed by a superposition of bulk unit cells.

As example, we report in Figure B.1 the thickness evolution of the mode effective charge of the ferroelectric soft mode of BaTiO$_3$/BaO superlattices discussed in Chapter 6. As we can see, the calculated mode effective charge of the ferroelectric instability increases with m and reach giant values (21 e for 8/2 periodicity and 22 e for 10/4 periodicity). However, these large mode effective charges are unphysical since for m=∞ the mode effective charge is infinite while it should tend toward the bulk BaTiO$_3$ mode effective charge.

The same artefact arises for the oscillator strengths:

$$S_{m,\alpha\beta} = \sum_{\kappa\alpha'} Z^*_{\kappa,\alpha\alpha'} \left(\eta^{TO_i}_{\kappa\alpha'}\right)^* \sum_{\kappa'\beta'} Z^*_{\kappa',\beta\beta'}\, \eta^{TO_i}_{\kappa'\beta'}. \tag{B.2}$$

which evolve as j, the number of bulk unit cell.

Nevertheless, these artefacts are not observed in the physical properties where the oscillator strength is mandatory like the static dielectric constant

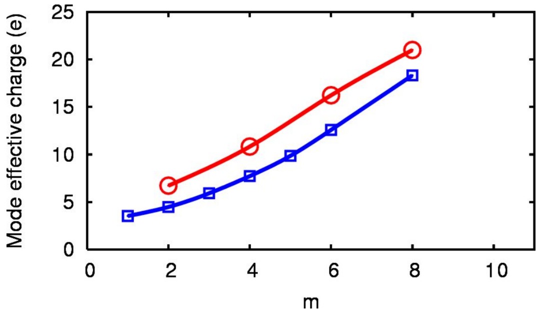

Figure B.1: Evolution of the mode effective charge of the ferroelectric soft mode of $(\mathrm{BaTiO_3})_m/(\mathrm{BaO})_n$ superlattices with respect to m. Red circles curve represents the thicknesses with n=2 and blue squares curve represents the thicknesses with n=4.

or in the LO-TO splitting [23]. For these physical properties, the artefact is compensated by the weighting of oscillator strength by the volume. Since the volume and the oscillator strength increase linearly with the number of unit cell j, the ratio $S_{m,\alpha\beta}/\Omega_0$, where Ω_0 is the volume of the supercell, is kept constant. For superlattices and supercell in general, the choice of the ratio $S_{m,\alpha\beta}/\Omega_0$ is then a quantity more significant than the oscillator strengths or mode effective charges for the discussions of the link between the eigenvectors and the Born effective charges.

List of Figures

List of Tables

Bibliography

[1] M. E. Lines and A. M. Glass, *Principles and applications of ferroelectrics and related materials* (Oxford, 1977), Clarendon Press edition.

[2] J. Valasek, *Piezo-electric and allied phenomena in rochelle salt*, Phys. Rev. **17**, 475 (1921).

[3] N. A. Spaldin, *Analogies and differences between ferroelectrics and ferromagnets*, in *Physcis of Ferroelectrics, A modern Perspective*, edited by K. Rabe, C. H. Ahn and J.-M. Triscone (Springer, 2007).

[4] J. F. Scott, *Ferroelectric Memories*, Advanced Microelectronics Series (Springer, 2000).

[5] T. Tybell, C. H. Ahn and J.-M. Triscone, *Ferroelectricity in thin perovskite films*, Appl. Phys. Lett. **75**, 856 (1999).

[6] C. H. Ahn, K. M. Rabe and J.-M. Triscone, *Ferroelectricity at the nanoscale: Local polarization in oxide thin films and heterostructures*, Science **303**, 488 (2004).

[7] P. Ghosez and J. Junquera, *First-principles modeling of ferroelectric oxide nanostructures*, in *Handbook of Theoretical and Computational Nanotechnology*, volume 9, edited by M. Rieth and W. Schommers, p. 623 (ASP, Stevenson Ranch, 2006).

[8] R. M. Martin, *Electronic Structure, Basic Theory and Practical Methods* (Cambridge University Press, 2004).

[9] X. Gonze, J.-M. Beuken, R. Caracas, F. Detraux, M. Fuchs, G.-M. Rignanese, L. Sindic, M. Verstraete, G. Zerah, F. Jollet, M. Torrent, A. Roy, M. Mikami, P. Ghosez, J.-Y. Raty and D. Allan, *First-principles computation of material properties: the ABINIT software project*, Computational Materials Science **25**, 478 (2002).

[10] R. P. Feynman, *Forces in molecules*, Phys. Rev. **56**, 340 (1939).

[11] O. H. Nielsen and R. M. Martin, *First-principles calculation of stress*, Phys. Rev. Lett. **50**, 697 (1983).

[12] P. Hohenberg and W. Kohn, *Inhomogeneous electron gas*, Phys. Rev. **136**, B864 (1964).

[13] W. Kohn and L. J. Sham, *Self-consistent equations including exchange and correlation effects*, Phys. Rev. **140**, A1133 (1965).

[14] D. M. Ceperley and B. J. Alder, *Ground state of the electron gas by a stochastic method*, Phys. Rev. Lett. **45**, 566 (1980).

[15] R. O. Jones and O. Gunnarsson, *The density functional formalism, its applications and prospects*, Rev. Mod. Phys. **61**, 689 (1989).

[16] J. P. Perdew, K. Burke and Y. Wang, *Generalized gradient approximation for the exchange-correlation hole of a many-electron system*, Phys. Rev. B **54**, 16533 (1996).

[17] Z. Wu and R. E. Cohen, *More accurate generalized gradient approximation for solids*, Phys. Rev. B **73**, 235116 (2006).

[18] O. Gunnarsson, M. Jonson and B. I. Lundqvist, *Descriptions of exchange and correlation effects in inhomogeneous electron systems*, Phys. Rev. B **20**, 3136 (1979).

[19] S. Baroni, S. de Gironcoli, A. Dal Corso and P. Giannozzi, *Phonons and related crystal properties from density-functional perturbation theory*, Rev. Mod. Phys. **73**, 515 (2001).

[20] X. Gonze and J.-P. Vigneron, *Density-functional approach to nonlinear-response coefficients of solids*, Phys. Rev. B **39**, 13120 (1989).

[21] X. Gonze, *Perturbation expansion of variational principles at arbitrary order*, Phys. Rev. A **52**, 1086 (1995).

[22] X. Gonze, *Adiabatic density-functional perturbation theory*, Phys. Rev. A **52**, 1096 (1995).

[23] X. Gonze and C. Lee, *Dynamical matrices, born effective charges, dielectric permittivity tensors, and interatomic force constants from density-functional perturbation theory*, Phys. Rev. B **55**, 10355 (1997).

[24] M. Veithen, X. Gonze and P. Ghosez, *Nonlinear optical susceptibilities, raman efficiencies, and electro-optic tensors from first-principles density functional perturbation theory*, Phys. Rev. B **71**, 125107 (2005).

[25] R. Resta, *Manifestations of Berrys phase in molecules and condensed matter*, J. Phys: Condens. Matter **112**, R107 (2000).

[26] R. Resta and D. Vanderbilt, *Theory of polarization: a modern approach*, in *Physcis of Ferroelectrics, A modern Perspective*, edited by K. Rabe, C. H. Ahn and J.-M. Triscone (Springer, 2007).

[27] R. M. Martin, *Comment on calculations of electric polarization in crystals*, Phys. Rev. B **9**, 1998 (1974).

[28] R. D. King-Smith and D. Vanderbilt, *Theory of polarization of crystalline solids*, Phys. Rev. B **47**, 1651 (1993).

[29] H. J. Monkhorst and J. D. Pack, *Special points for brillouin-zone integrations*, Phys. Rev. B **13**, 5188 (1976).

[30] D. R. Hamann, M. Schlüter and C. Chiang, *Norm-conserving pseudopotentials*, Phys. Rev. Lett. **43**, 1494 (1979).

[31] *Pseudopotential methods in condensed matter applications*, Computer Physics Report **9**, 115 (1989).

[32] M. Teter, *Additional condition for transferability in pseudopotentials*, Phys. Rev. B **48**, 5031 (1993).

[33] J. M. Soler, E. Artacho, J. D. Gale, A. García, J. Junquera, P. Ordejón and D. Sánchez-Portal, *The SIESTA method for ab initio order-N materials simulation*, J. Phys.: Condens. Matter **14**, 2745 (2002).

[34] E. Runge and E. K. U. Gross, *Density-functional theory for time-dependent systems*, Phys. Rev. Lett. **52**, 997 (1984).

[35] G. Onida, L. Reining and A. Rubio, *Electronic excitations: density-functional versus many-body Green's-function approaches*, Rev. Mod. Phys. **74**, 601 (2002).

[36] P. E. Blöchl, *Projector augmented-wave method*, Phys. Rev. B **50**, 17953 (1994).

[37] D. R. Hamann, X. Wu, K. M. Rabe and D. Vanderbilt, *Metric tensor formulation of strain in density-functional perturbation theory*, Phys. Rev. B **71**, 035117 (2005).

[38] K. A. Müller and H. Burkard, *$SrTiO_3$: An intrinsic quantum paraelectric below 4 K*, Phys. Rev. B **19**, 3593 (1979).

[39] V. Železný, E. Cockayne, J. Petzelt, M. F. Limonov, D. E. Usvyat, V. V. Lemanov and A. A. Volkov, *Temperature dependence of infrared-active phonons in $CaTiO_3$: A combined spectroscopic and first-principles study*, Phys. Rev. B **66**, 224303 (2002).

[40] C. Ang, A. S. Bhalla and L. E. Cross, *Dielectric behavior of paraelectric $KTaO_3$, $CaTiO_3$, and $(Ln_1/2Na_{1/2})TiO_3$ under a dc electric field*, Phys. Rev. B **64**, 184104 (2001).

[41] C. H. Perry and T. F. McNelly, *Ferroelectric "soft" mode in $KTaO_3$*, Phys. Rev. **154**, 456 (1967).

[42] G. A. Samara and B. Morosin, *Anharmonic effects in ktao3: Ferroelectric mode, thermal expansion,and compressibility*, Phys. Rev. B **8**, 1256 (1973).

[43] P. Hermet, M. Goffinet, J. Kreisel and P. Ghosez, *Raman and infrared spectra of multiferroic bismuth ferrite from first principles*, Physical Review B **75**, 220102 (2007).

[44] I. A. Kornev, S. Lisenkov, R. Haumont, B. Dkhil and L. Bellaiche, *Finite-temperature properties of multiferroic $BiFeO_3$*, Physical Review Letters **99**, 227602 (2007).

[45] D. J. Singh, *Structure and energetics of antiferroelectric $PbZrO_3$*, Phys. Rev. B **52**, 12559 (1995).

[46] M. D. Johannes and D. J. Singh, *Crystal structure and electric field gradients of $PbZrO_3$ from density functional calculations*, Physical Review B **71**, 212101 (2005).

[47] W. Cochran, *Crystal stability and the theory of ferroelectricity*, Adv. Phys. **9**, 387 (1960).

[48] R. M. Pick, M. H. Cohen and R. M. Martin, *Microscopic theory of force constants in the adiabatic approximation*, Phys. Rev. B **1**, 910 (1970).

[49] P. Ghosez, X. Gonze and J.-P. Michenaud, *Ab initio phonon dispersion curves and interatomic force constants of barium titanate*, Ferroelectrics **206**, 205 (1998).

[50] A. M. Glazer, *The classification of tilted octahedra in perovskites*, Acta Cryst. B **28**, 3384 (1972).

[51] C. J. Howard and H. T. Stokes, *Group-theoretical analysis of octahedral tilting in perovskites*, Acta Cryst. B **54**, 782 (1998).

[52] P. M. Woodward, *Octahedral tilting in peroskites, I geometrical considerations*, Acta Cryst. B **53**, 32 (1997).

[53] P. M. Woodward, *Octahedral tilting in peroskites, II structure stabilizing forces*, Acta Cryst. B **53**, 44 (1997).

[54] N. Sai and D. Vanderbilt, *First-principles study of ferroelectric and antiferrodistortive instabilities in tetragonal $SrTiO_3$*, Phys. Rev. B **62**, 13942 (2000).

[55] D. Vanderbilt and W. Zhong, *First-principles theory of structural phase transitions for perovskites: competing instabilities*, Ferroelectrics .

[56] A. García and D. Vanderbilt, *First-principles study of stability and vibrational properties of tetragonal $PbTiO_3$*, Phys. Rev. B **54**, 3817 (1996).

[57] S. A. T. Redfern, *High-temperature structural phase transitions in perovskite ($CaTiO_3$)*, Journal of Physics: Condensed Matter **8**, 8267 (1996).

[58] E. Cockayne and B. P. Burton, *Phonons and static dielectric constant in $CaTiO_3$ from first principles*, Phys. Rev. B **62**, 3735 (2000).

[59] W. Zhong and D. Vanderbilt, *Competing structural instabilities in cubic perovskites*, Phys. Rev. Lett. **74**, 2587 (1995).

[60] N. A. Pertsev, A. K. Tagantsev and N. Setter, *Phase transitions and strain-induced ferroelectricity in $SrTiO_3$ epitaxial thin films*, Phys. Rev. B **61**, R825 (2000).

[61] P. Ghosez, X. Gonze and J.-P. Michenaud, *Coulomb interaction and ferroelectric instability of $BaTiO_3$*, Europhys. Lett. **33**, 713 (1996).

[62] P. Ghosez, J.-P. Michenaud and X. Gonze, *Dynamical atomic charges: The case of ABO_3 compounds*, Phys. Rev. B **58**, 6224 (1998).

[63] W. Zhong, R. D. King-Smith and D. Vanderbilt, *Giant lo-to splittings in perovskite ferroelectrics*, Phys. Rev. Lett. **72**, 3618 (1994).

[64] P. Ghosez, E. Cockayne, U. V. Waghmare and K. M. Rabe, *Lattice dynamics of $BaTiO_3$, $PbTiO_3$, and $PbZrO_3$: A comparative first-principles study*, Phys. Rev. B **60**, 836 (1999).

[65] C. Lasota, C.-Z. Wang, R. Yu and H. Krakauer, *Ab initio linear response study of $SrTiO_3$*, Ferroelectrics .

[66] L. Bellaiche, *Piezoelectricity of ferroelectric perovskites from first principles*, Current Opinion in Solid State and Materials Science **6**, 19 (2002).

[67] E. Cockayne, *First-principles calculations of the dielectric properties of perovskite-type materials*, Journal of the European Ceramic Society **23**, 2375 (2003).

[68] G. Sághi-Szabó, R. E. Cohen and H. Krakauer, *First-principles study of piezoelectricity in $PbTiO_3$*, Phys. Rev. Lett. **80**, 4321 (1998).

[69] Z. Wu, G. Sághi-Szabó, R. E. Cohen and H. Krakauer, *Erratum: First-principles study of piezoelectricity in $PbTiO_3$ [Phys. Rev. Lett. 80, 004321 (1998)]*, Phys. Rev. Lett. **94**, 069901 (2005).

[70] M. Zgonik, P. Bernasconi, M. Duelli, R. Schlesser, P. Günter, M. H. Garrett, D. Rytz, Y. Zhu and X. Wu, *Dielectric, elastic, piezoelectric, electro-optic, and elasto-optic tensors of $BaTiO_3$ crystals*, Phys. Rev. B **50**, 5941 (1994).

[71] N. Choudhury, E. J. Walter, A. I. Kolesnikov and C.-K. Loong, *Large phonon band gap in $SrTiO_3$ and the vibrational signatures of ferroelectricity in $ATiO_3$ perovskites: First-principles lattice dynamics and inelastic neutron scattering*, Physical Review B (Condensed Matter and Materials Physics) **77**, 134111 (2008).

[72] K. M. Rabe and J. D. Joannopoulos, *Ab initio determination of a structural phase transition temperature*, Phys. Rev. Lett. **59**, 570 (1987).

[73] R. D. King-Smith and D. Vanderbilt, *First-principles investigation of ferroelectricity in perovskite compounds*, Phys. Rev. B **49**, 5828 (1994).

[74] W. Zhong, D. Vanderbilt and K. M. Rabe, *First-principles theory of ferroelectric phase transitions for perovskites: The case of* $BaTiO_3$, Phys. Rev. B **52**, 6301 (1995).

[75] U. V. Waghmare and K. M. Rabe, *Ab initio statistical mechanics of the ferroelectric phase transition in* $PbTiO_3$, Phys. Rev. B **55**, 6161 (1997).

[76] O. Diéguez, K. M. Rabe and D. Vanderbilt, *First-principles study of epitaxial strain in perovskites*, Phys. Rev. B **72**, 144101 (2005).

[77] W. Zhong, D. Vanderbilt and K. M. Rabe, *Phase transitions in* $BaTiO_3$ *from first principles*, Phys. Rev. Lett. **73**, 1861 (1994).

[78] L. D. Landau and E. M. Lifshitz, *Statistical Physics* (Mir, 1968).

[79] P. Chandra and P. Littlewood, *A Landau primer for ferroelectrics*, in *Physcis of Ferroelectrics, A modern Perspective*, edited by K. Rabe, C. H. Ahn and J.-M. Triscone (Springer, 2007).

[80] M. T. Dove, *Structure and Dynamics: An Atomic View of Materials*, Oxford Master Series in Condensed Matter Physics (Oxford University Press, 2002).

[81] L. Despont, C. Koitzsch, F. Clerc, M. G. Garnier, P. Aebi, C. Lichtensteiger, J.-M. Triscone, F. J. G. de Abajo, E. Bousquet and P. Ghosez, *Direct evidence for ferroelectric polar distortion in ultrathin lead titanate perovskite films*, Phys. Rev. B **73**, 094110 (2006).

[82] C. Bungaro and K. M. Rabe, *Coexistence of antiferrodistortive and ferroelectric distortions at the* $PbTiO_3$ *(001) surface*, Phys. Rev. B **71**, 035420 (2005).

[83] C. Lichtensteiger, J.-M. Triscone, J. Junquera and P. Ghosez, *Ferroelectricity and tetragonality in ultrathin* $PbTiO_3$ *films*, Phys. Rev. Lett. **94**, 047603 (2005).

[84] R. J. Nelmes and W. F. Kuhs, *The crystal structure of tetragonal* $PbTiO_3$ *at room temperature and at 700 K*, Solid State Communication **54**, 721 (1985).

[85] J. Padilla and D. Vanderbilt, *Ab initio study of* $BaTiO_3$ *surfaces*, Phys. Rev. B **56**, 1625 (1997).

[86] J. Padilla and D. Vanderbilt, *Ab initio study of* $SrTiO_3$ *surfaces*, Surface Science p. 64 (1998).

[87] J. Junquera, M. Zimmer, P. Ordejón and P. Ghosez, *First-principles calculation of the band offset at* $BaO/BaTiO_3$ *and* $SrO/SrTiO_3$ *interfaces*, Phys. Rev. B **67**, 155327 (2003).

[88] A. Munkholm, S. K. Streiffer, M. V. Ramana Murty, J. A. Eastman, C. Thompson, O. Auciello, L. Thompson, J. F. Moore and G. B. Stephenson, *Antiferrodistortive reconstruction of the* $PbTiO_3$*(001) surface*, Phys. Rev. Lett. **88**, 016101 (2001).

[89] K. M. Rabe, *Theoretical investigations of epitaxial strain effects in ferroelectric oxide thin films and superlattices*, Current Opinion in Solid State and Materials Science **9**, 122 (2005).

[90] K. J. Choi, M. Biegalski, Y. L. Li, A. Sharan, J. Schubert, R. Uecker, P. Reiche, Y. B. Chen, X. Q. Pan, V. Gopalan, L.-Q. Chen, D. G. Schlom and C. B. Eom, *Enhancement of ferroelectricity in strained* $BaTiO_3$ *thin films*, Science **306**, 1005 (2004).

[91] J. H. Haeni, P. Irvin, W. Chang, R. Uecker, P. Reiche, Y. L. Li1, S. Choudhury, W. Tian, M. E. Hawley, B. Craigo, A. K. Tagantsev, X. Q. Pan, S. K. Streiffer, L. Q. Chen, S. W. Kirchoefer, J. Levy and D. G. Schlom, *Room-temperature ferroelectricity in strained* $SrTiO_3$, Nature **430**, 758 (2004).

[92] O. Diéguez, S. Tinte, A. Antons, C. Bungaro, J. B. Neaton, K. M. Rabe and D. Vanderbilt, *Ab initio study of the phase diagram of epitaxial* $BaTiO_3$, Phys. Rev. B **69**, 212101 (2004).

[93] N. A. Pertsev, A. G. Zembilgotov and A. K. Tagantsev, *Effect of mechanical boundary conditions on phase diagrams of epitaxial ferroelectric thin films*, Phys. Rev. Lett. **80**, 1988 (1998).

[94] V. B. Shirokov, Y. I. Yuzyuk, B. Dkhil and V. V. Lemanov, *Phenomenological theory of phase transitions in epitaxial* $BaTiO_3$ *thin films*, Phys. Rev. B **75**, 224116 (2007).

[95] B.-K. Lai, I. A. Kornev, L. Bellaiche and G. J. Salamo, *Phase diagrams of epitaxial* $BaTiO_3$ *ultrathin films from first principles*, Appl. Phys. Lett. **86**, 132904 (2005).

[96] C. Ederer and N. A. Spaldin, *Effect of epitaxial strain on the spontaneous polarization of thin film ferroelectrics*, Phys. Rev. Lett. **95**, 257601 (2005).

[97] J. Junquera and P. Ghosez, *Critical thickness for ferroelectricty in perovskite ultrathin films*, Nature **422**, 506 (2003).

[98] I. Ponomareva, I. I. Naumov, I. Kornev, H. Fu and L. Bellaiche, *Atomistic treatment of depolarizing energy and field in ferroelectric nanostructures*, Physical Review B **72**, 140102 (2005).

[99] S. K. Streiffer, J. A. Eastman, D. D. Fong, C. Thompson, A. Munkholm, M. V. Ramana Murty, O. Auciello, G. R. Bai and G. B. Stephenson, *Observation of nanoscale* 180° *stripe domains in ferroelectric* $PbTiO_3$ *thin films*, Phys. Rev. Lett. **89**, 067601 (2002).

[100] C. Lichtensteiger, M. Dawber and J.-M. Triscone, *Ferroelectric size effects*, in *Physcis of Ferroelectrics, A modern Perspective*, edited by K. Rabe, C. H. Ahn and J.-M. Triscone (Springer, 2007).

[101] V. Nagarajan, J. Junquera, J. Q. He, C. L. Jia, R. Waser, K. Lee, Y. K. Kim, S. Baik, T. Zhao, R. Ramesh, P. Ghosez and K. M. Rabe, *Scaling of structure and electrical properties in ultrathin epitaxial ferroelectric heterostructures*, Journal of Applied Physics **100**, 051609 (2006).

[102] M. Dawber, C. Lichtensteiger, M. Cantoni, M. Veithen, P. Ghosez, K. Johnston, K. M. Rabe and J.-M. Triscone, *Unusual behavior of the ferroelectric polarization in $PbTiO_3/SrTiO_3$ superlattices*, Phys. Rev. Lett. **95**, 177601 (2005).

[103] N. Sai, K. M. Rabe and D. Vanderbilt, *Theory of structural response to macroscopic electric fields in ferroelectric systems*, Phys. Rev. B **66**, 104108 (2002).

[104] J. B. Neaton and K. M. Rabe, *Theory of polarization enhancement in epitaxial $BaTiO_3/SrTiO_3$ superlattices*, Appl. Phys. Lett. **82**, 1586 (2003).

[105] I. A. Kornev, L. Bellaiche, P. Bouvier, P.-E. Janolin, B. Dkhil and J. Kreisel, *Ferroelectricity of perovskites under pressure*, Phys. Rev. Lett. **95**, 196804 (2005).

[106] G. A. Samara, T. Sakudo and K. Yoshimitsu, *Important generalization concerning the role of competing forces in displacive phase transitions*, Phys. Rev. Lett. **35**, 1767 (1975).

[107] R. Cohen, *Origin of ferroelectricity in perovskite oxides*, Nature **358**, 136 (1992).

[108] I. A. Kornev and L. Bellaiche, *The nature of ferroelectricty under pressure*, Phase Transitions **80**, 380 (2007).

[109] P. Ghosez, X. Gonze, P. Lambin and J.-P. Michenaud, *Born effective charges of barium titanate: Band-by-band decomposition and sensitivity to structural features*, Phys. Rev. B **51**, 6765 (1995).

[110] R. E. Cohen and H. Krakauer, *Electronic structure studies of the differences in ferroelectric behavior of $BaTiO_3$ and $PbTiO_3$*, Ferroelectrics **136**, 65 (1992).

[111] X. Gonze, J.-C. Charlier, D. Allan and M. Teter, *Interatomic force constants from first principles: The case of α-quartz*, Phys. Rev. B **50**, 13035 (1994).

[112] C.-H. Lin, C.-M. Huang and G. Y. Guo, *Systematic ab initio study of the phase diagram of epitaxially strained $SrTiO_3$*, Journal of Applied Physics **100**, 084104 (2006).

[113] L. Kim, J. Kim, U. V. Waghmare, D. Jung and J. Lee, *Structural transition and dielectric response of an epitaxially strained* $BaTiO_3/SrTiO_3$ *superlattice: A first-principles study*, Phys. Rev. B **72**, 214121 (2005).

[114] K. Johnston, X. Huang, J. B. Neaton and K. M. Rabe, *First-principles study of symmetry lowering and polarization in* $BaTiO_3/SrTiO_3$ *superlattices with in-plane expansion*, Phys. Rev. B **71**, 100103 (2005).

[115] A. Sarkar and S. B. Krupanidhi, *Ferroelectric interaction and polarization studies in* $BaTiO_3/SrTiO_3$ *superlattice*, Journal of Applied Physics **101**, 104113 (2007).

[116] T. Tsurumi, T. Ichikawa, T. Harigai, H. Kakemoto and S. Wada, *Dielectric and optical properties of* $BaTiO_3/SrTiO_3$ *and* $BaTiO_3/BaZrO_3$ *superlattices*, Journal of Applied Physics **91**, 2284 (2002).

[117] A. Q. Jiang, J. F. Scott, H. Lu and Z. Chen, *Phase transitions and polarizations in epitaxial* $BaTiO_3/SrTiO_3$ *superlattices studied by second-harmonic generation*, Journal of Applied Physics **93**, 1180 (2003).

[118] T. Shimuta, O. Nakagawara, T. Makino, S. Arai, H. Tabata and T. Kawai, *Enhancement of remanent polarization in epitaxial* $BaTiO_3/SrTiO_3$ *superlattices with "asymmetric" structure*, Journal of Applied Physics **91**, 2290 (2002).

[119] W. Tian, J. C. Jiang, X. Q. Pan, J. H. Haeni, Y. L. Li, L. Q. Chen, D. G. Schlom, J. B. Neaton, K. M. Rabe and Q. X. Jia, *Structural evidence for enhanced polarization in a commensurate short-period* $BaTiO_3/SrTiO_3$ *superlattice*, Appl. Phys. Lett. **89**, 092905 (2006).

[120] S. Rios, A. Ruediger, A. Q. Jiang, J. F. Scott, H. Lu and Z. Chen, *Orthorhombic strontium titanate in* $BaTiO_3/SrTiO_3$ *superlattices*, Journal of Physics: Condensed Matter **15**, L305 (2003).

[121] E. Longo, E. Orhan, F. M. Pontes, C. D. Pinheiro, E. R. Leite, J. A. Varela, P. S. Pizani, T. M. Boschi, F. Lanciotti, A. Beltrán and J. Andrés, *Density functional theory calculation of the electronic structure of* $Ba_{0.5}Sr_{0.5}TiO_3$*: Photoluminescent properties and structural disorder*, Phys. Rev. B **69**, 125115 (2004).

[122] T. Harigai, D. Tanaka, H. Kakemoto, S. Wada and T. Tsurumi, *Dielectric properties of* $BaTiO_3/SrTiO_3$ *superlattices measured with interdigital electrodes and electromagnetic field analysis*, Journal of Applied Physics **94**, 7923 (2003).

[123] J. Lee, L. Kim, J. Kim, D. Jung and U. V. Waghmare, *Dielectric properties of* $BaTiO_3/SrTiO_3$ *ferroelectric thin film artificial lattice*, Journal of Applied Physics **100**, 051613 (2006).

[124] S. Lisenkov and L. Bellaiche, *Phase diagrams of* $BaTiO_3/SrTiO_3$ *superlattices from first principles*, Phys. Rev. B **76**, 020102 (2007).

[125] I. B. Misirlioglu, M. Alexe, L. Pintilie and D. Hesse, *Space charge contribution to the apparent enhancement of polarization in ferroelectric bilayers and multilayers*, Appl. Phys. Lett. **91**, 022911 (2007).

[126] V. R. Cooper, K. Johnston and K. M. Rabe, *Polarization enhancement in short period superlattices via interfacial intermixing*, Phys. Rev. B **76**, 020103 (2007).

[127] E. Bousquet, M. Dawber, N. Stucki, C. Lichtensteiger, P. Hermet, S. Gariglio, J.-M. Triscone and P. Ghosez, *Improper ferroelectricity in perovskite oxide artificial superlattices*, Nature **452**, 732 (2008).

[128] H.-M. Christen, E. D. Specht, D. P. Norton, M. F. Chisholm and L. A. Boatner, *Long-range ferroelectric interactions in* $KTaO_3/KNbO_3$ *superlattice structures*, Appl. Phys. Lett. **72**, 2535 (1998).

[129] E. D. Specht, H.-M. Christen, D. P. Norton and L. A. Boatner, *X-ray diffraction measurement of the effect of layer thickness on the ferroelectric transition in epitaxial* $KTaO_3/KNbO_3$ *multilayers*, Phys. Rev. Lett. **80**, 4317 (1998).

[130] M. Sepliarsky, S. R. Phillpot, D. Wolf, M. G. Stachiotti and R. L. Migoni, *Ferroelectric properties of* $KNbO_3/KTaO_3$ *superlattices by atomic-level simulation*, Journal of Applied Physics **90**, 4509 (2001).

[131] J. Sigman, D. P. Norton, H. M. Christen, P. H. Fleming and L. A. Boatner, *Antiferroelectric behavior in symmetric* $KNbO_3/KTaO_3$ *superlattices*, Phys. Rev. Lett. **88**, 097601 (2002).

[132] S. Hao, G. Zhou, X. Wang, J. Wu, W. Duan and B.-L. Gu, *Spontaneous polarizations of ultrashort-period epitaxial* $KNbO_3/(KTaO_3)_m$ *superlattices: An ab initio investigation*, Appl. Phys. Lett. **86**, 232903 (2005).

[133] N. Troullier and J. L. Martins, *Efficient pseudopotentials for plane-wave calculations*, Phys. Rev. B **43**, 1993 (1991).

[134] M. Dawber, N. Stucki, C. Lichtensteiger, S. Gariglio, P. Ghosez and J.-M. Triscone, *Tailoring the properties of artificially layered ferroelectric superlattices*, Adv. Mater **19**, 4153 (2007).

[135] A. P. Levanyuk and D. G. Sannikov, *Anomalies in dielectric properties in phase transitions*, Zh. Eksp. Teor. Fiz. **55**, 256 (1968).

[136] A. P. Levanyuk and D. G. Sannikov, *Improper ferroelectrics*, Usp. Fiz. Nauk **112**, 561 (1974).

[137] W. Cochran, *Structural Phase Transitions and Soft Modes*, Proceedings of the NATO Advanced Study Institute (Universitetsforlaget, 1971).

[138] J. Holakovský, *A new type of the ferroelectric phase transition*, Phys. Stat. Sol. B **56**, 615 (1973).

[139] S. C. Miller and W. F. Love, *Tables of Irreductible Representations of Space Groups and Co-Representations of Magnetic Space Groups* (Scandinavian University Books, 1967).

[140] K. M. Rabe and P. Ghosez, *First-principles studies of ferroelectric oxides*, in *Physcis of Ferroelectrics, A modern Perspective*, edited by K. Rabe, C. H. Ahn and J.-M. Triscone (Springer, 2007).

[141] W. Eerenstein, N. D. Mathur and J. F. Scott, *Multiferroic and magnetoelectric materials*, Nature **442**, 759 (2006).

[142] C. J. Fennie and K. M. Rabe, *Ferroelectric transition in* $YMnO_3$ *from first principles*, Phys. Rev. B **72**, 100103 (2005).

[143] R. A. McKee, F. J. Walker and M. F. Chisholm, *Crystalline oxides on silicon: The first five monolayers*, Phys. Rev. Lett. **81**, 3014 (1998).

[144] R. A. McKee, F. J. Walker, J. R. Conner, E. D. Speccht and D. E. Zelmon, *Molecular beam epitaxy growth of epitaxial barium silicide, barium oxide, and barium titanate on silicon*, Appl. Phys. Lett. **59**, 782 (1991).

[145] R. A. McKee, F. J. Walker and M. F. Chisholm, *Physical structure and inversion charge at a semiconductor interface with a crystalline oxide*, Science **293**, 468 (2001).

[146] O. Schütt, P. Pavone, W. Windl, K. Karch and D. Strauch, *Ab initio lattice dynamics and charge fluctuations in alkaline-earth oxides*, Phys. Rev. B **50**, 3746 (1994).

[147] M. Posternak, A. Baldereschi, H. Krakauer and R. Resta, *Non-nominal value of the dynamical effective charge in alkaline-earth oxides*, Phys. Rev. B **55**, R15983 (1997).

[148] S. Singh, S. Gupta and S. Goyal, *Elastic properties of alkaline earth oxides under high pressure*, Physica B **391**, 307 (2007).

[149] P. Cortona and A. V. Monteleone, *Ab initio calculations of cohesive and structural propertiesof the alkali-earth oxides*, J. Phys.: Condens. Matter **8**, 8983 (1996).

[150] A. R. Oganov and P. I. Dorogokupets, *All-electron and pseudopotential study of MgO: Equation of state, anharmonicity, and stability*, Phys. Rev. B **67**, 224110 (2003).

[151] D. Alfè, M. Alfredsson, J. Brodholt, M. J. Gillan, M. D. Towler and R. J. Needs, *Quantum monte carlo calculations of the structural properties and the B1-B2 phase transition of MgO*, Phys. Rev. B **72**, 014114 (2005).

[152] A. Strachan, T. Çağin and W. A. Goddard, *Phase diagram of MgO from density-functional theory and molecular-dynamics simulations*, Phys. Rev. B **60**, 15084 (1999).

[153] B. B. Karki and R. M. Wentzcovitch, *Vibrational and quasiharmonic thermal properties of CaO under pressure*, Phys. Rev. B **68**, 224304 (2003).

[154] M. Catti, *Ab initio predicted metastable TlI-like phase in the B1 to B2 high-pressure transition of CaO*, Phys. Rev. B **68**, 100101 (2003).

[155] D. H. Saunderson and G. E. Peckman, *The lattice dynamics of calcium oxide*, J. Phys. C : Solid St. Phys. **4**, 2009 (1971).

[156] Y.-D. Guo, X.-. Cheng, L.-P. Zhou, Z.-J. Liu and X.-D. Yang, *First-principles calculation of elastic nd thermodynamic properties of MgO and SrO under high pressure*, Physica B **373**, 334 (2006).

[157] K. H. Rieder, B. A. Weinstein, M. Cardona and H. Bilz, *Measurement and comparative analysis of the second-order raman spectra of the alkaline-earth oxides with a NaCl structure*, Phys. Rev. B **8**, 4780 (1973).

[158] A. Lichanot, *HartreeFock and density functional calculations of the elastic constants of the alkaline-earth oxides: comparison with experiment*, Solid State Communications **116**, 543 (2000).

[159] C. J. Först, C. R. Ashman, K. Schwarz and P. E. Blöchl, *The interface between silicon and a high-k oxide*, Nature **427**, 53 (2004).

[160] S. S. Chang, C. W. Tompson and L. D. Muhlestein, *Lattice dynamics of BaO*, J. Phys. Chem. Solids **36**, 769 (1975).

[161] K. H. Rieder, R. Migoni and B. Renker, *Lattice dynamics of strontium oxide*, Phys. Rev. B **12**, 3374 (1975).

[162] J. L. Jacobson and E. R. Nixon, *Infrared dielectric response and lattice vibrations of calcium and strontium oxides*, J. Phys. Chem. Solids **29**, 967 (1968).

[163] M. J. L. Sangster and A. M. Stoneham, *Calculations of off-centre displacements of divalent substitutional ions in CaO, SrO and BaO from model potentials*, Phil. Mag. B **43**, 597 (1981).

[164] A. Kalinichev, J. Bass, B. Sun and D. Payne, J. Mater. Res. **12**, 2623 (1997).

[165] G. Sághi-Szabó, R. E. Cohen and H. Krakauer, *First-principles study of piezoelectricity in tetragonal $PbTiO_3$ and $PbZr_{1/2}Ti_{1/2}O_3$*, Phys. Rev. B **59**, 12771 (1999).

[166] L. Bellaiche and D. Vanderbilt, *Intrinsic piezoelectric response in perovskite alloys: PMN-PT versus PZT*, Phys. Rev. Lett. **83**, 1347 (1999).

[167] H. D. Li, X. N. Zhang, Z. Zhang, Z. X. Mei, X. L. Du and Q. K. Xue, *Epitaxial growth of CaO films on MgO(001) surface: Strain relaxation at the CaO/MgO heterointerface*, Journal of Applied Physics **102**, 046103 (2007).

[168] H. Asaoka, T. Yamazaki, H. Yamamoto and S. Shamoto, *In situ characterization of the heterointerfaces between SrO films and dangling-bond-terminated Si surfaces*, Thin Sol. Films **508**, 175 (2006).

[169] O. Maksimov, V. D. Heydemann, P. Fisher, M. Skowronski and P. A. Salvador, *Structural properties of SrO thin films grown by molecular beam epitaxy on* $LaAlO_3$ *substrates*, Appl. Phys. Lett. **89**, 262903 (2006).

[170] P. A. Langjahra, T. Wagnera, F. F. Langeb and M. Ruhlea, *Epitaxial growth and structure of highly mismatched oxides with rock-salt structure on MgO*, J Cryst. Growth **256**, 162 (2003).

[171] J. Zachariae and H. Pfnur, *Growth conditions, stoichiometry, and electronic structure of lattice-matched SrO/BaO mixtures on Si(100)*, Phys. Rev. B **72**, 075410 (2005).

[172] G. Kresse and D. Joubert, *From ultrasoft pseudopotentials to the projector augmented-wave method*, Phys. Rev. B **59**, 1758 (1999).

[173] D. D. Fong, A. M. Kolpak, J. A. Eastman, S. K. Streiffer, P. H. Fuoss, G. B. Stephenson, C. Thompson, D. M. Kim, K. J. Choi, C. B. Eom, I. Grinberg and A. M. Rappe, *Stabilization of monodomain polarization in ultrathin* $PbTiO_3$ *films*, Phys. Rev. Lett. **96**, 127601 (2006).

[174] R. E. Cohen, ed., *Fundamental Physics of Ferroelectrics 2000*, volume 535 of *AIP Conf. Proc.* (AIP, Melville, NY, 2000).

[175] G. Geneste, E. Bousquet, J. Junquera and P. Ghosez, *Finite-size effects in* $BaTiO_3$ *nanowires*, Appl. Phys. Lett. **88**, 112906 (2006).

[176] D. D. Fong, G. B. Stephenson, S. K. Streiffer, J. A. Eastman, O. Auciello, P. H. Fuoss, and C. Thompson, *Ferroelectricity in ultrathin perovskite films*, Science **304**, 1650 (2004).

[177] A. Schilling, T. B. Adams, R. M. Bowman, J. M. Gregg, G. Catalan and J. F. Scott, *Scaling of domain periodicity with thickness measured in* $BaTiO_3$ *single crystal lamellae and comparison with other ferroics*, Phys. Rev. B **74**, 024115 (2006).

[178] C. Kittel, *Theory of the structure of ferromagnetic domains in films and small particles*, Phys. Rev. **70**, 965 (1946).